

1978

IMPULSE BREAKDOWN  
CHARACTERISTICS FOR ROD-PLANE  
GAPS IN MIXTURES OF SULPHUR-  
HEXAFLUORIDE AND NITROGEN.

ANGELO. YIALIZIS

*University of Windsor*

Follow this and additional works at: <http://scholar.uwindsor.ca/etd>

---

**Recommended Citation**

YIALIZIS, ANGELO., "IMPULSE BREAKDOWN CHARACTERISTICS FOR ROD-PLANE GAPS IN MIXTURES OF SULPHUR-HEXAFLUORIDE AND NITROGEN." (1978). *Electronic Theses and Dissertations*. Paper 2408.

This online database contains the full-text of PhD dissertations and Masters' theses of University of Windsor students from 1954 forward. These documents are made available for personal study and research purposes only, in accordance with the Canadian Copyright Act and the Creative Commons license—CC BY-NC-ND (Attribution, Non-Commercial, No Derivative Works). Under this license, works must always be attributed to the copyright holder (original author), cannot be used for any commercial purposes, and may not be altered. Any other use would require the permission of the copyright holder. Students may inquire about withdrawing their dissertation and/or thesis from this database. For additional inquiries, please contact the repository administrator via email ([scholarship@uwindsor.ca](mailto:scholarship@uwindsor.ca)) or by telephone at 519-253-3000ext. 3208.





National Library of Canada

Cataloguing Branch  
Canadian Theses Division

Ottawa, Canada  
K1A 0N4

Bibliothèque nationale du Canada

Direction du catalogage  
Division des thèses canadiennes

## NOTICE

The quality of this microfiche is heavily dependent upon the quality of the original thesis submitted for microfilming. Every effort has been made to ensure the highest quality of reproduction possible.

If pages are missing, contact the university which granted the degree.

Some pages may have indistinct print especially if the original pages were typed with a poor typewriter ribbon or if the university sent us a poor photocopy.

Previously copyrighted materials (journal articles, published tests, etc.) are not filmed.

Reproduction in full or in part of this film is governed by the Canadian Copyright Act, R.S.C. 1970, c. C-30. Please read the authorization forms which accompany this thesis.

**THIS DISSERTATION  
HAS BEEN MICROFILMED  
EXACTLY AS RECEIVED**

## AVIS

La qualité de cette microfiche dépend grandement de la qualité de la thèse soumise au microfilmage. Nous avons tout fait pour assurer une qualité supérieure de reproduction.

S'il manque des pages, veuillez communiquer avec l'université qui a conféré le grade.

La qualité d'impression de certaines pages peut laisser à désirer, surtout si les pages originales ont été dactylographiées à l'aide d'un ruban usé ou si l'université nous a fait parvenir une photocopie de mauvaise qualité.

Les documents qui font déjà l'objet d'un droit d'auteur (articles de revue, examens publiés, etc.) ne sont pas microfilmés.

La reproduction, même partielle, de ce microfilm est soumise à la Loi canadienne sur le droit d'auteur, SRC 1970, c. C-30. Veuillez prendre connaissance des formules d'autorisation qui accompagnent cette thèse.

**LA THÈSE A ÉTÉ  
MICROFILMÉE TELLE QUE  
NOUS L'AVONS REÇUE**

IMPULSE BREAKDOWN CHARACTERISTICS FOR  
ROD-PLANE GAPS IN MIXTURES OF SULPHUR  
HEXAFLUORIDE AND NITROGEN.

by

Angelo Yializis

A Dissertation

Submitted to the Faculty of Graduate Studies  
through the Department of Electrical Engineering  
in Partial Fulfillment of the Requirements for the  
Degree of Doctor of Philosophy at the  
University of Windsor

Windsor, Ontario, Canada  
1978

© Angelo Yializis

## ABSTRACT

Experimental results on negative and positive impulse breakdown characteristics of rod-plane gaps in  $\text{SF}_6/\text{N}_2$  and  $\text{SF}_6/\text{N}_2$  mixtures are presented, together with theoretical computations of streamer onset voltages in these gases.

The experimental results show that in positive rod-plane gaps, the impulse breakdown voltage of nitrogen increases approximately by a factor of two, with the addition of 0.1% to 0.2%  $\text{SF}_6$  at a total pressure of about 2 bar. Also, at a total pressure of 1 bar the breakdown voltage of  $\text{SF}_6/\text{N}_2$  mixtures with 80%  $\text{SF}_6$  rises 30% above that of  $\text{SF}_6$ . An attempt is made to explain this anomalous breakdown behaviour on the basis of the breakdown voltage measurements, and temporal and spatial information on the growth of ionization provided by photomultiplier and still photography results.

In the streamer onset calculations a new method was developed for the computation of electric fields, based on application of optimization techniques to the charge simulation method. The potential distribution of a rod-plane gap is obtained; and consideration is given to the solution of field configurations with non-axial symmetry. The new optimized approach proves to be more efficient, minimizing the time required to set up and implement a problem of this kind.

## ACKNOWLEDGEMENT

I would like to express my sincere thanks to my supervisor Professor E. Kuffel, Chairman of the Electrical Engineering Department for his supervision and guidance in this project.

I wish to thank Professor P.H. Alexander for his valuable assistance in the electrostatic field calculations and Professor W.J. McGonkey of the Molecular Physics group for his valuable discussions on part of this work.

I also wish to thank my wife Shirley for typing this dissertation and for her moral support through my graduate studies.

I am indebted to the National Research Council for providing funds for this project and awarding me the NRC graduate scholarship.

Thanks are also due to Mr. F.J. Ewasyshyn, L. Reiter, J.M. Novosad and D.K. Liebsuh for their technical assistance in the construction of the apparatus.

## TABLE OF CONTENTS

	<u>Page No</u>
ABSTRACT .....	iv
ACKNOWLEDGEMENTS .....	v
LIST OF FIGURES .....	ix
LIST OF TABLES .....	xvi
CHAPTER 1. INTRODUCTION .....	1
CHAPTER 2. IONIZATION AND BREAKDOWN MECHANISMS IN N <sub>2</sub> , SF <sub>6</sub> AND SF <sub>6</sub> /N <sub>2</sub> MIXTURES .....	4
2.1. Introduction .....	4
2.2. Ionization Phenomena in N <sub>2</sub> .....	5
2.3. Ionization and Breakdown Mechanisms in SF <sub>6</sub> ..	8
2.4. Ionization and Breakdown Phenomena in SF <sub>6</sub> /N <sub>2</sub> Mixtures .....	12
CHAPTER 3. ELECTROSTATIC FIELD CALCULATIONS .....	19
3.1. Introduction .....	19
3.2. Charge Simulation Techniques .....	21
3.2.1. Application to a Rod-Plane Gap .....	22
3.3. Limitations of the Conventional Charge Simulation Technique .....	25
3.4. Optimized Charge Simulation Technique .....	30
3.4.1. Application to a Rod-Plane Gap .....	31
3.5. Application of the Optimized Charge Simulation Technique to Field Distributions with Non-Axial Symmetry .....	41
CHAPTER 4. EXPERIMENTAL TECHNIQUES AND PROCEDURES .....	45



4.1. Experimental Design .....	45
4.2. Test Chamber .....	46
4.3. Electrode Arrangement .....	48
4.4. Gas Mixing Procedure .....	49
4.5. The Voltage Supply and the Data Acquisition System .....	51
4.6. Shielding of the Apparatus .....	54
4.7. Corona Onset Voltage Measurements .....	57
CHAPTER 5. EXPERIMENTAL RESULTS .....	58
5.1. Breakdown Characteristics of SF <sub>6</sub> under Negative and Positive Impulse Voltages .....	58
5.2. Negative Impulse Breakdown in SF <sub>6</sub> /N <sub>2</sub> Mixtures .....	65
5.3. Positive Impulse Breakdown in SF <sub>6</sub> /N <sub>2</sub> Mixtures .....	69
5.4. Temporal Growth of Ionization .....	77
5.4.1. Growth of Ionization in Negative Rod- Plane Gaps .....	78
5.4.2. Growth of Ionization in Positive Rod- Plane Gaps .....	80
5.5. Spatial Growth of Ionization .....	81
5.5.1. Spark Trajectories in N <sub>2</sub> , SF <sub>6</sub> and SF <sub>6</sub> /N <sub>2</sub> Mixtures .....	82
5.5.2. Impulse Corona in SF <sub>6</sub> /N <sub>2</sub> Mixtures with Low SF <sub>6</sub> Content .....	84
5.6. Corona Onset Measurements .....	85

CHAPTER 6. THEORETICAL ANALYSIS OF DISCHARGE CHARACTERISTICS IN SF <sub>6</sub> AND SF <sub>6</sub> /N <sub>2</sub> MIXTURES.....	95
6.1. Streamer Mechanism .....	95
6.2. Application of Streamer Theory for Calculating Streamer Onset Voltages in SF <sub>6</sub> and SF <sub>6</sub> /N <sub>2</sub> Mixtures .....	98
6.3. Streamer Onset Voltage Calculations in SF <sub>6</sub> , N <sub>2</sub> and SF <sub>6</sub> /N <sub>2</sub> Mixtures .....	100
6.4. Comparison of Theoretical and Experimental Results .....	104
6.5. Discussion .....	119
CHAPTER 7. DISCUSSION AND INTERPRETATION OF THE EXPERIMENTAL RESULTS .....	123
7.1. Negative Rod-Plane .....	125
7.2. The Negative Impulse Corona .....	129
7.3. Positive Rod-Plane - SF <sub>6</sub> /N <sub>2</sub> Mixtures with Less than 1% SF <sub>6</sub> .....	130
7.4. Positive Rod-Plane - SF <sub>6</sub> /N <sub>2</sub> Mixtures with SF <sub>6</sub> Content Higher than 5% .....	138
CHAPTER 8. CONCLUSION .....	140
8.1. Suggestions For Future Work .....	143
BIBLIOGRAPHY .....	145
APPENDIX 1 .....	152
APPENDIX 2 .....	171
APPENDIX 3 .....	190
APPENDIX 4 .....	198
VITA AUCTORIS .....	204

LIST OF FIGURES

No.	Page No
2.1 AC breakdown characteristics of SF <sub>6</sub> /N <sub>2</sub> mixtures .....	13
3.1 Simulation of the field distribution of a rod-plane gap. (a) Using one point charge and several line charges. (b) Using a number of ring charges, and a number of semi-infinite or segmented line charges.....	23
3.2 Percentage error of the simulated potential on cylindrical part of the electrode, for different gap lengths.....	26
3.3 Percentage error of the simulated potential on spherical part of the electrode, for different gap lengths.....	27
3.4 (a) A trigatron, with non-axial field distribution. (b) A high voltage divider, with field controlling electrodes. ....	29
3.5 Percentage error of the simulated potential along the spherical part of the electrode. (a) Results obtained using the constraints of Table II. (b) Results obtained using the constraints of Table I. ....	34
3.6 Percentage error of the simulated potential on the cylindrical part of the electrode. (a), and (b) correspond to constraints of Tables I and II respectively. ....	35
3.7 Percentage error of the simulated potential on the	

	cylindrical part of the electrode. (a) and (b) correspond to constraints of Tables I and II respectively. ....	36
3.8	Equipotential plot of a rod-plane electrode configuration with a gap length to point radius ratio $G/R = 10/1$ . ....	37
3.9	Equipotential plot of a rod-plane electrode configuration with a gap length to point radius ratio $G/R = 200/1$ . ....	38
3.10	Potential distribution along the axis of a rod-plane gap for various gap ratios $G/R$ . ....	39
3.11	(a) Cross-section of the spherical part of the electrode $V_1$ of figure 2(a). (b) Cross-section of the cylindrical part of the same electrode. (c) and (d) represent similar cross-sections as that of (a), before and after the optimization of the system. (e) Cross-section of electrode $V_2$ of figure 2(b). ....	42
4.1	Test Chamber. The photomultiplier is mounted in one of the chamber windows and it is optically aligned so that the full area of the cathode is illuminated. ....	47
4.2	Calibration curve for the HF50 gas analyzer. ....	50
4.3	Schematic diagram of apparatus and data acquisition system. ....	52
4.4	Schematic diagram of the grounding system of the impulse generator facility. Typical ground connect-	

	ions of a triax-cable and measuring instrument are shown, together with the generated ground loop GL. ....	56
5.1	Negative impulse breakdown voltage versus gap length characteristics of SF <sub>6</sub> for a pressure range of 1.0-5.0 bar. ....	60
5.2	Negative rod-plane impulse breakdown voltage-pressure relationship for SF <sub>6</sub> , in gap lengths ranging from 5 to 50 mm. ....	61
5.3	Negative impulse breakdown voltage-pressure characteristics of SF <sub>6</sub> for 10 mm gaps, compared with results obtained by similar experimental conditions. ....	63
5.4	Positive rod-plane impulse breakdown voltage-pressure characteristics for SF <sub>6</sub> . ....	64
5.5	Dependence of negative impulse breakdown voltage on mixture ratio for rod-plane gaps ranging from 5 to 50 mm at a total pressure of 1.0 bar. ....	65
5.6	Negative rod-plane impulse breakdown voltage and mixture ratio relationship for a pressure range of 1.0 - 5.0 bar. ....	67
5.7	Negative rod-plane impulse voltage and mixture ratio relationship for a pressure range of 1.0 - 5.0 bar. ....	68
5.8	Positive rod-plane impulse breakdown voltage and mixture ratio relationship for a pressure range of 1.0 - 5.0 bar, and a 10 mm gap length. ....	72
5.9	Positive rod-plane impulse breakdown voltage and mixture ratio relationship for a pressure range of	

1.0 - 5.0 bar. ....	73
5.10 Positive rod-plane impulse breakdown voltage-pressure relationship for various SF <sub>6</sub> /N <sub>2</sub> mixtures. Mixtures with 65% of SF <sub>6</sub> content or more at pressures less than 2.0 bar exhibit higher dielectric strength than pure SF <sub>6</sub> . ....	74
5.11 Positive rod-plane impulse breakdown voltage and pressure relationship for mixtures containing small traces of SF <sub>6</sub> . Gap length: 50 mm. ....	75
5.12 Positive rod-plane impulse breakdown voltage-pressure characteristics for; pure SF <sub>6</sub> , pure Nitrogen and an SF <sub>6</sub> /N <sub>2</sub> mixture with 0.2% of SF <sub>6</sub> content. ....	76
5.13 Photomultiplier records of discharge in various SF <sub>6</sub> /N <sub>2</sub> mixtures, (a) 5mm; (b) gap- 10mm; (c) gap - 50mm; (d) gap current with gap - 10mm. ....	79
5.14 Effect of pressure on the photomultiplier pulses in N <sub>2</sub> , in N <sub>2</sub> -containing 0.05% SF <sub>6</sub> and in SF <sub>6</sub> respectively. (a) N <sub>2</sub> ; (b) N <sub>2</sub> - SF <sub>6</sub> mixtures; (c) SF <sub>6</sub> . ....	80
5.15 Positive impulse breakdown of a 50mm rod-plane gap in SF <sub>6</sub> /N <sub>2</sub> mixtures with 0.1% SF <sub>6</sub> content. ....	87
5.16 In continuation of Figure 5.15 the effect of further reduction of the total pressure P <sub>t</sub> is shown in Figures (e) to (h) for pressures of 2.3 to 1.0 bar respectively. ....	88
5.17 Positive impulse breakdown of a 50 mm rod-plane gap in mixtures of SF <sub>6</sub> /N <sub>2</sub> at 1.7 bar of total pressure.	

Photographs (a) to (d) show the effect of the % of SF <sub>6</sub> content on the spark initiation point at the rod electrode. ....	89
5.18 Positive impulse breakdown of a 50 mm rod-plane gap in Nitrogen. The effect of pressure on the spark movement through the gap is, shown in photographs (a) and (b). ....	90
5.19 Positive impulse breakdown of a 50 mm rod-plane gap in SF <sub>6</sub> . ....	91
5.20 Positive impulse coronas in an SF <sub>6</sub> /N <sub>2</sub> mixture with 0.2% of SF <sub>6</sub> content. Photographs (a) and (b) show the difference in the position and intensity of the corona streamers, as the pressure increases from 0.1 to 1.7 bar respectively. ....	92
5.21 (a) Positive impulse corona in an SF <sub>6</sub> /N <sub>2</sub> mixture with 0.1% of SF <sub>6</sub> content and at a total pressure of 1.0 bar. (b) Negative impulse corona under the same mixture and pressure conditions. ....	93
5.22 Positive rod-plane impulse breakdown and corona onset voltage-pressure characteristics of nitrogen and a SF <sub>6</sub> /N <sub>2</sub> mixture with 0.2% SF <sub>6</sub> . ....	94
6.1 Field distribution along the axis of a rod-plane gap for various ratios G/R. ....	102
6.2 Experimental and theoretical corona onset voltage-pressure characteristics of a 10mm rod-plane gap in nitrogen. ....	105

6.3	Experimental and theoretical corona onset voltage-pressure characteristics of a 50mm rod-plane gap in nitrogen. ....	106
6.4	Experimental and theoretical corona onset voltage-pressure characteristics of a 10mm rod-plane gap in SF <sub>6</sub> . ....	107
6.5	Experimental and theoretical corona onset voltage-pressure characteristics of a 50mm rod-plane gap in SF <sub>6</sub> . ....	108
6.6	Comparison of Sangkasaad's (54) experimental results of breakdown voltage and corona onset of SF <sub>6</sub> in rod-plane gaps, with streamer onset values calculated by equation 6.4. ....	111
6.7	Experimental and theoretical corona onset voltage-mixture ratio characteristics of a 10mm rod-plane gap in SF <sub>6</sub> /N <sub>2</sub> mixtures. ....	113
6.8	Experimental and theoretical corona onset voltage-mixture ratio characteristics of a 50mm rod-plane gap in SF <sub>6</sub> /N <sub>2</sub> mixtures. ....	114
6.9	Comparison of experimental AC breakdown results of a rod-plane gap in mixtures of N <sub>2</sub> and SF <sub>6</sub> . ....	116
6.10	Critical length of initial avalanche (z <sub>c</sub> ), for a 5mm rod-plane gap in SF <sub>6</sub> /N <sub>2</sub> mixtures at a total pressure of 1.0 and 5.0 bar. ....	117
D.1	(a) Voltage input to the light emitting diode (LED), V <sub>3</sub> V <sub>2</sub> V <sub>1</sub> . (b) Photomultiplier current corresponding	



to different illumination intensities of the LED.

(c) Photomultiplier trace and relative streak photograph duration. (d) Photomultiplier current for single light pulses. .... 201

LIST OF TABLES

No.	Page No.
3.1 Constraints imposed on the variables of optimization. ...	40
3.2 Constraints imposed on the variables of optimization. ...	40
3.3 Optimized positions $(0, z_i')$ as derived from the constraints of table 3.1. ....	40
3.4 Optimized positions $(0_i')$ as derived from the constraints of table 3.2. ....	40
6.1 Streamer onset voltage $V_{onset}$ and critical length of the avalanche $z_c$ for 10mm and 50mm gaps in $SF_6/N_2$ mixtures at a total pressure of 1.0 bar. ....	118

## CHAPTER. 1.

### INTRODUCTION

In recent years sulphur hexafluoride ( $SF_6$ ) has found a number of applications as a dielectric insulating medium in a variety of high voltage apparatus. The high increase in power demand together with problems of land availability due to economical and environmental factors have recently accelerated research and development on gas insulated cables.  $SF_6$  for example, has a number of advantages over more conventional oil or solid insulation systems. These advantages include good voltage insulation, high current capacity due to low charging current, low dielectric losses and superior cooling capacity. However, re-evaluation of some of its insulating properties show that the dielectric strength of  $SF_6$ , unlike that of air, is highly sensitive to strong local fields which might be present in the cable due to dirt or metallic particles (1,2). In addition, a number of other limitations are also introduced due to the liquefaction of  $SF_6$  at low temperatures.

These problems have recently provided a strong incentive for the study of mixtures of  $SF_6$  and other gases such as Hydrogen, Nitrogen, Helium and Air (3-6). The use of a mixture of  $SF_6$  and a cheap inert gas would eliminate some of the problems and also reduce the cost, provided that the electric strength and other properties of the mixture are not inferior to those of the individual constituents.

The investigation undertaken by the author, had as an objective, the study of the dielectric behaviour of mixtures of sulfur hexafluoride and Nitrogen ( $SF_6 / N_2$ ) under certain controlled conditions. These conditions are designed to represent part of a more realistic system, so that quantitative data produced can be of use to future studies and related applications.

A literature survey on the subject indicated that very little was known about the properties of  $SF_6 / N_2$  mixtures in non-uniform fields subjected to impulse voltages. An experiment was then designed where the effect of a number of variables such as total pressure, ratio of the partial pressures of the two gases and gap length of a rod-plane gap were studied under the application of standard impulse voltages. The hemispherically capped rod-plane geometry provides excellent conditions for the study of the effect of non-uniformities in gas insulated systems. Most observations leading to the knowledge of such mechanisms as burst pulses, Trichel pulses and streamers, have been conducted in rod-plane gaps, because they provide localization of ionization (which improves observation), minimum interference of the plane electrode, convenience of fabrication and accuracy of adjustment.

The experimental investigation was mainly directed towards understanding the impulse breakdown behaviour of the  $SF_6 / N_2$  mixtures. Impulse breakdown measurements of both polarities were conducted for  $SF_6$ ,  $N_2$  and various mixtures of the two gases containing 0.01% to 100.0%  $SF_6$ , over a pressure range extending from 300 torr to 5 bar, and gap lengths ranging from 5 to 50 mm (52).

Previous work conducted in this laboratory (7,8) involved experimental studies of DC and Impulse breakdown of SF<sub>6</sub> and methods of determining the field distribution and corona onset in rod-plane gaps. This work led to a good understanding of corona onset computations in SF<sub>6</sub> and simultaneously indicated the need of a simpler and more efficient method for calculation of field distributions in rod-plane gaps. As a result of this, along with the experimental work in SF<sub>6</sub>/N<sub>2</sub> mixtures, the author undertook the task of developing or utilizing a more efficient method for the calculation of the field distribution in a rod-plane gap. This involved the development of an improved technique (53) for the calculation of electrostatic fields and subsequent application to the rod-plane geometry for computation of corona onset and breakdown voltage in SF<sub>6</sub> and SF<sub>6</sub>/N<sub>2</sub> mixtures.

## CHAPTER 2

### IONIZATION AND BREAKDOWN MECHANISMS IN $N_2$ , $SF_6$ AND $SF_6/N_2$ MIXTURES.

#### 2.1 Introduction

In this chapter a brief discussion of the mechanisms of ionization and breakdown will be presented for  $SF_6$ ,  $N_2$  and  $SF_6/N_2$  mixtures. The purpose of this is to familiarize the reader with previous work in this area, and so, facilitate the comprehension of conclusions and mechanisms presented in later chapters relating to the present investigations.

The discussion of breakdown phenomena in  $SF_6$  and  $N_2$  is kept short due to the availability of several review publications and previous work conducted in this laboratory (7,9). However, due to the lack of substantial information regarding the ionization processes in  $SF_6/N_2$  mixtures, reference is made to some work involving breakdown of  $N_2$  contaminated by small traces of  $O_2$ . The  $N_2/O_2$  ionization phenomena have been studied extensively over the years and one can benefit by correlating them with results from  $SF_6/N_2$  mixtures, which exhibit a certain degree of similarity due to the electronegative nature of  $O_2$  and  $SF_6$ .

Information on ionization and attachment coefficients is presented together with reactions leading to the formation of positive and negative ions in the two gases. The significance of these ions is discussed with reference to their effect in avalanche formation and spark onset.

## 2.2 Ionization phenomena in N<sub>2</sub>:

In uniform field distributions the voltage-current characteristics of N<sub>2</sub> follow Townsend's self-sustained discharge mechanism (10). The breakdown is a natural development of the prebreakdown ionization currents where the current I is given by

$$I = \frac{I_0 \exp(\alpha d)}{1 - \gamma(\exp(\alpha d) - 1)} \quad (2.1)$$

where  $\alpha$  = ionization coefficient

$\gamma$  = photo-ionization coefficient

d = gap length

The ionization coefficient is the most important factor in elementary ionization processes and it represents the number of electrons produced per centimeter by ionizing collisions.

For N<sub>2</sub>  $\alpha$  is given by the expression (10-12)

$$\frac{\alpha}{p} = A \exp(-Bp/E) \quad (2.2)$$

where p = pressure

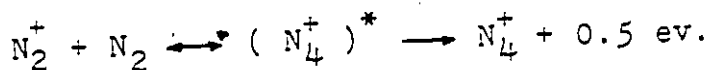
E = applied field

A = 5320 cm<sup>-1</sup> bar<sup>-1</sup>

B = 208 KV cm<sup>-1</sup> bar<sup>-1</sup>

Ionization of N<sub>2</sub> results in the formation of the N<sub>2</sub><sup>+</sup> ion via the reaction: N<sub>2</sub> + e → N<sub>2</sub><sup>+</sup> + 2e. The ground state of N<sub>2</sub><sup>+</sup> has an appearance potential of 15.6 ev (13). A number of other positive ions such as N<sub>3</sub><sup>+</sup>, N<sub>4</sub><sup>+</sup>, and N<sup>+</sup> can be present in the discharge and concentrations will vary with experimental conditions.

The most common of these is the N<sub>4</sub><sup>+</sup> produced by the reaction:



The concentration of  $N_4^+$  varies with  $E/p$  and it prevails over  $N_2^+$  at low  $E/p$  and higher pressures (14). The 0.5 ev energy is given out in the form of photon emission. The  $N_2$  molecule has a number of metastable and active states which can complicate the breakdown mechanism of  $SF_6/N_2$  mixtures in non-uniform fields.

The mechanism of breakdown of  $N_2$  in non-uniform field distributions will depend on the electrode geometry, polarity, and gas composition. The latter factor is very important due to the sensitivity of ionization phenomena in  $N_2$  contaminated with other gas impurities.

Weissler (15) investigated the mechanism of breakdown of pure  $N_2$  in a point-plane electrode arrangement under DC voltages. He reported that in the positive point-plane, unlike air where one observes a corona glow spread uniformly over the point, the corona in  $N_2$  seemed to be a succession of electron avalanches that formed at the tip of the point in a form of a localized spot. As voltage increases the corona becomes a luminous glow that extends to the cathode region. At higher voltage corona streamers appeared superimposed on the continuous glow and breakdown was initiated with further voltage increase, when the streamers reached a critical number and intensity.

Under negative point-plane conditions corona onset occurred at a lower voltage than the positive corona and again it appeared to be concentrated at the front of the spherical tip. At higher voltages a glow discharge was observed with



Crooke's and Faraday's dark spaces, negative glow and positive column. Further increase of the voltage resulted in a constriction of the glow, sudden increase in the current and transition to breakdown.

Weissler's results showed that no Trichel pulses or other irregularities were observed due to the chemical purity of the nitrogen. The addition of small amounts of  $O_2$  into pure  $N_2$  (0.1%) resulted in the generation of Trichel pulses(15). The choking effect of the space charge associated with these pulses caused a decrease in the corona current to about one-half of its magnitude in pure  $N_2$ . Similarly, in positive-plane corona, addition of less than 0.1% of  $O_2$  into pure  $N_2$  produced heavy corona streamers and burst pulses, but the magnitude of the corona current remained the same. The presence of  $O_2$  also helped to spread the corona glow over the tip of the point by increasing the efficiency of photoionization (15).

A number of investigations have been conducted in  $N_2$  containing small traces of  $O_2$  (0.1-1.0%)(16). Secondary electron coefficients have been calculated for a number of different electrode materials, in order to determine the origin of anomalous breakdown phenomena occurring in the mixture of the two gases. In contrast, very little data is available on the ionization parameters of  $SF_6/N_2$  mixtures and this is expected to make difficult the interpretation of the experimental results.

### 2.3 Ionization and Breakdown Mechanisms in SF<sub>6</sub>

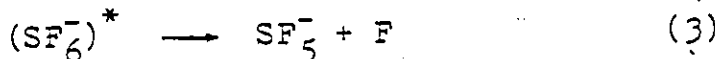
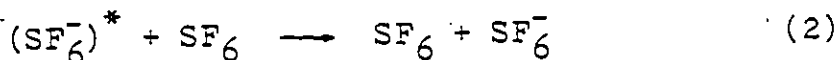
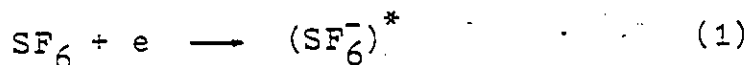
Among many electronegative gases having high dielectric strength, SF<sub>6</sub> has the most favourable properties that qualify it for high voltage insulation. Some of these properties are: chemically inert, non-flammable, incombustible, non-toxic and good heat conductor.

Experimental investigations in non-uniform fields have shown that the positive voltage-pressure characteristics exhibit a pronounced maximum at a pressure  $p_{max}$  in the range of 1 to 3 bar, depending on the electrode configuration. At a pressure  $p_{min}$  (slightly higher than  $p_{max}$ ) the breakdown voltage drops suddenly to a considerably lower level and then it increases again as the pressure increases (17). The most widely accepted explanation to date for the mechanism of breakdown in the region prior to  $p_{min}$  (known as the corona stabilised region), is given by Foord (18) and later supported by Works and Dakin (19) and Howard (55). In the corona stabilized region, streamer onset is observed to occur at a voltage considerably lower than spark onset. The corona streamers are generated in the high field region close to the anode and move towards the cathode leaving behind them a positive space charge. With the help of photoionization the positive charge spreads around the tip of the anode, producing in this manner a positive charge sheath which chokes further growth of ionization. The spark initiates when the avalanche activity in the cathode region is producing negative ions at a rate sufficiently high to neutralize the positive charge, allowing streamers to reach the cathode. As the pressure increases, photon

absorption of  $SF_6^-$  also increases, reducing photoionization in the anode area, and thus weakening the positive sheath. This brings the breakdown voltage closer to corona onset and above  $p_{min}$ , spark onset and corona onset occur at the same voltage level.

In general, the high dielectric strength of  $SF_6$  is the result of the electronegative character of the gas. That is, its electrophilic nature promotes the formation of negative ions by the capture of free electrons, before the electron energies become high enough to produce ionization.

Experimental data shows that the electron attachment in  $SF_6$  leads to the formation of a number of negative ions, with  $SF_6^-$  and  $SF_5^-$  as the principal species (21 - 24).  $SF_6^-$  and  $SF_5^-$  are produced by the following resonance capture reactions of near-zero-energy electrons.

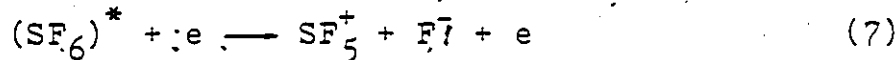
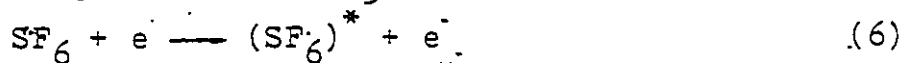
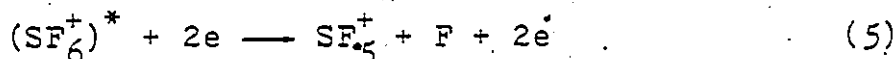
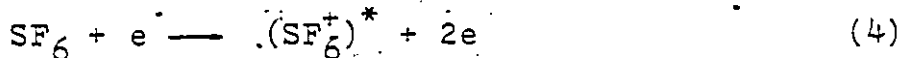


Reaction (1) requires electrons with energy of less than 0.1ev and the width of the peak of the resonance is approximately 0.05 ev.  $(SF_6^-)^*$  is a vibrationally excited ion which can stabilize through reaction (2), or with any other background gas.

Once stabilized, the life time of  $SF_6^-$  against autodetachment has been found to be of the order of tens of microseconds (25,27).

Reaction (3) is the result of a dissociative attachment process that can occur before the  $(SF_6)^*$  stabilizes. The activation energy for the production of  $SF_5^-$  has been found to be 0.43ev by some authors (25) or less than 0.1ev by others (21). The most abundant of the ions is the  $SF_6^-$  (28,30). However, it has been shown that the relative concentrations of  $SF_6^-$  and  $SF_5^-$  vary with E/p (79). High concentrations of  $SF_6^-$  occur at:  $E/p < 60 \text{ Vcm}^{-1} \text{ torr}^{-1}$  and of  $SF_5^-$  at:  $E/p > 80 \text{ vcm}^{-1} \text{ torr}^{-1}$ .

In the positive ion spectrum of  $SF_6$ ,  $SF_5^+$  is the most dominant ion. Dibler and Mohler found the first appearance potential of  $SF_5^+$  to be  $15.9 \pm 0.2 \text{ ev}$  (31). This value is in agreement with the results of Ta-Kong Liu et-al (32) who measured the absorption spectrum of  $SF_6$  in the vacuum ultraviolet region, and found a strong continuous absorption beginning fairly sharply at  $802 \text{ \AA}$  ( $15.5 \text{ ev}$ ), and continuing to shorter wavelengths. The reaction involved, is a secondary capture process followed by dissociation.



This suggests that the ionization potential of  $SF_6$  lies higher than the dissociation energy of  $SF_6$  into  $SF_5^+$  and  $F^-$ .

The appearance of the  $SF_5^+$  indicates the beginning of ionization in the gas, which will be governed by the values of the ionization and attachment coefficients ( $\alpha$  and  $\eta$  respectively). Both of these coefficients are a function of the field strength E and

the pressure p. Geballe and Harrison (30) and Bhalla and Griggs (31) have measured  $\alpha/p$  and  $\eta/p$  as functions of  $E/p$ , and  $(\alpha-\eta)/p$  can be approximated by the linear relation

$$(\alpha-\eta)/p = C(E/p - (E/p)_{cr}) \quad (2.4)$$

where  $C = 27 \text{ KV cm}^{-1}$

$$(E/p)_{cr} = 89 \text{ KV cm}^{-1} \text{ bar}^{-1}$$

Ionization by electron collision will therefore take place in the gap region where the ionization coefficient is equal or greater than the attachment coefficient.

#### 2.4. Ionization and Breakdown Phenomena in SF<sub>6</sub>/N<sub>2</sub> Mixtures.

One of the first investigations of SF<sub>6</sub>/N<sub>2</sub> mixtures was that of Foord (32). Using a positive point to plane gap under DC voltages Foord observed that the addition of nitrogen to SF<sub>6</sub> increased the corona current in a manner proportional to the partial pressure of nitrogen. In addition, by keeping the partial pressure of SF<sub>6</sub> constant and varying the total pressure, it was shown that the voltage-pressure characteristics of the mixtures exhibited a negative slope similar to that of pure SF<sub>6</sub>. The overall indication was that the addition of nitrogen in SF<sub>6</sub> reduced the dielectric strength of the mixture and a speculative explanation referred to a probable reduction or modification of the relative importance of the negative ion-forming mechanism.

Howard (20) examined and compared the electrical insulation properties of a number of electronegative gases and their mixtures with nitrogen, under quasi-uniform and non-uniform field conditions. In quasi-uniform fields with AC voltages, the dielectric strength of a mixture at constant total pressure decreased as the partial pressure of nitrogen increased. As shown in Figure 2.1a the voltage - mixture ratio characteristics exhibit a considerable change in their slope at about 10% of SF<sub>6</sub> content. In non-uniform fields as shown in Figure 2.1b, it can be seen that the addition of 20-40% of N<sub>2</sub> in SF<sub>6</sub> resulted in an increase of the dielectric strength of the mixture, which becomes more pronounced as the gap length increases. These curves provided probably the first illustration of the

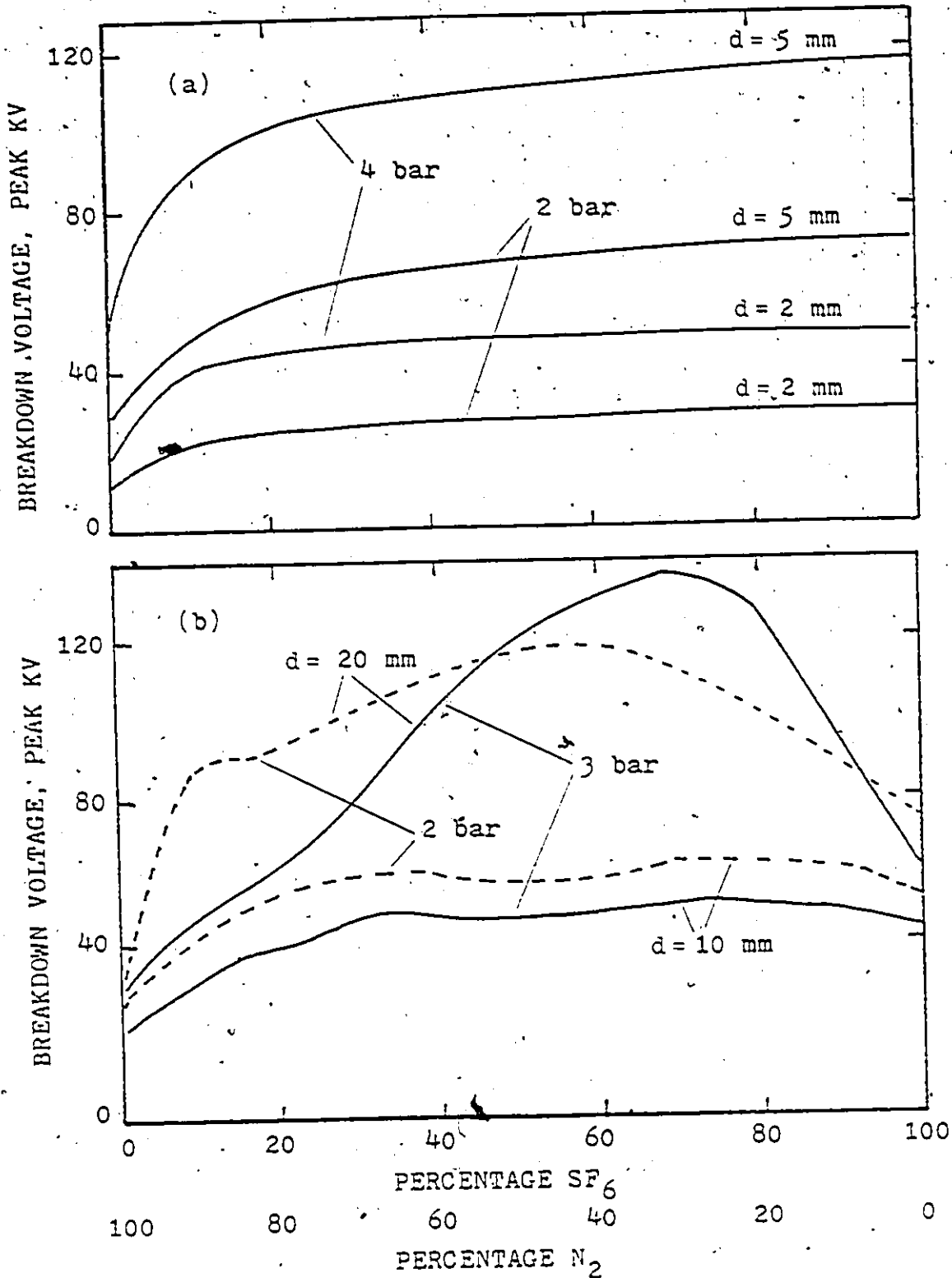


Figure 2.1 AC breakdown characteristics of SF<sub>6</sub>/N<sub>2</sub> mixtures (20). (a) 50 mm diameter sphere-sphere gap. (b) point-sphere gap.

possible advantages of the  $SF_6/N_2$  mixtures as an insulating medium. However, while Howard's publication received wide recognition for information contained on the properties of various electronegative gases, it did not generate noticeable interest in the area of gas mixtures.

A number of publications on mixtures of  $SF_6/N_2$  and  $SF_6$ /air followed(33-38). Most investigations were conducted in uniform or near-uniform fields and very few dealt with mixtures of  $SF_6/N_2$  with less than 10% of  $SF_6$  content.

Davidson et-al(39) conducted an investigation of corona and breakdown of  $SF_6/N_2$  mixtures in a positive point-plane gap under static and flowing gas conditions. Observation of the corona streamers showed that their amplitude decreased as %  $SF_6$  content increased, and the streamers were highly localized around the anode tip and did not cross the gap before spark onset. The amplitude of the streamers increased as the % of  $SF_6$  content was reduced below 0.1%. The breakdown voltage also increased by increasing the partial pressure of  $SF_6$  and was found to be 2.5 times that of pure  $N_2$  with 1% of  $SF_6$  content. Gas flow resulted in an increase of the breakdown voltage in mixtures containing 1% or less  $SF_6$ , and a slight increase for higher  $SF_6$  contents. This was explained as the result of a redistribution of the negative ion charge that had an effect on the shielding produced by the corona space-charge in the anode region.

Similar results were reported on impulse breakdown of mixtures of  $SF_6$  and  $H_2$  in positive rod-plane gaps by Farish et-al. (3). They found that impulse breakdown of  $H_2$  is extremely



sensitive to the addition of small traces of  $SF_6$ . For pressures up to 2 bar the breakdown voltage of  $SF_6/H_2$  with 0.2% of  $SF_6$  was found to be 2.0 times greater than that of pure  $H_2$ . Impulse measurements in  $SF_6/N_2$  mixtures conducted by Baumgartner (41) did not show any similar behaviour. The reason for this is that Baumgartner did not investigate  $SF_6/N_2$  mixtures with low  $SF_6$  content, and he conducted the experiments in a quasi-uniform coaxial-cylinder electrode geometry. Earlier work of Baumgartner (42) in rod-plane gaps indicated that the AC breakdown voltage increased 10% above that of pure  $SF_6$  with 80%  $SF_6$  content. Also, it was observed that the maximum in the breakdown voltage-mixture ratio characteristics moved towards lower concentrations of  $SF_6$  as the total pressure of the mixture increased.

More recently Watanabe and Takuma (5) examined the dielectric behaviour of mixtures of  $SF_6/N_2$  and  $SF_6$ /air in long rod-plane gaps (30-50 cm) under impulse voltages. Their findings show that addition of small percentages of  $SF_6$  into nitrogen does not increase the breakdown voltage of the mixture above that of pure  $N_2$ . However, in  $SF_6$ /air mixtures with 0.8% of  $SF_6$  content the breakdown voltage increased by about 80% higher than that of pure  $SF_6$ . One limitation in their experiment was that the pressure was kept constant at 1 bar, hence, any pressure effects in the behaviour of the mixtures could not have been observed. It is also interesting to note that for all gaps examined, the impulse breakdown voltage of  $SF_6$  was lower than that of  $N_2$  and air.

A considerable amount of attention has also been exhibited in the use of  $SF_6/N_2$  mixtures in circuit interrupters, where the

gas mixture is tested for its thermal conductivity and arc quenching capacity. Garson (41) and Grant et al. (6) have shown that mixtures of SF<sub>6</sub>/N<sub>2</sub> with 50% SF<sub>6</sub> content have superior arc interruption capability when compared to pure SF<sub>6</sub>. Garson tested the recovery voltage capability of a synchronous interrupter over the pressure range of 15 to 19 bar and found that the rate of rise of recovery voltage increased by 1.4 times when a 50% SF<sub>6</sub>/N<sub>2</sub> mixture was used instead of pure SF<sub>6</sub>.

The mechanism of breakdown in the SF<sub>6</sub>/N<sub>2</sub> mixtures is still at the speculation stage and there is no published data on measurements of the effective ionization coefficient of the different mixtures. However, breakdown results in uniform and quasi-uniform fields such as the ones presented in Fig. 2.1(a), do not show any irregularities and semi-empirical relations for streamer onset have been developed that are in agreement with experiments.

Takuma et-al. (37) proposed a simple equation that relates the breakdown voltage of the mixture under uniform field conditions with those of the individual gases.

$$V_m = V_2 + \frac{K}{K + C(1-K)} (V_1 - V_2) \quad (2.4)$$

where  $V_m$  = breakdown voltage of the mixture

$V_1, V_2$  = breakdown voltage of the two component gases

$K$  = partial pressure ratio of gas 1

$C$  = constant, depending on gas mixture and experimental system.

Takuma showed that for  $C=0.08$  there is good agreement between equation (2.4) and Howards experimental results of Figure 2.1a.

Although the agreement with the experimental results is good, the use of equation (2.4) is considered to be a rather impractical approach for prediction of breakdown voltage in SF<sub>6</sub>/N<sub>2</sub> mixtures, because, it requires advance knowledge of voltages V<sub>1</sub> and V<sub>2</sub> for a particular electrode arrangement.

Wieland (35), developed an improved relation for the calculation of V<sub>m</sub> in uniform fields, by showing that the ionization and attachment coefficients in a mixture, are a function of the total pressure, and the coefficients of the individual components added in a manner proportional to their partial pressures. Baumgartner (38) postulating Wieland's assumption derived an expression for the calculation of corona onset in quasi-uniform fields, using streamer mechanism theory which will be discussed in a later chapter. The effective ionization coefficient for the SF<sub>6</sub>/N<sub>2</sub> mixtures as derived by Baumgartner is given by the relation

$$\frac{\alpha_{eff}}{p} = \frac{1}{k_1+1} K (E/p - (E/p)_{cr}) \frac{k_1 A}{k_1+1} \exp(-Bp/E) \quad (2.5)$$

where  $\alpha_{eff}$  = effective coefficient of ionization

p = total pressure

k<sub>1</sub> = (partial pressure of N<sub>2</sub>) / (partial pressure of SF<sub>6</sub>)

K = 27 KV<sup>-1</sup>

A = 5320 cm<sup>-1</sup> bar<sup>-1</sup>


B = 208 KV cm<sup>-1</sup> bar<sup>-1</sup>

(E/p)<sub>cr</sub> = 89 KV cm<sup>-1</sup> bar<sup>-1</sup>

The above relation has not been validated as yet by direct measurement of the  $\alpha_{eff}$ . However, Weiland's and Baumgartner's experimental results show good agreement with Townsend's and

streamer breakdown mechanisms that make use of equation (2.5). Similarly, Crichton et-al. (43,44) have used the above expression, in their calculations of breakdown voltage in  $SF_6/N_2$  mixtures in uniform fields perturbed by a projection and coaxial cylinder electrodes having a specified surface roughness. Their analysis shows a good agreement with experiments and this indicates that equation (2.5) can in fact lead to meaningful results if used within certain constraints imposed by factors such as pressure, gap length and field uniformity.

In general, the existing information on the dielectric properties of the  $SF_6/N_2$  mixtures indicates that certain properties of the mixtures are superior to those of pure  $SF_6$  and nitrogen. This fact justifies the undertaking of systematic studies such as the one presented in this work, which will help to identify and understand the dielectric behaviour of the mixtures, especially with respect to basic and applied aspects such as, the theoretical prediction and the measurement of their breakdown voltage characteristics under various experimental conditions.



## CHAPTER 3

### ELECTROSTATIC FIELD CALCULATIONS

#### 3.1 Introduction.

In calculating electric field distributions, analytical solution of Laplace's equation can only be obtained for a limited number of electrode configurations with practical significance. Field distributions of some of the geometries used in high voltage apparatus, such as the hemispherically capped cylindrical point-plane gap, cannot be generated by such simple charge distributions and therefore, cannot be expressed in simple analytical terms.

As an alternative to purely analytical techniques, numerical methods are often used to solve such problems. These include the Finite Difference method, the Finite Element method, and the Charge Simulation technique. In the application of the finite-difference method, the field region is usually covered with a rectangular grid. In the finite-element method, the whole region is subdivided into a large number of triangular elements, each being defined by three nodes. Within each element the electrostatic potential is a function of the potentials at the nodes, or vertices, of the triangle. It is difficult to see which one of these methods is more economical and reliable due to their basic similarities. In addition, solution for potential or field values in unbounded regions (regions that are not surrounded by electrode surfaces) becomes intricate and difficult to implement.

The charge-simulation method is basically a numerical

method but it results in an analytical expression for the field quantities of interest, expressed in terms of a number of fictitious charges or finite charge distributions. These charges are placed outside the region where the field is to be calculated (that is, usually inside the volume occupied by the electrodes), and their exact positions and values are found so that the boundary conditions of the particular configuration are satisfied to an acceptable degree of accuracy.

Usually the method of solution used is a direct one which involves a priori assumptions about the location of the equivalent charge distribution, which are made on the basis of experience, and may be different for various researchers. The assumptions determine the degree of accuracy in the result.

The work described here makes use of the charge simulation technique to calculate the potential and field distribution in a rod-plane electrode arrangement. The limitations of the technique at the present state of the art are examined and analyzed for possible improvement. A new optimized version of the charge simulation technique is developed, which, with the use of optimization techniques eliminates the need for assumptions concerning the position of the charges and the points where the boundary conditions are applied. The optimized version has the advantage of minimizing reliance on personal experience and makes the achievable accuracy optimally related to the computing resources of the worker.

### 3.2 Charge Simulation Technique.

For a given charge distribution the potential  $\phi(r, z)$  is a summation of the potentials resulting from the individual charges.

$$\phi(r, z) = \sum_{i=1}^n P_{ji} Q_i = V_j \quad j=1, 2, \dots, m \quad (3.1)$$

where  $n$ : number of charges in the system

$m$ : number of points at which the potential is specified

$P_{ji}$ : potential coefficients which are also written as

$$P_{ji} = P(r_j, z_j, r'_i, z'_i) \quad (3.2)$$

where  $(r_j, z_j)$  are the coordinates of a point on the electrode boundary and  $(r'_i, z'_i)$  are the coordinates of the source point charge  $Q_i$ .

For a set of  $m$  points selected on a surface at potential  $V^{(1)}$ , equation (3.1), when written in a matrix form becomes

$$\begin{bmatrix} P_{11} & P_{12} & \dots & P_{1n} \\ P_{21} & P_{22} & & \\ \vdots & & & \\ P_{n1} & & & P_{nn} \end{bmatrix} \begin{bmatrix} Q_1 \\ Q_2 \\ \vdots \\ Q_n \end{bmatrix} = \begin{bmatrix} V^{(1)} \\ V^{(1)} \\ \vdots \\ V^{(1)} \end{bmatrix} \quad (3.3)$$

Ordinarily, the number of boundary points  $m$  is equal to the number of charges  $n$ . Given a particular configuration the coefficients  $P_{ji}$  will be determined by the boundary conditions. Hence, equation (3.3) can then be solved for the charges  $Q_i$ .

### 3.2.1 Application to a Rod-Plane Gap.

One of the first applications of the charge simulation technique in high voltage problems was in the calculation of the field distribution of rod-plane gaps. As shown in Figure 3.1, there are a number of ways that one can simulate this distribution. A solution involving the charge distribution of Figure 3.1(a) was presented by Abou-Seada (46) and earlier by Leob (47). They used one point charge and nine semi-infinite line charges. The solution yielded an equipotential surface with an error of  $\pm 3\%$  in the neighbourhood of the spherical tip(46). However the error increased substantially for values of the gap-length to point-radius ratio less than fifty ( $G/R < 50$ ). This error was found to be due to a system equation slightly different from the present equation (3.3) (40, 45). Thus, using part of the information given by Leob and Seada on the positions  $(r_i', z_i')$  and  $(r_j, z_j)$  and then forming the matrix equation (3.3), the accuracy of the simulated potential for values of  $G/R$  down to  $G/R = 1$  was greatly improved.

The solution of equation (3.3) proceeds as follows. The plane is assumed to be infinite at zero potential and the electrode semi-infinite with potential  $V^{(1)}$  set to one volt. Therefore, on the cylindrical part we have ..

$$\phi(r, z) = \phi(R, z) \quad z \geq G+R \quad (3.4)$$

On the spherical part, transforming the variables as shown in Figure 3.5 we have



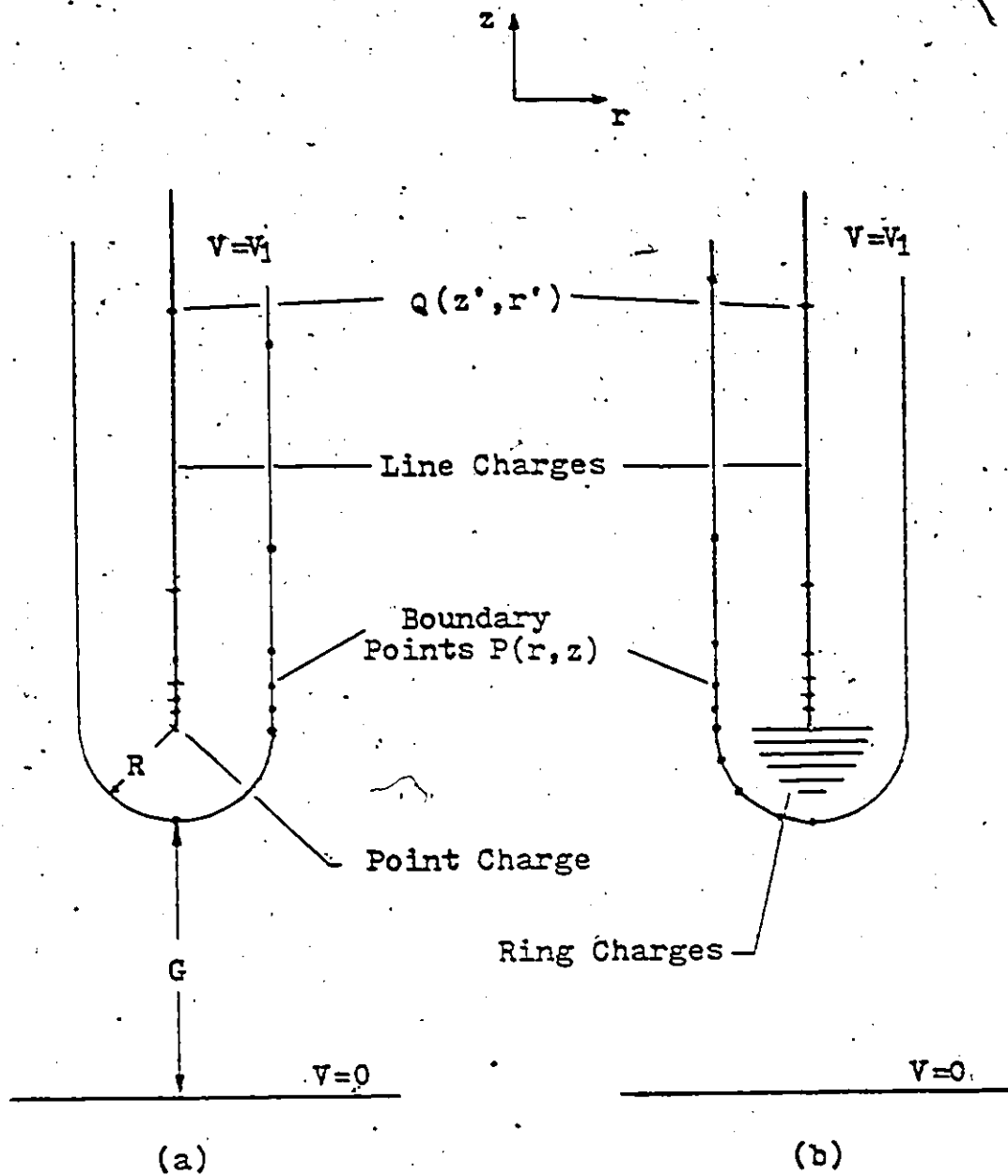


Figure 3.1 Simulation of the field distribution of a Rod-Plane gap. (a) Using one point charge and several line charges. (b) Using a number of ring charges, and a number of semi-infinite or segmented line charges.

$$(r, z) = (\sin\theta, G+R-\cos\theta) \quad (3.5)$$

The analytic expression for the potential  $\phi(r, z)$  of the nine semi-infinite lines and one point charge with their corresponding image charges, is

$$\begin{aligned} \phi(r, z) = & \sum_{i=1}^9 Q_i \ln \left[ \frac{z'_i + z + (r^2 + (z'_i + z)^2)^{\frac{1}{2}}}{z'_i - z + (r^2 + (z'_i - z)^2)^{\frac{1}{2}}} \right] \\ & + Q_{10} \left[ \frac{1}{(r^2 + (z'_{10} - z)^2)^{\frac{1}{2}}} - \frac{1}{(r^2 + (z'_{10} + z)^2)^{\frac{1}{2}}} \right] \quad (3.6) \end{aligned}$$

By convention the radius R is set to unity so that the gap-length G is also equal to the ratio G/R, which relates to the uniformity of the gap field along the axis of symmetry.

Equations (3.4), (3.5) and (3.6) were used to generate the matrix equation (3.3). A computer program was written (in Fortran) for the generation and solution of equation (3.3). Comments and a computed example are included in Appendix 1. Having solved for the charges  $Q_i$ , equation (3.6) can now be used to calculate the potential  $\phi(r, z)$  at any point in the inter-electrode area, provided that the simulated potential  $\phi(r, z)$  on the boundary of the electrode is equal to one volt.

In order to check the accuracy of the simulated potential distribution, the percent error

$$\left( \frac{V_{\text{applied}} - V_{\text{simul.}}}{V_{\text{applied}}} \right) \times 100 \quad (3.6(a))$$

is calculated for points along the boundary of the electrode.

The results are shown in Figures 3.2 and 3.3. In Figure 3.2 the percent error for various gap-lengths is plotted versus distance along the cylindrical part of the electrode from the point

$G+R = G+1$  to  $G+1+50$  that is, 50 radius units away from the tip the percent error along the spherical part of the electrode is shown in Figure 3.3. Here the position on the spherical boundary is given by the radial distance from the z-axis through equation (3.5). Figures 3.2 and 3.3 show that the percent error of the simulated potential along the cylindrical boundary is small, when compared with uncertainty in experimental measurements or other numerical techniques, and trivial along the spherical part which represents the region of interest (since most breakdown criteria involve calculations along the axis of highest field stress).

### 3.3 Limitations of the Conventional Charge Simulation

#### Technique

In applying the charge simulation method to calculate field distributions, the main task is to find the proper positions  $(r_i', z_i')$  and  $(r_j, z_j)$ . In order to gauge the amount of effort required to solve the rod-plane configuration, a number of calculations were made disregarding previous information on the positions  $(r_j, z_j)$ . Different sets of  $(r_i, z_i)$  and  $(r_i', z_i')$  were carefully selected by considering the distribution of each of these locations with respect to each other, and to the electrode boundary. The results showed that even after the first few adjustments, the error in the neighbourhood of the spherical tip was larger than 10%.

A solution of the field distribution for the case of Figure 3.1(b) was attempted using ten ring charges and five

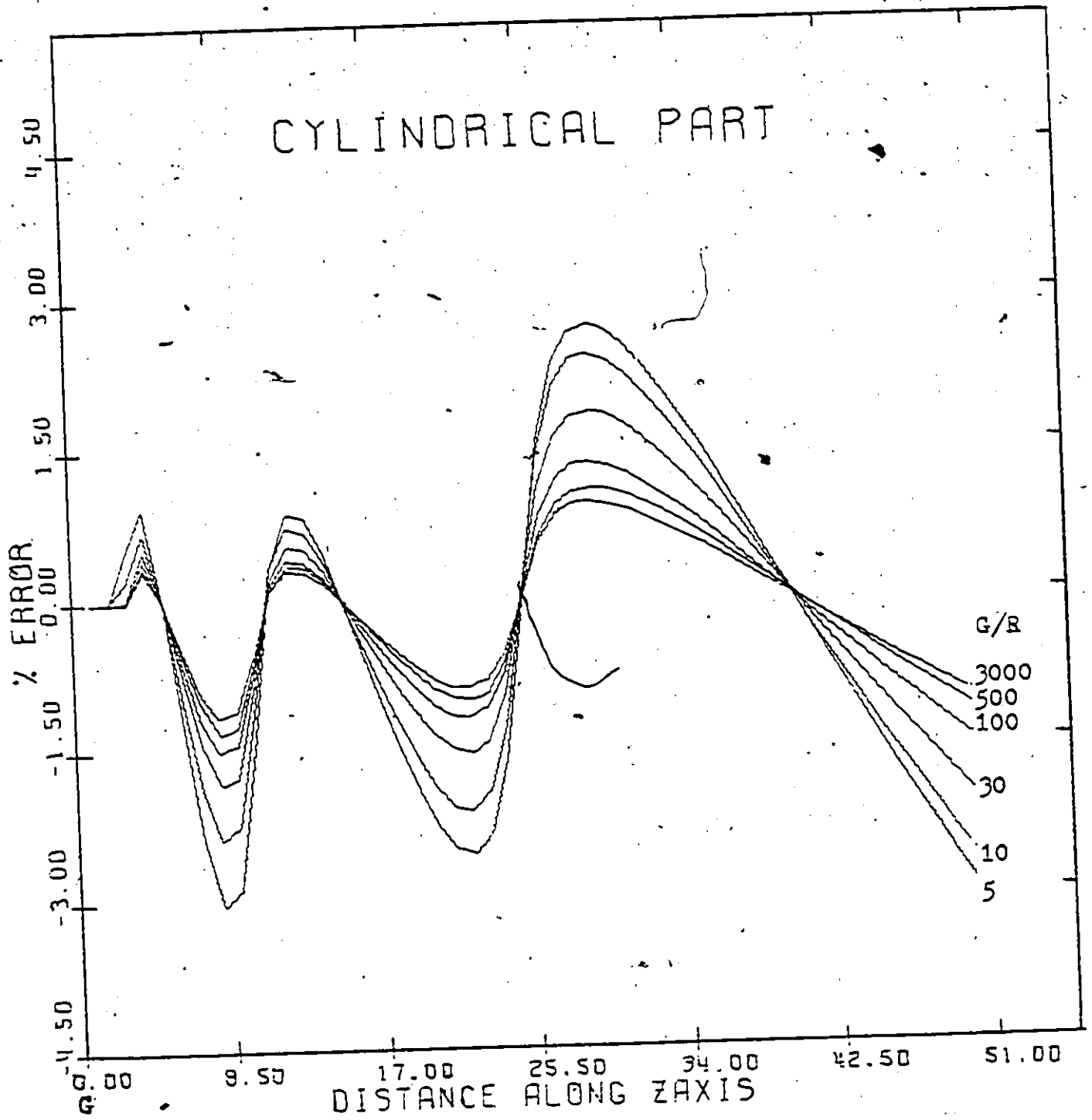


Figure 3.2 Percentage error of the simulated potential on cylindrical part of the electrode, for different gap lengths.

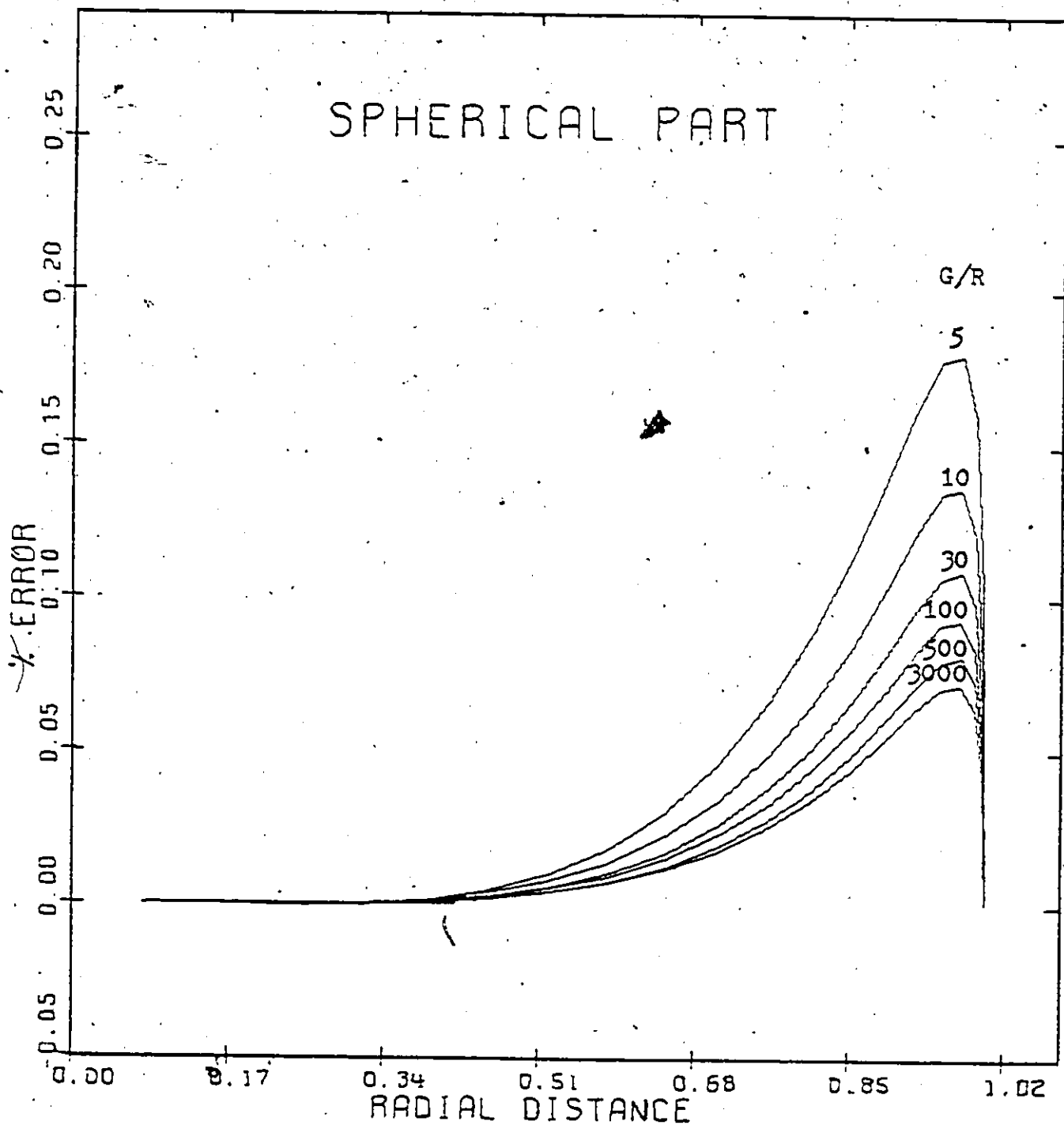


Figure 3.3 Percentage error of the simulated potential on spherical part of the electrode, for different gap lengths.

semi-infinite line charges. Again the results indicated that a considerable amount of time would have to be spent in finding a good combination of points  $(r_i, z_i)$  and  $(r_j, z_j)$  in order to produce a uniformly equipotential surface.

The difficulty increases when one attempts to solve for more complicated field distributions. Figure 3.4 shows two geometries that are frequently used in high voltage apparatus. The solution of these configurations with the use of the charge simulation technique, and especially the one with no axial symmetry (Figure 3.4a), would have to involve line and ring charges of variable density (45). As will be shown later, this requires a thorough knowledge of electrostatics, and perhaps a large amount of educated guess work. Hence, many experimenters might dismiss the technique in favour of other methods.

However, the charge simulation technique has a very important property; that is, given the positions and the values characterizing the charge distribution, the field at any point can be calculated analytically. This is important because it eliminates the need of a grid node at that point, and in addition, if a space charge is included in the calculations, the field at any point will be given by the summation of the field components due to the individual charges constituting the whole system.

Hence, in view of this advantage and the task of constructing a three-dimensional grid if one of the discretization methods is chosen, an attempt is made here to simplify the conventional approach using optimization techniques.

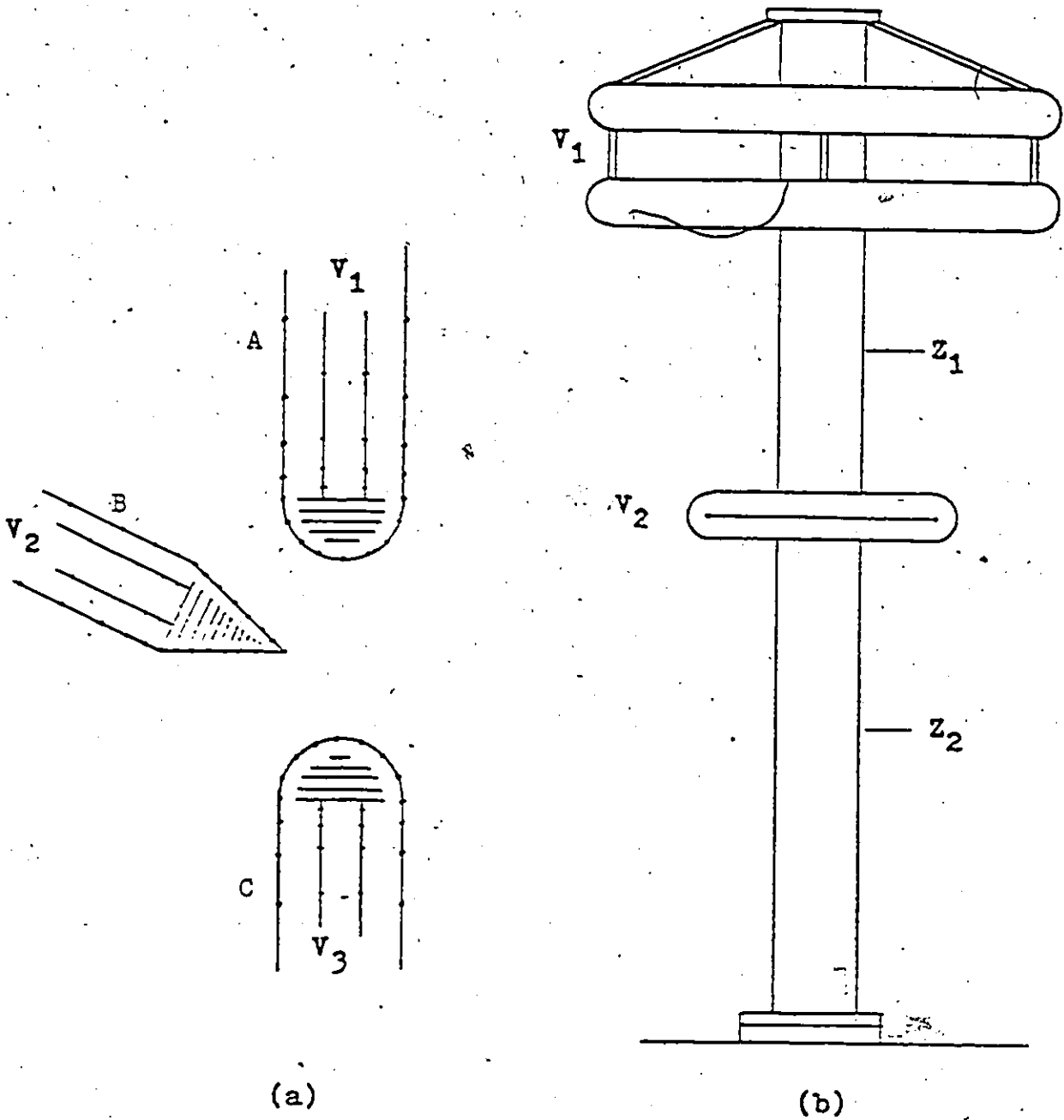


Figure 3.4 (a) A trigatron, with non-axial field distribution.  
(b) A high voltage divider, with field controlling electrodes.

### 3.4 Optimized Charge Simulation Technique.

One of the most important parameters in the optimization of any design or processes, is the choice of the optimization criterion or objective function. This usually varies according to the nature of the problem. The objective function used here is the cumulative squared error, which is very simple to apply and is represented by

$$U = \sum_{j=1}^m (V - \phi_j(r, z))^2 \quad (3.7)$$

$$\text{or } U = \int_S (V - \phi_j(r, z))^2 ds$$

where  $V$ : is the value of the potential at the physical conductor positions,

$\phi_j(r, z)$ : the value of the simulated potential,

$m$ : the number of points  $(r_j, z_j)$  on the electrode boundary,

and  $S$ : represents the electrode surface.

The variables of optimization which primarily are the position of the charges and their values, are subject to the following equality and inequality constraints.

$$f(x_i) = A; \quad f(x_i) \geq B; \quad f(x_i) \leq C; \quad D \leq f(x_i) \leq E \quad (3.8)$$

where  $f(x_i)$  can be any one of the variables  $x_i$ , or, a linear or non-linear expression involving a number of variables (e.g.,  $x_1 + x_2 + 5x_3 = F$ ).  $A, B, C, D$ , and  $F$  are constants related to the physical system.

The final consideration is the choice of the optimization.



technique or algorithm. The technique must be capable of handling highly nonlinear objective functions, equality and inequality constraints, and constraints that are described by linear or non-linear functions of the variables. Furthermore, it should be possible to change the constraints or the objective function without modifying the optimization algorithm.

The availability of the first and second derivatives of the objective function  $U$ , will determine whether or not gradient techniques that require these derivatives will be used. A number of optimization subroutines are available in the FORTRAN and WATFIV scientific subroutine manuals. Rosenbrock's method (48) is one of the earlier and most reliable techniques, but with a relatively slow rate of convergence. One of the fast-converging techniques is Davidson's method as modified by Fletcher and Powell (50), combined with the Created Response Surface Technique of Carroll (49).

#### 3.4.1 Application to a Rod-Plane Gap.

In demonstrating the principle and for comparison purposes, the potential distribution of Figure 3.1(a) is simulated with one point charge and nine semi-infinite line charges. For simplicity the potential on the surface of the electrode is assumed to be equal to one volt. Then for any point  $(r_j, z_j)$  on the electrode surface the values of  $Q_i$  and positions  $(r_i, z_i)$  must be such that the resulting potential  $\phi(r_j, z_j) = 1$ . Thus the values of the charges  $Q_i$  and their positions  $(r_i, z_i)$  are assigned to be the variables of optimization and as an objective function we take the cumulative square error, as follows.

$$U = \sum_{j=1}^m (1 - \phi_j(r, z))^2 \quad (3.9)$$

where  $\phi(r, z)$  is given by equation (3.6) and  $m$  is the number of points at which the potential  $\phi(r, z)$  is calculated. Therefore, by choosing several points  $(r, z)$  along the boundary of the electrode and minimizing the function  $U$ , the required  $Q_i$  and  $(r_i, z_i)$  are found for which the potential at the points  $(r, z)$  is equal to the applied potential (1 volt). A value of  $m=65$  was arbitrarily chosen. This corresponds to fifteen points  $(r, z)$  on the hemi-spherical part of the electrode and fifty on the cylindrical part from  $G+R$  to  $G+R+48R$  (or with  $R=1$  from  $G+1$  to  $G+1+48$ ).

The problem was solved for two separate sets of constraints. In one set of constraints the positions of the charges are constrained on the basis of previous information (47), between  $G+1$  and  $G+1+250$  as shown in table 3.1. In another set, the positions of the charges are arbitrarily constrained between  $G+1$  and  $G+1+48$ , as shown in table 3.2. In this manner, one can test of the uniqueness of the positions  $(r_i, z_i)$ .

The initial values of the optimization variables  $(r_i, z_i)$  and  $q_i$ , were selected arbitrarily within their corresponding constraints.

Rosenbrock's optimization technique (48,51) is used for the minimization of the objective function, modified accordingly to account for equality and inequality constraints.

The results for two different gap lengths  $G$  are shown in Figures 3.5, 3.6 and 3.7 where the percentage error of the simulated potential is plotted versus position on the surface of the electrode.  $\phi_j(r, z)$  is calculated for a number of points other than the original  $(r_j, z_j)$  to check for possible non-uniformities of the simulated potential. The resulting values of the positions  $(r_j, z_j)$  are shown in Tables 3.3 and 3.4. Equipotential plots for the two different gap lengths are presented in Figures 3.8 and 3.9. Similarly, Figure 3.10 shows the potential distribution along the axis of highest field strength for a number of  $G/R$  ratios.\*

In general the results indicate that the error for both sets of constraints is of the same order of magnitude and that there is no unique set of positions for the line charges. Their position depends on the ratio  $G/R$  and the imposed constraints. Figure 3.6 and 3.7 show that unlike the results of Figure 3.3 the error along the cylindrical part approaches zero as the distance from the spherical tip increases. This could be due to the fact that the position and the value of the charges is an optimum for the given set of constraints.

No further attempt was made to refine the model since the results obtained were of acceptable accuracy. The degree of accuracy of the optimized approach at this introductory level helps to demonstrate the ease and efficiency of this method.

The objective function was in all cases minimized to  $U \approx 0.01$  for comparison purposes. The computation time depends

---

\* A computer program with a sample solution is given in Appendix 2.

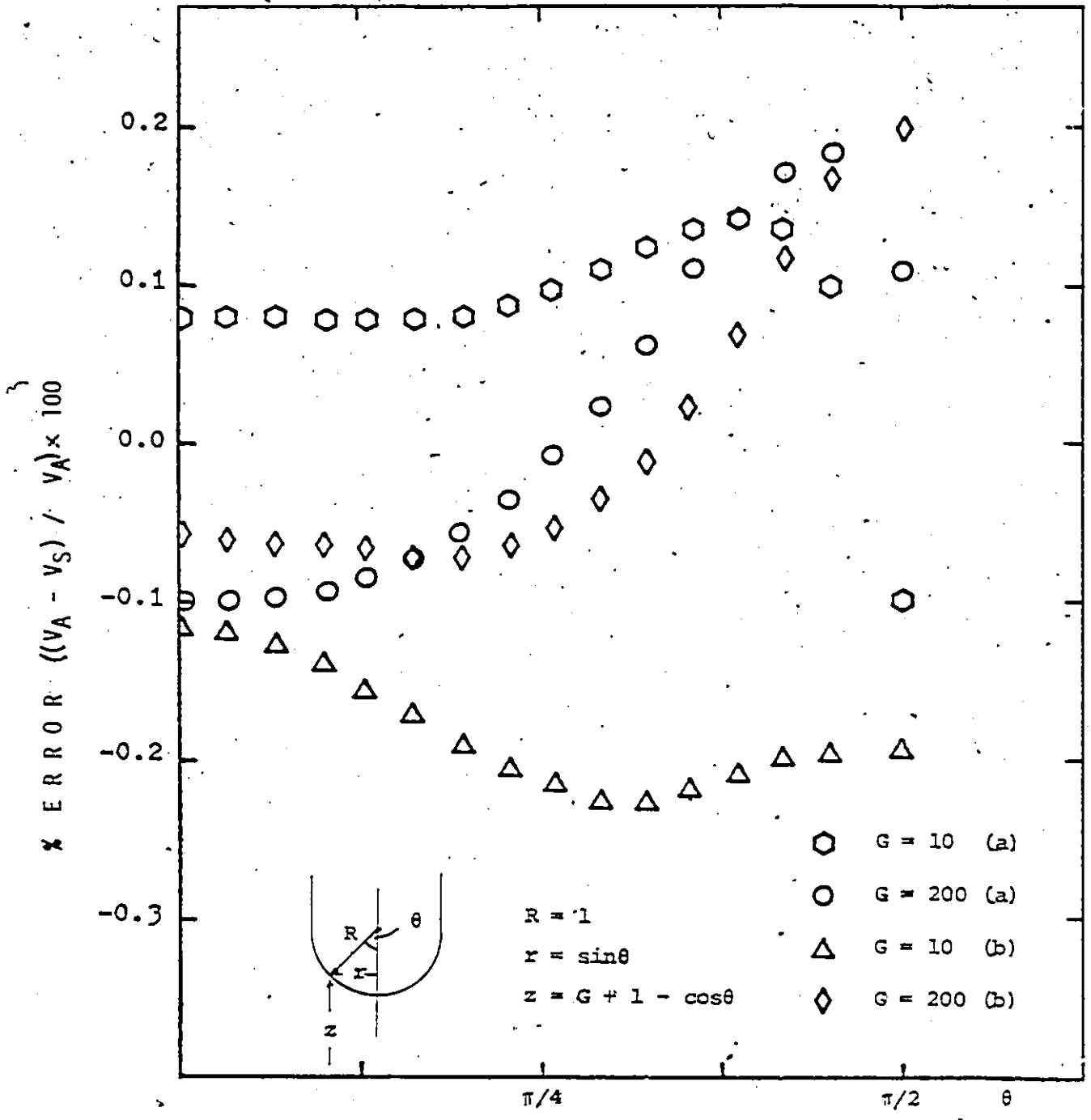


Figure 3.5 Percentage error of the simulated potential along the spherical part of the electrode. (a) Results obtained using the constraints of Table 3.1. (b) Results obtained using the constraints of Table 3.2.

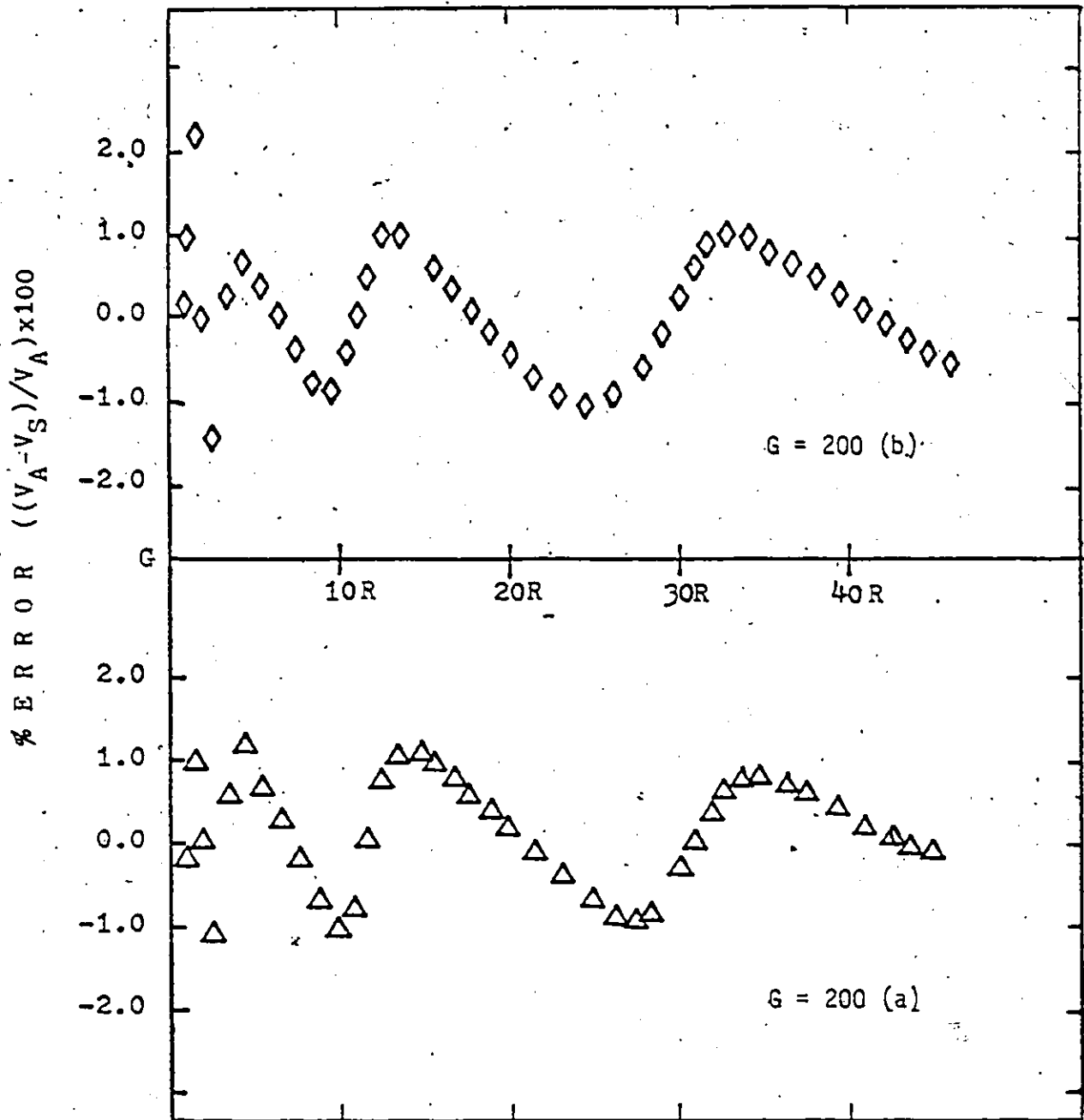


Figure 3.6 Percentage error of the simulated potential on the cylindrical part of the electrode. (a); and (b) correspond to constraints of Tables 3.1 and 3.2 respectively.

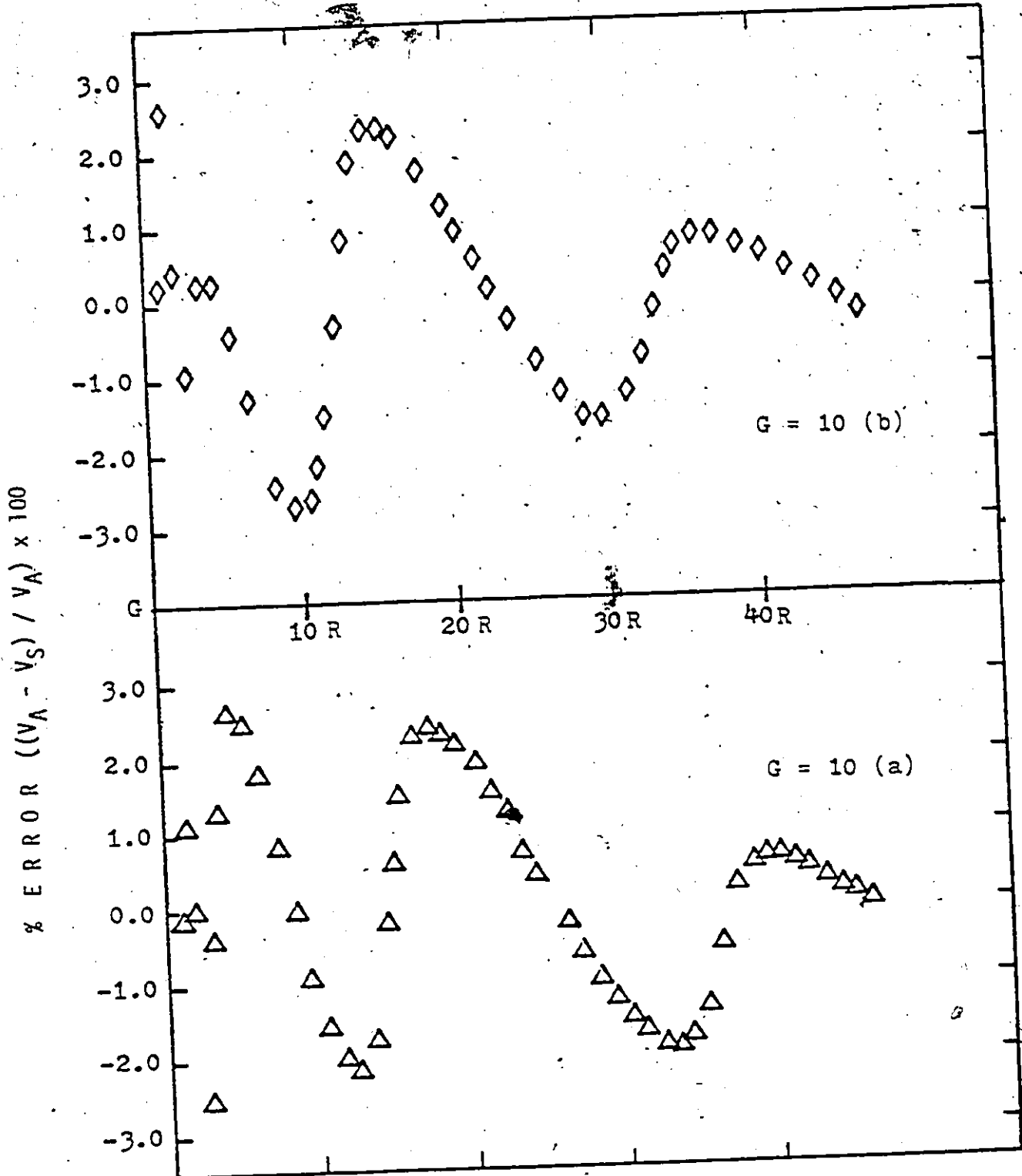


Figure 3.7 Percentage error of the simulated potential on the cylindrical part of the electrode. (a) and (b) correspond to constraints of Tables 3.1 and 3.2 respectively.

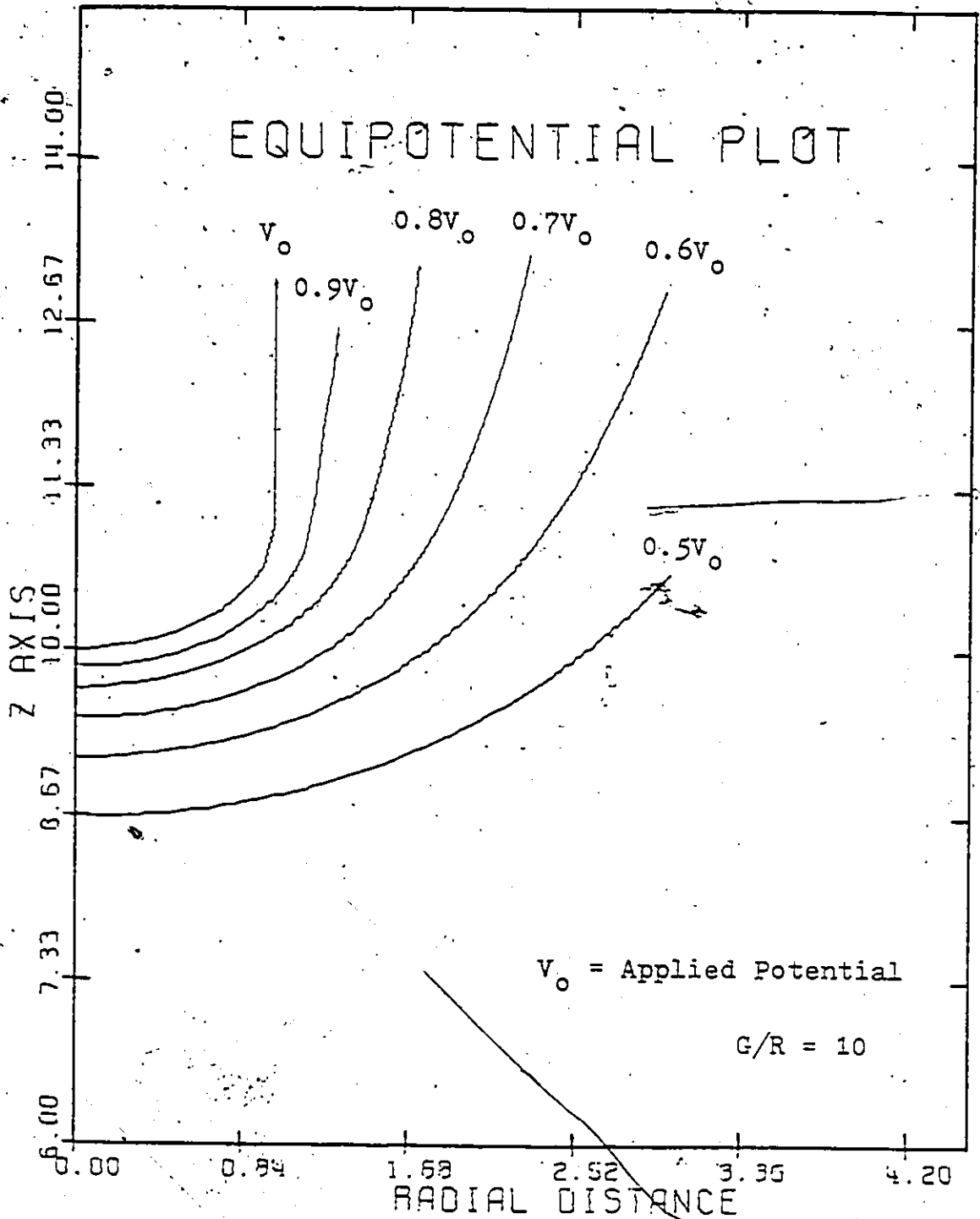


Figure 3.8 Equipotential plot of a rod-plane electrode configuration with a gap length to point radius ratio  $G/R = 10/1$ .

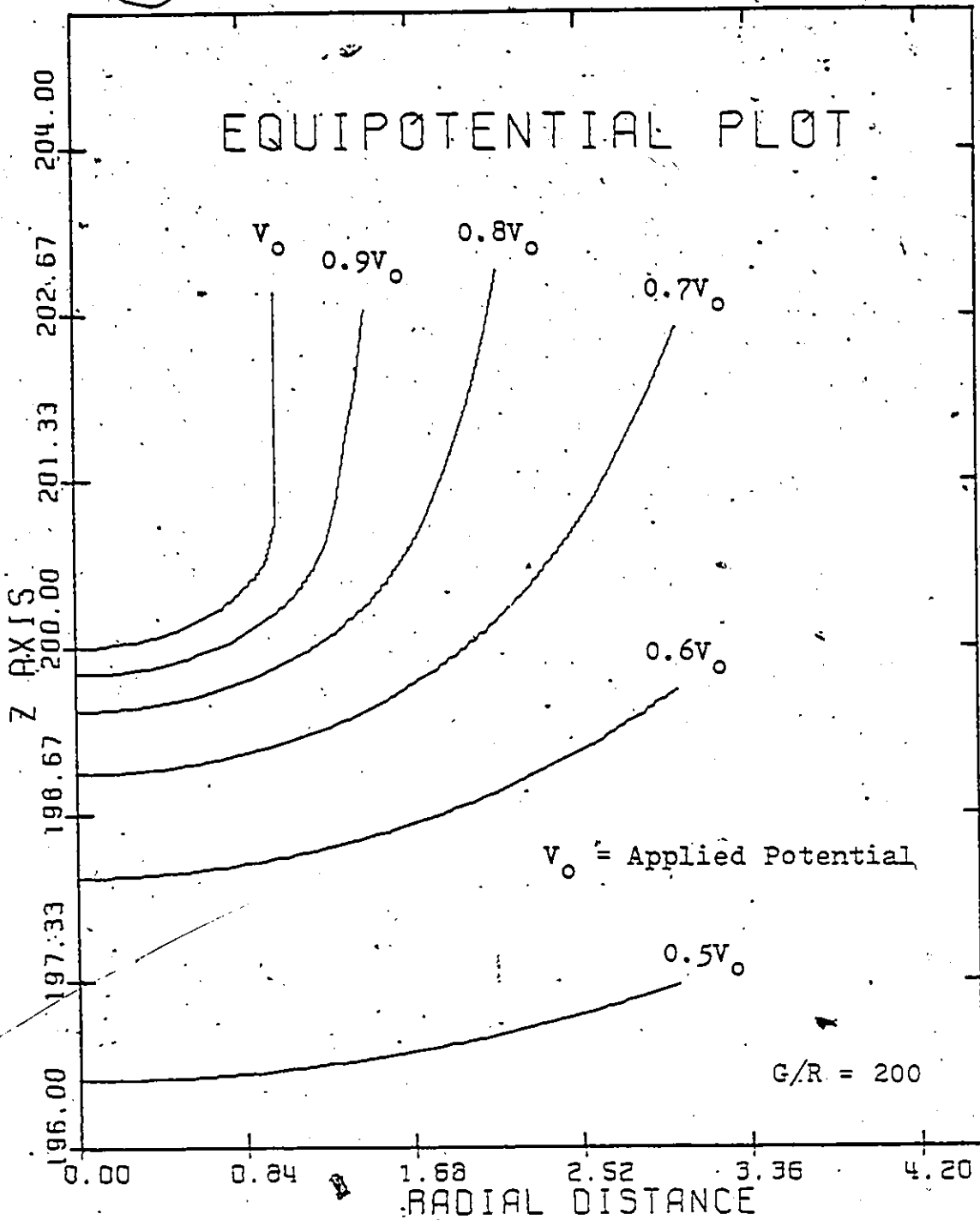
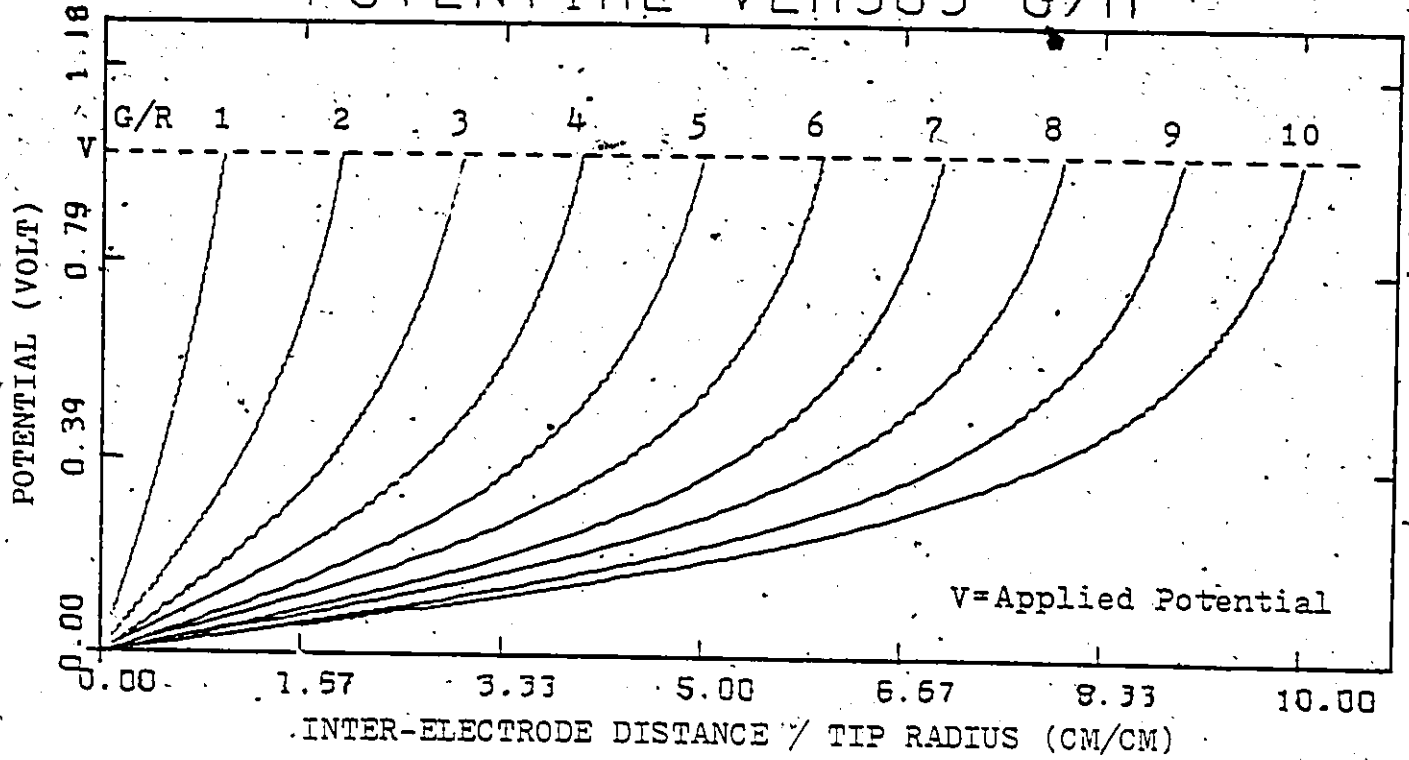


Figure 3.9 Equipotential plot of a rod-plane electrode configuration with a gap length to point radius ratio  $G/R = 200/1$ .



# POTENTIAL VERSUS G/R



# POTENTIAL VERSUS G/R

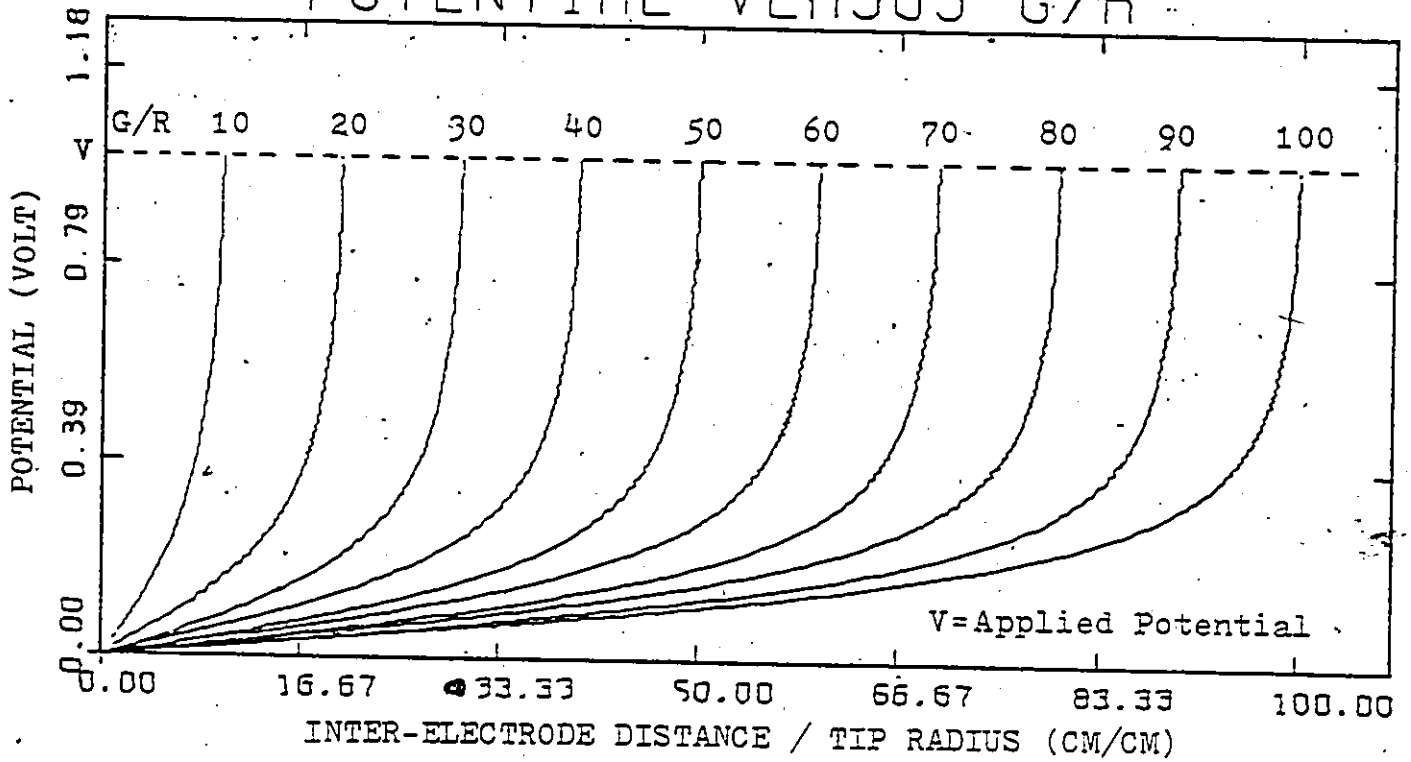


Figure 3.10 Potential distribution along the axis of a rod-plane gap for various gap ratios  $G/R$ .

Table 3.1. Constraints imposed on the variables of optimization

$$\begin{aligned}
 (0, z_1^i) &= G+R \\
 G+R &\leq (0, z_2^i) \leq 1.5 \\
 &" \leq (0, z_3^i) \leq " \\
 &" \leq (0, z_4^i) \leq " \\
 &" \leq (0, z_5^i) \leq " \\
 G+R+5.0 &\leq (0, z_6^i) \leq G+R+10.0 \\
 G+R+25.0 &\leq (0, z_7^i) \leq G+R+35.0 \\
 G+R+80.0 &\leq (0, z_8^i) \leq G+R+100.0 \\
 G+R+200.0 &\leq (0, z_9^i) \leq G+R+250.0 \\
 (0, z_{10}^i) &\leq G+R \\
 A \leq Q_i \leq B & \quad i=1,2,\dots,10
 \end{aligned}$$

where B is a large positive number and A = -B

Table 3.2 Constraints imposed on the variables of optimization

$$\begin{aligned}
 (0, z_1^i) &= G+R \\
 G+R &\leq (0, z_{1,2,\dots,9}^i) \leq G+R+48.0 \\
 (0, z_{10}^i) &= G+R \\
 A \leq Q_i \leq B & \quad i=1,2,\dots,10
 \end{aligned}$$

Tables 3.3 and 3.4. Optimized positions  $(0, z_i^i)$  as derived from the constraints of Tables 3.1 and 3.2 respectively.

Table 3.3

i	G=200	G=10
1	201.00	11.00
2	201.11	11.10
3	201.19	11.15
4	201.55	11.57
5	202.16	12.18
6	210.97	20.20
7	228.94	41.60
8	296.06	110.99
9	410.80	238.59
10	201.00	11.00

Table 3.4

i	G=200	G=10
1	201.00	11.00
2	201.11	11.10
3	201.15	11.11
4	201.18	11.38
5	201.35	11.49
6	201.45	12.22
7	202.03	23.55
8	212.29	46.30
9	231.12	58.81
10	201.00	11.00

mainly on the rate of convergence of the optimization method used to minimize the objective function. Rapidly converging techniques should be used if computer time is an important parameter. Other factors that could influence the computation time are initial values of the optimization variables and the effectiveness of the objective function. The latter factor is very important, since for more complex configurations it is possible that the minimum accumulated square error may not be an efficient criterion.

### 3.5 Application of the Optimized Charge Simulation Technique to Field Distributions with Non-Axial Symmetry.

As mentioned earlier, charge simulation solutions of field distributions with non-axial symmetry are not favoured due to the introduction of variable density charges. Let us for example consider the trigatron case of Figure 3.4(a). Figures 3.11(a) and 3.11(b) show two cross-sections of electrode 'A', one at the spherical tip, and one at the cylindrical part respectively. The variable density rings of Fig. 3.11(a) are obtained by dividing the originally charged distribution into two parts, a constant part, and a variable part consisting of cosinusoidal harmonics with unknown peak values  $\lambda_\mu$ . The charge distribution is a function of the angle  $\alpha$  and is given by (45)

$$\lambda(\alpha) \approx \sum_{\mu=0}^{m_i} \lambda_\mu \cos(\mu\alpha) \quad (3.10)$$

where,  $m_i$  is the number of points  $(r'_i, z'_i)$  on the circumference of the ring.

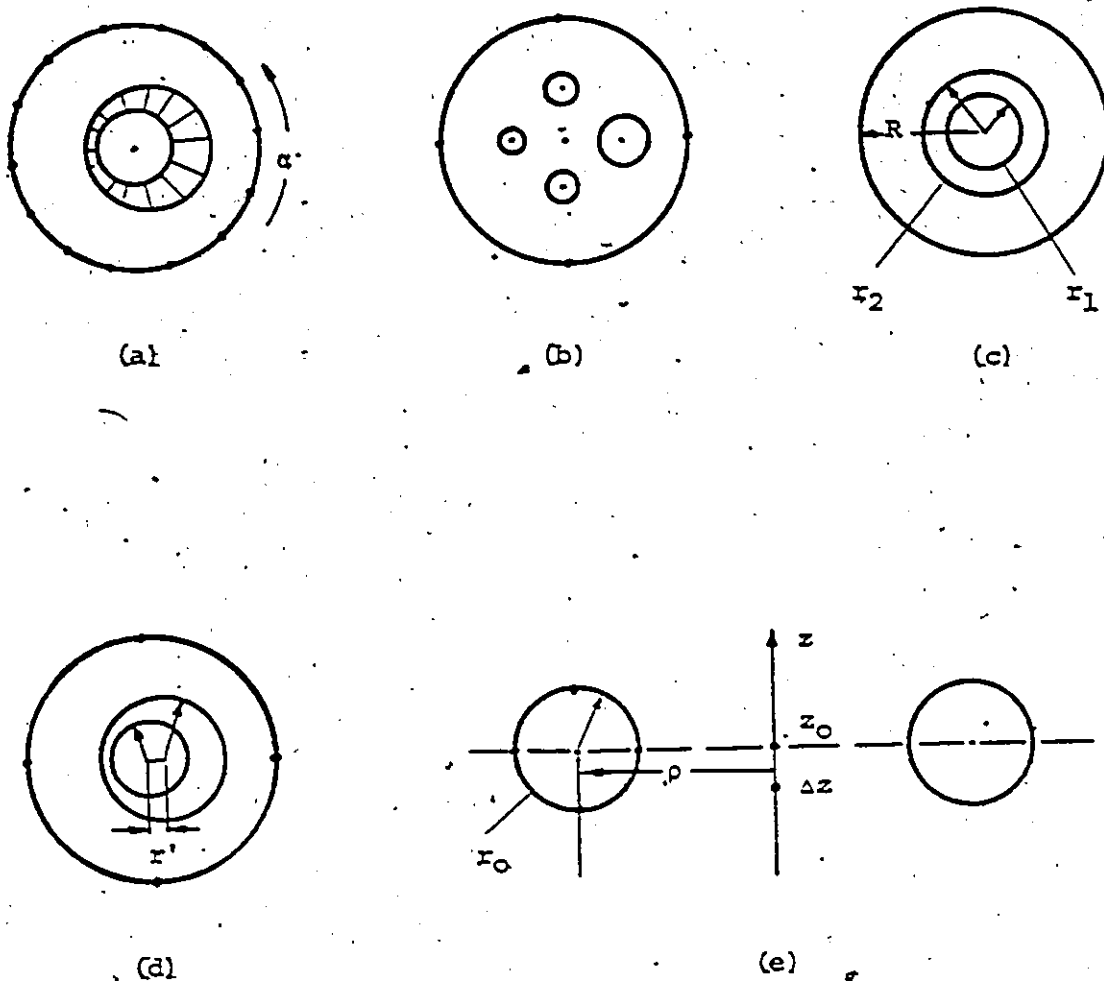


Figure 3.11 (a) Cross-section of the spherical part of the electrode  $V_1$  of figure 3.4(a). (b) Cross-section of the cylindrical part of the same electrode. (c) and (d) represent similar cross-sections as that of (a), before and after the optimization of the system. (e) Cross-section of electrode  $V_2$  of figure 3.4(b).

In this way the  $i^{\text{th}}$  ring contains  $m_i+1$  number of charges. In order to determine the values of these charges, an equal number of boundary points  $(r_j, z_j)$  should be placed along the circumference of the electrode, and on the plane that contains the  $i^{\text{th}}$  ring.

However, the problem can again be simplified with the proper choice of optimization parameters. The variable density ring charges can be obtained as shown in Figure 3.11(c) and 3.11(d). In this case the ring of radius  $r_1$  is fixed, and the centre of ring  $r_2$  is free to move on the plane of the page along the  $r$ -axis. This movement is constrained in a region  $r_x$  such that

$$\begin{aligned} & r_x \leq r_2 - r_1 \\ \text{where } & r_1 < r_2 \ll R \end{aligned} \quad (3.11)$$

Therefore, a variable density ring is simulated with the addition of only two variables, that is the charge of ring  $r_2$ , and its position  $r$  with respects to the  $z$ -axis.

It becomes apparent that a number of new optimization parameters can be introduced, the nature of which depends on the particular configuration.

As another example, we consider the potential divider of Figure 3.4(b). The field configuration of the doughnut shaped electrode at potential  $V_2$ , can be simulated with one ring charge as shown in Figure 3.11(e). Assuming  $V_1$  and  $V_2$  to be positive potentials, the ring charge at  $V_2$  will be slightly displaced from its original position in the torroid. However, since we do not know the exact position of the ring,

we can constrain its centre to move between  $z_0 - \Delta z$ , where  $\Delta z < r_0$ . The radius  $r_0$  could also vary and therefore it will be set as an optimization parameter, since we suspect that if the ring moves down, it could change in diameter. Similar arguments will apply to the top electrode and the system will be solved simultaneously, considering the image charges with respect to ground.

Furthermore, one can proceed to simulate even more complicated field distributions by the use of non-linear constraints, which could force point charges to move on predetermined contours, and line charges to tilt, or, simply change size and position.

The field distribution of the rod-plane gap (as obtained by the charge simulation technique), was used in the calculation of streamer onset voltages in  $SF_6$  and  $SF_6/N_2$  mixtures, which will be presented in Chapter 6.

## CHAPTER 4

### EXPERIMENTAL TECHNIQUES AND PROCEDURES

#### 4.1 Experimental Design.

The ability of high voltage power equipment to withstand lightning stroke and switching surges is usually evaluated with impulse or chopped impulse voltages. In this work, standard impulse voltage (1.5 $\mu$ s front, 50 $\mu$ s tail) was chosen to examine the dielectric behaviour of the SF<sub>6</sub>/N<sub>2</sub> mixtures.

A rod-plane electrode arrangement was used, for as mentioned earlier, this configuration provides excellent conditions for simulation and observation of the effects produced by various non-uniformities.

The experimental variables were: the total pressure of the mixture, the partial pressure of the component gases (or % of SF<sub>6</sub> content in the mixture), and the gap length of the rod-plane gap. The number of variables was kept small so that a complete investigation of both positive and negative impulses could be made. This allowed continuous monitoring of impulse voltage, discharge current, photomultiplier current, and photography of the various phenomena under both polarities.

In experiments of this nature there is usually a trade-off between the experimental variables and the parameters that one can monitor. Advance design and the use of factorial experiments can be useful; however, there are limitations in the design of an experiment, imposed mainly by the nature of the problem that is investigated. In the present case due to the limited information

on impulse breakdown measurements of SF<sub>6</sub>/N<sub>2</sub> mixtures, the basic design involved impulse voltage and current measurements, and study of the temporal growth of ionization at different gap lengths and pressures. In addition, a good deal of effort was invested in the development of the data-acquisition system, which will be discussed in the following sections.

#### 4.2 Test Chamber.

The measurements were carried out in a stainless steel pressure vessel 60cm high and 36cm in diameter, fitted with a high voltage bushing and four quartz windows. A cross section of the major components is shown in Figure 4.1.

The high voltage bushing is rated at 115 KVAC in an outdoors environment and was successfully tested indoors at 350 KV of impulse voltage.

The electrode adjustment was made with the use of a micrometer screw. Initially the vernier was located on the high voltage side through the HV bushing. This arrangement was found inefficient and a new vernier was constructed and fitted at the bottom plate of the chamber which is at ground potential. The gap-length was adjusted by first lifting the plane until a contact with the rod electrode was detected with the ohm-meter and then lowered to the desired length. The zero adjustment was performed at the operating pressure due to small variations of the inter-electrode distance with pressure changes.

The photomultiplier was an EMI-9781R side window tube. The EMI-9781R has relatively high sensitivity in the blue region,



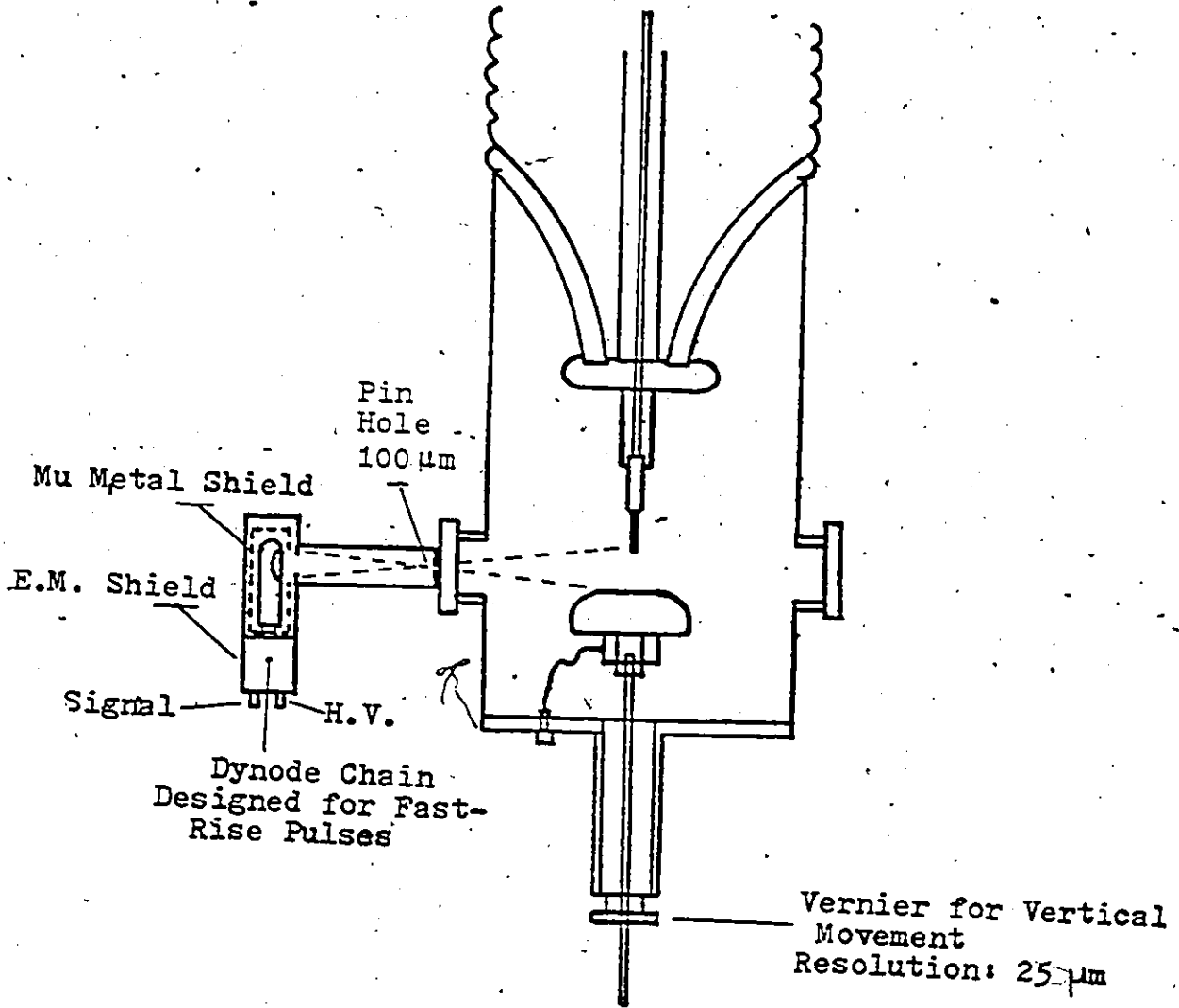


Figure 4.1 Test chamber. The photomultiplier is mounted in one of the chamber windows and it is optically aligned so that the full area of the PM cathode was illuminated.

low dark current, fast response time (2 nsec. pulse rise time) and high gain at low overall voltage (typically 750 V).

The photomultiplier was mounted in one of the windows of the chamber and was optically aligned so that the full area of the PM cathode was illuminated.

#### 4.3 Electrode Arrangement.

Both electrodes were made of brass. The upper electrode consisted of a hemi-spherically capped rod of 0.8mm radius. The lower plane electrode was 12cm in diameter, machined to a 90° Rogowski profile, and was electrically isolated from the rest of the chamber which was permanently grounded. Before each series of measurements the electrodes were polished to a surface finish of about 1 micron.

A number of different polishing methods were employed in order to determine a convenient and practical way of polishing. At first polishing powders were used from grade 400 to grade 1000. Each grade was applied for a period of time until the surface showed a uniform roughness and then the electrode was cleaned thoroughly with methanol before the higher grade was used. This method while it gives good results, proved to be rather laborious. Great care must be taken to ensure that the surface is absolutely clean before a higher grade is used. The reason for this being that one powder grain from a lower grade can produce scratches on the surface that can be removed only by returning to that grade.

Chemical polishing was subsequently used. A solution of

three acids was used at elevated temperature.

<u>Acid</u>	<u>% content</u>	
Phosphoric - $H_3PO_4$	55	
Acetic - $CH_3COOH$	25	$60^\circ < T < 80^\circ$
Nitric * $HNO_3$	20	

The heating and chemical etching was conducted inside a fume-hood. The results indicated that the surface finish depended critically on the time that the electrode was immersed in the solution. A typical time for a uniformly pitted electrode was 1.5 minutes. However, after the etching was completed the surface of the electrode contained discolourations from residual oxides that were difficult to remove with a cleaning agent.

Thus, at times further polishing with a fine powder was necessary.

Finally, it was decided that both of the above methods were too elaborate to be used after each series of experiments, considering that the pressure range and gap-length used, could involve a spark mechanism insensitive to the electrode surface. Instead, after each series of measurements the electrodes were uniformly polished with an abrasive compound (Brasso) with maximum grain size of 20 $\mu$ m and then with red rouge lapping compound of 0.5 $\mu$ m grain size. This process provided a polish compatible to the previous methods in a much shorter time, and was used through-out the experiments.

#### 4.4 Gas Mixing Procedure.

The gases were mixed by adjusting the pressure ratio, and the final mixture was checked for accuracy using a gas analyzer.

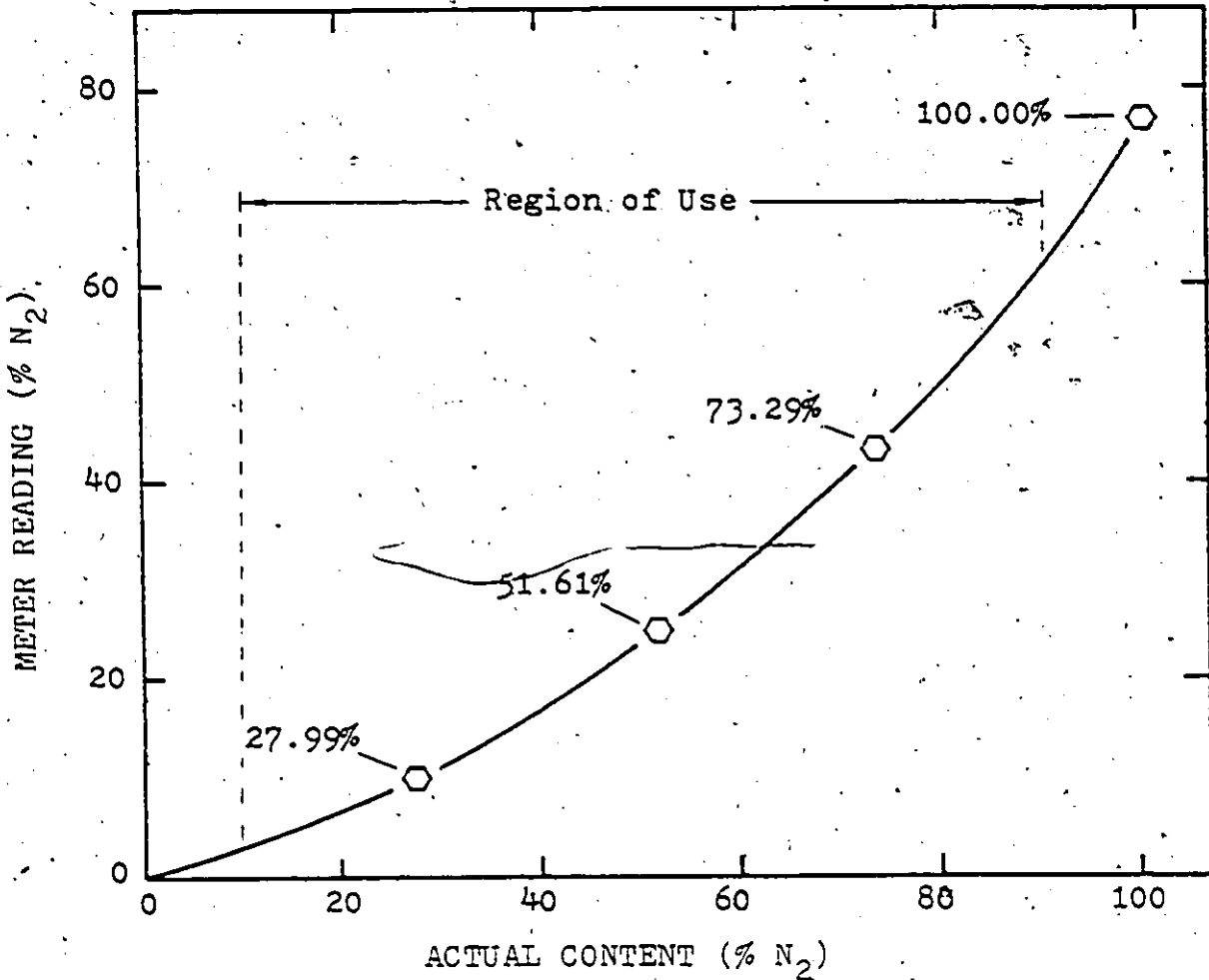


Figure 4.2. Calibration curve for the HF50 Gas Analyzer. The SF<sub>6</sub>/N<sub>2</sub> gas mixture was monitored for N<sub>2</sub> content in the above shown range.

The gas analyzer was a HF50 H<sub>2</sub>/N<sub>2</sub> mixture monitor, calibrated for SF<sub>6</sub>/N<sub>2</sub> mixtures. The HF50 analyzer provides a reading of the % content of nitrogen by measuring the thermal conductivity of the mixture with a precision thermister. The instrument had to be recalibrated periodically and a typical calibration curve is shown in Figure 4.2. Three standard mixtures were used for the

calibration. For consecutive use, after the calibration curve was obtained the 0%  $N_2$  point had to be reset each time before a reading was taken. The gas analyzer was used in the range of 10-90% of  $N_2$  content and it provided a measurement of the mixture ratio with an accuracy better than  $\pm 1\%$ . Mixtures containing low percentage of one of the constituent gases were mixed under vacuum conditions. The chamber was first evacuated to 0.01 Torr and the lower constituent was admitted to a partial pressure corresponding to the desired mixture. The second constituent was then added to the predetermined total pressure. A thermocouple vacuum gauge was used to measure the low pressures rather than a mercury gauge to avoid any contamination of the test chamber with mercury vapour.

Measurements in nitrogen and  $SF_6$ -nitrogen mixtures were made after evacuating the chamber to 0.01 Torr, flushing it with nitrogen and subsequently by evacuating to 0.1 Torr. The nitrogen used was high purity while the  $SF_6$  was commercial grade 99.8% pure. The gases were dried and filtered through 1 micron filter prior to admission into the chamber and in addition a small amount of activated alumina was placed at the base of the chamber to remove chemically active compounds produced by the discharge.

#### 4.5 The Voltage Supply and the Data Acquisition System.

The schematic diagram of the voltage supply and the measuring system is shown in Figure 4.3. The impulse generator was adjusted to supply an impulse wave of 1.5/50 $\mu$ sec. The voltage was measured with an R.C. Haefely type divider. Additional voltage signal division inside the control room was obtained using

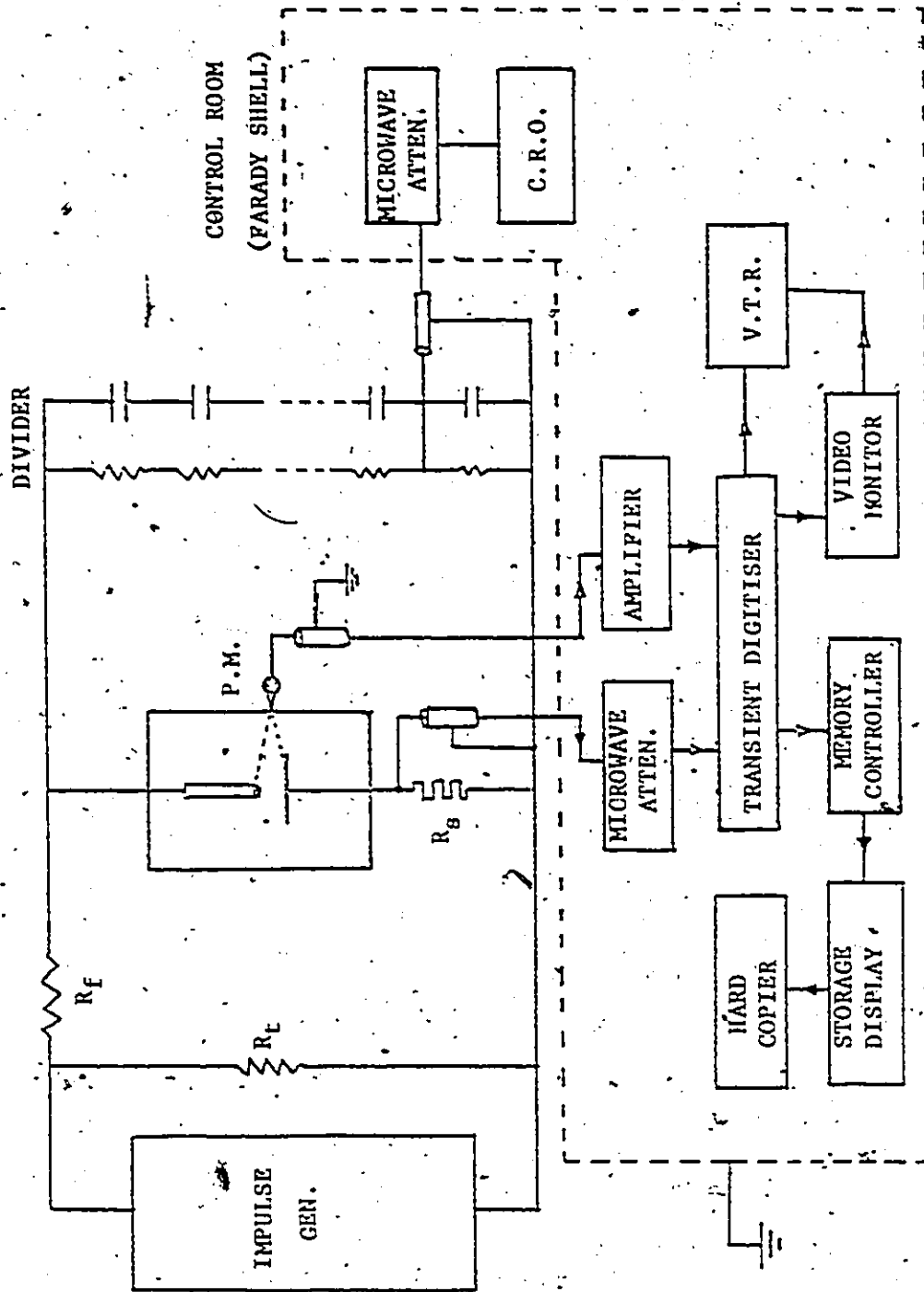


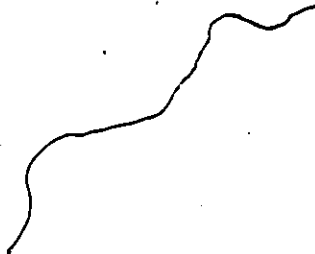
Figure 4.3. Schematic diagram of apparatus and data acquisition system

microwave attenuators whose performance was found superior to that of conventional dividers.

The 50% impulse breakdown voltage was obtained using the "up and down" method. For each breakdown value, at least 25 impulses were applied at a voltage close to breakdown. The current shunt used for the measurement of breakdown current was a "squirrel cage" type (64) constructed of carbon resistors.

The photomultiplier and the current signals were fed into a R7912 Tektronix transient digitizer. The R7912 Transient digitizer is a high speed signal acquisition instrument capable of operating in either the analog or digital mode. Acquired waveforms up to 500 MHz (or 1 GHz direct access) are converted to a more useful speed and format suitable for viewing on a standard video monitor. Incoming signals can be viewed on a monitor and simultaneously stored on video tape. The Memory Controller (or 1350 memory display unit) provides all the controls necessary to load the R7912 memory. It can then read data from the memory and convert it to x-y analog data for driving non-raster displays. The storage display (or 603 storage monitor) is connected to the 1350 control unit and simultaneously interfaced with the 4631 hard copy unit, so incoming signals can be viewed on the display and subsequently stored in a hard copy form.

This type of arrangement is not only convenient, but it allows the storage of a large number of waveforms that can be used for statistical study, which is essential in most high voltage measurement.



#### 4.6 Shielding of the Apparatus

The measurement of rapidly changing voltages and currents requires special measuring techniques and procedures. Operation of an impulse generator gives rise to electromagnetic interference caused by transient potentials and by strong electromagnetic fields associated with the charging and discharging of stray capacitances to ground. The stray capacitances are mainly distributed capacitances to ground along the Impulse generator, test chamber, and interconnecting leads. Because of the high rate of voltage change, the charging and discharging currents may reach peak values of some Kiloamperes (65). Thus, electromagnetic interference will be generated either through the air or from transient potentials caused by the return of these currents to the generators grounding plate (or grounding rods) through the ground impedance. Even at fairly low ground impedance, equalizing currents will be driven through the entire ground system and result in unwanted noise.

In order to reduce the noise input to the measuring system a number of precautions were taken,

1. A shielded room was built to try to prevent the electromagnetic fields from penetrating inadequately shielded instrument cabinets. The walls, floor, and ceiling of the shielded cage (12'x10'x10') were made of double copper mesh which was electrically connected to the ground plate of the impulse generator.
2. All measuring instruments were located inside the cage and were powered through an isolation transformer placed between the cage and the mains. However, it was found



that the over-all shielding was inefficient due to noise transmitted through the power lines. This conducted interference was suppressed by conventional RFI power-line filters. In order to achieve high quality wide-band attenuation, the filters were positioned in the power lines feeding the cage and in contact with the external wall of the cage.

3. Multiple grounding of the measuring circuit generates currents on the cable shields, which induce noise in the signal via capacitive coupling. This type of interference was attenuated to a large extent by reducing the grounding paths to a practical minimum. A copper strip (1m wide) was connected to the ground plate of the generator and extended to the base of the test object as shown in Figure 4.4. The cage was introduced to the ground circuit by a similar copper strip connected to its base and extending in the interior to provide earth-taps for the measuring equipment. The signal cables were triaxial and a typical ground connection is shown in Figure 4.4.

Since electromagnetic interference enters a measuring system in its radiated and conducted form, and because each of the above measures provides an attenuation rather than complete suppression, the performance of the present system can be claimed simply as "adequate" for the type of measurements involved.

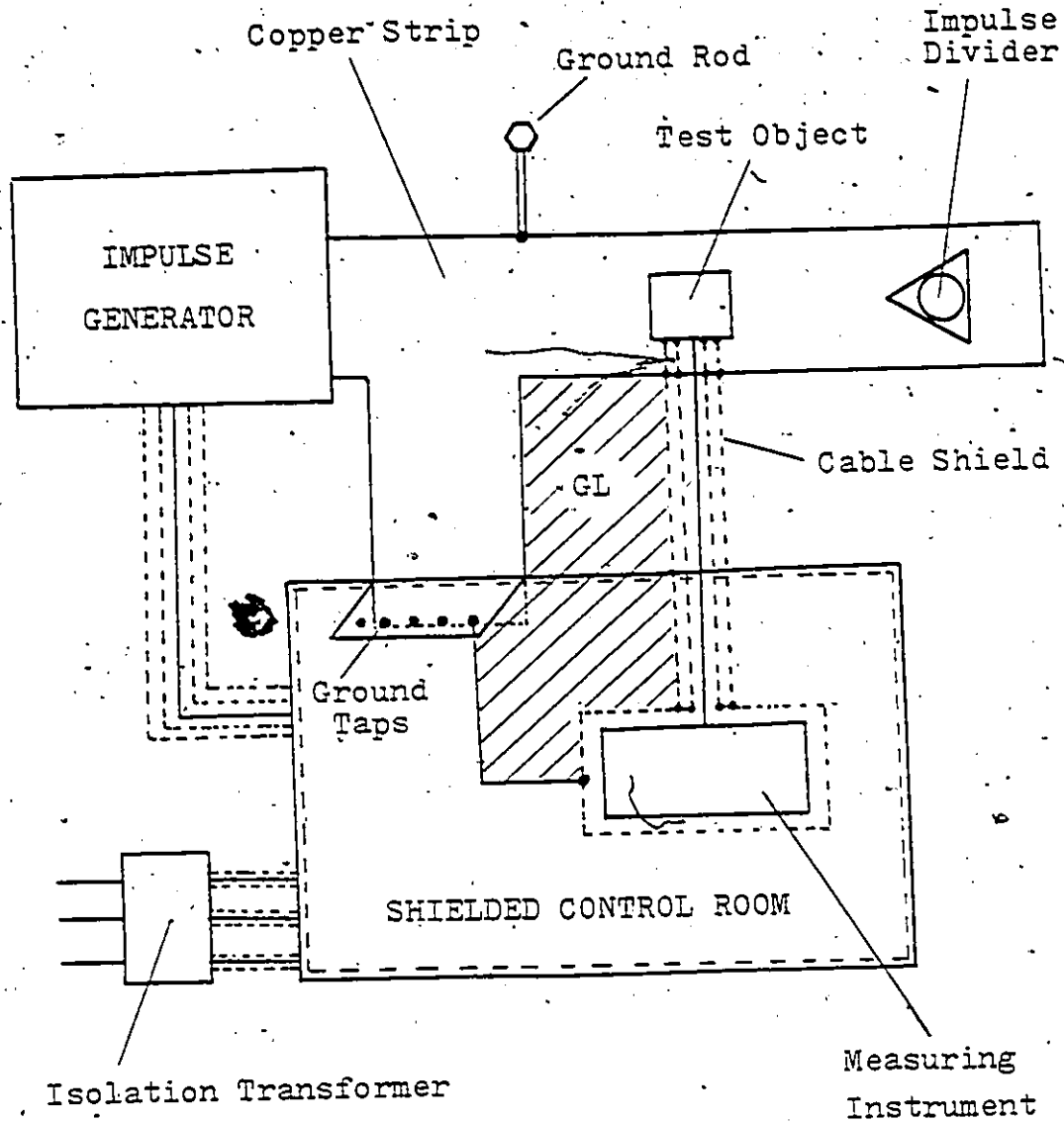


Figure 4.4. Schematic diagram of the grounding system of the impulse generator facility. Typical ground connections of a triax-cable and measuring instrument are shown, together with the generated ground loop GL.

#### 4.7 Corona Onset Voltage Measurements.

The corona onset voltage measurements were performed under direct voltage conditions. The detection circuit consisted of a 10 kilo-ohm resistor in series with the test gap and an oscilloscope, that monitored the voltage drop across the resistor. A pair of fast responding diodes connected back to back were also included in the circuit, to protect the oscilloscope from overvoltages that could result from high breakdown currents.

The high voltage supply was a Deltaray HVDC generator with an output voltage of 0 - 1000KV, output current 0 - 2 milliamperes and a superimposed ripple within 0.01% of the output voltage.

The applied voltage was raised up to 90% of the onset value at a rate of 10 KV/sec and thereafter at a rate of 0.5 KV/sec until the onset voltage was detected. The corona onset voltage is defined here as the voltage at which the first "voltage jump" is detected on the oscilloscope. The corona onset voltage values presented in this work represent the mean value of at least ten individual measurements.

## CHAPTER 5

### EXPERIMENTAL RESULTS

In this chapter, impulse breakdown measurements of both polarities are presented for  $\text{SF}_6$ ,  $\text{N}_2$  and mixtures of the two gases. Mixtures containing 0.01% to 100.0%  $\text{SF}_6$  are investigated over a pressure range extending from 300 torr to 5 bar and gap lengths ranging from 5 to 50mm. Results on the temporal growth of ionization are presented through photomultiplier and discharge current measurements. Further information on the spatial growth of impulse coronas and spark trajectories in the inter-electrode area is given in the form of still photographs.

The 50% breakdown voltage ( $V_{50}$ ) for most measurements had a standard deviation of less than 10% of  $V_{50}$ . Repeatability of results was in most cases good. However, for  $\text{SF}_6/\text{N}_2$  mixtures under certain mixture ratio and total pressure conditions, the repeatability of the results was relatively poor. Hence, unless otherwise stated the repeatability of the results will be considered as being within experimental uncertainty limits. Uncertainty bars, are included in areas where the error was relatively large, or in cases where the error bars could have an effect in the interpretation of the results.

#### 5.1 Breakdown Characteristics of $\text{SF}_6$ under Negative and Positive Impulse Voltages.

The breakdown characteristics of  $\text{SF}_6$  were examined separately from those of the  $\text{SF}_6/\text{N}_2$  mixtures. Unlike  $\text{N}_2$  which

has uniform breakdown voltage pressure-characteristics under both polarities.  $SF_6$  was expected to exhibit a discontinuity in the breakdown voltage-pressure characteristics in the pressure range of 1 to 5 bar (17,19,57).

By applying negative impulse voltage on the rod electrode and varying the gap length, the breakdown voltage-gap length characteristics of Figure 5.1 were obtained at various gas pressures. One observes that the slope of the curves is larger at the lower gap-length region. This is because at high gap lengths the corona onset voltage depends mainly on the radius of the hemispherical tip of the rod electrode. Hence the corona and spark onset voltage-pressure characteristics have a saturation tendency at higher gap lengths.

Figure 5.2 illustrates the negative impulse breakdown voltage-pressure characteristics of  $SF_6$  for different gap lengths. The 50% breakdown voltage increases with pressure uniformly over the pressure range of 1-5 bar. There was very little scatter in the values of  $V_{50}$  and the degree of reproducibility was relatively high.

The measurement of  $V_{50}$  was made with a Tektronix 549 storage oscilloscope. The signal prior to its input to the oscilloscope was attenuated 897:1 with the high voltage divider and 10:1 inside the cage with a microwave attenuator. The overall division of the signal was tested with the aid of low voltage calibration pulses (100-500V). This method, while acceptable for high voltage divider calibrations, has been criticized for its effectiveness to present a realistic situation where the input signal has high  $dV/dt$  values. As an added means of checking

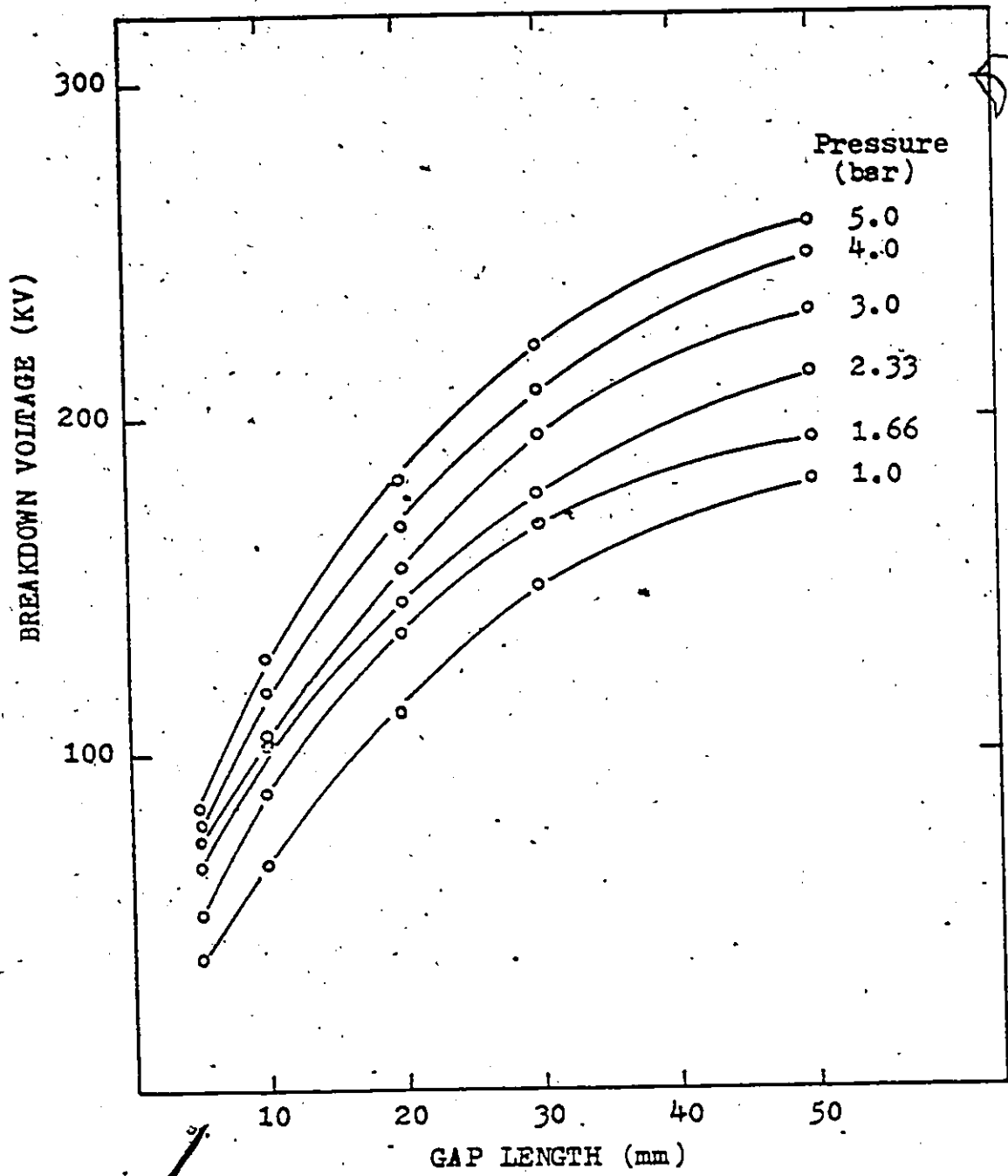


Figure 5.1 Negative impulse breakdown voltage versus gap length characteristics of SF<sub>6</sub> for a pressure range of 1.0-5.0 bar.

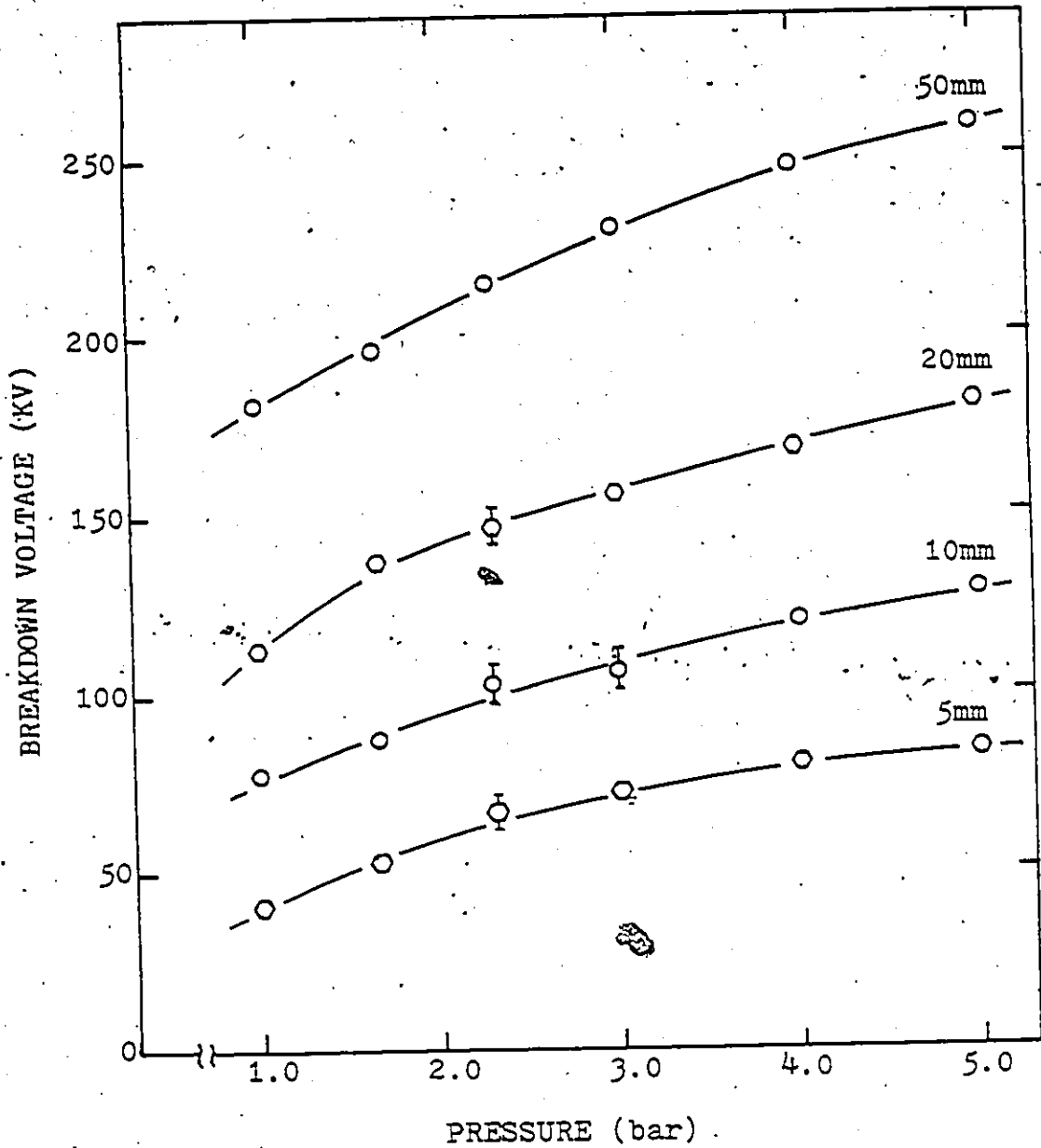


Figure 5.2: Negative rod-plane impulse breakdown voltage-pressure relationship for SF<sub>6</sub>, in gap lengths ranging from 5 to 50 mm.

the measured breakdown voltage level, a comparison is made of the present measurements with results obtained by Howard (20) and Sangassad (55) under similar experimental conditions. As shown in Figure 5.3 all results compare well through out the pressure range and for both gap lengths.

Positive rod-plane results are shown in Figure 5.4 where the breakdown voltage is plotted versus pressure for a 10mm and a 50mm gap. It is seen that a corona stabilized region appears in the 50mm gap for pressures less than  $P_{min}$ . The breakdown voltage increases rather rapidly with pressure up to  $P_{max}$ , which corresponds to a local maximum in the voltage-pressure characteristics followed with a negative slope in the  $P_{max}-P_{min}$  region. Past  $P_{min}$ , the breakdown voltage increases again with pressure but, at a lower rate of increase. For the 10mm gap, the voltage maximum and the corona stabilized region seem less distinct and shifted towards higher pressures. This is in agreement with results presented by Works and Dakin (19), Hazel (7), and Sangassad (55).

In comparing the curves of Figures 5.2 and 5.4 one observes that breakdown under the same gap-length and pressure conditions was always lower for positive impulse. In addition, no voltage maximum was observed under negative polarity in the pressure range of 1-5 bar.

It should be noted that a voltage maximum for negative polarity does exist but, it occurs at a higher pressure than  $P_{max}$  of the positive polarity (78).



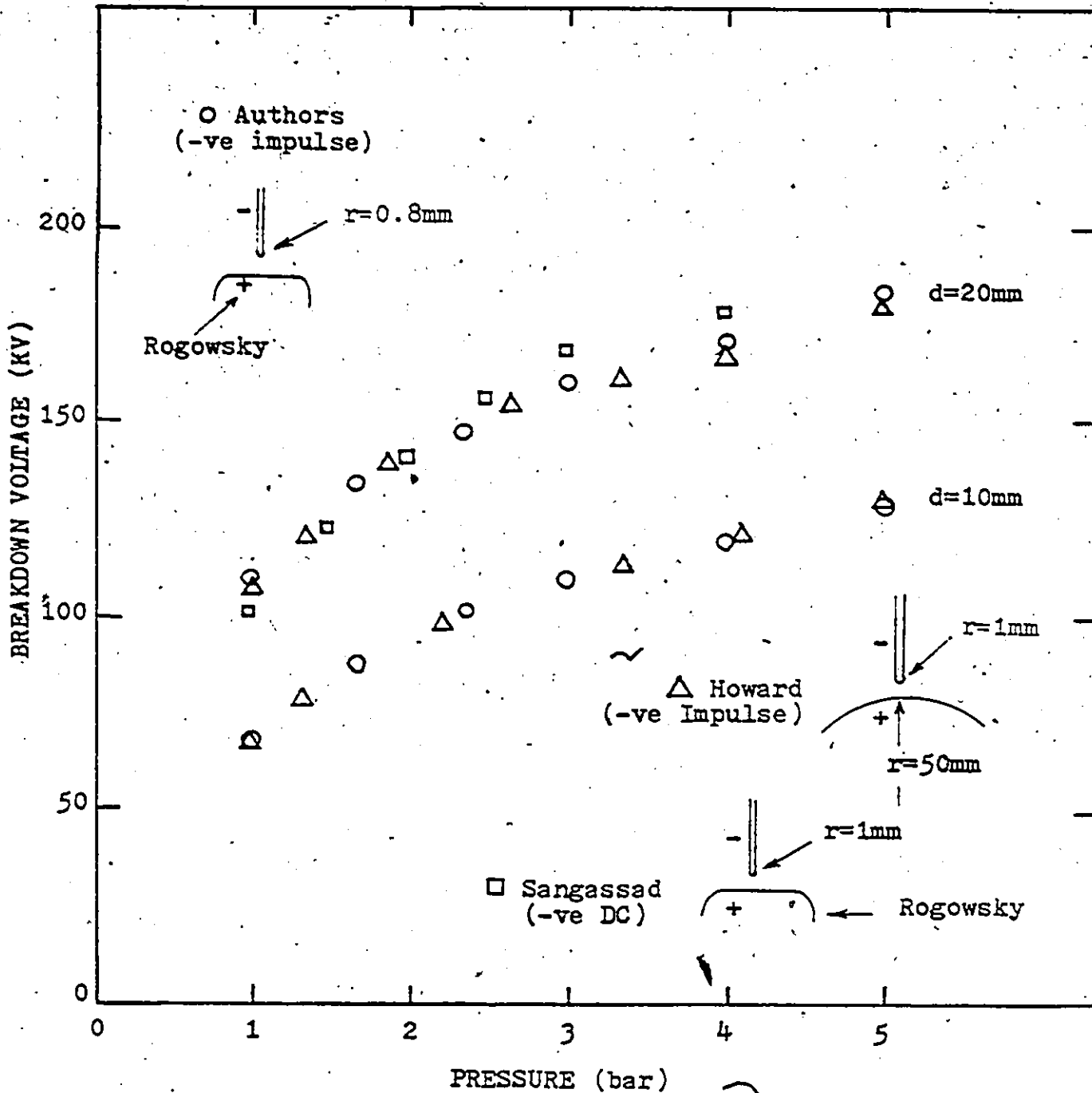


Figure 5.3 Negative impulse breakdown voltage-pressure characteristics of SF<sub>6</sub> for 10 and 20 mm gaps, compared with results obtained by similar experimental conditions.

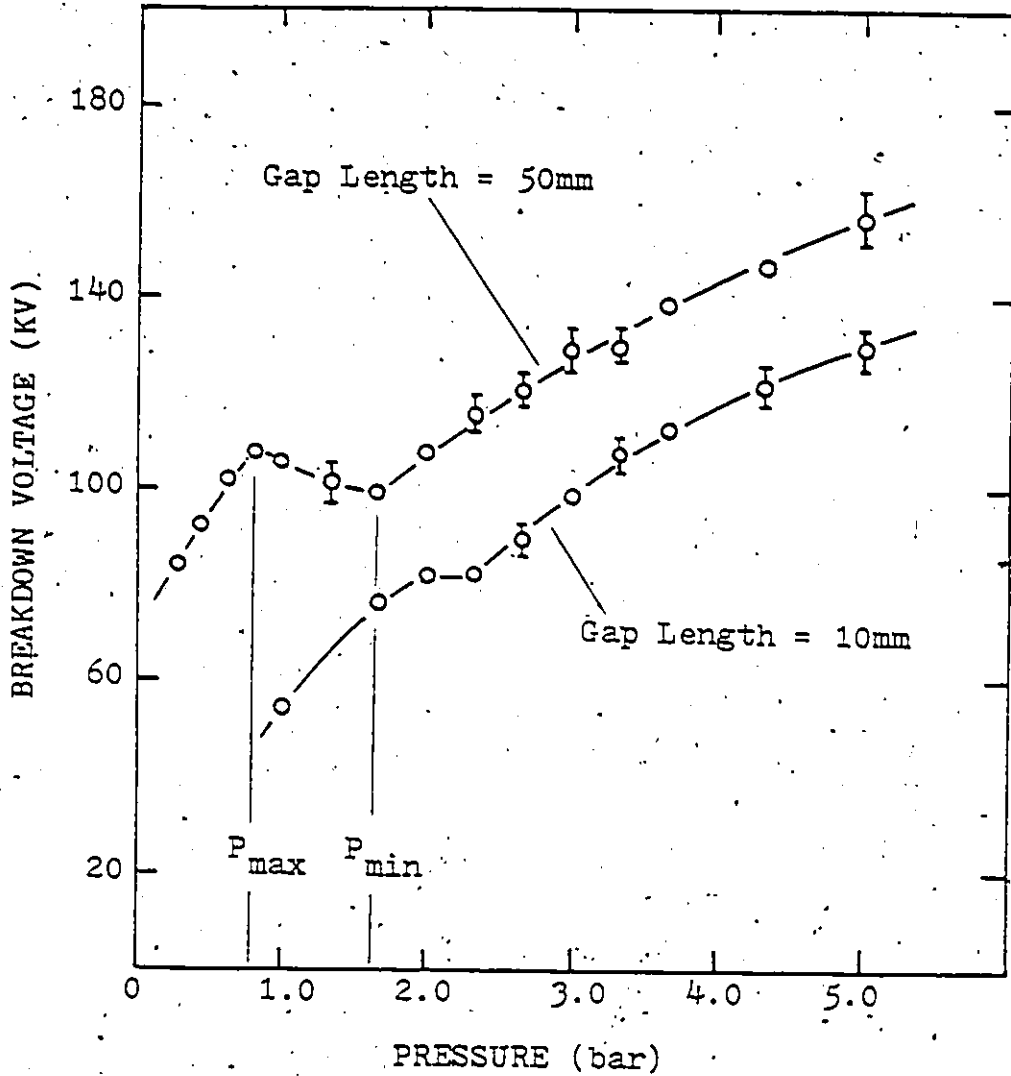


Figure 5.4. Positive rod-plane impulse breakdown voltage-pressure characteristics for SF<sub>6</sub>. Note that the corona stabilized region is not as well defined for the 10mm gap.

## 5.2 Negative Impulse Breakdown in SF<sub>6</sub>/N<sub>2</sub> Mixtures.

The SF<sub>6</sub>/N<sub>2</sub> mixtures were mixed by the procedure described in the previous chapter. After the two gases were admitted into the test chamber, the mixture was allowed a minimum of one hour before any breakdown measurements were taken.

Figure 5.5 shows negative impulse breakdown voltage data obtained at a total pressure of 1 bar for different mixture ratios and gap lengths. Each curve represents the breakdown voltage of a mixture plotted as a function of mixture ratio. The latter was varied from 100% SF<sub>6</sub> to 100% N<sub>2</sub> for a fixed gap length. The curves of Figure 5.5 follow a pattern reported earlier by Howard(20) (Figure 2.1) and Weiland (35), for quasi-uniform and uniform field gaps. As the % of SF<sub>6</sub> content is reduced, the dielectric strength of the mixture decreases at a constant rate down to about 10% of SF<sub>6</sub> and thereafter the rate of decrease becomes more rapid.

Figure 5.6 presents breakdown data for different mixture ratios in a 10mm gap, at pressures ranging from 1.0 to 5.0 bar. Starting at the low pressure end, one observes that for pressures up to about 3.5 bar the breakdown voltage-mixture ratio relationship is similar to that of Figure 5.5. However, at 5.0 bar of total pressure the dielectric strength of the mixture shows an unexpected decrease at relatively high contents of SF<sub>6</sub>. This effect is more pronounced in longer or less uniform field gaps, as shown in Figure 5.7, where breakdown voltage data obtained for a 50mm gap are plotted. In this case the dielectric strength of the mixture is drastically reduced as the content of SF<sub>6</sub> is

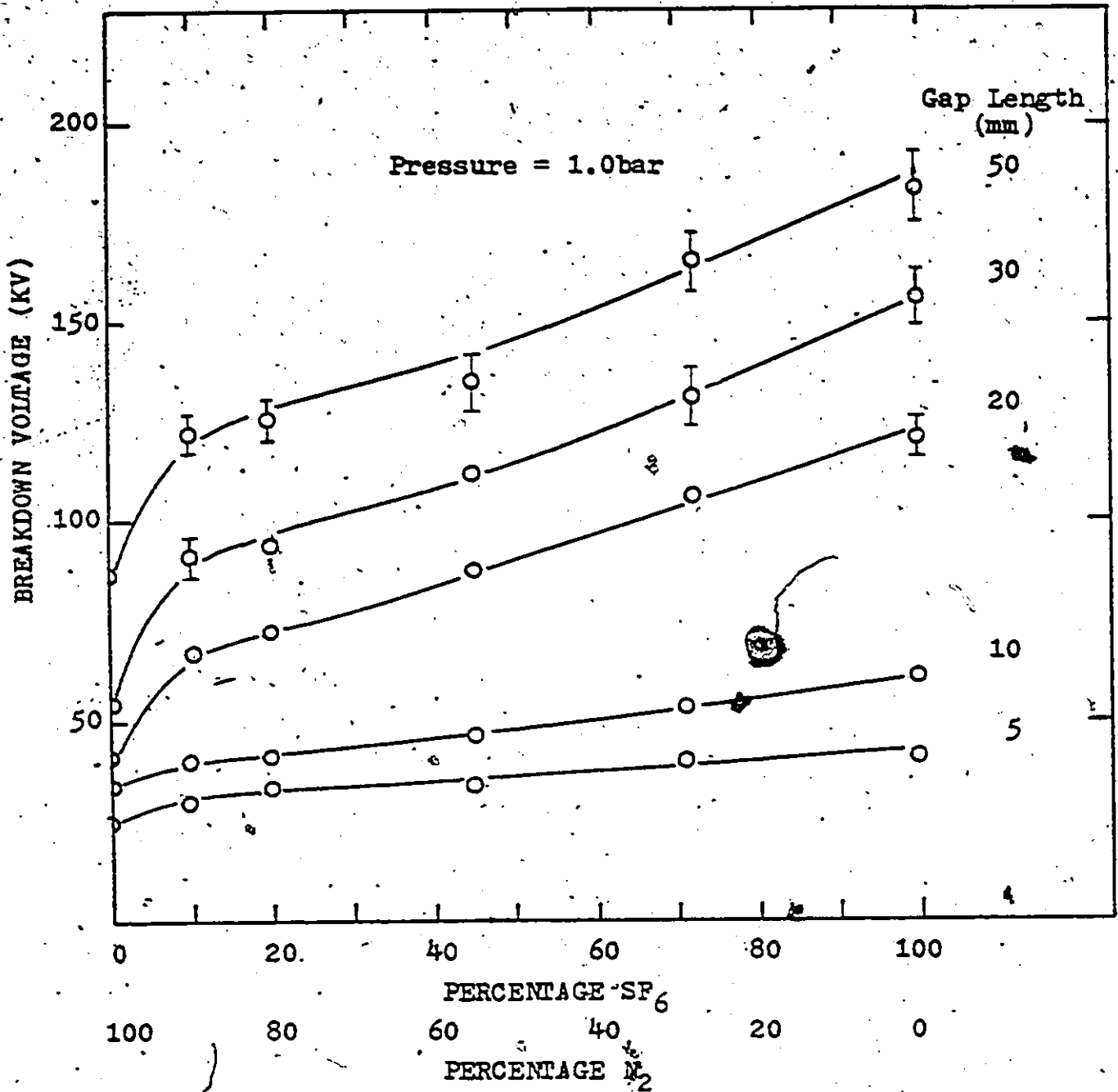


Figure 5.5. Dependence of negative impulse breakdown voltage on mixture ratio for rod-plane gaps ranging from 5 to 50 mm at a total pressure of 1.0 bar.

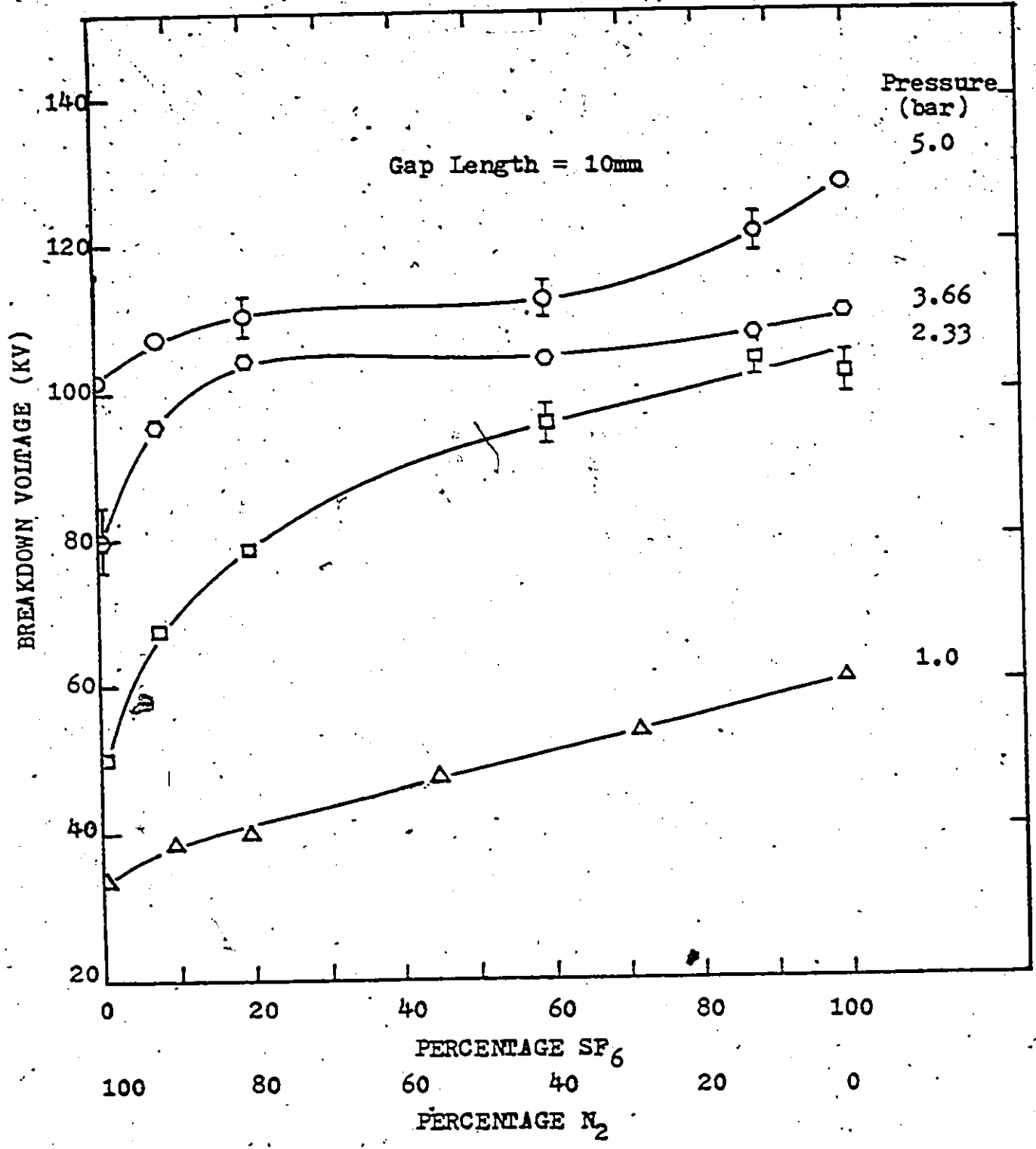


Figure 5.6. Negative rod-plane impulse breakdown voltage and mixture ratio relationship for a pressure range of 1.0-5.0 bar.

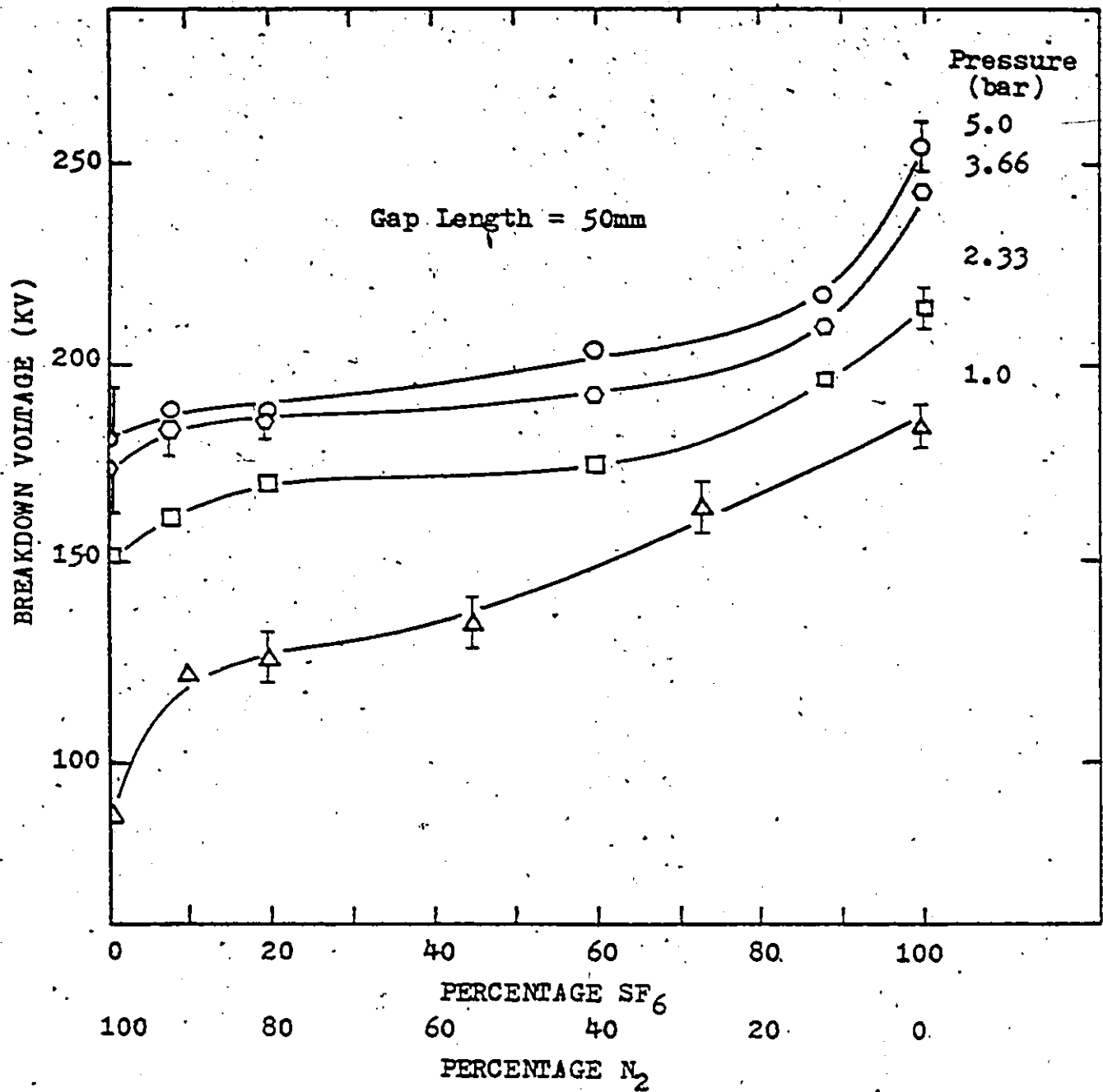


Figure 5.7. Negative rod-plane impulse voltage and mixture ratio relationship for a pressure range of 1.0-5.0 bar.

reduced from 100% to 80%.

Although the curves of Figure 5.6 indicated a trend of loss of dielectric strength at high pressure and/or gap length, the sudden drop exhibited in the 3.7 and 5.0 bar curves of Figure 5.7 was not anticipated. Due to the lack of published data relating to this effect, the repeatability of the breakdown results in this region was methodically tested, and found to be satisfactory. Similarly, the scatter in the values of  $V_{50}$  was generally lower than 5%.

### 5.3 Positive Impulse Breakdown in SF<sub>6</sub>/N<sub>2</sub> Mixtures.

The breakdown characteristics of positive rod-plane gaps in pure SF<sub>6</sub> have been studied more intensively than those of negative polarity. Several investigators have shown that the non-uniform field breakdown voltage-pressure characteristics of pure SF<sub>6</sub> exhibits a negative slope at the lower pressures. The phenomenon has been ascribed to a space charge modification of the field (19).

Figure 5.8 shows the breakdown characteristics of SF<sub>6</sub>/N<sub>2</sub> mixtures for a 10mm gap and pressures in the range from 1.0 to 5.0 bar. At the higher pressures the breakdown voltage mixture ratio relationship is nearly linear with a plateau between approximately 40 to 60% SF<sub>6</sub> content. At the lower pressures, notably at 1 bar, a new trend begins to develop. The addition of a small amount of N<sub>2</sub> to SF<sub>6</sub> increases the breakdown strength of the mixture above that of pure SF<sub>6</sub>. Figure 5.9 shows that this anomalous increase becomes more pronounced and

rather unpredictable as the length of the rod-plane gap increases (or the field distribution becomes less uniform). In the extreme case, the dielectric strength of mixtures composed of some 50% to 80%  $\text{SF}_6$  with 50% to 20% of  $\text{N}_2$  at a pressure of 1 bar approaches the dielectric strength of the same mixtures at a pressure of 5 bar. Figure 5.9 also shows the breakdown values for pure  $\text{N}_2$  (dark points on the vertical axis) at 5.0, 4.0, 3.0, 2.0 and 1.0 bar in descending order.

It should be noted that for pressures above 2 bar, the breakdown values in pure nitrogen exceed the corresponding values in mixtures composed of 20% and 10%  $\text{SF}_6$ . The anomalous behaviour of the breakdown characteristics in mixtures of high and low content of  $\text{SF}_6$  may be better appreciated from Figure 5.10 in which the breakdown characteristics for pure  $\text{N}_2$ , pure  $\text{SF}_6$  and for different mixtures have been plotted versus the total pressure. At lower pressure (below 1 bar), the curves for the mixture with high  $\text{SF}_6$  content exhibit the familiar steep increase in breakdown voltage with pressure, generally described as "corona stabilized breakdown", followed by the negative slope at higher pressure. Addition of 15% of nitrogen to  $\text{SF}_6$  causes a large increase in the dielectric strength.

At pressures higher than 2 bar the breakdown voltages of the 95%, 85% and 65%  $\text{SF}_6$  mixtures drop below that of pure  $\text{SF}_6$  and continue to do so up to 5 bar of total pressure.

At lower  $\text{SF}_6$  contents and pressures above 2 bar (Figure 5.10) the addition of some 10% to 20% of  $\text{SF}_6$  to  $\text{N}_2$  causes a reduction in the dielectric strength, a phenomenon not recorded



previously in the literature. Additional studies were therefore undertaken in mixtures containing less than 10% of SF<sub>6</sub>.

The content of SF<sub>6</sub> was varied from 10% down to 0.01%. As the content of SF<sub>6</sub> was reduced below 10%, at first the breakdown characteristics followed the trend shown in Figure 5.10 that is, the peak breakdown voltage observed at the lower pressure continued to fall with decreasing the content of SF<sub>6</sub>. As the content of SF<sub>6</sub> was reduced below about 5%, the breakdown strength of the mixture started to increase, reaching a strength well in excess of that of pure SF<sub>6</sub> as shown in Figure 5.11 and 5.12. The highest strength was observed in a mixture of 99.8% of nitrogen and 0.2% of SF<sub>6</sub>. Further decrease of SF<sub>6</sub> content lowered the peak breakdown values. Comparison of the curves shown in Figures 5.10 and 5.11 show that the maximum strength in mixtures containing a fraction of a percent of SF<sub>6</sub> occurs at a pressure of about 2 bar, while in mixtures composed of high SF<sub>6</sub> contents (higher than about 5.0% SF<sub>6</sub>) the voltage maximum is observed at about 1 bar of total pressure. For mixtures with less than 0.1% of SF<sub>6</sub>, the peak of maximum voltage is shifting to higher pressures proportionally to the partial pressure of SF<sub>6</sub>.

Figure 5.12 shows that the addition of 0.2% of SF<sub>6</sub> to nitrogen approximately doubles the strength of pure nitrogen at about 1.7 bar of total pressure, an effect similar to that recently reported by Farish et-al.(3) for mixtures of SF<sub>6</sub>/H<sub>2</sub>.

At pressures above 2 bar the pattern of the breakdown

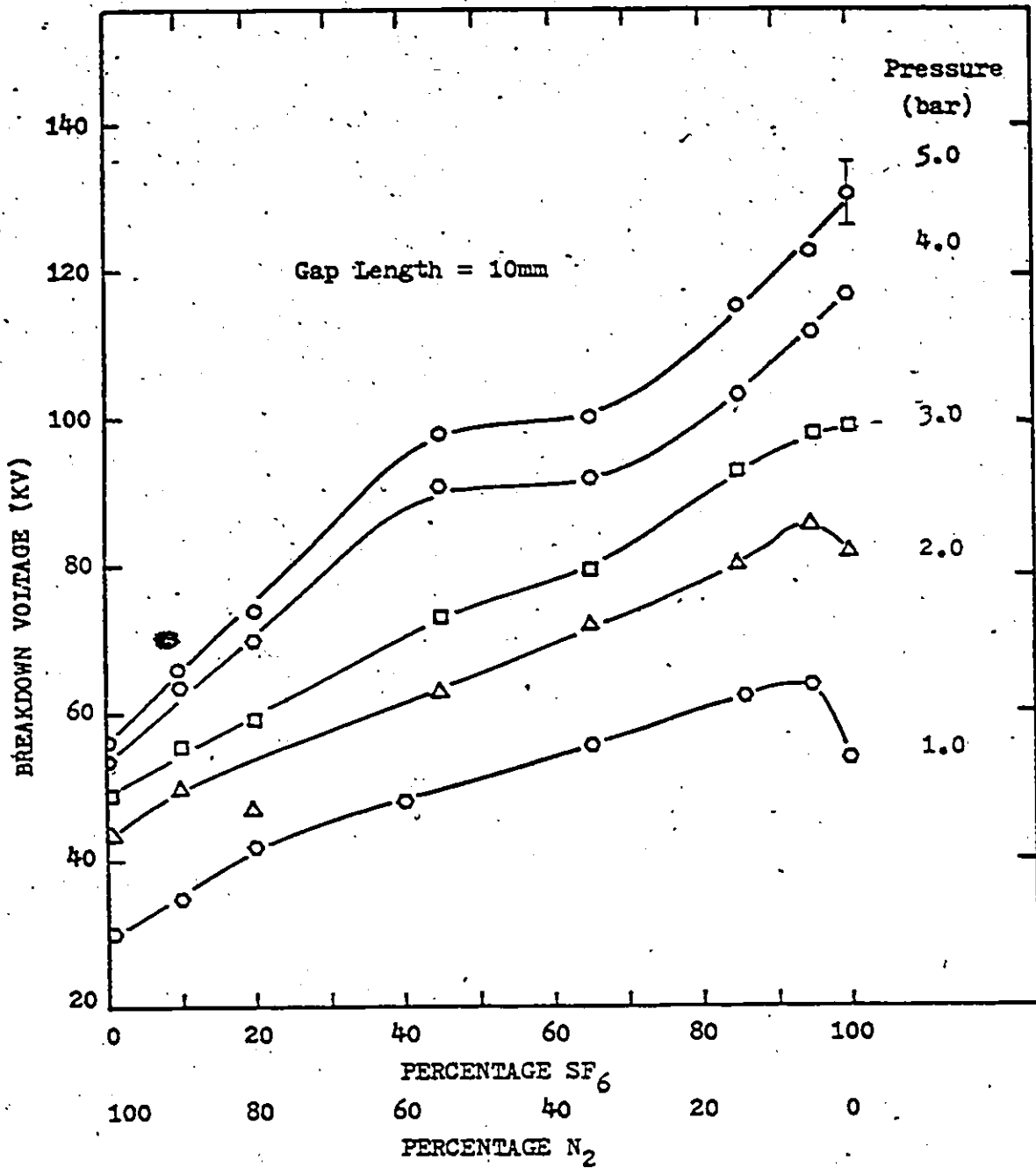


Figure 5.8 Positive rod-plane impulse breakdown voltage and mixture ratio relationship for a pressure range of 1.0-5.0 bar, and a 10 mm gap length.

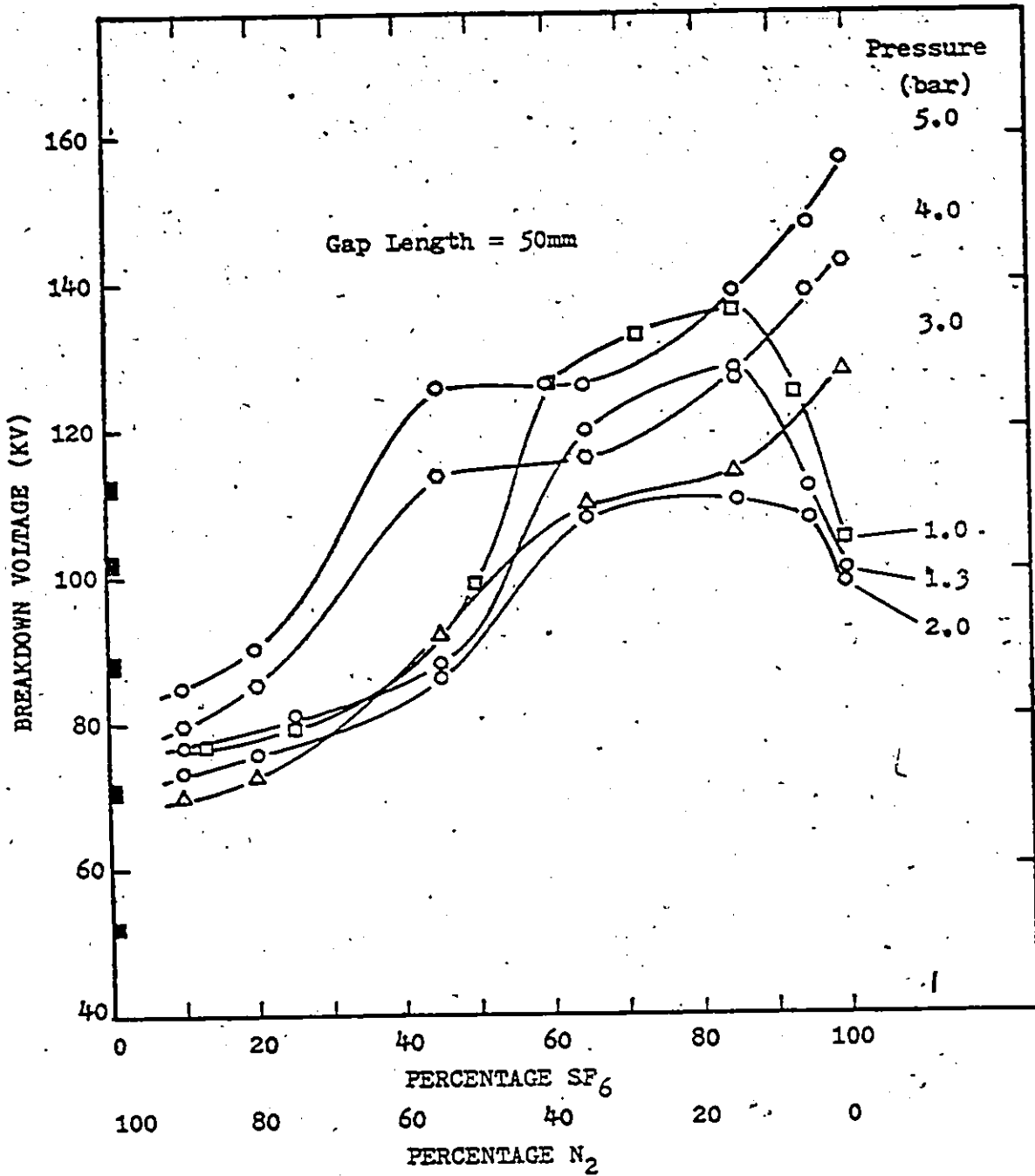


Figure 5.9 Positive rod-plane impulse breakdown voltage and mixture ratio relationship for a pressure range of 1.0-5.0 bar. The dark points on the vertical axis represent the impulse breakdown voltage of 100% N<sub>2</sub> at 1.0-5.0 bar in ascending order.

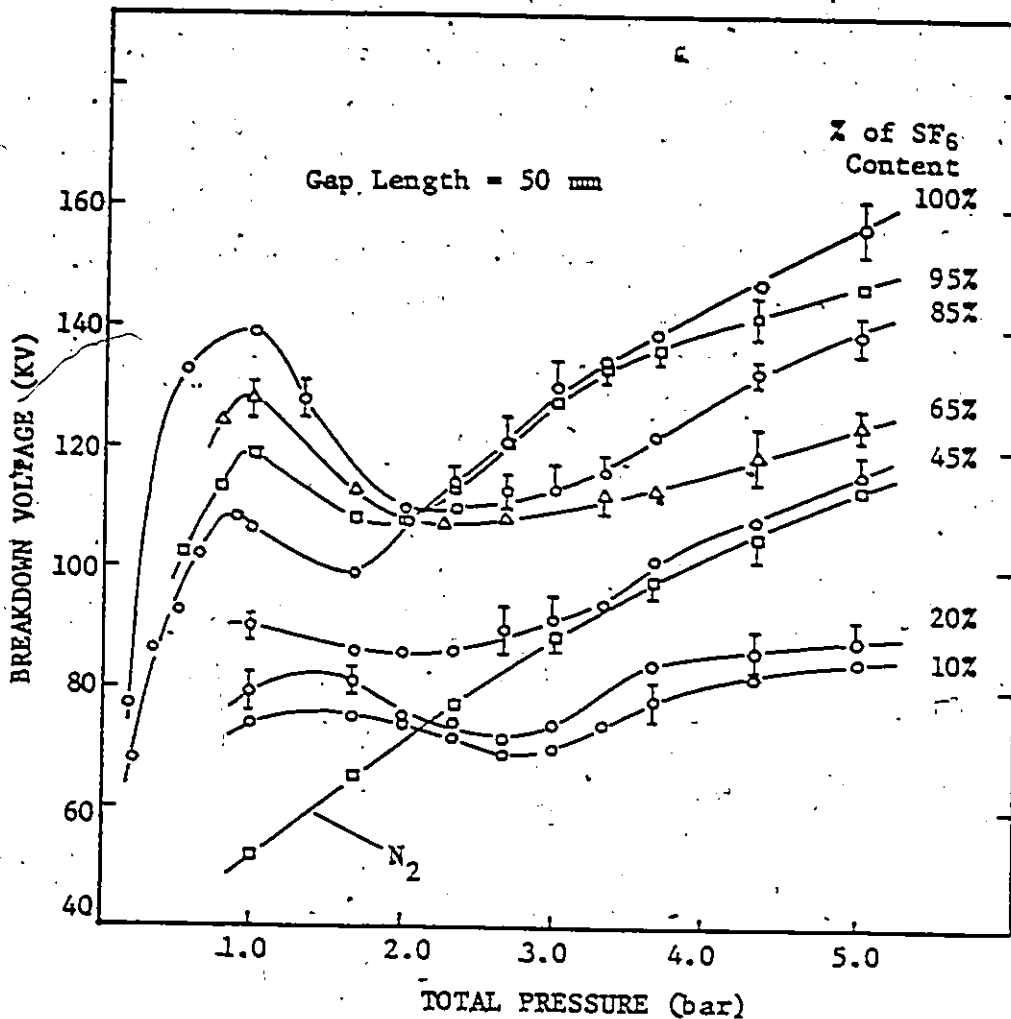


Figure 5.10 Positive rod-plane impulse breakdown voltage-pressure relationship for various SF<sub>6</sub>-N<sub>2</sub> mixtures. Mixtures with 65% of SF<sub>6</sub> content or more at pressures less than 2.0 bar exhibit higher dielectric strength than pure SF<sub>6</sub>.

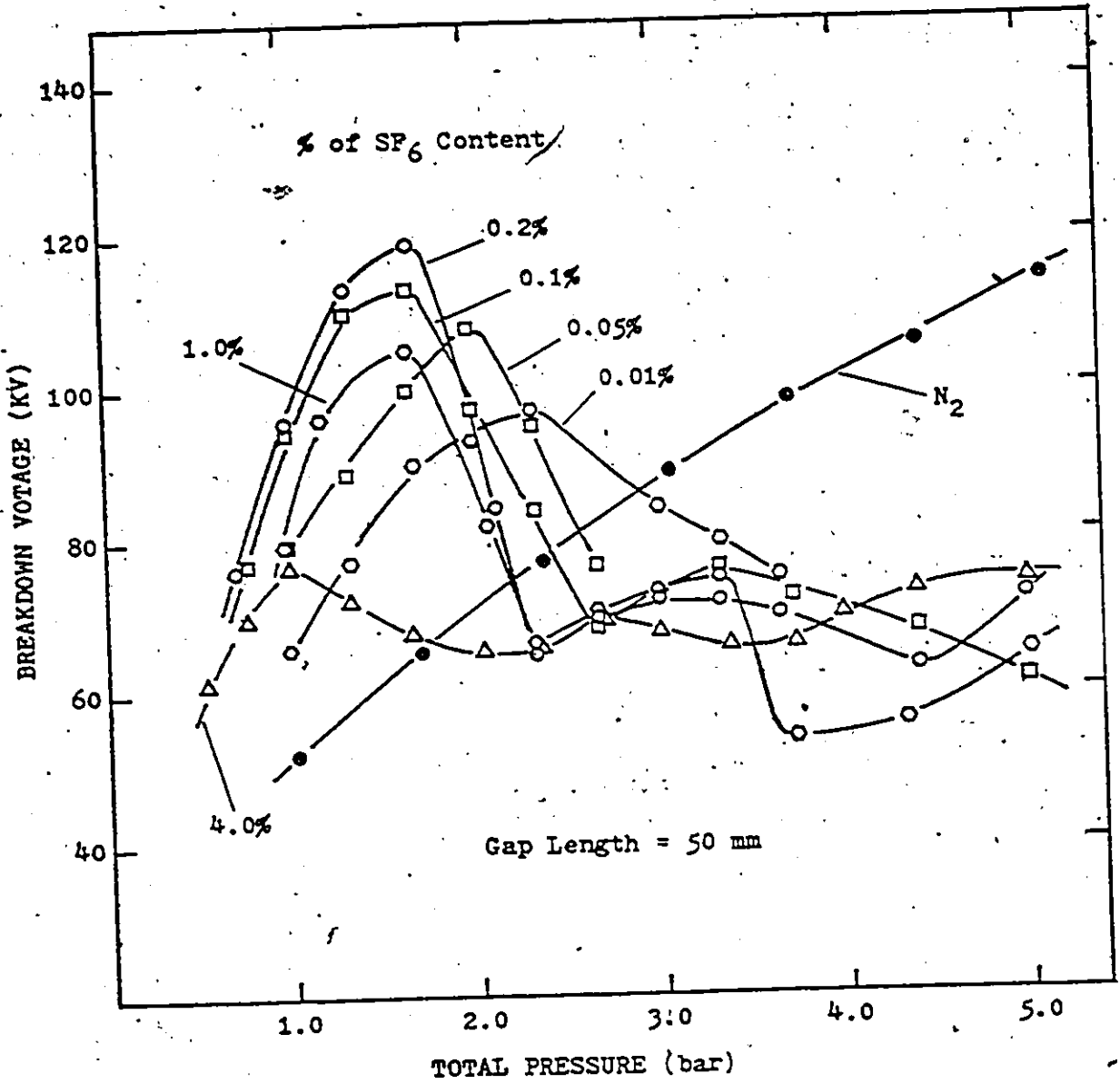


Figure 5.11 Positive rod plane impulse breakdown voltage and pressure relationship for mixtures containing small traces of SF<sub>6</sub>. Gap length: 50 mm.

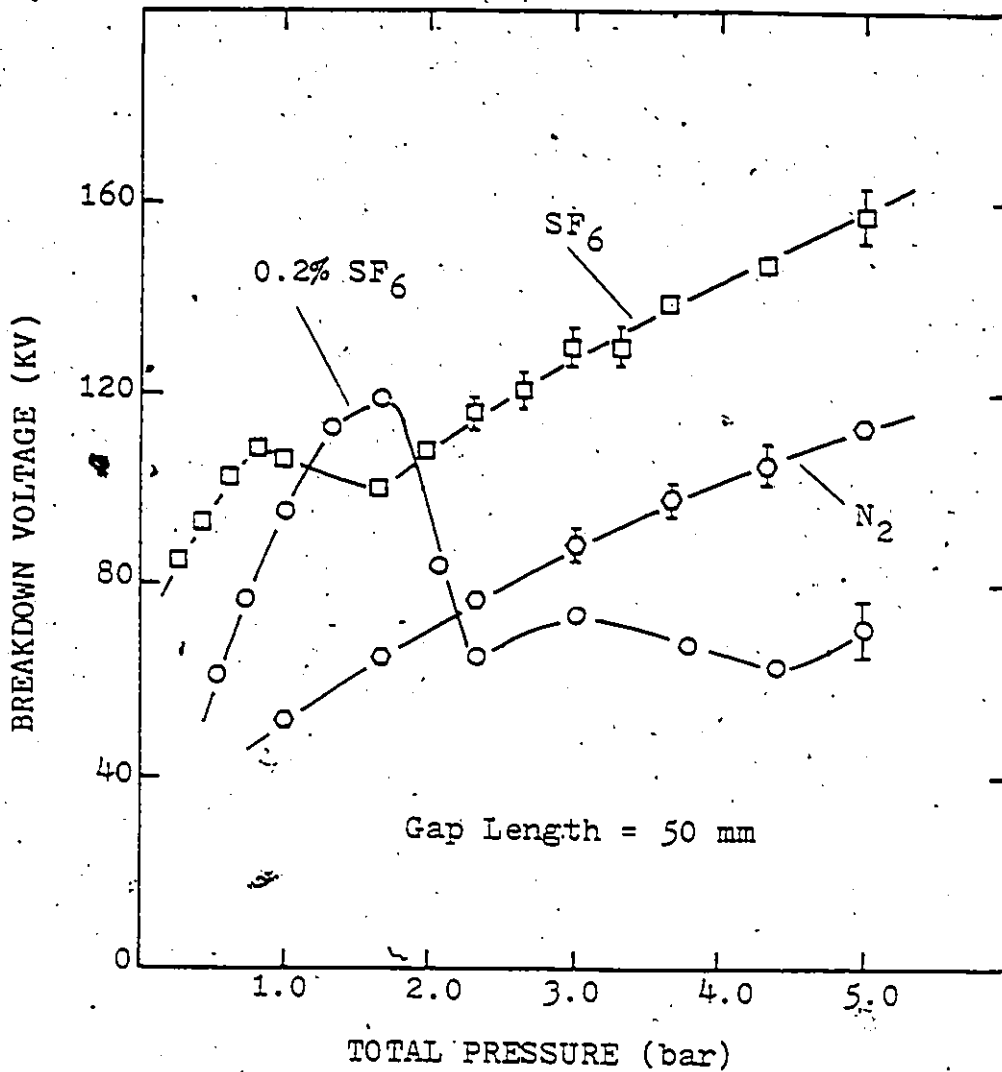


Figure 5.12. Positive rod-plane impulse breakdown voltage-pressure characteristics for: pure SF<sub>6</sub>, pure Nitrogen and an SF<sub>6</sub>-N<sub>2</sub> mixture with 0.2% of SF<sub>6</sub> content. Note that the breakdown voltage of the 0.2% SF<sub>6</sub> mixture at 1.7 bar (P<sub>max</sub>), is higher than that of pure SF<sub>6</sub> and approximately twice as high as that of pure N<sub>2</sub> at the same pressure.

characteristics as shown in Figure 5.11 becomes complicated and unpredictable. While the scattering in the values of  $V_{50}$  was small, the repeatability of the measurements was very poor. However, if the breakdown voltage pattern in this region is highly sensitive to the mixture ratio, then the repeatability of the results cannot be properly examined since the error involved in producing a 0.05%  $SF_6$  mixture could be as high as ten to thirty percent.

Under positive polarity and both long and short gaps, it was observed that the measured breakdown values for different mixtures were influenced in different ways by the immediate history of the gas. Phenomena such as residual gas ionization and electrode and gas temperatures caused by previous sparks were found to affect the breakdown values of different mixtures differently. To minimize such effects, a time interval of 1 minute between consecutive impulses was adopted. This time was found sufficient to give consistent results.

#### 5.4 Temporal Growth of Ionization.

The temporal growth of ionization during and following breakdown was investigated mainly with the use of a photomultiplier. Each photomultiplier signal is a typical trace, representing at least 5 to 10 similar traces recorded for each different set of conditions. The photoelectric records were supplemented with current measurements during the spark development. The main emphasis in these measurements was placed on breakdown rather than prebreakdown phenomena. Hence the current

measurements were not pursued to a great extent.

The photomultiplier-transient digitizer system used in these experiments is designed to give a high degree of temporal resolution. The results presented in this work show the complete photon activity in the gap from prebreakdown to recombination process which take place in a time interval of the order of microseconds. Therefore interference of the measuring system which has a sensitivity of the order of nanoseconds is minimal.

#### 5.4.1 Growth of Ionization in Negative Rod-Plane Gaps.

Figure 5.13(a) shows typical photomultiplier current records during the breakdown of a 5mm gap at a pressure of 1 bar in mixtures ranging from 100% SF<sub>6</sub> to 100% of nitrogen. In pure SF<sub>6</sub> at breakdown, the sharp rise indicates the formation of the leader stroke, followed by the main stroke which is barely distinguishable and a broad pulse a few microseconds later. Simultaneous current records showed no significant current flow corresponding to the last pulse (Figure 5.13(d)). Dale (84), obtained similar photomultiplier traces from sparks in air gaps, which he also photographed with the use of a streak camera. The streak photographs did not record any light during the last pulse and Dale concluded that this pulse was a saturation effect of the photomultiplier tube. In the light of these results a number of tests were conducted by the author to determine the origin of this pulse. The results of these tests (see Appendix 4) suggest a similar saturation effect as that described by Dale.



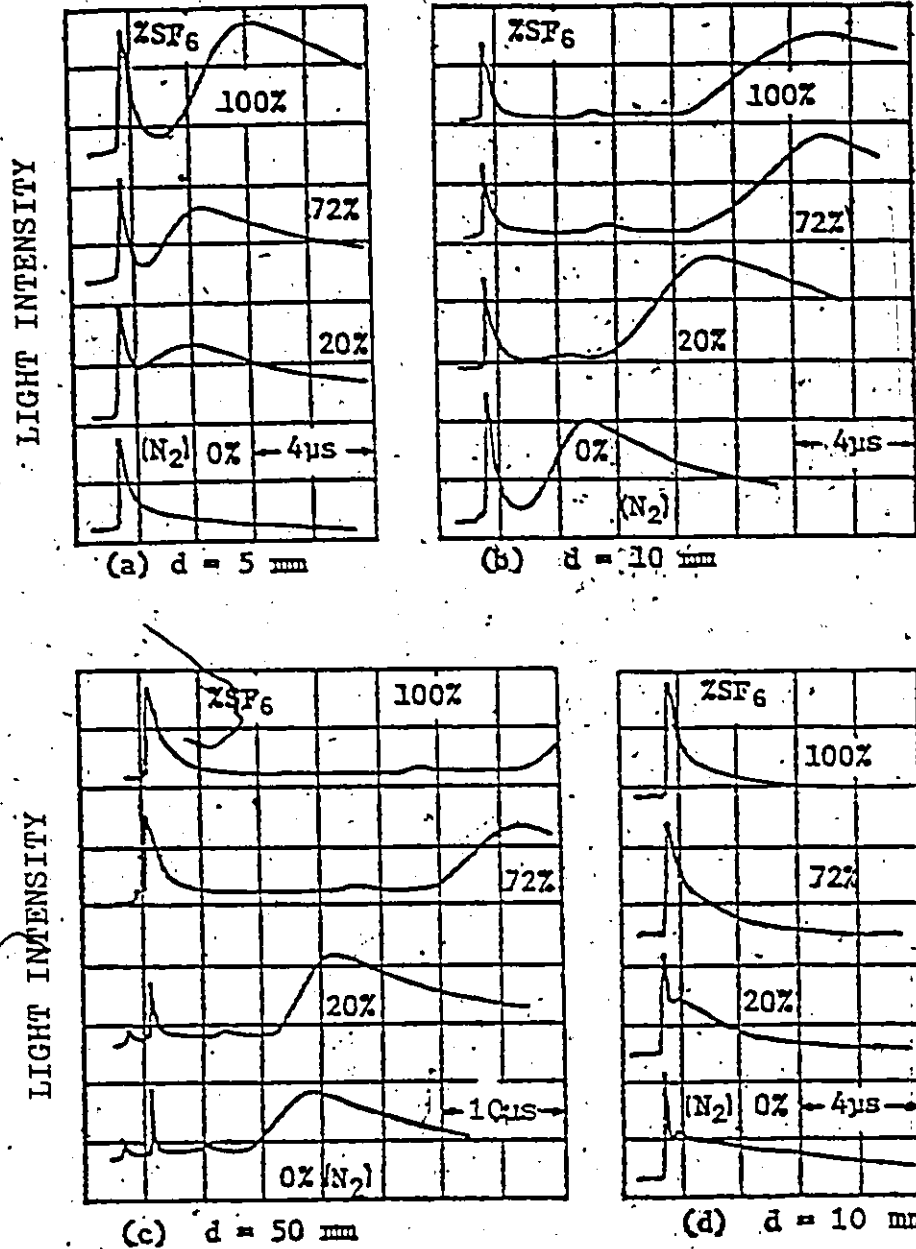


Figure 5.13 Photomultiplier records of gap discharge in various SF<sub>6</sub>-N<sub>2</sub> mixtures, (a) 5mm; (b) gap - 10 mm; (c) gap - 50 mm; (d) gap current with gap - 10 mm

As the gap was increased from 10mm to 50mm, corona pulses were observed in mixtures of high nitrogen content, but the overall pattern of the photomultiplier pulses remained unchanged.

#### 5.4.2 Growth of Ionization in Positive Rod-Plane Gaps.

Representative photomultiplier records of positive impulse rod-plane gap discharges in  $\text{SF}_6/\text{N}_2$  mixtures and in the constituent gases are included in Figure 5.14(a) to (c). At a pressure of 1 bar the photomultiplier records were very similar to those observed under negative polarity (Figure 5.13 (c)).

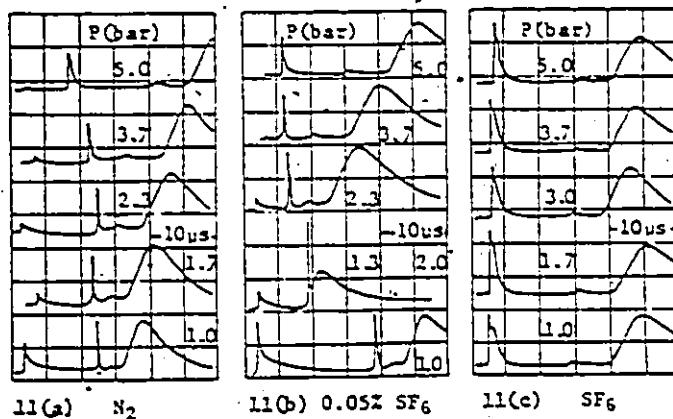


Fig.5.14 Effect of pressure on the photomultiplier pulses in  $\text{N}_2$ , in  $\text{N}_2$ -containing 0.05%  $\text{SF}_6$  and in  $\text{SF}_6$  respectively. (a)  $\text{N}_2$ ; (b)  $\text{N}_2$  -  $\text{SF}_6$  mixture; (c)  $\text{SF}_6$

The photomultiplier traces observed at a total pressure of about 2 bar in pure nitrogen, in nitrogen containing a small amount of  $\text{SF}_6$  (0.05), and  $\text{SF}_6$  are represented with the second lowest trace in Figures 5.14(a) to 5.14(c) respectively. As it is seen, addition of a trace of  $\text{SF}_6$  to nitrogen at that pressure caused an increase in the magnitude of both the corona and the leader stroke pulses.

The time lag between the corona pulse and the leader stroke is closely related to the statistical time lag for breakdown. Corona discharges take place in the front of the impulse wave close to the peak voltage, while the leader stroke represents bridging of the gap by the discharge at breakdown. No exact measurement of time lags was made, but statistical time lags were observed to be longer at low pressure and small gap lengths.

#### 5.5 Spatial Growth of Ionization.

During the course of breakdown voltage measurements in  $\text{SF}_6/\text{N}_2$  mixtures, observation of the electrodes after a series of breakdowns showed that the rod electrode was at times pitted or dis-colourized along the cylindrical part, away from the spherical tip. This observation suggested that under certain conditions, depending on mixture ratio and pressure, the spark was forced to initiate away from the tip of the electrode. On the basis of those observations a still camera was introduced into the system. An FTb Canon, 35mm single lens reflex camera was used with a 50mm macro lens. The camera was mounted on one of the test chamber windows. Photographs of spark trajectories were obtained in  $\text{SF}_6$ ,  $\text{N}_2$  and  $\text{SF}_6/\text{N}_2$  mixtures, and impulse coronas under both polarities were also photographed whenever possible. The magnification in all the illustrations is approximately 0.9 times that of the real object.

### 5.5.1 Spark Trajectories in $N_2$ , $SF_6$ , and $SF_6/N_2$ Mixtures.

Spark discharges in nitrogen were photographed under both polarities in the pressure range of 1.0 to 5.0 bar. Under negative polarity, the spark paths were slightly curved as they approached the plane electrode, irrespective of gas pressure. Under positive polarity and low pressure, the sparks followed the minimum path distance along the line of highest field strength. As the pressure increased the spark trajectories curved in a proportional manner.

Figure 5.18 shows two typical discharges at 1.0 and 5.0 bar of nitrogen. These photographs indicate that there is a certain relationship between the gas pressure and the number and distribution of the positive ions in  $N_2$ . At higher pressures, the space charge surrounding the anode is apparently larger and corona streamers that would ordinarily move towards the cathode are retarded and choked, until the voltage becomes high enough for them to reach the cathode by travelling around it.

In  $SF_6$ , photographs of discharges under negative polarity did not show any definite trend as the pressure varied. For positive rod-plane, previous investigations (18,19,56,57) have either indicated or shown that the spark trajectories are highly curved in the corona stabilized region (around  $P_{max}$ , Figure 5.4). The photos taken here are in agreement with these observations. At 1.0 bar where  $P_{max}$  occurs, the spark advanced from the tip of the anode to the cathode along a highly curved path. As the pressure increased to  $P_{min}$  (1.7 bar) the curvature of the paths decreased, and for pressures higher than  $P_{min}$  the spark paths

were moderately curved. Two typical spark trajectories in 1.0 and 5.0 bar of SF<sub>6</sub> are shown in Figure 5.19. Most of the sparks in SF<sub>6</sub> travelled along the line of highest field strength for a few millimeters before they finally curved.

In comparing Figures 5.19 and 5.18 one observes that while in N<sub>2</sub> the curvature increased with pressure, in SF<sub>6</sub> the spark paths reached maximum curvature in the region where corona onset preceded breakdown. Also, curved spark paths are in both cases associated with locally maximum breakdown voltage.

Spark discharges in SF<sub>6</sub>/N<sub>2</sub> mixtures with high SF<sub>6</sub> contents did not show significant differences from pure SF<sub>6</sub>. However investigating SF<sub>6</sub>/N<sub>2</sub> mixtures with less than 1.0% SF<sub>6</sub>, a most unusual phenomenon was observed under positive impulse conditions. The point of spark initiation on the rod electrode moved away from spherical tip as the pressure varied. An extensive investigation of SF<sub>6</sub>/N<sub>2</sub> mixtures with 0.1 and 0.2% SF<sub>6</sub>, showed that the effect responsible for the movement of the spark which will be referred to as "creep effect", has a definite dependence of the partial pressure of SF<sub>6</sub>, as well as the total pressure of the mixture.

With reference to Figure 5.11, the breakdown voltage-pressure characteristics of the various mixtures have a positive slope at low pressures, followed by a negative slope and thereafter the breakdown voltage remains at a low level without a definite trend. Spark trajectories at the high pressure end initiated at the point and reached the plane electrode via moderately curved paths. Reducing the pressure to the region of the nega-

tive slope, the spark initiation point moved away from the spherical tip. At the voltage maximum (1.7 bar), the creep distance along the rod electrode reached a maximum value and the spark trajectories a maximum curvature. In reducing the pressure below  $P_{max}$  (to about 1.0 bar), the creep distance was reduced to zero and the curvature of the trajectories was minimized.

A typical set of results for an  $SF_6/N_2$  mixture with 0.1%  $SF_6$  is shown in Figures 5.15 and 5.16. Photograph 5.16(b) displays the maximum creep distance and curvature.\* Observations of the rod electrode after the measurements showed that, at 1.7 bar the creep distance was as high as 3.5 to 4.0 cm.

These results indicate the existence of a space charge surrounding the rod electrode and probably extending to the inter-electrode area. Also, while the curvature of the trajectory is associated with  $P_{max}$ , the creep distance seems to depend on the partial pressure of  $SF_6$ . Figure 5.17 displays how the creep distance varies with the percentage content, or partial pressure of  $SF_6$ . As it is shown in photograph 5.17(d) the creep distance is reduced to zero at about 7.0% of  $SF_6$  content.

#### 5.5.2 Impulse Coronas in $SF_6/N_2$ Mixtures With Low $SF_6$ Content.

Impulse coronas were photographed in pressure regions and mixtures in which corona onset preceded spark onset. Ilford film 400 ASA was used and in most cases the negatives were push-

---

\* Note that the spark ends at the edge of the plane electrode

processed at 1800 to 2000 ASA. The lens used was a Canon FD,  $f=1.8$ . Figure 5.20 shows two positive impulse coronas in an  $SF_6/N_2$  mixture with 0.2%  $SF_6$  at 1.0 and 1.7 bar of total pressure. Both coronas show intense streamers concentrated around the spherical tip of the electrode and unlike pure  $N_2$  and  $SF_6$  one can observe streamers of moderate intensity surrounding the cylindrical part of the electrode. At 1.0 bar the corona streamers grow in the direction of the plane electrode, coinciding with the trajectory of the sparks at this pressure which have low curvature and zero creep distance. While the corona pulse at 1.0 bar is generated at a voltage closer to breakdown than that of 1.7 bar, the streamers associated with the latter have a considerably higher luminosity.

Figure 5.21 shows a positive and a negative corona pulse at 1.7 ( $P_{max}$ ) for a 0.1%  $SF_6$  mixture. The positive corona is similar to that of Figure 5.20(b). The intensity of the streamers is somewhat higher, but again no long range streamers are observed. One would expect that streamers extending to the cathode should start above the tip, with a creep distance equal to that of the discharge. The negative corona, shows a flare-like character and advances to the anode in a curved path.

#### 5.6 Corona Onset Measurements.

The corona onset measurements in  $SF_6$ , nitrogen and  $SF_6/N_2$  mixtures will be presented in the next chapter for comparison with the theoretically calculated streamer onset voltage.

The lowest corona onset voltage measured was that of nitrogen. It is interesting to note that mixtures with low  $SF_6$

content that exhibited a positive impulse breakdown voltage at high pressures considerably lower than nitrogen, have an onset voltage at these pressures higher than that of nitrogen.

This is shown in Figure 5.22, where the breakdown and onset voltage of a 50mm gap in 0.2% SF<sub>6</sub> mixture and nitrogen are plotted versus pressure. . As it is seen, the onset voltage of the 0.2% SF<sub>6</sub> mixture is slightly higher than that of nitrogen and coincides with the breakdown voltage at the higher pressures. This behaviour is similar to that of pure SF<sub>6</sub> and one could attribute the voltage maximum to a corona stabilized breakdown process. However in a further discussion (chapter 7), it is suggested that there are some basic differences between the mechanism responsible for the breakdown voltage peak of the 1 to 0.01% SF<sub>6</sub> mixtures and that of SF<sub>6</sub>.





(a)  $P_t = 5.0$  bar



(b)  $P_t = 4.3$  bar

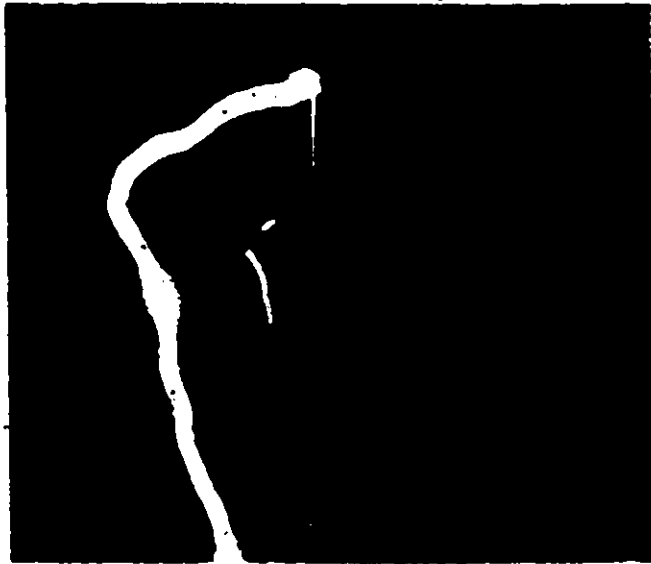


(c)  $P_t = 3.7$  bar



(d)  $P_t = 3.0$  bar

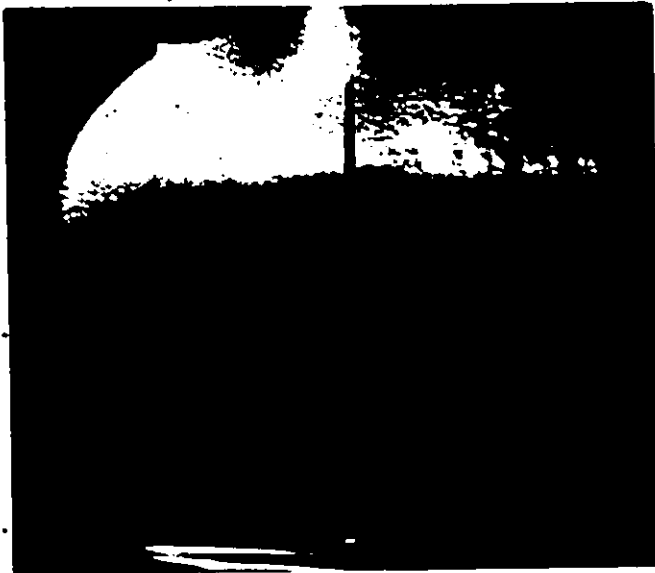
Figure 5.15. Positive impulse breakdown of a 50 mm rod-plane gap in  $SF_6/N_2$  mixture with 0.1%  $SF_6$  content. The effect of the total pressure  $P_t$  on the spark initiation point is shown, for pressures of 5.0 to 3.0 bar, respectively.



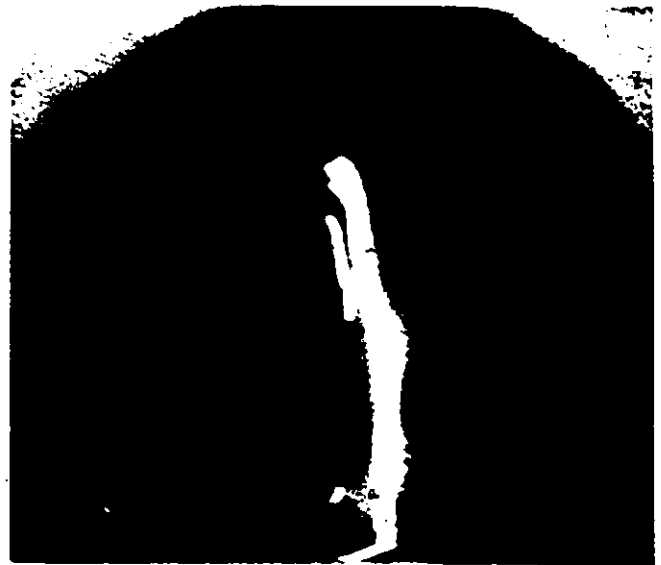
(e)  $P_t = 2.3$  bar



(f)  $P_t = 1.7$  bar



(g)  $P_t = 1.7$  bar



(h)  $P_t = 1.0$  bar

Figure 5.16. In continuation of Figure 5.15 the effect of further reduction of the total pressure  $P_t$  is shown in Figures (e) to (h) for pressures of 2.3 to 1.0 bar respectively. Photographs (f) and (g) are taken under the same conditions, note that the spark in (g) ended on the wall of the chamber.



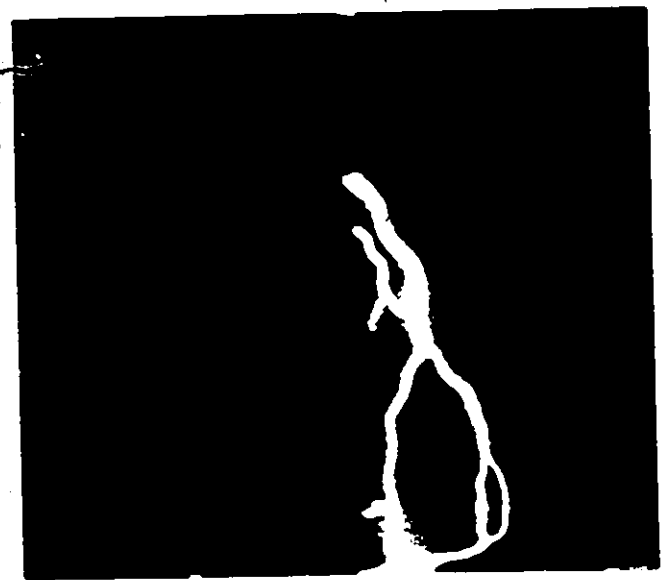
(a) 0.1% SF<sub>6</sub>



(b) 0.2% SF<sub>6</sub>



(c) 2.5% SF<sub>6</sub>



(d) 7.0% SF<sub>6</sub>

Figure 5.17. Positive impulse breakdown of a 50 mm rod-plane gap in mixtures of SF<sub>6</sub>/N<sub>2</sub> at 1.7 bar of total pressure. Photographs (a) to (d) show the effect of the % of SF<sub>6</sub> content on the spark initiation point at the rod electrode.



(a)  $N_2$ ,  $P=5.0$  bar

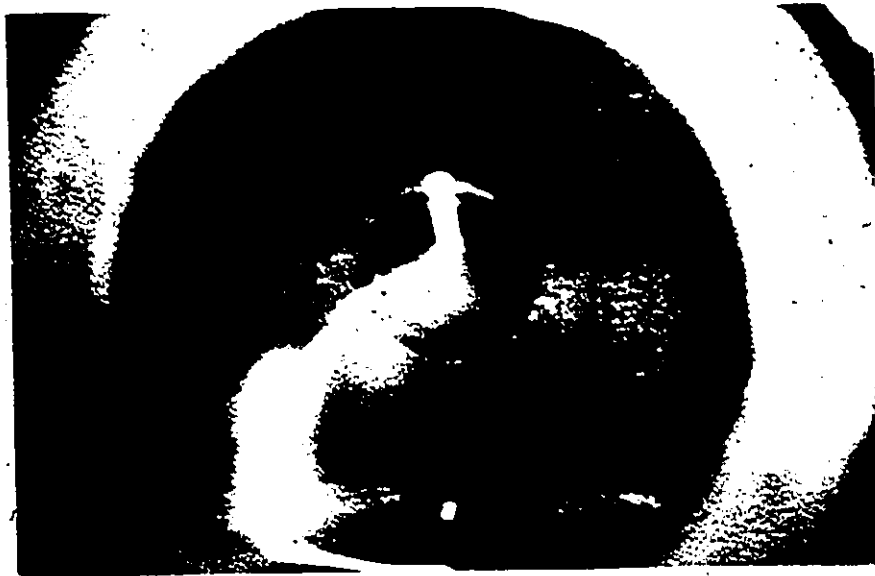


(b)  $N_2$ ,  $P=1.0$  bar

Figure 5.18. Positive impulse breakdown of a 50 mm rod-plane gap in Nitrogen. The effect of pressure on the spark movement through the gap is shown in photographs (a) and (b). This indicates a dependence of the positive charge concentration on the gas pressure.

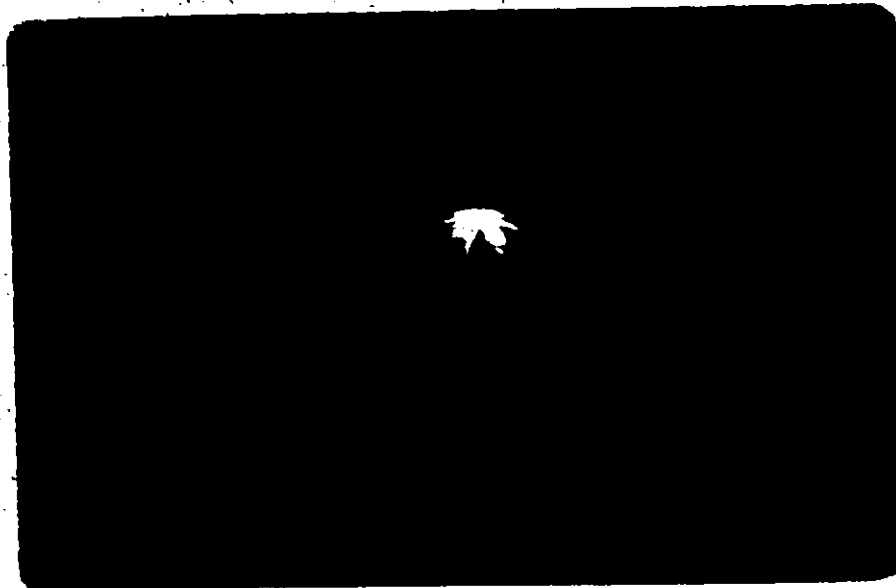


(a) SF<sub>6</sub>, P=5.0 bar



(b) SF<sub>6</sub>, P=1.0 bar

Figure 5.19. Positive impulse breakdown of a 50 mm rod-plane gap in SF<sub>6</sub>. The unusually high curvature of the spark trajectory at 1.0 bar (as compared to that of Figure 5.18(b)), is related to the presence of the corona stabilized breakdown mechanism at this pressure.



(a) 0.2% SF<sub>6</sub>, P<sub>t</sub>=1.0bar

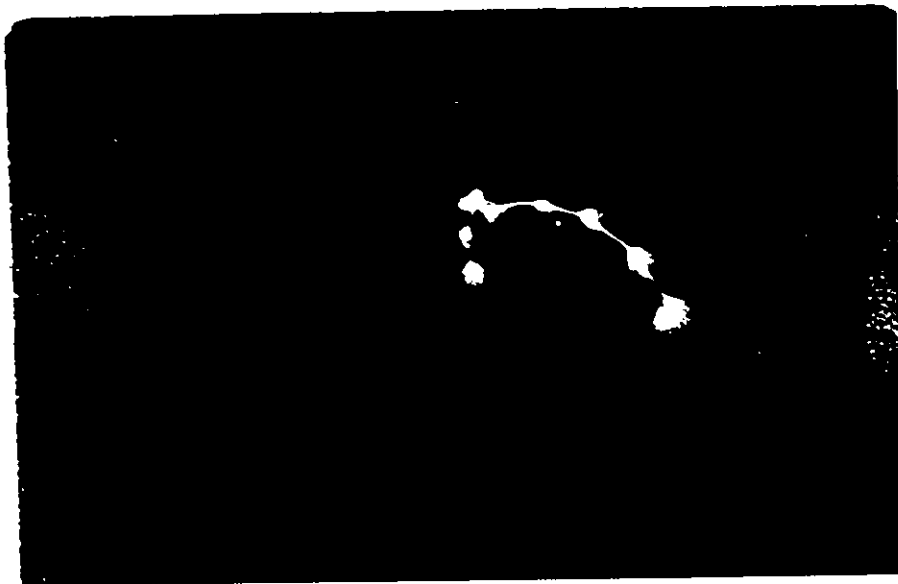


(b) 0.2% SF<sub>6</sub>, P<sub>t</sub>=1.7bar

Figure 5.20. Positive impulse coronas in an SF<sub>6</sub>/N<sub>2</sub> mixture with 0.2% of SF<sub>6</sub> content. Photographs (a) and (b) show the difference in the position and intensity of the corona streamers, as the pressure increases from 1.0 to 1.7bar respectively.



(a) Positive



(b) Negative

Figure 5.21. (a) Positive impulse corona in an  $\text{SF}_6\text{N}_2$  mixture with 0.1% of  $\text{SF}_6$  content and at a total pressure of 1.0 bar. (b) Negative impulse corona under the same mixture and pressure conditions.

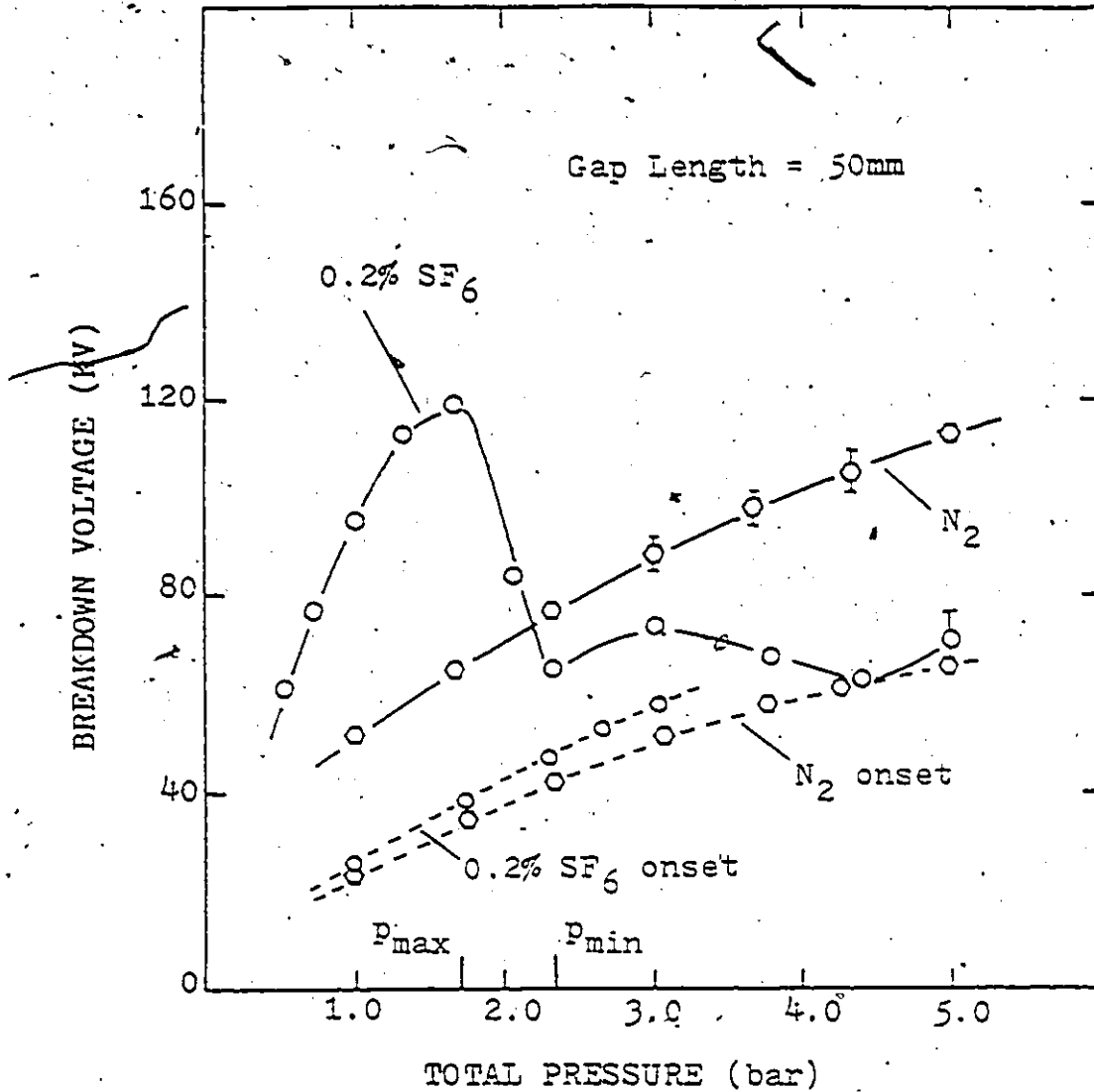


Figure 5.22 Positive rod-plane impulse breakdown and DC corona onset voltage-pressure characteristics of nitrogen and a SF<sub>6</sub>-N<sub>2</sub> mixture with 0.2% SF<sub>6</sub>. Note that although the breakdown voltage of the 0.2% SF<sub>6</sub> mixture is considerably lower than that of nitrogen for pressures higher than 2 bar, the corona onset voltage of the same mixture is higher than the onset voltage of nitrogen.



## CHAPTER 6

### THEORETICAL ANALYSIS OF DISCHARGE CHARACTERISTICS IN SF<sub>6</sub> AND SF<sub>6</sub>/N<sub>2</sub> MIXTURES.

The aim of this chapter is to present an informative description of the mechanism of breakdown operative under the present experimental conditions, and to calculate a number of parameters associated with corona and spark onset in SF<sub>6</sub> and in SF<sub>6</sub>/N<sub>2</sub> mixtures.

The streamer mechanism is briefly discussed and reference is made to various streamer formation criteria. In calculating streamer voltages in rod-plane gaps, use is made of the optimized charge simulation technique developed in chapter 3. Finally the theoretical results are discussed in conjunction with experimental results obtained in this work and elsewhere

#### 6.1 Streamer Mechanism.

The streamer mechanism was developed to explain certain phenomena that occur in electrical discharges and are not accounted for by the Townsend mechanism. The Townsend theory is limited to uniform or near-uniform fields and constant voltage conditions during the prebreakdown developments. It is a relatively slow mechanism that requires the generation of successive avalanches prior to spark onset. In this sense, it fails to explain a number of phenomena, such as formative time lags of the order of 10<sup>-9</sup> sec that occur in various overvolted gaps, and most of the observations associated with non-uniform fields of

symmetrical or asymmetrical electrodes.

The streamer theory is based on the assumption that the discharge initiates with a single avalanche, which leads to the formation of a fast moving plasma channel that bridges the gap and produces a collapse of the applied voltage. The main contributions to the development of the theory are those of Raether (11), Loeb (30) and Meek (58). Raether investigated both anode and cathode directed streamers in uniform and slightly overvolted gaps. By measuring the number of charge carriers in a single avalanche he showed that avalanches in a Townsend discharge have a carrier number  $10^6$ , while streamer avalanches (produced with a certain amount of over-voltage) have a carrier number of the order of  $10^8$ .

This additional space charge and the field produced by it were regarded as the reasons for the transition of the avalanche to an anode or cathode directed streamer. A streamer that moves from the anode to cathode for example, requires the initial avalanche to reach the anode with a carrier number of  $N_c = 10^8$ . The rear portion of the avalanche enhances the field in that region and attracts photoelectrons which create new avalanches that attach to the old one and rapidly extend the plasma to the cathode. A condition automatically develops for a streamer formation; that is, the distance between the electrodes and the applied voltage should be sufficient for the carriers of the avalanche to reach  $N_c = 10^8$ .

Meek developed his streamer theory from observations of a cathode directed positive corona streamer and Raether's obser-

vations of mid-gap streamers. When a voltage higher than the minimum breakdown voltage was applied across the electrodes, the mid gap streamers indicated that the field of the space charge of the avalanche is of the order of the applied field, before the avalanche reaches the anode. Meek then considered the transition from an electron avalanche into a streamer to occur when the radial field  $E_r$  produced by the positive ions at the head of the avalanche, is of the order of the externally applied field.

While both Raether and Meek recognized the need of photoelectrons for the streamer propagation, they did not conduct any calculations involving photoionization. Loeb (30) developed a more explicit theory of streamer onset by introducing photoionization in the calculations via the absorption coefficient  $\mu$ . Accompanying the ionization of an avalanche that yields  $N$  ions, there is an  $f_1 N$  number of photons generated. The absorption coefficient  $\mu$  will determine how many of these  $f_1 N$  photons will be absorbed within a region close to the avalanche and the fraction  $f_2$  of these photons that will lead to ionization. Hence on the basis of constants such as the probabilities  $f_1$  and  $f_2$ , and the absorption coefficient  $\mu$ , Loeb developed an explicit relation for the threshold of streamer propagation, applicable for gases in which these parameters are known.

In more recent years there has been a considerable number of publications dealing with a variety of refinements of the streamer theory. The influence of different secondary processes has been investigated for various gases, including electronegative

insulants such as  $SF_6$ , for a number of electrode arrangements and gaps ranging from meters to millimeters.

To summarize, some of the properties of streamer breakdown include, concentration of the discharge in a narrow channel with branches and abrupt changes in direction, high discharge currents before the avalanche space charge diffuses to the cathode (negative cathode), propagation of a streamer without any contribution from the cathode, high speed propagation that results in short formative time lags, and absence of this mechanism in rare or atomic gases.

## 6.2 Application of Streamer Theory for Calculating Streamer Onset Voltages in $SF_6$ and $SF_6/N_2$ Mixtures.

The main feature of the streamer mechanism is the perturbation of the applied field by the space charge of the initial avalanche and the effect of that perturbation on subsequent ionization. A number of streamer onset criteria in  $SF_6$  have been developed over the years, most of them based on analytical calculations of Raether, Loeb and Meek. Loeb and Raether performed a number of calculations on the influence of the space charge on the ionization coefficients and successor avalanches. Relatively recent computer accessibility has allowed many workers to carry out many of these analytical calculations and in almost all cases there is reasonable agreement with experiment. However, most of these calculations apply to uniform or quasi-uniform electrode geometries. The reason for this is that under non-uniform fields the mechanism of breakdown in  $SF_6$  is far from being clear. There

is a lack of knowledge of constants such as: secondary ionization coefficients, absorption coefficients, and various probabilities of excitation, attachment, and detachment under these conditions. Variables measured under uniform field conditions do not show any unusual pressure behaviour that would account for the negative slope of the breakdown voltage-pressure characteristics of SF<sub>6</sub>. Hence calculations that make use of uniform field and low pressure data should not be expected to exhibit a behaviour as complex as that of the SF<sub>6</sub> breakdown voltage-pressure characteristics. This is shown in a recent attempt of Khalifa et al (60) to calculate positive spark-breakdown of SF<sub>6</sub> in non-uniform fields. Using Loeb's streamer criterion as presented by Nasser in his book (63), and  $\alpha$ ,  $\eta$ ,  $\mu(p)$ ,  $f_1$ , and  $f_2^*$  derived under uniform field conditions, they obtained a monotonically increasing breakdown voltage-pressure characteristic. Khalifa's relation does not apply to non-uniform fields any more than Nitta's simplistic relationship (59) which is used for quasi-uniform field distributions, and was shown by the authors to be within 10% of their own calculations.

In the following section, streamer onset calculations in SF<sub>6</sub> are carried out using the onset criteria of Pederson (61,62) and Nitta (59). Pederson's criterion is also used for calculations in SF<sub>6</sub>/N<sub>2</sub> mixtures, with Baumgartner's effective ionization coefficient for SF<sub>6</sub>/N<sub>2</sub> as given in chapter 2.4.

---

\*  $f_1$  is the ratio of excited to ionized states and  
 $f_2$  is the probability of photoionization

### 6.3 Streamer onset Voltage Calculations in SF<sub>6</sub>, N<sub>2</sub> and SF<sub>6</sub>/N<sub>2</sub>.

As mentioned earlier, Raether proposed that avalanche to streamer onset will occur when the number of charge carriers in a single avalanche reaches  $N_c = 10^8$ . For SF<sub>6</sub>, the total number of free electrons will be given by

$$N = N_0 \exp\left(\int_0^x (\alpha - \eta) dx\right) \quad (6.1)$$

where  $N_0$ : the initial number of electrons

$\alpha$ : ionization coefficient

$\eta$ : electron attachment coefficient

In Raether's criterion,  $N = N_c = 10^8$ . This number was shown to be independent of the gas and field uniformity. Nitta (59), using Raether's criterion and assuming that the field distribution near the surface of the highly stressed electrode is the same as that of two concentric spheres, with the radius of the inner sphere equal to the radius of curvature of the highly stressed electrode, developed the following relationship for predicting streamer onset or breakdown of SF<sub>6</sub> in quasi-uniform fields.

$$V_n = (E/p)_{cr} \cdot u \cdot p \cdot G \cdot \left(1 + \frac{k}{\sqrt{pR}}\right) \quad (6.2)$$

where  $(E/p)_{cr}$ : 89 KV cm<sup>-1</sup> bar<sup>-1</sup>

$u$ : utilization coefficient.

$p$ : gas pressure in bar

$G$ : gap length in cm

$k$ : 0.175 bar<sup>1/2</sup> cm<sup>1/2</sup>

and  $R$ : the radius of curvature of the highly stressed electrode.

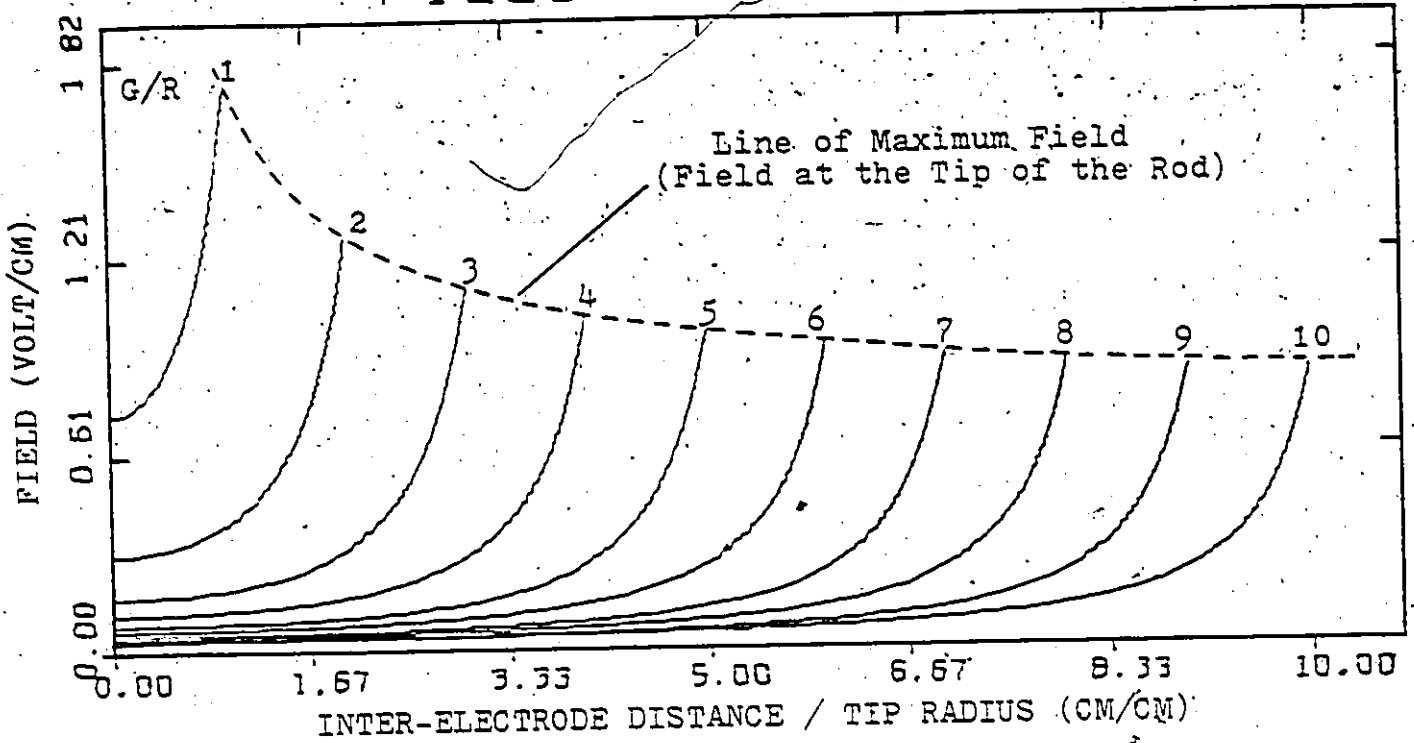
The calculated values of breakdown voltage  $V_n$  were found to be in good agreement with experimental results of rod-plane, rod-rod, and sphere-sphere electrode arrangements in pressures less than 5.0 bar (82). The only unknown in the above equation is the utilization factor  $u$  which is equal to the (average field)/(maximum field) or  $E_{av}/E_{max}$ .  $E_{max}$  is the field at the surface of the highly stressed electrode, which in this case is the hemispherical tip of the rod electrode. In the present calculations, the field along the axis of highest field strength in a rod-plane gap is given by,

$$E(z) = \sum_{i=1}^9 Q_i \left[ \frac{R+(z'_i+z)/((z'_i+z)^2)^{\frac{1}{2}}}{z'_i+z+((z'_i+z)^2)^{\frac{1}{2}}} + \frac{R+(z'_i-z)/((z'_i-z)^2)^{\frac{1}{2}}}{z'_i-z+((z'_i-z)^2)^{\frac{1}{2}}} \right] + Q_{10} \left[ \frac{z_{10}+z}{((z_{10}-z)^2)^{\frac{3}{2}}} + \frac{z_{10}+z}{((z_{10}+z)^2)^{\frac{3}{2}}} \right] \quad (6.3)$$

The above equation is a derivative of equation 3.6 with respect to  $z$  and the values of the charges  $Q_i$  and their position  $z'_i$  are those obtained with the charge simulation technique.  $E_{max}$  is obtained by setting  $z$  equal to the gap length  $G$ . Figure 6.1 shows the field distribution along the  $z$ -axis of a rod-plane gap for different  $G/R$  ratios. A reference table of utilization factors up to  $G/R=500$  is presented in Appendix 3.

Pedersen (61,62) proposed a semiempirical quantitative breakdown criterion on the basis of Meek's (58) streamer onset relationships. In an approximated form, this is given by,

# FIELD VERSUS G/R



# FIELD VERSUS G/R

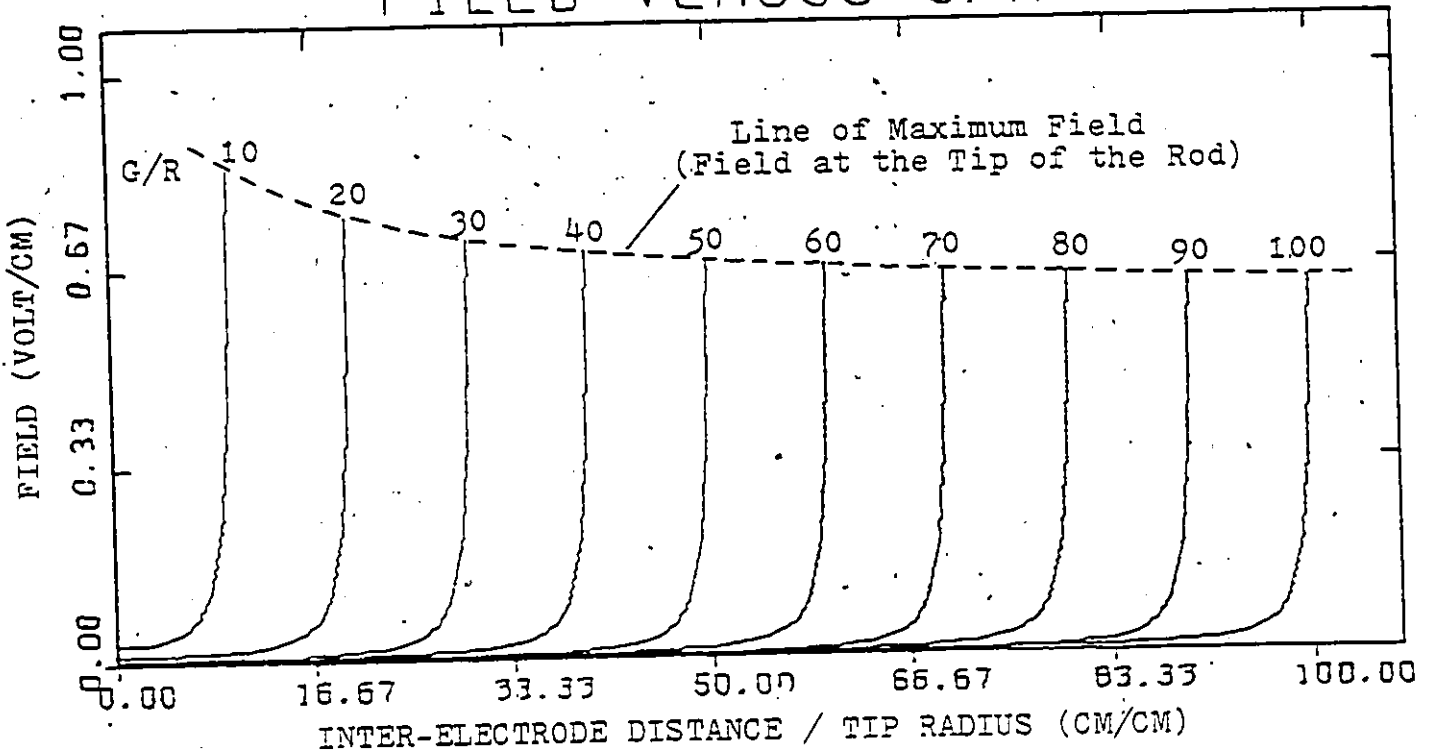


Figure 6.1 Field distribution along the axis of a rod-plane gap for various gap ratios G/R.



$$\int_0^{z_c} (\alpha - \eta) dz = K \quad (6.4)$$

where  $z_c$  : critical length of the avalanche

$K$  : a constant equal to 10.5\*

The ionization and attachment coefficients can be expressed as functions of the pressure and the applied field by the relation (see chapter 2.3)

$$(\alpha - \eta) / p = C(E(z)/p - (E/p)_{cr}) \quad (6.5)$$

where  $E(z)$  is the field along the  $z$ -axis given by the equation (6.3). At the point  $z_0$  where an electron initiates the first avalanche, equation (6.5) can be written as

$$\alpha - \eta \Big|_{z=z_0} = p C(E(z)/p - (E/p)_{cr}) = 0 \quad (6.6)$$

The above equation is solved for  $z_0$  using the Dichotomous technique (that is by a univariant search). Having found  $z_0$ , equation (6.4) can be written in the form

$$\int_{z_0}^G p C(E(z)/p - (E/p)_{cr}) = K \quad (6.7)$$

where  $G$  is the value of  $z$  at the surface of the hemispherical tip. The LHS of equation 6.7 is evaluated and compared to  $K$ . A higher

---

\* Pedersen had initially given  $K$  a value equal to 18.0, but in a later publication (62) he showed that  $K=10.5$  is a more appropriate value for  $SF_6$ . Note that with  $K=18.0$  equation (6.4) is equivalent to equation (6.1) with  $N_0=1$

or lower value than  $K$  will indicate if the voltage applied to the electrode will be lowered or increased respectively. A change in the applied voltage will result in a change of the values of the field  $E(z)$ , hence, equation 6.6 is solved again for  $z_0$  and the process is repeated. When the LHS of equation 6.7 is equal to  $K$ , the applied voltage is equal to the breakdown or streamer onset voltage of  $SF_6$ , for the particular rod-plane gap (defined by  $G/R$ ) and pressure  $p$ .

Calculation of streamer onset voltages in nitrogen and  $SF_6/N_2$  mixtures were carried out in a similar fashion, using Pedersen's criterion of equation 6.4. Equation 6.5 was substituted by equation 2.2 for nitrogen and equation 2.5 for  $SF_6/N_2$  mixtures.

#### 6.4 Comparison of Theoretical and Experimental Results.

Figures 6.2 to 6.5 show the corona onset voltage-pressure characteristics for nitrogen and  $SF_6$  in 10mm and 50mm gaps and pressures ranging from 1 to 5 bar. The experimental results show that the negative corona onset voltage is in all cases lower than the positive onset voltage.

As it is seen in Figures 6.2 and 6.3, the theoretical streamer onset voltage of nitrogen is at best 50% lower than that of the negative corona onset. Similarly, Figures 6.4 and 6.5 show that in  $SF_6$  the theoretical results are also considerably lower than the experimental ones. An error analysis is in order at this point to determine if such differences between the theoretical and experimental results are due to errors involved

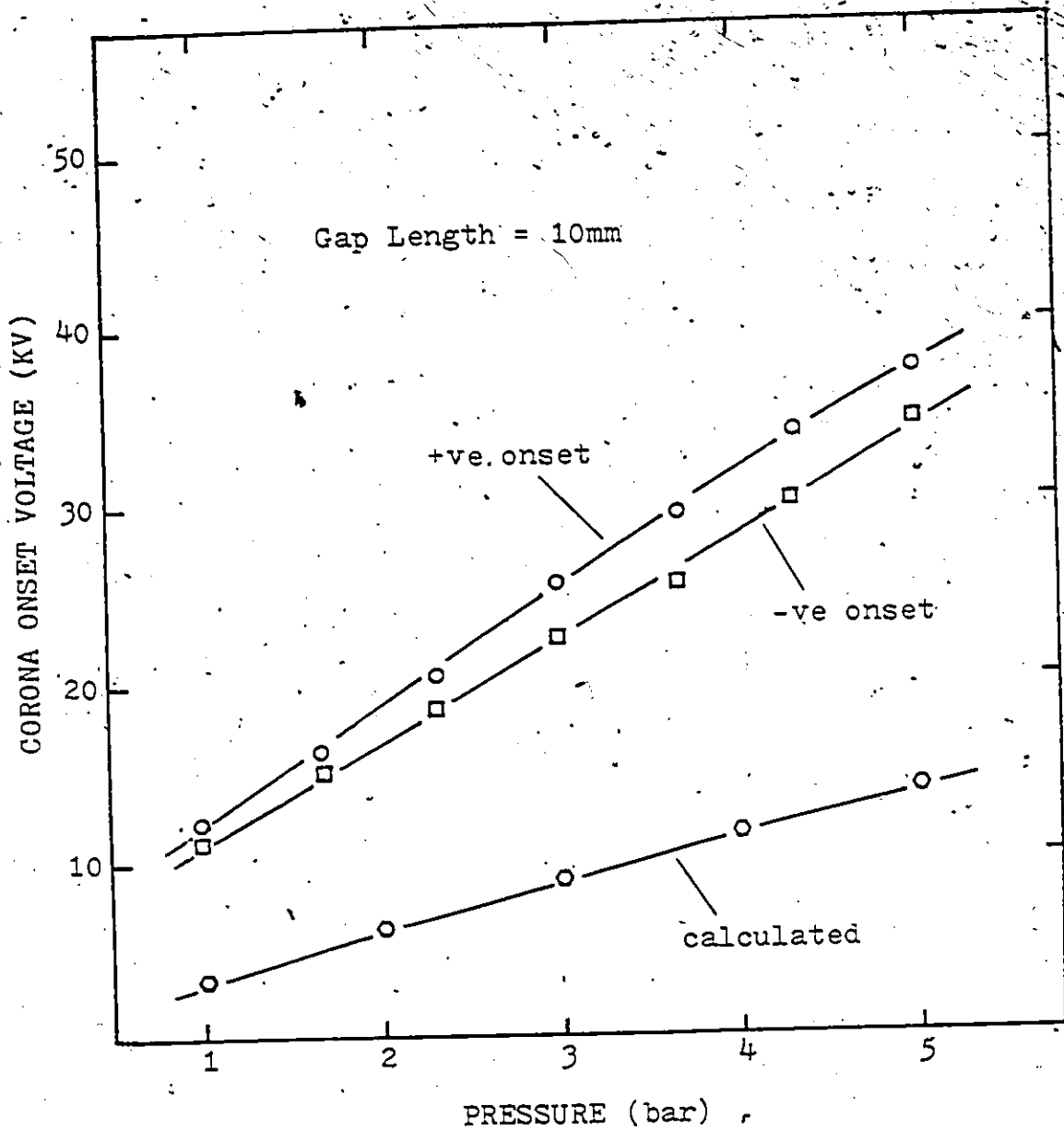


Figure 6.2 Experimental and theoretical corona onset voltage-pressure characteristics of a 10mm rod-plane gap in nitrogen. The theoretical results are derived from equation 6.4 with  $K=18$  and  $\alpha$  as given by equation 2.2.

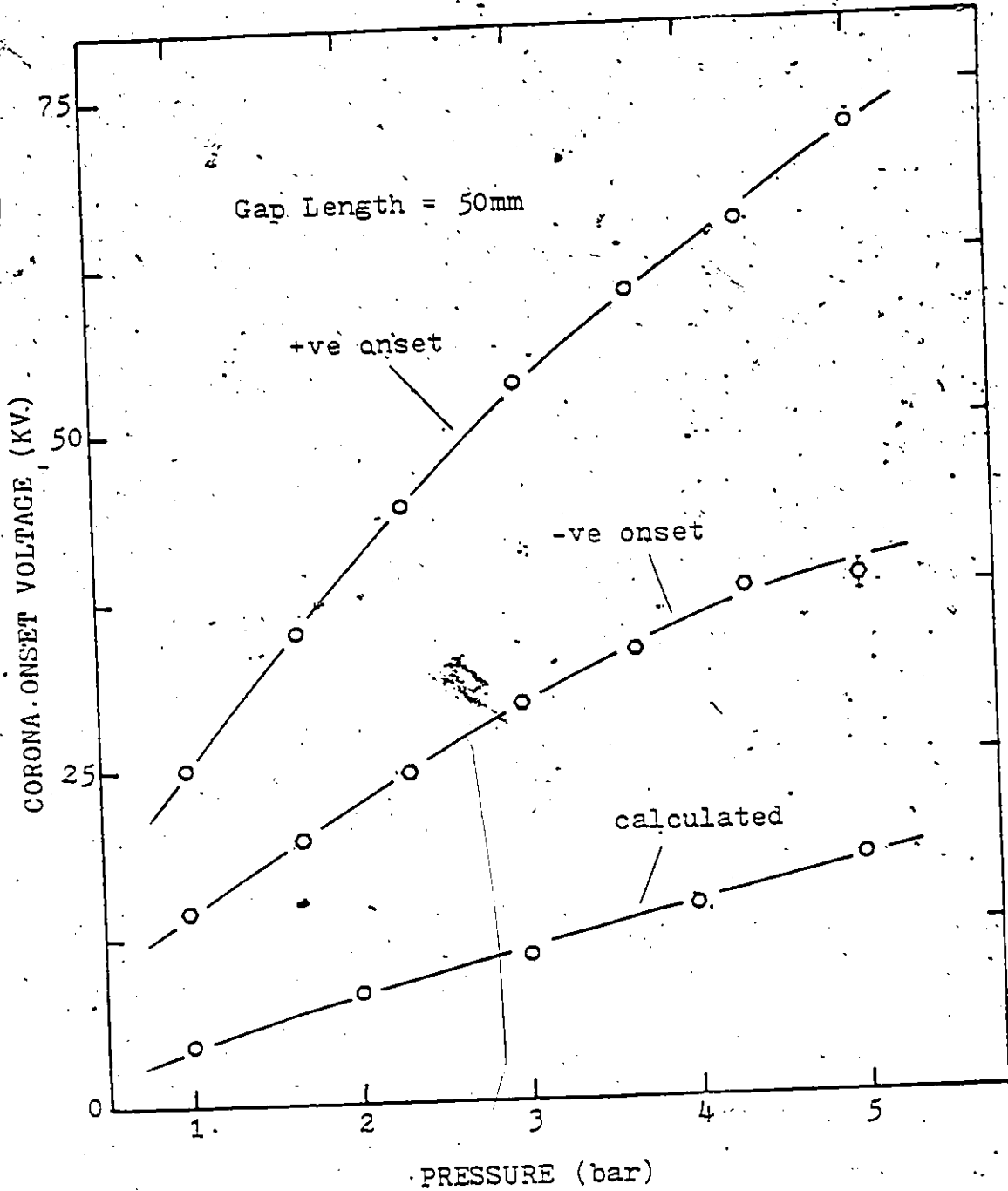


Figure 6.3 Experimental and theoretical corona onset voltage-pressure characteristics of a 50mm rod-plane gap in nitrogen. The theoretical results are derived from equation 6.4 with  $K=18$  and  $\alpha$  as given by equation 2.2.

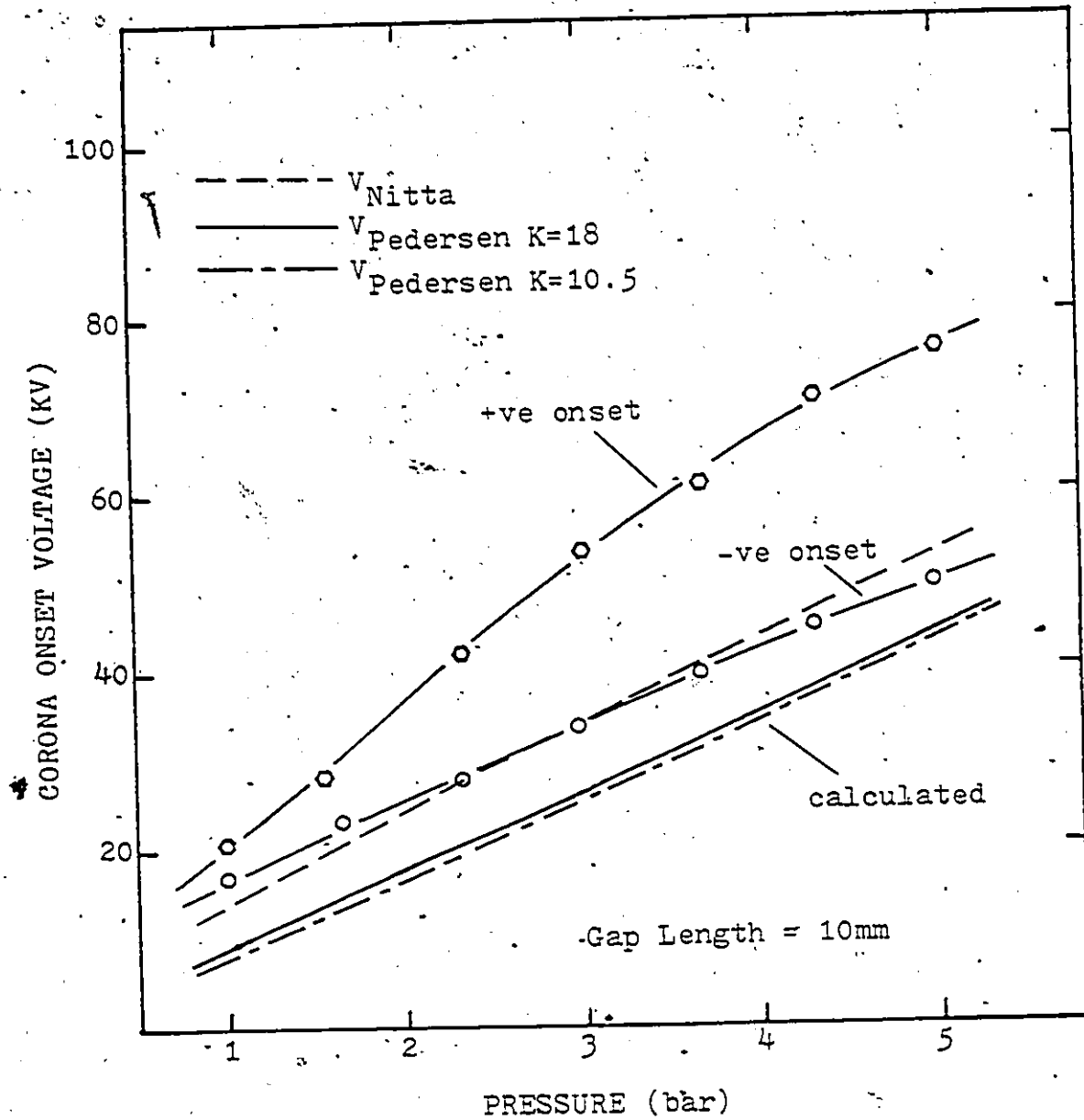


Figure 6.4 Experimental and theoretical corona onset voltage-pressure characteristics of a 10mm rod-plane gap in SF<sub>6</sub>. The theoretical values of the onset voltage are calculated with both Nitta's and Pedersen's criteria using equations 6.2 and 6.4 respectively.

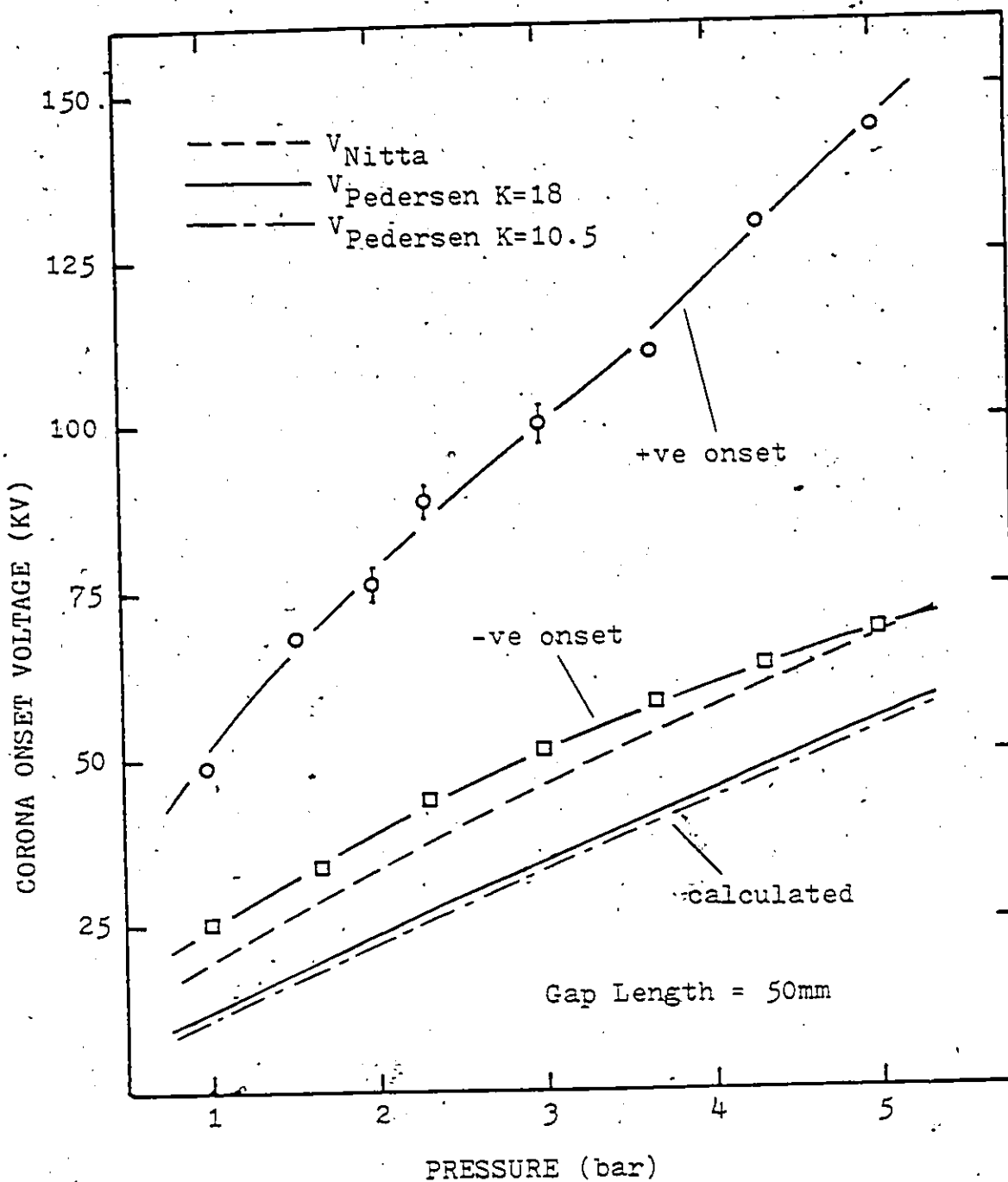


Figure 6.5 Experimental and theoretical corona onset voltage-pressure characteristics of a 50mm rod-plane gap in SF<sub>6</sub>. The theoretical values of the onset voltage are calculated with both Nitta's and Pedersen's criteria using equations 6.2 and 6.4 respectively.

in the measurement or calculation of the corona onset voltage, or, the failure of the streamer onset criteria to make an accurate prediction of the streamer onset voltage under the present experimental conditions.

Experimental errors could involve uncertainties introduced in the system by such factors as, voltage measurement, accuracy of gap length, pressure measurement, dimensions of the rod electrode, and other less defined parameters such as impurities in the gas volume and the electrode surface. From the measurable parameters, the magnitude of the measured voltage is the largest single source of uncertainty in the system. The output of the HVDC generator (which was measured with a digital voltmeter connected to the generator's feed-back loop) was calibrated with a high voltage resistance divider. The accuracy of the HV divider was better than 1% and hence the total error in the measured values of the output of the HVDC generator for a fixed gap length and pressure, is expected to be less than 3-5%.

In the theoretical calculations errors can arise from mis-representation of the experimental system by a semi-infinite rod electrode and an infinite plane electrode. Kuffel and Husbands (80), Binns (81), and Singer (45) have studied the effect of nearby earth objects to a spark gap, both from a theoretical and experimental point of view. Their results show that for the present experimental system, inclusion of the chamber walls in the calculations would have reduced the theoretical values of the onset voltage by as much as 1-2%. In addition, the finite size of the plane electrode is expected to

result in lower field factors and therefore lower onset voltages. Kratzenstein (83) has shown that for a similar electrode arrangement, the error in the calculated values of the utilization factor was less than 0.1% for  $d/D$  less than 0.1 ( $d$ =gap length,  $D$ =diameter of the plane electrode) and 3.0% for  $d/D = 0.4$ , which corresponds to a 50mm gap in the present system. These arguments indicate that the theoretical results could be in error by as much as 2-5% and that a more rigorous analysis would have decreased the present values by that amount.

Thus the difference between the theoretical and experimental results of nitrogen (Figures 6.2 and 6.3) is too large to be accounted for by a systematic error. Similarly, Figures 6.4 and 6.5 show that for  $SF_6$ , although Nitta's equation gives satisfactory results, onset values by Pedersen's criterion are considerably lower. A small difference was however anticipated; streamer onset voltages in  $SF_6$  derived by Nitta's or Pedersen's criteria could be either lower or even higher than the experimental ones (82), depending on uniformity and surface condition of the electrodes. A good agreement is usually expected for electrode geometries with quasi-uniform field distribution. In figure 6.6 streamer onset voltages calculated with equation 6.4 ( $K=18$ ) are compared with Sangkasaad's experimental results. In the case of the quasi-uniform field gap ( $d=10mm$ ,  $r=10mm$ ,  $d/r=1$ ) the calculated streamer onset voltage is in good agreement with the experimental spark onset. For the less uniform gap ( $d=20mm$ ,  $r=1mm$ ,  $d/r=20$ ) although the calculated corona onset does not seem to be considerably lower than that of the negative and AC onset, the



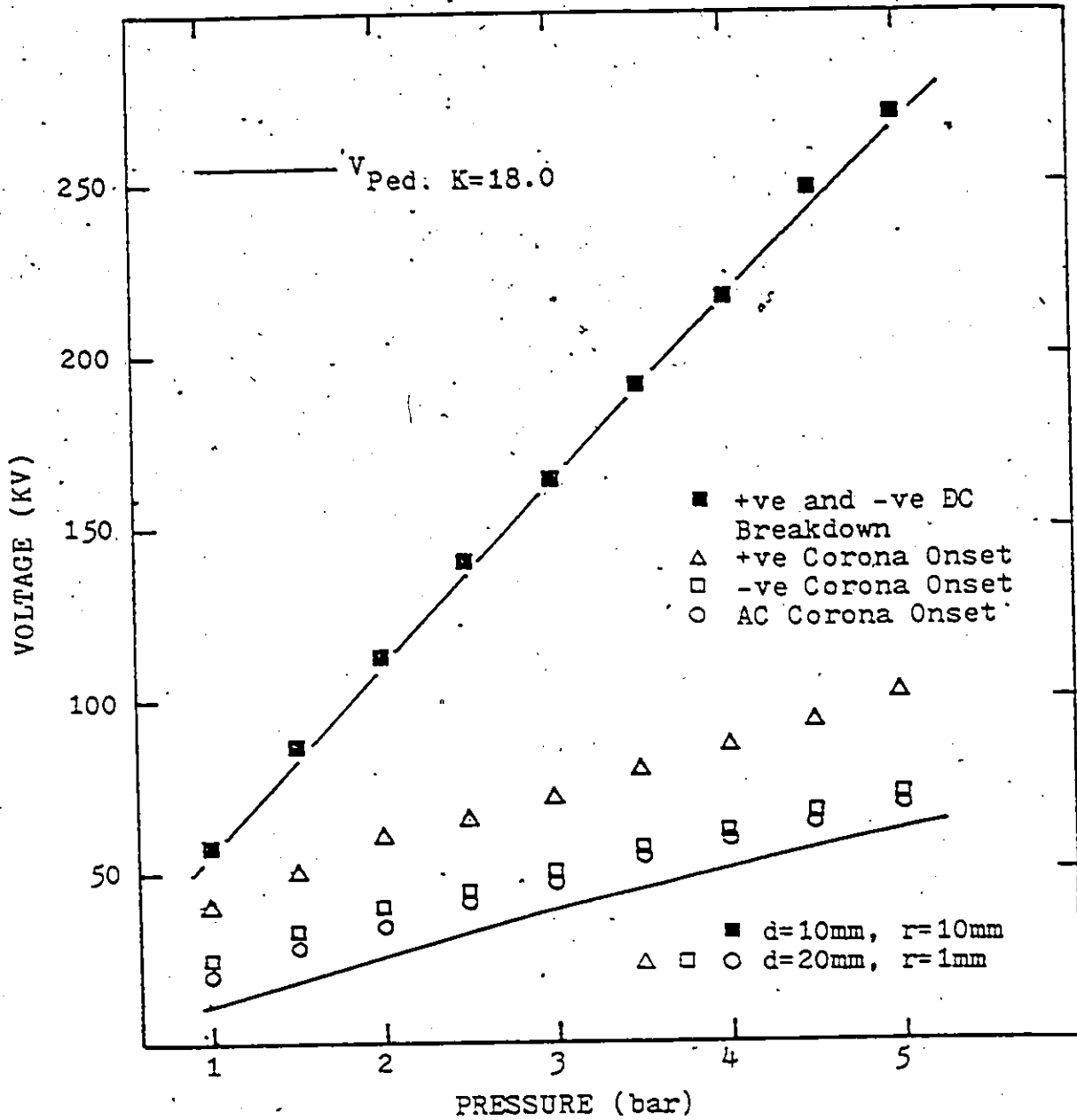


Figure 6.6 Comparison of Sangkasaad's (54) experimental results of breakdown voltage and corona onset of  $SF_6$  in rod-plane gaps, with streamer onset values calculated by equation 6.4.

difference is approximately 50% at 1 bar of pressure.

In SF<sub>6</sub>/N<sub>2</sub> mixtures, the calculations of the streamer onset voltage are carried out in a similar manner. Pedersen's criterion of equation 6.4 is used with K=18, since as shown in Figures 6.4 and 6.5, this gave an inbetween value of onset voltage, with respect to onset voltages obtained with K=10.5 and Nitta's expression of equation 6.2. Equation 6.5 was substituted by Baumgartner's effective ionization coefficient of equation 2.5, which relates the effective ionization coefficients of the different SF<sub>6</sub>/N<sub>2</sub> mixtures with those of SF<sub>6</sub> and nitrogen through a weighting factor that depends on the partial pressure of the component gases. This means that for one hundred percent of either SF<sub>6</sub> or nitrogen the calculated values of the streamer onset voltage will be the same as those derived by equations 6.5 and 2.2 respectively.

Thus, observation of Figures 6.2 to 6.5 should indicate the degree by which the corona onset voltage in SF<sub>6</sub>/N<sub>2</sub> mixtures can be predicted, at least in the neighbourhood of 100% SF<sub>6</sub> or 100% N<sub>2</sub>. Figures 6.7 and 6.8 demonstrate this by showing that if the behaviour of the corona onset voltage for various SF<sub>6</sub>/N<sub>2</sub> mixtures is similar to the pattern exhibited in the breakdown characteristics of the mixtures under uniform conditions (Figure 2.1(a)), one should expect the calculated corona onset levels to be as accurate as those of the individual gases.

The agreement between the experimental results and equation 6.4 in Figures 6.7 and 6.8 could improve if Pedersen's criterion resulted in a more accurate prediction of the corona

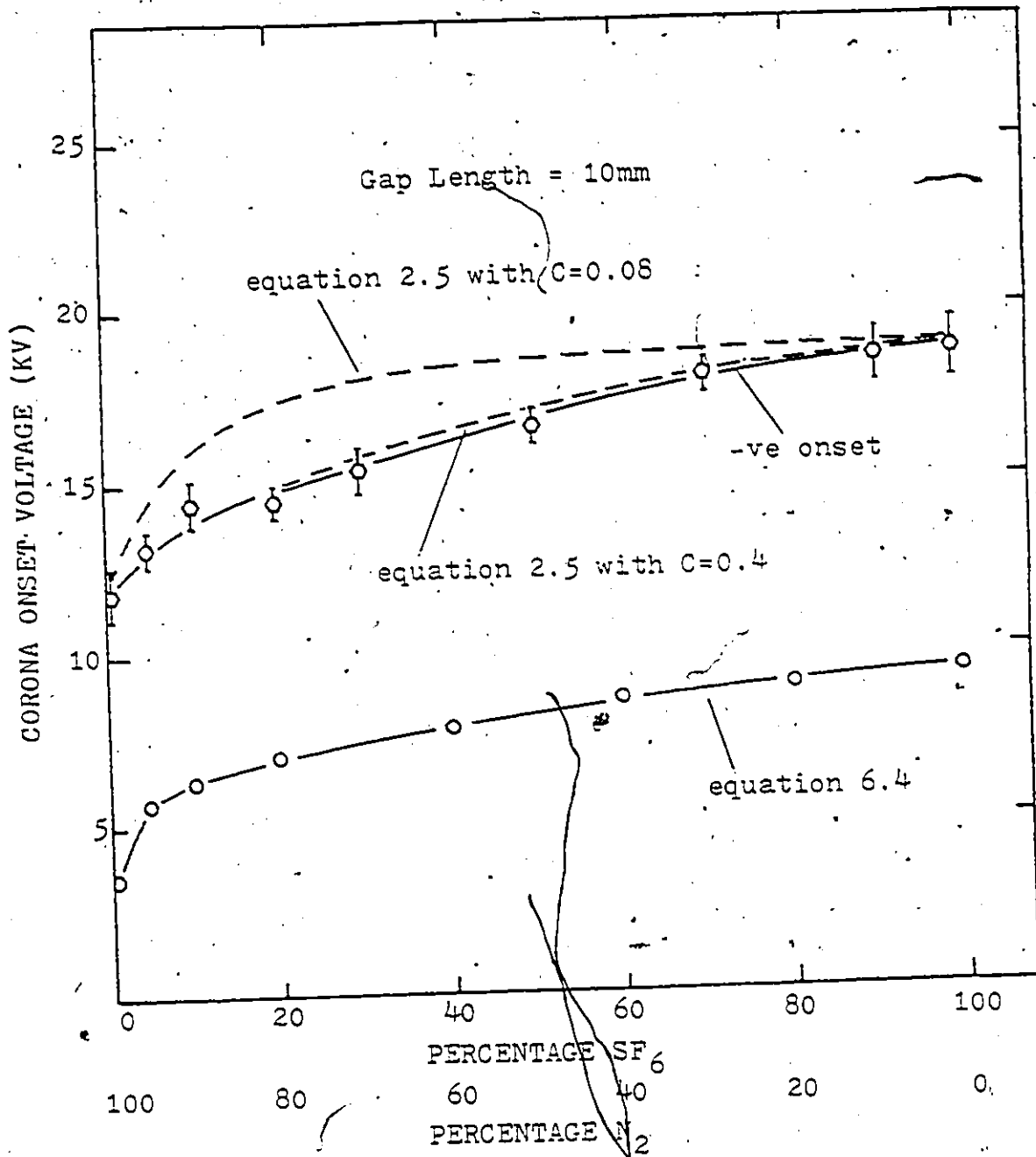


Figure 6.7 Experimental and theoretical corona onset voltage-mixture ratio characteristics of a 10mm rod-plane gap in SF<sub>6</sub>/N<sub>2</sub> mixtures. The theoretical values of the onset voltage are calculated using Pedersen's criterion (equation 6.4, with K=18 and α- as given by equation 2.5) and also Takuma's empirical equation with C=0.08 and C=0.4.

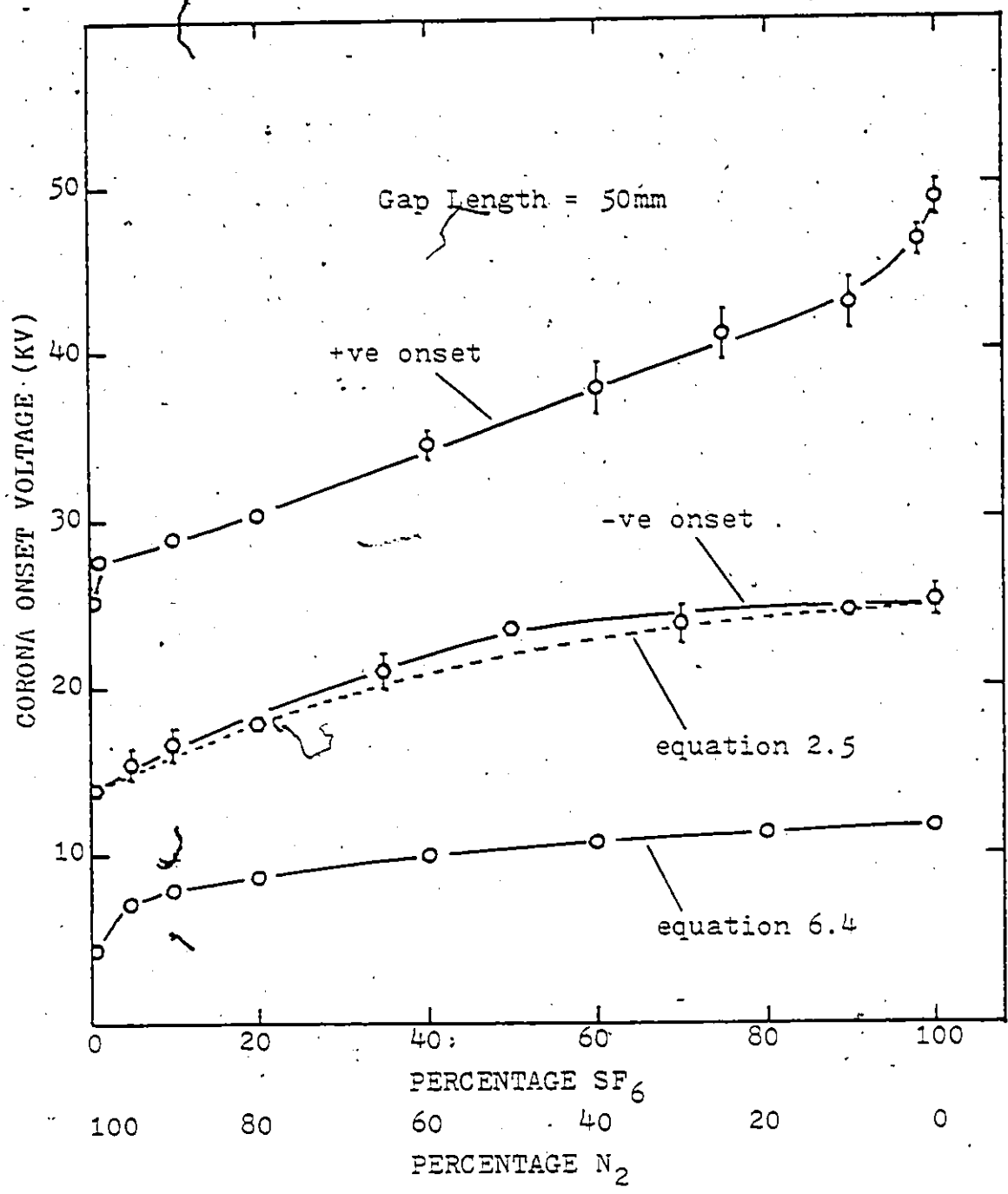


Figure 6.8 Experimental and theoretical corona onset voltage-mixture ratio characteristics of a 50mm rod-plane gap in SF<sub>6</sub>/N<sub>2</sub> mixtures. The theoretical values of the onset voltage are calculated using Pedersen's criterion (equation 6.4, with K=18 and  $\alpha$  as given by equation 2.5) and also Takuma's empirical equation 2.4 with C=0.4.

onset voltage in the individual gases under the same experimental conditions. An example of this is given in Figure 6.9, in which a good agreement is shown between experimental and theoretical results for SF<sub>6</sub>/N<sub>2</sub> mixtures in a quasi-uniform rod-plane gap. Results of comparable accuracy can also be obtained for the present electrode configurations by making use of the empirical equation of Takuma and Watanabe (37) (equation 2.4), which makes use of the experimentally found onset voltages of 100% SF<sub>6</sub>, 100% N<sub>2</sub> and the partial pressures of the two gases. The constant C in equation 2.4 acts as a form factor that regulates the convergence of V<sub>m</sub> to V<sub>1</sub> (N<sub>2</sub>), as the partial pressure of SF<sub>6</sub> is decreased. Takuma and Watanabe showed that for C=0.08 there is a good agreement between equation 2.4 and Howard's experimental results of Figure 2.1(a). However for the results presented in Figures 6.7 and 6.8 it was found that equation 2.4 gives a better fit for C=0.4.

Figure 6.10 shows the critical length of the avalanche z<sub>c</sub> plotted for different SF<sub>6</sub>/N<sub>2</sub> mixtures for a 5mm gap. As it is seen, the critical length z<sub>c</sub> is relatively small for 100% SF<sub>6</sub> and it increases abruptly as the SF<sub>6</sub> content is reduced below 5%. Table 6.1 shows the streamer onset voltage and the critical length of the avalanche z<sub>c</sub> for 10mm and 50mm gaps in SF<sub>6</sub>/N<sub>2</sub> mixtures. For 100% N<sub>2</sub>, z<sub>c</sub> is of the same order of magnitude as the radius of the hemi-spherical tip of the rod electrode (R=0.8mm), and much smaller than R as the SF<sub>6</sub> content of the mixture increases. This indicates that for highly diverging fields the onset voltage depends mainly on the magnitude of the

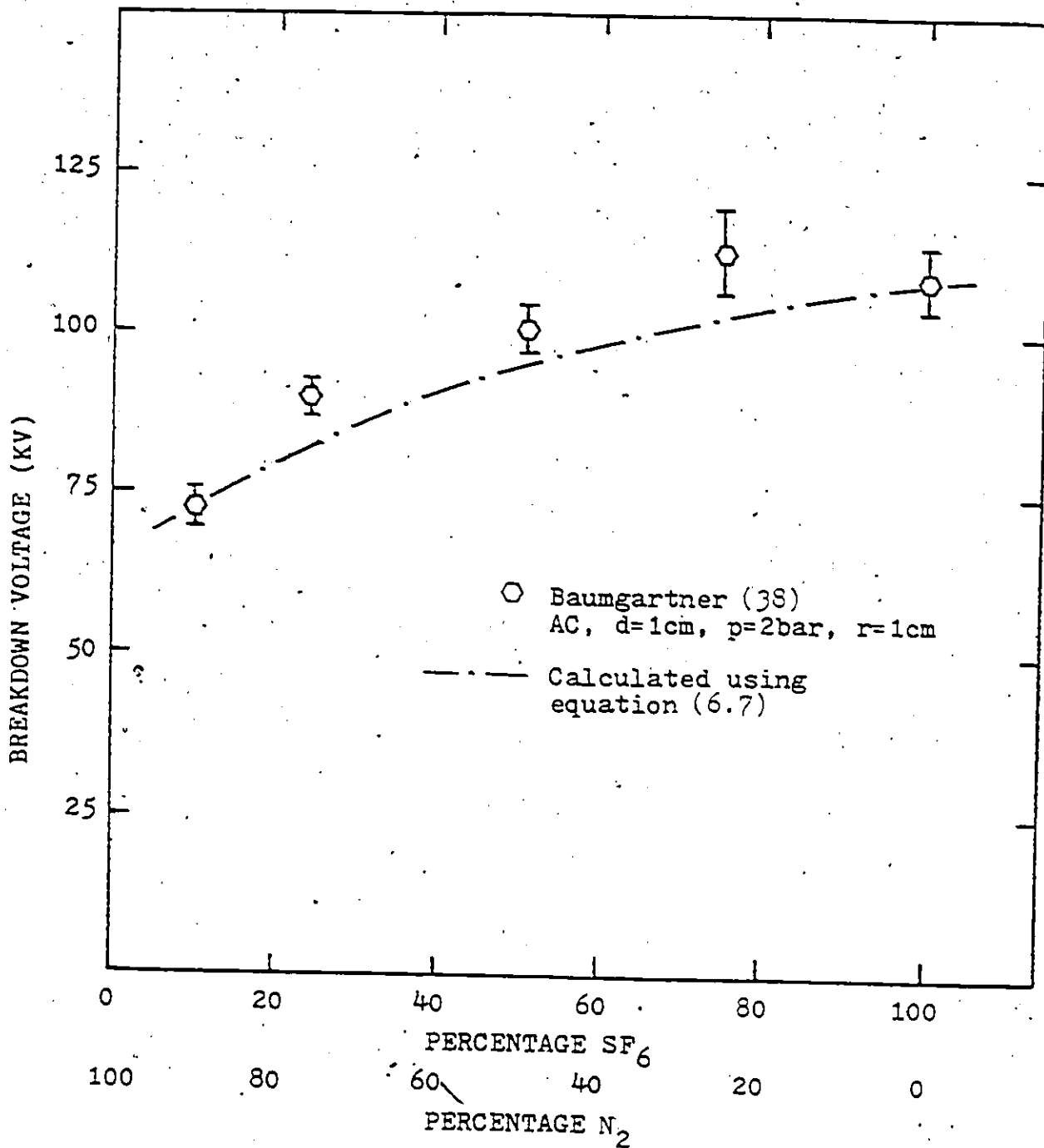


Figure 6.9 Comparison of experimental AC breakdown results of a rod-plane gap in mixtures of N<sub>2</sub> and SF<sub>6</sub>, with calculated ones using equation (6.7)

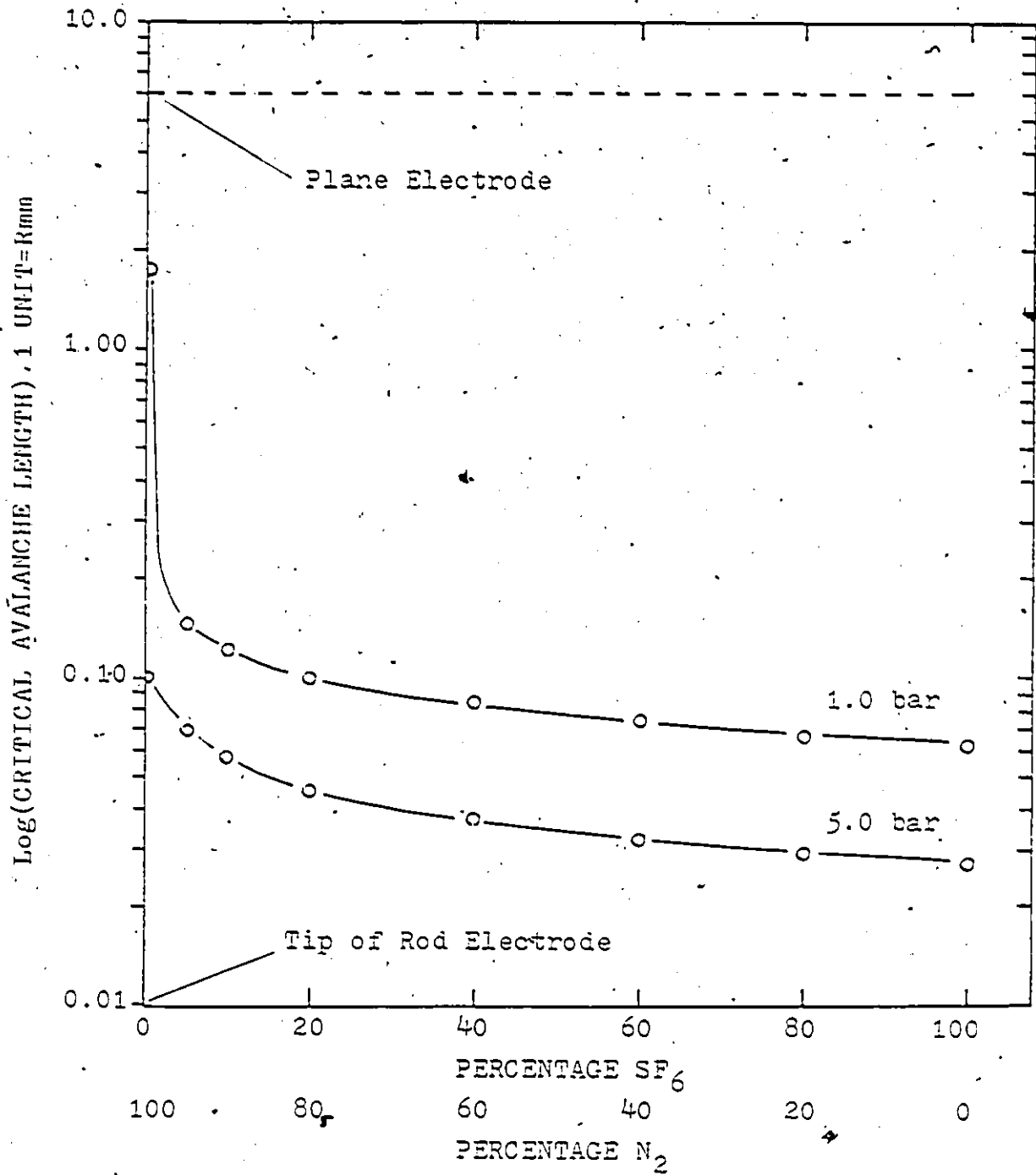


Figure 6.10 Critical length of initial avalanche ( $z_c$ ), for a 5 mm rod-plane gap in  $SF_6/N_2$  mixtures at a total pressure of 1.0 and 5.0 bar. ( $r=0.8$  mm,  $d/r=6.25$ )

Table 6.1. Streamer onset voltage  $V_{onset}$  and critical length of the avalanche  $z_c$  for 10mm and 50mm gaps in  $SF_6/N_2$  mixtures at a total pressure of 1.0 bar.

10 mm gap

Utilization Factor = 0.096

<u>% <math>SF_6</math></u>	<u><math>V_{onset}</math> (V)</u>	<u><math>z_c</math> (mm)</u>
0.0	3158	0.9568
5.0	5408	0.1118
10.0	5941	0.0937
20.0	6608	0.0773
40.0	7475	0.0636
60.0	8085	0.0563
80.0	8466	0.0511
100.0	8800	0.0475

50 mm gap

Utilization Factor = 0.024

<u>% <math>SF_6</math></u>	<u><math>V_{onset}</math> (V)</u>	<u><math>z_c</math> (mm)</u>
0.0	4277	0.9778
5.0	7294	0.1162
10.0	8000	0.0967
20.0	8913	0.0798
40.0	10063	0.0656
60.0	10825	0.0578
80.0	11381	0.0522
100.0	11841	0.0490



field in the neighbourhood of the rod-electrode. The maximum field however, varies very little for high values of  $G/R$  (see table of Appendix 3) and hence the onset voltage-gap length characteristics are expected to saturate as the gap length  $G$  increases. This can be seen in Table 6.1, where the difference in the values of  $V_{onset}$  between the 10mm and 50mm gaps is relatively small.

### 6.5 Discussion

The charge simulation method, combined with optimization techniques to solve Pedersen's criterion for streamer onset voltages was found to be efficient and relatively easy to implement. Unlike other techniques (7) that require a good estimate of the breakdown voltage to assure convergence, the present method converged to the right value irrespectively of the initial value of the applied potential. Computing time for the solution of equation 6.7 was relatively small and could be reduced further by replacing the Dichotomous technique (that was used in equation 6.6), with the Fibonacci or the Golden Rule methods. The advantage of using the charge simulation technique to calculate the field distribution of a particular electrode geometry, is that, streamer modelling can be handled in a quasi-analytical manner.

Apart from calculations using Nitta's and Pedersen's relations, the author carried out calculations based on a number of other models such as, Meek's critical field criterion (58), Khaled's ring charge model (71), and a hybrid of the two. In the latter one, the charge accumulated in an avalanche was calculated

in steps, assuming that it is concentrated in spheres of increasing diameter. The ionization and attachment coefficients were calculated ahead of every sphere taking into account the perturbation of the field from the accumulating charge. The results showed that in all models (including Nitta's and Pedersen's), the calculated onset voltages were within a few percent of each other, thus presentation of elaborate modelling was considered unnecessary.

The results presented in Figures 6.2 and 6.3 show that for nitrogen, the calculated onset voltages using equation 6.4 were at best 50% lower than the experimental ones. This large discrepancy cannot be accounted for by errors in either the experimental or the theoretical results. However the effect of parameters such as impurities in the gas volume and on the electrode surface is not very clear. The engineering nature of the experiment did not allow high purity conditions that could have resulted from degasing of the electrodes and evacuation of the chamber to pressures better than  $10^{-5}$  torr. As described in chapter 4, measurements in 100%  $N_2$  were taken after evacuating the chamber to  $10^{-1}$ - $10^{-2}$  torr, flushing it with nitrogen and then evacuating it again. With this procedure, possible traces of  $O_2$  or residual traces of  $SF_6$  are expected to be present in amounts less than 0.01% of the minimum working pressure (760 torr).

Weissler's (15) corona onset results of nitrogen in point-to-plane gaps (ranging from 3.1 to 4.6cm) show that the negative onset voltage of pure nitrogen (3700V) is increased to 4300V with the addition of 0.1%  $O_2$ . Similarly, the results

of Figure 5.22 show that the onset voltage of nitrogen increases substantially with the addition of 0.2% SF<sub>6</sub>.

So, although an increase in the experimental values of the nitrogen onset voltage can be expected due to impurities in the gas volume, its magnitude cannot be determined due to their undefined character and amount. However it should be noted that Weissler's results (15) and those of the Figures 6.7 and 6.8, indicate that the onset voltage increases as the percentage of the impurity increases and thus the increase of the onset voltage for impurity contents less than 0.01% is not expected to be high. In conclusion, the difference between the experimental and theoretical results of Figures 6.2 and 6.3 is much higher than any onset voltage increase that one could expect from impurities in the gas volume.

Figures 6.4 and 6.5 show that for SF<sub>6</sub> the calculated onset values are within 50 to 10% of the measured ones for the 10mm gap and 50 to 20% for the 50mm gap. As it is seen, the calculated onset voltage-pressure characteristics are lower than the experimental ones and have approximately the same slope. As a result of this, the discrepancy is higher at the lower pressures, with a maximum deviation of 50% at 1 bar.

The incapability of making an accurate prediction of the onset voltage in nitrogen and at low pressures of SF<sub>6</sub>, is reflected in Figures 6.7 and 6.8, where the onset voltages of a 10mm and a 50mm gap are plotted for different mixture ratios. These results indicate that the calculated onset characteristics using Baumgartner's ionization coefficient of equation 2.5, exhibit

a behaviour similar to that of the experimental results, displaced however by an amount relative to the 100% SF<sub>6</sub> and 100% N<sub>2</sub> onset levels. In addition, the use of Takuma and Watanabe's empirical relation of equation 2.4 showed that different form factors (constants C) are required to fit the present results of Figures 6.7 and 6.8 and Howard's experimental results of Figure 2.1(a) (37). Baumgartner's coefficient of equation 2.5 has a fixed relationship between the partial pressures of the two gases and their corresponding ionization coefficients and thus, it makes no provisions for any anomalous behaviour of the onset voltage between 100% SF<sub>6</sub> and 100% N<sub>2</sub>.

In conclusion, it could be stated that the use of Baumgartner's ionization coefficient is limited to uniform and probably quasi-uniform field configurations. Future improvements in the calculation of onset voltages in SF<sub>6</sub>/N<sub>2</sub> mixtures are expected to be associated with experimentally measured ionization and attachment coefficients.

## CHAPTER 7

### DISCUSSION AND INTERPRETATION OF THE EXPERIMENTAL RESULTS.

The results of the present work indicate that the dielectric behaviour of different  $\text{SF}_6/\text{N}_2$  mixtures under both impulse polarities is much more complex than that of the individual component gases in their pure form. In general,  $\text{SF}_6$  mixtures lack investigation and relatively little is known of the various reactions and reaction rates between  $\text{SF}_6$  and different gas molecules.  $\text{SF}_6$  and its ions ( $\text{SF}_6^+$ ,  $\text{SF}_5^+$ ,  $\text{F}^+$ ,  $\text{SF}_4^+$ ,  $\text{F}_2^+$ ,  $\text{SF}_3^+$  and  $\text{SF}_2^+$ ) are not expected to react chemically with nitrogen. Charge transfer (72) and three body reactions will however involve both molecules, but the significance of such reactions is not known. Charge transfer reactions in particular, are of little importance under impulse voltage conditions due to the quasi-static nature of the charge. It is also important to note that the rate of two body reactions in  $\text{SF}_6$  such as, the associative and dissociative attachment reactions presented in Chapter 2.3 will proceed at a rate independent of the carrier gas. The collisional stabilization of  $\text{SF}_6^-$  at pressures of about 1 torr occurs so fast that the nature of the third body (nitrogen) is not very important (25). Davis and Nelson (85,86) have shown that the apparent rate constant for the production of negative ions in  $\text{SF}_6$  mixtures with low  $\text{SF}_6$  concentrations remained constant for a variety of different  $\text{SF}_6$  mixtures (including  $\text{SF}_6/\text{N}_2$ ,  $\text{SF}_6/\text{H}_2$ ,  $\text{SF}_6/\text{He}$ ,  $\text{SF}_6/\text{CO}_2$ ..).

Factors that are expected to play an important role in the dielectric properties of the different  $\text{SF}_6/\text{N}_2$  mixtures will depend mainly on the molecular structure of the individual gases.

The nitrogen molecule, although not as complex as the SF<sub>6</sub>, has metastable and active states which could affect the secondary ionization process of the different mixtures. The nitrogen metastables have been long known to interact with gas impurities such as mercury (74) and produce a Penning effect, large enough to alter the value of the first Townsend coefficient of ionization. The metastable states in nitrogen\* have a relatively long lifetime (1-2 sec), that allows them to store energy which is released upon a collision in either the gas volume or the surface of the electrodes. From the latter type of collision, secondary electrons will be emitted with an energy and efficiency depending on the nature of the electrode material and the energy of the metastable state. In the gas volume, a collision or an absorption of a photon will usually result in an energy transfer or a radiative emission.

SF<sub>6</sub> exhibits a relatively low photon absorption in the visible part of the spectrum. It has however, a number of broad absorption peaks in the ultra violet region, followed by an absorption continuum that starts sharply at the ionization wavelength (780A°) (28, 68, 69). The relatively high absorption of SF<sub>6</sub> and its variation with pressure and mixture ratio could introduce significant changes in the ionization coefficients of

---

\* Some of the metastable states are:  $A^3\Sigma_u^+ = 6.1\text{ev}$ ,  $B^3\Sigma_u^- = 8.1\text{ev}$ ,  $\alpha^1\Sigma_u^- = 8.3\text{ev}$  and  $\alpha^1\Pi_g = 8.5\text{ev}$ . Potential curves for N<sub>2</sub>, N<sub>2</sub><sup>+</sup> and N<sub>2</sub><sup>-</sup> are also given in reference (70).

the mixtures, by enhancing the effects of secondary mechanisms such as photoionization and thus altering the space charge distribution in the inter-electrode region.

The number of unknowns involved in the interaction of SF<sub>6</sub> with nitrogen under the different experimental conditions rule out a quantitative interpretation of the results. The discussion in this chapter includes negative polarity effects, negative coronas, positive polarity effects in mixtures with high and low SF<sub>6</sub> content, positive coronas, and qualitative interpretations when results obtained in this work (and/or elsewhere) allowed.

### 7.1 Negative Rod-Plane.

The negative rod-plane data shows that at low pressure and gap length, the breakdown voltage of the mixture is nearly proportional to the SF<sub>6</sub> content. At higher gap length and pressure, as shown in Figure 5.7, the SF<sub>6</sub>/N<sub>2</sub> mixture loses most of its differential strength at relatively high contents of SF<sub>6</sub>. It is not known why such little amounts of nitrogen can result in such a dramatic decrease in the breakdown voltage. A somewhat similar behaviour has been noted to occur in mixtures of N<sub>2</sub>/O<sub>2</sub> (Loeb's discussion on results of Huber, and Mohr and Weissler, reference (16) p. 244.). The breakdown voltage of the N<sub>2</sub>/O<sub>2</sub> mixtures was found to decrease slightly in going from 20% to 70% O<sub>2</sub>. Loeb's interpretation of this effect is based on the suppression of the negative ion sheath through a reduction of the photoionization in the gas.

Under the present experimental conditions it is not known if the photoionization in the gas volume has either been decreased or increased with the addition of nitrogen in SF<sub>6</sub>. Blair's et-al. (66,67) absorption measurements of SF<sub>6</sub>/N<sub>2</sub> mixtures with 0%(100% N<sub>2</sub>), 10%, 20% and 100% SF<sub>6</sub> at 1 bar of total pressure show that the apparent absorption coefficient of the mixtures (in the range of 900A° to 1500A°) increases with the content of SF<sub>6</sub>. This however does not imply that the number of photons absorbed per unit length during the ionization process will be a maximum for 100% SF<sub>6</sub>. Nitrogen, has a large number of electronic transitions in the visible-ultraviolet region and addition of nitrogen into SF<sub>6</sub> could increase the total photon emission in this region. Thus, a mixture that has for example 20% SF<sub>6</sub> could absorb more photons in a certain region of the spectrum than pure SF<sub>6</sub> at the same total pressure (67). The photomultiplier traces of Figure 5.13(c) show that the corona pulses become more visible as the percentage content of nitrogen in the mixture increased. This indicates that the light emitted in the visible range during the formation of the corona streamers has increased, since SF<sub>6</sub> is optically transparent in this region (29) and the reduction of its partial pressure is not expected to alter the absorption characteristics of the mixture.

Figure 5.21(b) shows that ionization starts at the tip of the cathode and electrons are initially repelled along the lines of force in a space charge perturbed diverging field.

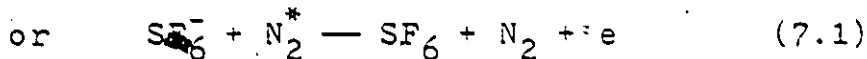
SF<sub>6</sub> will form most of its negative ions in the field reg-



ions where the electrons move slowly enough to undergo resonance capture reactions, which require electron energies less than 1 ev. These electrons are produced either by photoionization, or, they are created by decaying streamers and have escaped recombination. If the number of negative ions was proportional to the amount of  $SF_6$  in the mixture, one would expect the breakdown voltage to increase proportionally to the percentage of  $SF_6$ . The results of Figure 5.7 indicate that this is not true for high values of pressure and gap length, where the breakdown voltage drops sharply as the percentage of  $SF_6$  is reduced below 100%.

A reduction of the mean free path of photons with the addition of nitrogen could have accounted for the sudden drop in the breakdown voltage, through a decrease of the photoionization in distant regions where the photoelectrons would be slow enough to produce negative ions (16). However as previously indicated, there is no detailed information on the absorption coefficients of the different  $SF_6/N_2$  mixtures to either substantiate or refute the latter argument.

Apart from the effect of photoionization on the rate of production of negative ions, one should also consider the probable changes in the rate of their destruction. It is possible that the rate of detachment of electrons from the  $SF_6$  negative ions has increased greatly in the presence of the excited or metastable nitrogen molecules. Massey (75) indicates that one of the most efficient detachment reactions is,



where  $N_2^*$  is an excited, or metastable nitrogen molecule. The above reaction occurs when the energy of  $N_2^*$  is higher than the electron affinity of  $SF_6^-$  (or  $SF_5^-$ ), and the excess energy is transferred to kinetic energy of the released electron (75). The free electron will in most cases be captured through an attachment process or it will recombine with a positive ion. This however depends on its energy, the mean free path between collisions, and the direction of the applied field. That is, the significance of the detachment process as a whole will be expected to vary with gas pressure, partial pressure of  $SF_6$  and polarity of the gap.

## 7.2 The Negative Impulse Corona.

The negative corona of Figure 5.21(b) provides a reasonable illustration of the spatial growth of the corona streamers under negative impulse conditions. Photographs obtained by Watanabe and Takuma (5) under similar conditions show that the flare-like character of the streamers is not affected much by the changes in the gap length or the percentage content of  $SF_6$ .

The initial streamers (first generation) propagate towards the anode along a curved path due to the perturbation of the applied field by a space charge. Moving in a diverging field, mutual repulsion forces them to diffuse in space and create the flare-like effect. During the expansion of the initial streamers, the small gap between the space charge and the cathode is bridged either by slight movement of the positive charges or field emission. Some of the electrons are then expected to flow into the space charge to neutralize the positive ions. The streamers of the first generation stop propagating at the point where the electrons do not have sufficient energy to ionize, due to the weakening external field and the retarding effect of the positive space charge. As it appears, one of the streamers in the flare develops conditions that prolong its lifetime and expansion into the gap. This streamer will be the only one that is effectively conducting and electrons from the cathode will flow through, producing a luminous conducting channel of plasma. Depending on the resistivity of this channel some of the cathode voltage will be conducted to

the head of the streamer, which will become an effective cathode and the whole process will be repeated.

The streamer generation finally stops when the field ahead of the streamers is not sufficient to sustain ionization. In this case further propagation into the gap can only be obtained by increasing the applied voltage until the streamers reach the anode and provide favorable conditions for spark onset.

### 7.3 Positive Rod-Plane - SF<sub>6</sub>/N<sub>2</sub> mixtures with Less than 1% SF<sub>6</sub>

SF<sub>6</sub>/N<sub>2</sub> mixtures with low SF<sub>6</sub> content exhibited a number of unusual phenomena under positive impulse conditions. Figures 5.11 and 5.12 show that at low pressures, the dielectric strength of mixtures with less than 1% SF<sub>6</sub> increased well above that of nitrogen. The breakdown voltage-pressure characteristics of these mixtures show a voltage peak similar to that of SF<sub>6</sub> under DC conditions (7, 17, 19, 32, 56). Under impulse voltage conditions this peak is not as pronounced as that of the DC voltage (Figure 5.4 and ref. 19), or that of the SF<sub>6</sub>/N<sub>2</sub> mixtures with less than 1% SF<sub>6</sub> (see Figure 5.12).

The breakdown voltage-pressure characteristics of these mixtures suggest that the breakdown mechanism could be similar to that of SF<sub>6</sub>, yet a number of other observations indicate that there are some fundamental differences in the temporal and spacial behaviour of the ionization, prior to and during the breakdown.

The creep effect shown in the illustrations of Figures 5.15 to 5.17 occurred only in mixtures with less than 1% SF<sub>6</sub>

and it is related to the voltage maximum of the positive impulse breakdown characteristics. Cookson and Wootton (76) have recently reported a similar effect in mixtures of  $SF_6/H_2$  in rod-plane gaps under AC voltages, but due to the limited information in their report with regard to the conditions of occurrence, one cannot comment on any similarities. In comparing spark trajectories associated with the creep effect and spark trajectories in  $SF_6$  under both impulse (Figure 5.19) and DC conditions (7,54), it is seen that the only similarity is that in all cases the curvature of the trajectories becomes a maximum at the voltage peak of the breakdown characteristics. Sparks that exhibited a creep effect have a maximum path length twice as long as that of the sparks in  $SF_6$ . Also, comparison of the illustrations of Figure 5.17 with Figures 5.10 and 5.11 shows that the magnitude of the voltage peak decreases proportionally to the creep distance. Thus, unlike  $SF_6$ , the mechanism responsible for the voltage peak in  $SF_6/N_2$  mixtures with less than 1%  $SF_6$  is directly related to the ionization process that forces the spark to initiate away from the tip of the electrode. In addition the photomultiplier results of Figure 5.14 show that the magnitude of the corona pulses and the statistical time lags of the 0.05%  $SF_6/N_2$  mixture, do not resemble those of  $SF_6$ , but the ones of nitrogen. The  $SF_6$  traces (fig. 5.14(c)) show relatively small statistical time lags (2 to 3  $\mu s$ ) and the light emitted during the formation of the corona streamers (not including ultra-violet) was too small to be detected.

The observations of the creep effect along the rod-

electrode assumes the presence of a space charge around the tip of the anode that produces a choking or retarding effect on the corona streamers in that area. This space charge is believed to be composed mainly of positive ions. Negative ions are too few to form significant space charges. As argued by Loeb (16) for mixtures of  $N_2/O_2$ , the formation of a negative charge sheath would require at least a few percent of the electronegative component. The effect of a negative space charge (that is a breakdown voltage increase) is in general expected to be proportional to the  $SF_6$  content. But as shown in Figure 5.11 the breakdown voltage between 1 and 2 bar increases as the percentage content of  $SF_6$  is reduced.

The presence of a positive charge in regions away from the spherical tip is the result of ionization in that area. The positive coronas of Figure 5.20 and 5.21 show that corona streamers do indeed surround the cylindrical part of the rod-electrode as far as 3 to 4 cm away from the tip. Thus, in the cases where breakdown occurs with a certain creep distance, the pre-breakdown streamers that reach the cathode should also start above the tip of the rod. Photographic evidence of such streamers was recently obtained by Watanabe and Takuma (5).

The initial ionization will take place in the region of highest field strength (spherical tip of the anode) by electron collision. Photoelectrons are then created away from the tip, at a distance related to the mean free path of the photons  $1/\mu_m$ ; where  $\mu_m$  is the photon absorption coefficient of the mixture. The photoelectrons that are produced in a region where  $\alpha \gg \eta$  will result in further ionization by collision, generating new ava-

lanches and thus new photoelectrons further away from the tip. The initial boundary of the  $\alpha$ - $\eta$  region for a space charge free environment is defined by the radius  $z_c + R$ , where  $z_c$  is the critical length of the first avalanche and  $R$  the radius of the spherical tip of the rod-electrode. Table 6.1 gives the values of  $z_c$  for a 10mm and a 50mm gaps in  $SF_6/N_2$  mixtures at a total pressure of 1 bar. Photoelectrons generated inside  $z_c$  will lead to further ionization while photoelectrons generated outside  $z_c$  will undergo capture and create negative ions through an associative or dissociative attachment process (reactions 1 and 3 of page 9).

The mean free path of the photons  $\lambda$  for  $N_2$ ,  $SF_6$  and 10% and 20%  $SF_6$  mixtures at 1 bar of total pressure are obtained from the absorption coefficients of these gases as given by Blair et-al. (66,67). In nitrogen the average absorption coefficient for wavelengths between  $1000\text{\AA}$  to  $1500\text{\AA}$  is  $0.6\text{mm}^{-1}$ . Addition of 20%  $SF_6$  increases this coefficient approximately by an order of magnitude to  $6.7\text{mm}^{-1}$ . These coefficients correspond to mean free photon paths of  $\lambda_{N_2} = 1.7\text{ mm}$  and  $\lambda_{20\%SF_6} = 0.14\text{ mm}$ . From Table 6.1 the values of  $z_c$  for nitrogen and 20%  $SF_6$  mixture are 0.98 mm and 0.08 mm respectively. Therefore radiation in the above range of wavelengths will be absorbed mostly outside the ionizing zone, thus if it does result in the ionization of already excited molecules, the generated photoelectrons will be

---

\* The coefficients of individual lines could differ considerably, for example, for the  $1084\text{\AA}$  nitrogen line  $\lambda_{N_2} = 2.8\text{ mm}$  and  $\lambda_{20\%SF_6} = 0.08\text{ mm}$

captured (in the case of a mixture) to produce negative ions. Photons of higher energy will be absorbed inside the ionizing zone: Simpson et-al(69) have measured the absorption cross section of SF<sub>6</sub> in the far ultraviolet region and found that an absorption continuum begins sharply at 15.5ev with a cross section of 10<sup>-16</sup>cm<sup>2</sup>. This cross section corresponds to a mean photon path of

$$\begin{aligned}\lambda_{SF_6} &= 1/N_0 \cdot \sigma_a \text{ (cm}^{-3}\text{)(cm}^2\text{)} & (7.1) \\ &= 1/2.7 \cdot 10^{19} \cdot 10^{-16} \\ &= 0.0037 \text{ mm}\end{aligned}$$

where N<sub>0</sub> is Loschmidt's number and  
σ<sub>a</sub> is the absorption cross section.

Table 6.1 shows that for SF<sub>6</sub> z<sub>c</sub>=0.05mm, hence for SF<sub>6</sub>, as well as nitrogen (90), most of the absorption in the far ultraviolet region will take place inside the ionizing zone.

In general, energetic radiation (above 10ev) will be absorbed both inside and outside the ionizing zone and this after all is one of the basic assumptions of the streamer theory (30). However, as it is shown above, the mean free path of the photons can vary significantly with SF<sub>6</sub> content and this could have an effect on the photoionization process of the different mixtures. Loeb (30) investigating the importance of secondary mechanisms in non-uniform fields, suggested two types of photoionization action in the anode depending on the absorption coefficient of the mixture.

1. If the coefficient of absorption for photoionizing action is of the order of 10cm<sup>-1</sup> (ionizing free path



1mm), breakdown characterized by spread over the anode surface occurs. (Burst-pulse or Geiger counter actions.)

2. If the coefficient of absorption for photoionizing action is of the order of  $100\text{cm}^{-1}$  or less with appropriate geometry, a self-sustaining process projects radially into the gap by photoionization and space-charge action leading to breakdown. (Streamer action)

For nitrogen with small impurities of  $\text{SF}_6$ ,  $\lambda_{\text{SF}_6/\text{N}_2}$  is expected to be relatively long. This could result in photoionization of  $\text{SF}_6$  molecules that are in the neighbourhood of the ionizing zone but relatively distant from the origin of ionization. Such type of photoionizing action could spread rapidly over the anode surface, suppressing further ionization until the space charge moves away from the anode, or the voltage is high enough for the breakdown streamers to initiate away from the tip of the anode and reach the cathode by travelling around the space charge. This type of action is expected to depend mainly upon the nature of the gas volume, yet the effects of the electrode surface should also be considered and in particular the photoelectric emission from the surface of the brass anode.

If one assumes that the brass electrode has the work function of copper ( $W \approx 4.5$  ev), then photons with wavelength  $\lambda = 2755\text{\AA}$  are needed to produce photoelectrons from the anode. In addition the ionization potential of the Cu vapour is  $V_i = 7.7$  ev and that corresponds to  $1610\text{\AA}$  photons. Emission data (87) shows that both the above wavelengths are well within the emission spectrum of  $\text{N}_2$  (and that of  $\text{SF}_6$  and  $\text{SF}_6/\text{N}_2$  mixtures (67)). Hence electron emission from the anode will depend on the value of the sec-

ondary photon emission coefficient  $\gamma_p$ . The effect of  $\gamma_i$  (secondary ion emission coefficient) should be small due to the static nature of the space charge under impulse conditions. The values of these coefficients for a brass or copper anode in both  $SF_6$  and  $SF_6/N_2$  mixtures are unknown. However,  $\gamma_i$  and  $\gamma_p$  in mixtures of  $SF_6/N_2$  with a small trace of  $SF_6$  are not expected to vary significantly from those of pure  $N_2$ . \* Since ionization above the tip is not present in pure  $N_2$  (or pure  $SF_6$ ), it is less than likely that a small trace of  $SF_6$  in  $N_2$  will alter the surface properties of the anode to such an extent that corona streamers on the cylindrical part of the electrode will be produced by some efficient  $\gamma_p$  mechanism alone. Hence, although the surface of the anode will be active, the main source of the free electrons that are required to initiate the ionization in regions surrounding the anode is believed to be photoionization of the  $SF_6$  impurity in the gas volume.

As mentioned earlier, the ionization could spread around the surface of the anode, if the ionizing radiation has a relatively long path and if it is absorbed in the neighbourhood of the ionizing zone, so that the generated photoelectrons can gain enough energy between collisions to ionize. The lack of absorption measurements in  $SF_6/N_2$  mixtures with less than 1%  $SF_6$  does not allow much speculation as to the type of radiation involved

---

\* In mixtures of  $N_2/O_2$  with a platinum anode the addition of 5.0%  $O_2$  in  $N_2$  resulted in a decrease of  $\gamma_i$  by a factor of 5 and an increase of  $\gamma_p$  by one order of magnitude. (reference (16) page 433).

in this process. However under the assumption that the photon paths are relatively long, the ionizing radiation can not be from the far ultraviolet region since both SF<sub>6</sub> and nitrogen have relatively high photon absorption coefficients in this region (69, 90). If the ionizing radiation has a wavelength in the region of 900A° to 1500A° this would mean that a two (or more) step ionization process is involved. In this case both the partial pressure of SF<sub>6</sub> and the total pressure of the mixture are expected to have an effect on the spread of the ionization. The partial pressure of SF<sub>6</sub> will regulate the absorption of the mixture in the ultraviolet region and the total pressure will have an effect on the probability of excitation by collision, that is needed to complete the two (or more) step ionization process.

Under DC conditions (88), the breakdown voltage-pressure characteristics of SF<sub>6</sub>/N<sub>2</sub> mixtures with less than 1% SF<sub>6</sub> show a behaviour similar to that of the impulse voltage, but with almost zero creep distance. That is, the space charge has probably drifted into the inter-electrode region away from the anode, but it is still effective in raising the breakdown voltage.

In conclusion the increase of the dielectric strength of mixtures containing small traces of SF<sub>6</sub> at low total pressures, is believed to be the result of a photoionization process that generates a positive space charge around the anode which impedes further ionization. The density and the extent of this space charge depend on the partial pressure of SF<sub>6</sub> and the total pressure of the mixture. The creep effect indicates the extent of the space charge above the tip of the anode and the creep dist-

ance is expected to vary with different impulse fronts.

#### 7.4 Positive Rod-Plane - SF<sub>6</sub>/N<sub>2</sub> mixtures with SF<sub>6</sub> Content Higher than 5%.

Under positive impulse conditions SF<sub>6</sub>/N<sub>2</sub> mixtures with high SF<sub>6</sub> content exhibit a similar behaviour to that of pure SF<sub>6</sub>. As shown in Figure 5.10 the corona stabilized region in the mixtures occurs at about the same pressure as that of SF<sub>6</sub>. The shielding of the anode seems to be so effective in preventing streamers from reaching the cathode that at P<sub>max</sub> the breakdown voltage of mixtures with 60% - 95% of SF<sub>6</sub> is higher than that of pure SF<sub>6</sub>.

On the basis of the discussion in the previous section, the addition of nitrogen into SF<sub>6</sub> can affect both the rate of production of negative ions, as well as the distribution of the space charge in the anode region. However as shown in Figure 5.9 the breakdown voltage-mixture ratio characteristics are far too complex for one to attempt their interpretation on the basis of the present information.

At higher pressures (Figures 5.8 and 5.9), the breakdown voltage drops with percentage of SF<sub>6</sub> in a manner similar to that of the negative polarity (Figure 5:7). But unlike the negative breakdown voltage-pressure characteristics, the breakdown voltage of the 50 mm gap (Figure 5.10) for pressures higher than 2.0 bar and mixtures with less than 20% SF<sub>6</sub>, drops below that of pure nitrogen. This suggests that the effective coefficient of ionization of these mixtures has increased above

that of SF<sub>6</sub> or nitrogen. However, it is interesting to note that the corona voltage of a mixture exhibiting this effect is higher than that of nitrogen. This is shown in Figure 5.22 for a 0.2% SF<sub>6</sub> mixture. In pure nitrogen, breakdown occurs at voltages higher than the corona onset voltage through a corona stabilized mechanism. Addition of small amounts of SF<sub>6</sub> seems to reduce the efficiency of the corona stabilized process at the higher pressures. That is, the initial corona streamers have sufficient intensity and length soon after they are generated to lead to a breakdown. But further speculation along these lines would require a more detailed study of the temporal and spatial growth of ionization under both impulse and DC voltage conditions.

CHAPTER 8  
CONCLUSIONS

1. In negative rod-plane gaps, and for low values of pressure and gap length, the breakdown voltage of the  $SF_6/N_2$  mixtures decreases at a slow rate as the percentage of  $SF_6$  content is reduced from 100% to about 10%. Lower contents of  $SF_6$  result in a higher rate of the dielectric strength loss, which becomes a minimum for 100%  $N_2$ .

2. Under negative impulse conditions and high values of pressure and gap length, the breakdown voltage of the mixtures decreases significantly at relatively high contents of  $SF_6$ . In a case of a 50 mm rod-plane gap and 5.0 bar of total pressure, most of the differential strength of the mixture is lost as the  $SF_6$  content reduces to 80%. The process responsible for this effect is by enlarge unknown. A reduction of the negative space charge with the addition of nitrogen could account for the sudden drop in the dielectric strength, but experimental evidence relating to such mechanism is not available.

3. For positive rod-plane gaps in  $SF_6$ , the impulse breakdown voltage-pressure characteristics exhibit a voltage maximum similar to that of the DC characteristics, which is attributed to a corona stabilization process. The voltage peak occurs at about the same pressure and has a lower magnitude, due to the limited time allowed for the formation and diffusion of the space charge.

4. In positive rod-plane gaps, the breakdown voltage-pressure characteristics of mixtures with more than 5-10% of

SF<sub>6</sub> exhibit a voltage maximum, at about the same pressure as that of SF<sub>6</sub>. The magnitude of the voltage peak varies with the percentage of SF<sub>6</sub>, and it is higher than that of SF<sub>6</sub> for mixtures with 60% to 95% SF<sub>6</sub>. This effect is believed to be the result of an intensified corona stabilization mechanism due to an increase of the photoionization in the gas.

5. Under positive impulse conditions the addition of small percentages of SF<sub>6</sub> (1.0%) in nitrogen result in an increase of the breakdown voltage for total pressures less than 2.0 to 3.0 bar. At a total pressure of 1.7 bar a mixture with 0.2% of SF<sub>6</sub> exhibits a breakdown voltage approximately double that of nitrogen.

6. The increase of positive impulse breakdown voltage in SF<sub>6</sub>/N<sub>2</sub> mixtures with less than 1.0% SF<sub>6</sub> is manifested as a movement of the initiation point of the spark along the rod electrode. This movement which is referred to here as "creep effect", is the result of a shielding mechanism produced by a positive space charge, which is generated by ionization that extends above the spherical tip of the rod. The extent and effectiveness of the space charge are controlled by the pressure of the mixture and the partial pressure of SF<sub>6</sub>.

7. The positive impulse breakdown voltage of SF<sub>6</sub>/N<sub>2</sub> mixtures with 40% to 0.05% SF<sub>6</sub> and total pressures higher than 2.0 to 3.0 bar, is lower than that of nitrogen. At 5.0 bar of total pressure the breakdown voltage with 0.1% to 0.2% SF<sub>6</sub> can be 50% that of N<sub>2</sub>.

8. The solution for the potential distribution of the

rod-plane configuration with the present optimized approach, indicates that the time required in setting up a problem of this kind is drastically reduced, and it is believed to be the shortest when compared to any other technique achieving comparable accuracy. When compared with the conventional charge simulation approach, we find that unnecessary guess-work is eliminated, and some of the insight required in solving such problems is replaced by computation time.

9. The streamer onset calculations in  $SF_6$  and  $SF_6/N_2$  mixtures suggest that, although the ionization and attachment coefficients of the mixtures are calculated from those of the individual gases, the degree of prediction is of the same order as that of  $SF_6$ . That is, in the region where the various breakdown criteria are applicable (quasi-uniform fields), the comparability of theoretical and experimental results in  $SF_6/N_2$  mixtures is about the same as that of  $SF_6$ . For non-uniform field electrode configurations such as the ones used in this work, the calculated corona onset voltage is in poor comparison with the experimentally measured one. Further improvements in this area are expected to include experimentally measured ionization and attachment coefficients for different  $SF_6/N_2$  mixtures.

10. In general, the behaviour of the  $SF_6/N_2$  mixtures under both impulse polarities is found to be far more complex than that of the individual gases. The results of this work suggest that certain  $SF_6/N_2$  mixtures have an impulse breakdown strength superior to that of  $SF_6$ . However, unlike the simpli-



city of the single component gases, the use of mixtures will involve a much more intricate set of constraints, regarding parameters such as uniformity factor of the system, partial pressure of SF<sub>6</sub>, and total pressure of the mixture.

### 8.1 Suggestions for Future Work.

The results of the present work indicate that SF<sub>6</sub>/N<sub>2</sub> mixtures could prove to be an insulating medium that is desirable both technically and economically. Including this work, there are relatively few investigations on the properties of the different mixtures and a great number of suggestions for future work could be made, ranging from arc quenching properties to thermal conductivity of the mixtures. For this reason, the suggestions presented below are limited to material along the lines of the present investigation.

- Breakdown voltage measurements in SF<sub>6</sub>/N<sub>2</sub> mixtures under both AC and DC voltages have not been pursued to any great detail and this could justify a number of general systematic studies in both quasi-uniform and non-uniform electrode arrangements.

- Study of different corona modes and their variations with percentage of SF<sub>6</sub> content. This type of information could provide a better understanding of some of the effects observed in the present work. For example, when small amounts of SF<sub>6</sub> are added to nitrogen at total pressures higher than 2 bar, the breakdown strength of nitrogen is found to decrease. This suggests that corona streamers soon after their onset have enough intensity and length to bridge the gap and lead to a breakdown. Knowledge of the evolution of the corona pulses

during the short time interval prior to breakdown could aid the understanding of the effects produced by the SF<sub>6</sub> impurity, and possibly provide certain clues relating to the mechanism of breakdown under these conditions.

- Breakdown studies of different SF<sub>6</sub>/N<sub>2</sub> mixtures with impulses of variable front, ranging from standard impulse to switching surges. This study will not only provide useful data on the behaviour of SF<sub>6</sub>/N<sub>2</sub> mixtures under switching surges, but it will also relate to some of the arguments put forward in this work with regard to the "creep effect" mechanism. Application of slower impulses are expected to result in lower creep distances due to movement of the space charge away from the anode.

- Introduction of a chromatographer for the analysis of mixtures containing small percentages of one of the component gases. Mixtures with small percentages of SF<sub>6</sub> under negative impulse polarity should take priority in this study, as the author believes that there might be an anomalous behaviour of the breakdown voltage of nitrogen with impurities of SF<sub>6</sub> (or SF<sub>6</sub> and O<sub>2</sub>) less than 0.01%.

- Spectroscopic studies of SF<sub>6</sub>/N<sub>2</sub> mixtures are in great need, to provide information about the ionization, attachment, and swarm parameters of the different mixtures. Such information is expected to elucidate to some extent the irregular behaviour of the dielectric strength of the mixtures and lead to improvements in the calculation of the corona and spark onset voltage.

## BIBLIOGRAPHY

1. A.H. Cookson and R.E. Wootton, "Particle-initiated AC and D.C. breakdown in compressed  $N_2$ ,  $SF_6$  and  $N_2/SF_6$  mixtures", Conference on Electrical Insulation and Dielectric Phenomena, Montreal, October 1973.
2. A.H. Cookson and O. Farish, "Particle-initiated breakdown between coaxial electrodes in compressed  $SF_6$ ", IEEE Trans. PAS- 92, pp 871-876, 1973.
3. O. Farish, S.J. Dale and A.M. Sletten, "Impulse breakdown of positive rod-plane gaps in  $H_2$  and  $H_2/SF_6$  mixtures", IEEE Trans. PAS- 95, pp 1639-1647, 1976.
4. Koshi Itaka and Giichi Ikeda, "Dielectric characteristics of compressed gas insulated cables", IEEE Trans. PAS- 89, No. 8, pp 1986-1994, 1970
5. T. Watanabe and T. Tacuma, "The breakdown and discharge extension of long gaps in  $N_2/SF_6$  and air/ $SF_6$  mixtures", J. of Applied Physics, V.48, N8. 8, pp. 3281-3287, 1977.
6. D.M. Grant, J.F. Perkins, L.C. Campbell, O.E. Ibrahim, and O. Farish, "Comparative Interruption studies of gas-blasted arcs in  $SF_6/He$  mixtures", Proc. Int. Conf. Gas discharges, IEE, London, pp. 48-51 1976.
7. R.L. Hazel, "DC breakdown and anode corona characteristics of sphere and rod-plane gaps insulated with compressed  $SF_6$ ", Ph.D. Thesis, University of Windsor, Ontario 1974
8. J. Chakkalackal, "Study of the effect of electrode surface roughness on breakdown voltage in compressed  $SF_6$  under DC, Impulse and Surge Voltages", Masters Thesis, University of Windsor, Ontario, 1975.
9. F.J. Ewasyshyn, "The effects of low temperatures on the DC breakdown characteristics of plane-plane and rod-plane gaps insulated with compressed  $SF_6$ ", Masters Thesis, University of Windsor, Ontario, 1976.
10. J. Dutton, S.C. Haydon and F. Llewellyn Jones, "Electrical breakdown of gases: II Spark mechanisms in  $N_2$ ", Proc. Royal Society, A213, pp. 203-214, 1952.
11. H. Raether, "Electron avalanches and breakdown in gases", London, Butterworths, 1964.
12. E.A.D. Heylen, "Townsend's first ionization coefficient in pure nitrogen", Nature, V. 183, pp. 1545-1546, 1959.

13. R.E. Fox and W.M. Hickam, "Study of Carbon monoxide, nitrogen, propylene and benzene ionization probability curves near threshold"; J. of Chemical Physics, V.22, No. 12, pp. 2059-1063, 1954.
14. See reference (11).page 68.
15. G.L. Weisler, "Positive and Negative point-to-plane corona in pure and impure Hydrogen, Nitrogen and Argon", Physical review, V. 63, pp. 96-107, 1943:
16. L.B. Loeb, "Electrical Coronas", University of California Press, Berkeley, 1965.
17. H.C. Pollock and F.S. Cooper, "The effect of pressure on the positive point-to-plane discharge in  $N_2$ ,  $O_2$ ,  $CO_2$ ,  $SO_2$ ,  $SF_6$ ,  $CCl_2F_2$ , A, He and  $H_2$ ", Physical Review, V. 66, pp. 170-175, 1959.
18. T.R. Foord, "Positive point-to-plane breakdown in compressed gases", Nature, V. 166, pp. 688, 1950.
19. C.N. Works and T.W. Dakin, "Dielectric breakdown of Sulphur Hexafluoride in non-uniform fields", AIEE Trans, V. 72, Part I, pp. 682-687, 1953.
20. P.R. Howard, "Insulation properties of compressed electro-negative gases", Proc. IEE, V. 104, Part A, pp. 123-138, 1957.
21. W.M. Hickam and R.E. Fox, "Electron attachment in sulphur-hexafluoride using monoenergetic electrons", J. of Chemical Physics, V. 25, No. 4, pp.642-647, 1955.
22. A.J. Ahearn and N.B. Hannag, "The formation of negative ions of sulphur Hexafluoride", J. of Chemical Physics, V. 24, No.1, pp. 119-124, 1953.
23. K.B. Mc Afee Jr, "Pulse technique for measurement of the probability of formation and mobility of negative ions", J. of Chemical Physics, V. 23, No.8, pp.1435-1440, 1955.
24. M.S. Naidu and A.N. Prasad, "Mobility and diffusion of negative ions in Sulphur hexafluoride", J. Physics D, Appl. Phys, V. 3, pp. 951-956, 1970.
25. F.C. Fehsenfeld "Electron attachment to  $SF_6$ ", J. Chemical Physics, V. 53, pp. 2000-2004, 1970.
26. D. Edelson, J.E. Griffiths and K.B. Mc Afee, "Autodetachment of electrons in  $SF_6$ ", J. Chemical Physics, V. 37, pp. 917-918, 1962.

27. R.N. Compton, L.G. Christophorou, G.S. Hurst and P.W. Reinhardt, "Nondissociative electron capture in complex molecules and negative-ion lifetimes", *J. Chemical Physics*, V. 45, pp. 4634-4639, 1966.
28. V.H. Dibeler and F.L. Mohler, "Dissociation of SF<sub>6</sub>, CF<sub>4</sub> and SiF<sub>4</sub> by electron impact", *J. Research National Bureau of Stand.*, Washington, V. 40, pp. 25, 1948.
29. Ta-Kong Liu, G. Moe and A.B.F. Duncan, "The absorption spectrum of SF<sub>6</sub> in the vacuum ultraviolet region", *J. of Chemical Physics*, V. 49, No. 1, pp. 71-71, 1951.
30. L.B. Loeb, "Basic processes of gaseous electronics", *University of California Press*, p.415, 1955.
31. M.S. Bhalla and J.D. Craggs, "Measurement of ionization and attachment coefficients in Sulphur Hexafluoride in uniform fields", *Proc. Physical Society*, V. 80, pp.151-160, 1962.
32. T.R. Foord, "Some experiments on positive point-to-plane corona and spark breakdown of compressed gases", *Proc. IEE*, V. 100, Part 2, No. 78, pp.585-590, 1953.
33. M.J. Mulcahy, "Electrical breakdown of air and SF<sub>6</sub> mixtures", *Proc. IEE*, V. 113, pp. 1878-1880, 1966.
34. E. Kuffel, M.J. Mulcahy and C.B. Guelkey, "The breakdown voltage between spheres in SF<sub>6</sub> and mixtures of air and SF<sub>6</sub>", *Proc. of the 5th inter. conf. on ionization phenomena in gases*, V. 1, pp. 976-985, 1961.
35. A. Wieland, "Gasdurchschlagmechanismen in elektro-negativen Gasen (SF<sub>6</sub>) und in Gasgemischen", *ETZ-A Band 94*, pp.370-373, 1973.
36. M. Ermel, "Das N<sub>2</sub>/SF<sub>6</sub> Gasgemisch als Isoliermittel der Hochspannungstechnik", *ETZ-A Band 96*, pp. 231-235, 1975.
37. T. Takuma, T. Watanabe and K. Kita, "Breakdown characteristics of compressed-gas mixtures in nearly uniform fields", *Proc. IEE*, V. 119, pp. 927-928, 1972.
38. R.G. Baumgartner, "Dielectric characteristics of mixtures of Sulphur Hexafluoride and Nitrogen", *Proc. 3rd Int. Conf, Gas discharges*, IEE, London, pp. 366-369, 1974.
39. R.C. Davidson, B.R. Lynch and O. Farish, "Corona and breakdown in N<sub>2</sub>/SF<sub>6</sub> and N<sub>2</sub>/O<sub>2</sub> mixtures in static and flowing gas", *Proc. Int Conf, Gas discharges*, IEE London, pp. 242-244, 1976.

40. M.S. Abou-Seada, "Computer determination of the potential and electric field in a hemispherically-capped cylindrical point-plane gap", M.S. Thesis, Iowa State U., Ames, 1967.
41. R.G. Baumgartner, "Breakdown characteristics of SF<sub>6</sub> and N<sub>2</sub> in a coaxial cylinder system", Internat. High Voltage Symposium, Zurich, pp. 326-331, 1975.
42. R.D. Garson, "The effect of SF<sub>6</sub>/N<sub>2</sub> mixtures upon the recovery capability of a synchronous interrupter", IEEE Trans, PAS-95, No. 1, pp. 140-144, 1976.
43. B.H. Crichton, D.I. Lee and D.J. Tedford, "Prebreakdown in compressed SF<sub>6</sub> and SF<sub>6</sub>/N<sub>2</sub> mixtures in projection perturbed uniform fields", Proc. Int Conf. Gas Discharges, IEE, London, pp. 199-202, 1976.
44. B.H. Crichton, O.E. Ibrahim and O. Farish, "The dependence of breakdown voltage in SF<sub>6</sub> mixtures on electrode-surface roughness", Proc. Int. Conf. Gas discharges, IEE London, pp. 117-120, 1976.
45. H. Singer, H. Steinbigler and P. Weiss, "A charge simulation method for the calculation of high voltage fields", IEEE Winter meeting, N.Y. Jan 27- Feb 1, 1974.
46. M. S. Abou-Seada and E. Nasser, "Digital computer calculation of the electric potential and field of a rod gap", Proceedings of IEEE, V. 56, No. 5, pp. 813-820, 1968.
47. L. B. Loeb, H. Parker, E.E. Dodd and W.N. English, "The choice of suitable gap forms for the study of corona breakdown and the field along the axis of a hemispherically capped cylindrical point-to-plane gap", The revue of scientific instruments. V. 21, No. 1, January 1950.
48. H.H. Rosenbrock, "An automatic method for finding the greatest or the least value of a function", Computer J. V.3, pp. 175-184, 1960.
49. C.W. Carroll, "The created response surface technique for optimizing restrained systems", J. Oper. Res. Soc. Am., pp. 169-185, 1961.
50. R. Fletcher and M.J.D. Powell, "A rapidly converging descent method for minimization", Computer J. V. 6, pp.163-168, 1963.
51. WATFIV Scientific Subroutine Manual, Hill climbing subroutine CLIMBD (Double precision version of CLIMBS).
52. E. Kuffel and A. Yializis, "Impulse breakdown of positive

and negative rod-plane gaps in SF<sub>6</sub>/N<sub>2</sub> mixtures", IEEE Winter power meeting, N.Y. Jan - Feb 1978.

53. A. Yializis, E. Kuffel and P.H. Alexander, "An optimized charge simulation method for the calculation of high voltage fields", IEEE Winter power meeting, N.Y. Jan-Feb 1978.
54. S. Sangkasaad "Dielectric strength of compressed SF<sub>6</sub> in non-uniform fields"; Ph. D. Dissertation, Swiss Federal Institute of Technology, Zurich, 1976.
55. P.R. Howard, "Processes contributing to the breakdown of electronegative gases in uniform and non-uniform electric fields", Proc. IEE, V. 105, pp. 139-142, 1957.
56. S. Sangkasaad "Corona inception and breakdown voltages in non-uniform fields in SF<sub>6</sub>", International High Voltage Symposium, Zurich, pp. 378-384, 1975.
57. R. Hazel and E. Kuffel, "Static field mode corona characteristics in SF<sub>6</sub>", IEEE Trans, PAS-95, pp.178-186, 1976.
58. J.M. Meek and J.D. Craggs, "Electrical breakdown of gases", Oxford, Clarendon Press, 1953.
59. T. Nitta and Y. Shibuya, "Electrical breakdown of long gaps in SF<sub>6</sub>", IEEE Trans, PAS-90, pp. 1065-1071, 1971.
60. M. Khalifa, S. El-Debeiky and M. Abdel-Salam, "Calculating the positive spark-breakdown and pre-breakdown threshold voltages in compressed SF<sub>6</sub>", IEEE Summer Power Meeting, F-76-324-4, July 1976.
61. A. Pedersen, "Criteria for spark breakdown in Sulphur Hexa-fluoride", IEEE Trans, PAS-89; pp. 2043-2048, 1970.
62. A. Pedersen, "The effect of surface roughness on breakdown in SF<sub>6</sub>", IEEE, PAS-94, pp. 1749-1753, 1975.
63. E. Nasser, "Fundamentals of gaseous Ionization and plasma electronics", J. Wiley and Sons, 1970.
64. R. Malewski and W. Malewski, "Low inductance resistors for measurements of impulse currents", Canadian Communications and Power Conf, Nov. 1974, Montreal, pp. 173-174.
65. D. Kind and T. Sirait, "Über die Ermittlung der Erdströme von Stosspannungsanlagen", (Evaluation of ground transients in impulse test set ups), ETZ A 85, pp. 848-849, 1964.
66. D.T.A. Blair, N.M. MacLeod and J.S. Orr, "Radiation from gases in the vacuum ultra-violet range", IEE conf, publication No. 118, Gas discharges, London pp. 68-72, 1974.

67. D.T.A. Blair and N.M. MacLeod, "Radiation in the vacuum ultra-violet from discharges in gas mixtures", Proc. Int. Conf. Gas discharges, IEE London, pp. 401-403, 1976.
68. E.D. Nostrand and A.B.F. Duncan, "Effect of pressure on Intensity of some electronic transitions in SF<sub>6</sub>, C<sub>2</sub>H<sub>2</sub> and C<sub>2</sub>D<sub>2</sub> vapors in the vacuum ultra-violet region", J<sup>2</sup> of Chemical Physics, V. 76; pp.3377-3379, 1954.
69. J.A. Simpson, C.E. Kuyatt and S.R. Mielezerek, "Absorption spectrum of SF<sub>6</sub> in the far ultra-violet by electron impact", J. of Chemical Physics, V. 44, No. 12, pp.4403-4404, 1966.
70. F.R. Gilmore, "Potential energy curves for N<sub>2</sub>, NO, O<sub>2</sub> and corresponding ions", J. Quant. Spectrosc. Radiat. Transfer, V. 5, pp. 369-390, 1965.
71. M. Khaled, "Computation of corona onset using the ring-charge method", Proc. IEE V. 122, No.1, pp. 107-110. 1975
72. F.C. Fehsenfeld, "Ion chemistry of SF<sub>6</sub>", J. Chemical Physics, V. 59, pp.438-439, 1971.
73. P.L. Patterson, Bulletin of American Physical Society, p. 459, V. 14, 1969.
74. W.E. Bowls, "The effect of cathode material on the second Townsend coefficient for ionization by collision in pure and contaminated N<sub>2</sub> gas", Phys. Review, V. 53, pp. 293-301, 1937.
75. H.S.W. Massey, "Negative Ions", University Press, Cambridge, England, 1950.
76. A.H. Cookson and R.E. Wootton, "AC corona and breakdown characteristics for rod gaps in compressed hydrogen, SF<sub>6</sub> and hydrogen - SF<sub>6</sub> mixtures", IEEE, PES Summer meeting Mexico City, Mexico, July 17-22, 1977, F-77-657-0.
77. G. Anis, A. Zeitoun, M. El-Ragheb and M. El-Desouka, "Field calculations around non-standard electrodes using regression and their spherical equivalence", IEEE Trans. PAS, no. 6, V. PAS-96, pp. 1721-1730, 1977.
78. R.C. Klewe and B.A. Tozer, "Impulse breakdown of a point-plane gap in SF<sub>6</sub>", Internat. Conf. of Gas Discharges, IEE London, pp.36-41, 1970.
79. K.B. Jun. McAffe and D. Edelson, "Identification and mobility of ions in a Townsend discharge by time-resolved mass spectrometry", Proc. Phys. Soc., V. 81, pp. 382-384, 1963.



80. E. Kuffel and M. Abdullah, "High voltage Engineering", Pergamon Press, p. 199, 1970.
81. D.F. Binns, "Calculation of field factor for a vertical sphere gap, taking account of surrounding earthed surfaces", IEE Proc., V. 112, pp. 1575-1582, 1965.
82. T. Nitta, "Electrical breakdown characteristics of SF<sub>6</sub>", Central Research Laboratory, Mitsubishi Electric CO., 1974.
83. M.G. Kratzenstein, "Der Stossdurchschlag Isolieröl", Ph.D. Thesis, Technical University Munich, 1969.
84. S.J. Dale, "Breakdown mechanisms in long nonuniform field gaps in atmospheric air under the influence of impulse and switching surge voltages", Ph.D. Thesis, University of Strathclyde, Glasgow, 1976.
85. F.J. Davis and D.R. Nelson, "Attachment rate of thermal electrons to SF<sub>6</sub>", J. Chem. Phys. Lett., V.6, pp.277-278, 1969.
86. F.J. Davis and D.R. Nelson, "Pseudo-first-order attachment rates of thermal electrons by SF<sub>6</sub> in different carrier gases", J. Chem. Phys. Lett., V.3, pp.461-463, 1968.
87. Hand Book of Chemistry and Physics, Chemical Rubber Publishing Co., 44th Edition, 1963:
88. S. Trajmar and A. Chutjian, "Electron impact excitation of SF<sub>6</sub>", J. Phys. B: Atom. Molec. Phys., V.10, pp.2943-2949, 1977.
89. Recent developments in this laboratory by N. Malik in "Breakdown Measurements of SF<sub>6</sub>/N<sub>2</sub> mixtures in rod-plane gaps under DC voltage conditions", (not published).
90. R.E. Huffman, Y. Tanaka, and J.C. Larrabee, "Absorption coefficients of nitrogen in the 1000-580A wavelength region", J. Chem. Phys., V.39, no.4, pp.910-925, 1963.

## APPENDIX 1

### COMPUTER PROGRAM FOR THE POTENTIAL DISTRIBUTION OF A ROD-PLANE GAP USING THE CHARGE SIMULATION TECHNIQUE.

The following program represents a solution of equation 3.3 for nine semi-infinite line charges and one point charge (46). Ten boundary points  $(r_j, z_j)$  are used, three of which lie on the spherical part of the boundary and the remaining seven along the cylindrical part starting at  $z=G+R$  (see Figure 3.1(a)). The problem is solved on the basis of the following data.

1. Radius of spherical tip  $R = 1$  unit (cm)
2. Gap length  $G = 10R$
3. Gap potential  $GPOT = 1V$

Having solved equation 3.3, the value of the charges  $Q_i$  ( $i=1,2,\dots,10$ ) are substituted in equation 3.6. The potential  $\phi(r,z)$  can then be calculated at any point  $(r,z)$  in the inter-electrode region and along the boundary of the electrode to test for the accuracy of the simulated potential.

POTENTIAL DISTRIBUTION OF A ROD-PLANE GAP

```

DOUBLE PRECISION ZS,TS,T1,DSIN,DCQS,XS(20),DLOG,XC,PN(10),PSF6(10)
DOUBLE PRECISION X1,X2,PT,PE,TS1,TS2,PCL(20)
DOUBLE PRECISION A(9),Z(9),PUT(10),VOLT(100,20),YY(100),V(10,10)
DOUBLE PRECISION PA,PR,PZ,U(10),VNITA,UTILF
DOUBLE PRECISION ZED,AA,AP,PP,VTOTAL,ZZ,ZZZ,ZZZ,Z1,XX(20)
DOUBLE PRECISION B,C,D,E,F,G,P,J,R,S,T,X,Y,V1,V2,V4,P2,PA,VA,RR
DOUBLE PRECISION BB,CC,DD,EE,FA1,FA2,FA3,FA4,VR,VZ,PA1,PA2,PA3
DOUBLE PRECISION GPL,PTRAD,GPOT,POTFCR,FLDFCR,GA(90)
DOUBLE PRECISION XL,ZSO,PRESS,APPLV,FZ,FLDZ, RD,XU,Y32
DOUBLE PRECISION ETOT,ERAD,DEXP,DA8S
DOUBLE PRECISION EPNT,EANCD,FZ1,FZ2,ZP(50),CRG(50),OZ
DOUBLE PRECISION DLOG10,DSORT,TT1,TT2,FCT,C1
DIMENSION XCD(100),YCD(100),XCJI(50),YCDI(60),XCOJ(20),YCOJ(20)
DIMENSION VALT(100,20)

```

READ IN THE FOLLOWING DATA  
 GPL = GAP LENGTH - IN CENTIMETERS  
 PTRAD = RADIUS OF THE HEMISPHERICAL ELECTRODE - IN CENTIMETERS  
 GPOT = POTENTIAL ACROSS THE GAP - (1 VOLT)

```

READ (5,111) GPL,PTRAD,GPOT
111 FORMAT (F8.2/F5.2/F8.2)
998 WRITE (6,8) GPL,PTRAD,GPOT
8 FORMAT (1H0,/,24X,'GAP LENGTH =',F7.2,/,22X,'POINT RADIUS =',F7.2
1,/,22X,'GAPPOTENTIAL =',F7.2//)

```

INTRODUCE THE POSITIONS (0,Z')=A(I) OF THE SEMI-INFINITE  
 LINE CHARGES, AND THE POINTS (R,Z) ON THE BOUNDARY OF THE  
 ELECTRODE WHERE THE BOUNDARY CONDITIONS ARE APPLIED.

```

TT1 = 0.0500
TT2 = 0.100
TS1 = (180.000/3.1415900)*TT1
TS2 = (180.000/3.1415900)*TT2
G=GPL/PTRAD
F=G+1.000
A(1)=F
A(2)=F+.100
A(3)=F+.200
A(4)=F+.500
A(5)=F+1.000
A(6)=F+9.000
A(7)=F+24.000
A(8)=F+89.000
A(9)=F+239.000
Z(1)=F
Z(2)=F+1.000
Z(3)=F+4.000
Z(4)=F+14.000
Z(5)=F+39.000
Z(6)=F+139.000
Z(7)=F+439.000
Z(8) = G+(1.000-DCQS(TT1))
Z(9) = G+(1.000-DCQS(TT2))

```

FORM MATRIX OF COEFFICIENTS

```

COMPUTE V(0,G A(J)) AND LOCATE POSITION IN MATRIX OF COEFFICIENTS
12 FORMAT ('1',/,47X,1HA,14X,'V(0,',F6.1,'A)')
WRITE (6,12) G

```

```

DO 14 J=1,9
R = 0.000
X=A(J)
B=X+G
C=X-G
D = F -G
E=F+G
V1= DLOG((B+DSORT(R*R+B*B))/(C+DSORT(R*R+C*C)))
I = 10
V(I,J)=V1

```

```

WRITE V(0,G A(J))

```

```

WRITE (6.13) A(J),V(I,J)
13 FORMAT ('0',42X,F6.1,13X,F10.8)
14 CONTINUE

```

COMPUTE P(O,G) AND LOCATE POSITION IN MATRIX OF COEFFICIENTS

```

I = 10
J = 10
P=1.000/(DSQRT (R*R+D*D))-1.000/(DSQRT(R*R+E*E))-
V(I,J)=P

```

WRITE P(O,G)

```

WRITE (6.15) G,P
15 FORMAT ('0',//,45X,4HP(O,F6.1,3H) =,F11.8)
WRITE (6.21)
21 FORMAT ('1',//,9X,1HZ,5X,9HV(I,Z A1),2X,9HV(1,Z A2),2X,9HV(1,Z A3)
1.2X,9HV(1,Z A4),2X,9HV(1,Z A5),2X,9HV(1,Z A6),2X,9HV(1,Z A7),2X,9H
2V(1,Z A8),2X,9HV(1,Z A9))

```

COMPUTE V(I,Z(I) A(J)) AND LOCATE POSITION IN MATRIX OF COEFFT'S

```

DO 23 I=1,9
DO 23 J=1,9
IF(I-8) 801,802,803
801 R = 1.000
GO TO 805
802 R = DSIN(TT1)
GO TO 805
803 R = DSIN(TT2)
805 Y=Z(I)
X=A(J)
B=X+Y
C=X-Y
D=F-Y
E=F+Y
V1= DLOG((B+D*SQRT(R*R+B*B))/(C+D*SQRT(R*R+C*C)))
V(I,J)=V1

```

23 CONTINUE

WRITE V(1,Z(I) A(J))

```

WRITE (6.25) (Z(I),(V(I,J),J=1,9),I=1,9)
25 FORMAT ('0',6X,F5.1,2X,9F11.8)
WRITE (6.26)
26 FORMAT ('1',//,51X,5H(R,Z),14X,6HP(R,Z))

```

COMPUTE P(1,Z(I)) AND LOCATE POSITION IN MATRIX OF COEFFICIENTS

```

DO 28 I=1,9
J = 10
IF(I-8) 901,902,903
901 R=1.000
GO TO 905
902 R = DSIN(TT1)
GO TO 905
903 R = DSIN(TT2)
905 Y = Z(I)
D=F-Y
E=F+Y
P=1.000/(DSQRT(R*R+D*D))-1.000/(DSQRT(R*R+E*E))
V(I,J)=P

```

WRITE P(1,Z(I))

```

WRITE (6.27) Z(I),P
27 FORMAT ('0',48X,3H(1.,F5.1,1H),10X,F10.8)
28 CONTINUE

```

WRITE MATRIX OF COEFFICIENTS

```

WRITE (6.51)
51 FORMAT ('0',//,48X,41HMATRIX OF COEFFICIENTS PJI (EQUATION 3.3)
1/,10X,'(1)',9X,'(2)',
19X,'(3)',9X,'(4)',9X,'(5)',9X,'(6)',9X,'(7)',9X,'(8)',9X,'(9)',9X,
2'(10)')
WRITE (6.53) (I,(V(I,J),J=1,10),I=1,10)
53 FORMAT('0',1H(,12,1H),10F12.8)

```

MAIN

```

WRITE (6,61)
61 FORMAT ('1',14X,20HPOTENTIAL VECTOR VJ )

```

FORM THE POTENTIAL VECTOR VJ

```

DO 73 I=1,10
71 U(I)=1.000
73 CONTINUE

```

WRITE THE POTENTIAL VECTOR VJI

```

DO 74 I=1,10
74 WRITE (6,75) U(I)
75 FORMAT ('0',22X,F3.1)

```

SOLVE FOR POTENTIAL COEFFICIENTS

```

CALL DSIMQ(V,U,10,0)
WRITE (6,81)

```

```

81 FORMAT ('1',///,3CX,'CHARGE VALUES OF THE NINE LINE CHARGES AND THE
1 POINT CHARGE')

```

WRITE POTENTIAL COEFFICIENTS

```

DO 88 I = 1,10
83 WRITE (6,84) I,U(I)
84 FORMAT ('0',48X,5H(0,Z',I2,1H),2X,1H=,2X,F11.6)
88 CONTINUE

```

```

DO 233 I = 1,9
J = 11+I
XS(I) = U(I)
233 XS(J) = A(I)
XS(10) = U(10)
XS(11) = F

```

```

R = 0.000
RR = 0.000
JJ=1

```

```

102 ZS= G
II=1
105 DO 101 I = 1,9
YY(II)=ZS
J = 11+I

```

```

POT(I) = XS(I)*DLOG((XS(J)+ZS+DSQRT(RR+(XS(J)+ZS)*(XS(J)+ZS)))/
1(XS(J)-ZS+DSQRT(RR+(XS(J)-ZS)*(XS(J)-ZS))))
101, CONTINUE
POT(10) = XS(10)*(1.000/DSQRT(RR+(XS(11)-ZS)*(XS(11)-ZS))) -
21.000/DSQRT(RR+(XS(11)+ZS)*(XS(11)+ZS)))

```

```

VTOTAL = 0.000
DO 103 K = 1,10
VTOTAL = VTOTAL+POT(K)

```

```

103 CONTINUE
VOLT(II,JJ) = VTOTAL
Z1 = ZS-61.000
IF (F-Z1) 200,200,201

```

```

201 CONTINUE
IF(ZS-G) 212,212,213
212 ZS = ZS-G /100.000
II = II+1
IF(II-100) 105,105,231

```

```

213 CONTINUE
ZS = ZS+1.000
II = II+1
GO TO 105
231 CONTINUE
IF(R-5.000) 202,203,203

```

```

202 CONTINUE
R = R+0.500
RR = R*R
JJ = JJ+1
GO TO 102
203 CONTINUE

```

```

WRITE (6,106)
106 FORMAT ('1',35X,49HPOTENTIAL DISTRIBUTION IN INTER-ELECTRUDE REGIO
1N //,4X,5HZ /,R,5X,3
1H0.0,8X,3H0.5,8X,3H1.0,8X,3H1.5,8X,3H2.0,8X,3H2.5,8X,3H3.0,8X,3H3.
25,8X,3H4.0,8X,3H4.5,8X,3H5.0)

```



```
VALT(II,1) = VOLT(II,1)
YCCJ(II) = (1.000-VALT(II,1))*100.000
XCOJ(II) = XX(II)
402 CONTINUE
WRITE(6,1302)
1302 FORMAT('1',30X,'POTENTIAL DISTRIBUTION ALONG THE SPHERICAL PART OF
1 THE BOUNDARY')
CALL PLOT 3(XCOJ,YCOJ,20)
STOP
END
```

SUBROUTINE DSIMO(A,B,N,KS)

FOR THE SOLUTION OF A LINEAR SYSTEM OF EQUATIONS.  
DESCRIPTION OF PARAMETERS

- A - MATRIX OF COEFFICIENTS STORED COLUMNWISE
- B - VECTOR OF UNKNOWNNS, REPLACED BY THE FINAL SOLUTION VALUES (VECTOR X).
- N - NUMBER OF EQUATIONS AND VARIABLES
- KS - OUTPUT DIGIT
  - 0 FOR NORMAL SOLUTION
  - 1 FOR SINGULAR SET OF EQUATIONS

DOUBLE PRECISION A(100) .B(10) .TOL .BIGA .SAVE .DABS

TOL = 0.000

KS = 0

JJ = -N

DO 65 J=1,N

JY = J + 1

JJ = JJ + N+1

BIGA = 0.000

IT = JJ-J

DO 30 I = J,N

IJ = IT + I

IF(DABS(BIGA)-DABS(A(IJ))) 20,30,30

20 BIGA = A(IJ)

IMAX = I

30 CONTINUE

IF(DABS(BIGA)-TOL) 35,35,40

35 KS = 1

RETURN

40 I1 = J + N\*(J-2)

IT = IMAX - J

DO 50 K = J,N

I1 = I1 + N

I2 = I1 + IT

SAVE = A(I1)

A(I1) = A(I2)

A(I2) = SAVE

50 A(I1) = A(I1)/BIGA

SAVE = B(IMAX)

B(IMAX) = B(J)

B(J) = SAVE/BIGA

IF(J-N) 55,70,55

55 IQS = N\*(J-1)

DO 65 IX = JY,N

IXJ = IQS + IX

IT = J-IX

DO 60 JX = JY,N

IXJX = N\*(JX-1) + IX

JJX = IXJX + IT

60 A(IXJX) = A(IXJX)-(A(IXJ)\*A(JJX))

65 B(IX) = B(IX)-(B(J)\*A(IXJ))

70 NY = N-1

IT = N\*N

DO 80 J = 1,NY

IA = IT-J

IB = N-J

IC = N

DO 80 K = 1,J

B(IB) = B(IB)-A(IA)\*B(IC)

IA = IA-N

80 IC = IC-1

RETURN

END



GAP LENGTH = 10.00  
POINT RADIUS - 1.00  
GAFFCTENTIAL = 1.00

A	V(0, 10.0-A)
11.0	3.04452244
11.1	2.95396286
11.2	2.87167962
11.5	2.66258783
12.0	2.39789527
20.0	1.09361229
35.0	0.58778666
100.0	0.20057070
250.0	0.08004271

P(0, 10.0) = 0.95238095

Z	V(1,Z A1)	V(1,Z A2)	V(1,Z A3)	V(1,Z A4)	V(1,Z A5)	V(1,Z A6)	V(1,Z A7)	V(1,Z A8)	V(1,Z A9)
11.0	J.78470576	J.68940218	J.59505624	3.32594413	2.94774006	1.23395044	0.65027195	0.22002256	0.08805615
12.0	4.71048724	4.64231491	4.57043187	4.33101181	3.87163476	1.30265485	0.71427428	0.24114970	0.09607306
15.0	6.04632588	6.02561853	6.00429880	5.93636819	5.80777387	1.93626022	0.91576630	0.30222517	0.12014334
25.0	7.61031655	7.60599927	7.60152297	7.58785283	7.56382021	6.81237145	1.78933623	0.51079718	0.20066906
50.0	9.16096198	9.16003261	9.15909456	9.15622449	9.15125302	9.03631566	8.53811700	1.64652341	0.40546164
150.0	11.40219524	11.40205649	11.40199684	11.40169245	11.40116703	11.30965069	11.15163652	10.988227	1.38627092
450.0	13.60419429	13.60418337	13.60417235	13.60413870	13.60408064	13.60281475	13.55872429	13.55414866	13.23565882
10.0	3.04520843	2.55464339	2.87234767	2.66320292	2.39842215	1.07877338	0.38780374	0.23006959	0.08005272
10.0	3.04726700	2.53668559	2.87435240	2.66504870	2.40000306	1.09225634	0.58807477	0.20077152	0.08008273

(H, Z)  
 0.754572J4  
 0.66366956  
 0.20410250  
 0.042347998  
 0.00924136  
 0.00098300  
 0.00010871  
 0.95230392  
 0.95239202

MATRIX OF COEFFICIENTS P1 (EQUATION 3-3)

(1)	(2)	(3)	(4)	(5)	(6)	(7)	(8)	(9)	(10)
11	3.78470576	3.08940218	3.59505624	3.32594413	2.94774006	1.23395044	0.65027152	0.22088256	0.02005615
12	4.71048724	4.64231491	4.57043107	4.31101101	3.87161476	1.30265485	0.71423423	0.24114970	0.09007306
13	6.04632508	6.02561823	6.00429800	5.93636819	5.80777327	1.93626092	0.91570630	0.30226517	0.12014334
14	7.61033655	7.60565927	7.60182297	7.50765203	7.56302321	6.81237145	1.70933024	0.51079718	0.20006906
15	9.16050130	9.16003261	9.15909406	9.15622449	9.15125302	9.03631566	8.63811400	1.09852341	0.40546164
16	11.40219524	11.40205645	11.40195664	11.40169245	11.40116703	11.30265069	11.35160824	10.81208227	1.38627092
17	13.60419429	13.60418337	13.60417235	13.60413870	13.60408904	13.60201475	13.59372429	13.55414866	13.23565882
18	3.04520843	2.95464339	2.87234767	2.66320292	2.30842215	1.09077330	0.58786374	0.20006952	0.08005272
19	3.04726700	2.95666555	2.87435240	2.66504870	2.40000106	1.09925334	0.58403477	0.20077152	0.08004273
20	3.04452244	2.95316266	2.87107462	2.66250703	2.39789527	1.09801229	0.58776633	0.20004070	0.08004271

POTENTIAL VECTOR VJ

1.0  
1.0  
1.0  
1.0  
1.0  
1.0  
1.0  
1.0  
1.0  
1.0

CHARGE VALUES OF THE NINE LINE CHARGES AND THE POINT CHARGE

(0,Z' 1) = -44.912401  
(0,Z' 2) = 82.200071  
(0,Z' 3) = -45.354784  
(0,Z' 4) = 10.213713  
(0,Z' 5) = -1.483524  
(0,Z' 6) = -0.030520  
(0,Z' 7) = -0.022561  
(0,Z' 8) = -0.021720  
(0,Z' 9) = -0.015278  
(0,Z' 10) = 3.166699

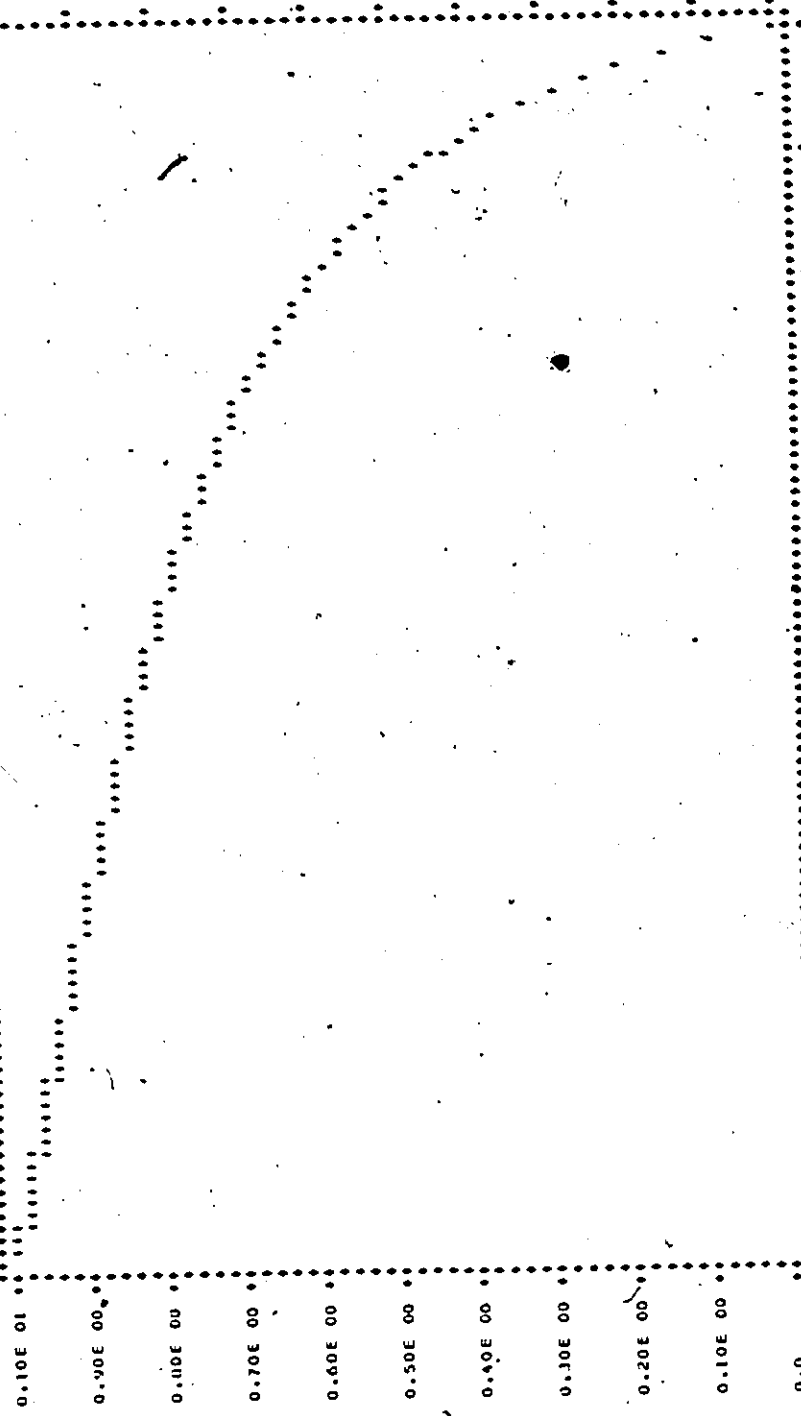
POTENTIAL DISTRIBUTION IN INTER-ELECTRODE REGION

Z / R	0.0	0.5	1.0	1.5	2.0	2.5	3.0	3.5	4.0	4.5	5.0
10.00	1.0000	0.9120	0.7049	0.6409	0.5660	0.5059	0.4670	0.4211	0.3877	0.3510	0.3100
9.00	0.9236	0.8571	0.7350	0.6317	0.5551	0.4974	0.4522	0.4150	0.3848	0.3508	0.3162
8.00	0.8598	0.8079	0.7064	0.6146	0.5415	0.4808	0.4453	0.4097	0.3799	0.3544	0.3223
7.00	0.8050	0.7644	0.6754	0.5977	0.5320	0.4801	0.4384	0.4040	0.3750	0.3501	0.3204
6.00	0.7587	0.7255	0.6530	0.5811	0.5204	0.4714	0.4314	0.3992	0.3700	0.3457	0.3206
5.00	0.7176	0.6866	0.6256	0.5649	0.5099	0.4626	0.4244	0.3923	0.3650	0.3413	0.3206
4.00	0.6816	0.6590	0.6068	0.5492	0.4975	0.4539	0.4174	0.3860	0.3600	0.3369	0.3167
3.00	0.6493	0.6304	0.5854	0.5339	0.4863	0.4453	0.4104	0.3790	0.3549	0.3325	0.3127
2.00	0.6202	0.6042	0.5652	0.5190	0.4752	0.4366	0.4034	0.3740	0.3499	0.3281	0.3088
1.00	0.5919	0.5802	0.5462	0.5047	0.4644	0.4281	0.3964	0.3689	0.3442	0.3236	0.3049
0.00	0.5698	0.5580	0.5282	0.4900	0.4536	0.4196	0.3895	0.3631	0.3370	0.3192	0.3000
0.90	0.5470	0.5375	0.5112	0.4776	0.4432	0.4112	0.3824	0.3572	0.3347	0.3147	0.2968
0.80	0.5274	0.5185	0.4952	0.4643	0.4330	0.4030	0.3757	0.3514	0.3297	0.3103	0.2929
0.70	0.5086	0.5007	0.4800	0.4523	0.4240	0.3980	0.3722	0.3480	0.3246	0.3050	0.2880
0.60	0.4911	0.4841	0.4653	0.4404	0.4133	0.3880	0.3622	0.3390	0.3166	0.3014	0.2848
0.50	0.4747	0.4685	0.4519	0.4289	0.4038	0.3789	0.3536	0.3301	0.3076	0.2925	0.2769
0.40	0.4593	0.4538	0.4387	0.4178	0.3945	0.3711	0.3490	0.3284	0.3076	0.2925	0.2772
0.30	0.4440	0.4399	0.4263	0.4071	0.3855	0.3635	0.3424	0.3220	0.3017	0.2881	0.2729
0.20	0.4312	0.4267	0.4144	0.3968	0.3767	0.3560	0.3360	0.3172	0.2977	0.2837	0.2699
0.10	0.4183	0.4142	0.4030	0.3860	0.3681	0.3487	0.3297	0.3110	0.2918	0.2773	0.2649
0.00	0.4060	0.4024	0.3921	0.3772	0.3597	0.3414	0.3234	0.3061	0.2899	0.2749	0.2610
7.00	0.3944	0.3910	0.3816	0.3679	0.3516	0.3343	0.3172	0.3007	0.2851	0.2706	0.2570
6.00	0.3833	0.3802	0.3716	0.3580	0.3436	0.3274	0.3111	0.2953	0.2803	0.2662	0.2531
5.00	0.3727	0.3699	0.3619	0.3501	0.3366	0.3206	0.3051	0.2899	0.2755	0.2619	0.2492
4.00	0.3626	0.3600	0.3527	0.3417	0.3283	0.3139	0.2991	0.2847	0.2702	0.2576	0.2453
3.00	0.3524	0.3506	0.3437	0.3335	0.3210	0.3073	0.2933	0.2794	0.2661	0.2534	0.2414
2.00	0.3435	0.3413	0.3350	0.3255	0.3130	0.3009	0.2875	0.2743	0.2614	0.2491	0.2375
1.00	0.3346	0.3325	0.3267	0.3178	0.3068	0.2946	0.2819	0.2692	0.2568	0.2449	0.2337
0.90	0.3260	0.3241	0.3186	0.3103	0.2999	0.2884	0.2763	0.2641	0.2522	0.2400	0.2290
0.80	0.3176	0.3159	0.3108	0.3030	0.2932	0.2823	0.2708	0.2591	0.2477	0.2360	0.2260
0.70	0.3096	0.3079	0.3032	0.2959	0.2867	0.2763	0.2653	0.2542	0.2432	0.2325	0.2222
0.60	0.3010	0.3003	0.2950	0.2890	0.2803	0.2705	0.2600	0.2493	0.2387	0.2284	0.2185
0.50	0.2943	0.2920	0.2887	0.2822	0.2740	0.2647	0.2547	0.2445	0.2343	0.2243	0.2147
0.40	0.2870	0.2856	0.2817	0.2757	0.2679	0.2591	0.2495	0.2397	0.2299	0.2203	0.2110
0.30	0.2799	0.2787	0.2750	0.2693	0.2619	0.2535	0.2444	0.2350	0.2256	0.2163	0.2072
0.20	0.2730	0.2719	0.2684	0.2630	0.2561	0.2481	0.2394	0.2304	0.2213	0.2123	0.2036
0.10	0.2664	0.2652	0.2620	0.2569	0.2503	0.2427	0.2344	0.2258	0.2170	0.2083	0.1999
0.00	0.2599	0.2580	0.2550	0.2509	0.2447	0.2374	0.2295	0.2214	0.2128	0.2044	0.1962

6.20	0.2535	0.2497	0.2451	0.2392	0.2323	0.2247	0.2167	0.2086	0.2005	0.1926
6.10	0.2474	0.2437	0.2394	0.2336	0.2272	0.2199	0.2123	0.2045	0.1967	0.1890
6.00	0.2413	0.2379	0.2338	0.2284	0.2222	0.2152	0.2074	0.2004	0.1928	0.1854
5.90	0.2355	0.2322	0.2283	0.2232	0.2172	0.2106	0.2035	0.1960	0.1885	0.1819
5.80	0.2297	0.2266	0.2229	0.2181	0.2124	0.2060	0.1993	0.1923	0.1853	0.1783
5.70	0.2241	0.2212	0.2176	0.2130	0.2076	0.2015	0.1950	0.1883	0.1815	0.1746
5.60	0.2186	0.2159	0.2125	0.2081	0.2029	0.1970	0.1904	0.1844	0.1778	0.1713
5.50	0.2132	0.2106	0.2074	0.2032	0.1982	0.1926	0.1867	0.1804	0.1741	0.1676
5.40	0.2079	0.2054	0.2024	0.1984	0.1937	0.1883	0.1826	0.1766	0.1705	0.1644
5.30	0.2028	0.2004	0.1975	0.1937	0.1891	0.1840	0.1785	0.1727	0.1668	0.1609
5.20	0.1977	0.1954	0.1927	0.1891	0.1847	0.1798	0.1745	0.1685	0.1632	0.1575
5.10	0.1927	0.1906	0.1879	0.1845	0.1803	0.1756	0.1705	0.1651	0.1597	0.1541
5.00	0.1878	0.1858	0.1833	0.1800	0.1760	0.1716	0.1669	0.1614	0.1561	0.1508
4.90	0.1830	0.1811	0.1787	0.1755	0.1717	0.1674	0.1626	0.1577	0.1526	0.1474
4.80	0.1783	0.1764	0.1742	0.1711	0.1675	0.1633	0.1590	0.1540	0.1491	0.1441
4.70	0.1737	0.1719	0.1697	0.1668	0.1633	0.1593	0.1550	0.1504	0.1456	0.1408
4.60	0.1691	0.1674	0.1653	0.1626	0.1592	0.1553	0.1512	0.1467	0.1421	0.1375
4.50	0.1646	0.1629	0.1610	0.1583	0.1551	0.1514	0.1474	0.1431	0.1387	0.1342
4.40	0.1601	0.1586	0.1567	0.1542	0.1511	0.1475	0.1437	0.1396	0.1353	0.1310
4.30	0.1558	0.1543	0.1525	0.1500	0.1471	0.1437	0.1400	0.1360	0.1319	0.1277
4.20	0.1514	0.1500	0.1483	0.1460	0.1431	0.1399	0.1363	0.1325	0.1286	0.1245
4.10	0.1472	0.1458	0.1442	0.1420	0.1392	0.1361	0.1327	0.1290	0.1252	0.1213
4.00	0.1430	0.1417	0.1401	0.1380	0.1354	0.1324	0.1291	0.1256	0.1219	0.1181
3.90	0.1388	0.1376	0.1361	0.1340	0.1316	0.1287	0.1253	0.1221	0.1186	0.1150
3.80	0.1347	0.1335	0.1321	0.1302	0.1278	0.1250	0.1220	0.1187	0.1153	0.1118
3.70	0.1307	0.1295	0.1282	0.1263	0.1240	0.1214	0.1185	0.1153	0.1121	0.1087
3.60	0.1267	0.1256	0.1243	0.1225	0.1203	0.1178	0.1150	0.1120	0.1088	0.1056
3.50	0.1227	0.1217	0.1204	0.1187	0.1166	0.1142	0.1115	0.1086	0.1056	0.1025
3.40	0.1188	0.1178	0.1166	0.1150	0.1130	0.1106	0.1081	0.1053	0.1024	0.9994
3.30	0.1149	0.1140	0.1128	0.1113	0.1093	0.1071	0.1047	0.1020	0.9992	0.9963
3.20	0.1111	0.1102	0.1091	0.1076	0.1058	0.1036	0.1013	0.9987	0.9960	0.9932
3.10	0.1073	0.1064	0.1054	0.1039	0.1022	0.1002	0.9979	0.9954	0.9929	0.9902
3.00	0.1035	0.1027	0.1017	0.1003	0.9986	0.9967	0.9945	0.9922	0.9897	0.9871
2.90	0.9998	0.9990	0.9980	0.9967	0.9951	0.9933	0.9912	0.8890	0.8866	0.8841
2.80	0.9960	0.9953	0.9944	0.9932	0.9916	0.8899	0.8879	0.8857	0.8835	0.8811
2.70	0.9924	0.9917	0.9908	0.8896	0.8882	0.8865	0.8844	0.8825	0.8804	0.8781
2.60	0.9887	0.9880	0.9872	0.8861	0.8847	0.8831	0.8813	0.8794	0.8773	0.8751
2.50	0.9851	0.9845	0.9837	0.8826	0.8813	0.8798	0.8781	0.8762	0.8742	0.8722
2.40	0.9815	0.9814	0.9809	0.8799	0.8779	0.8764	0.8748	0.8730	0.8711	0.8692
2.30	0.9779	0.9774	0.9767	0.8757	0.8745	0.8731	0.8715	0.8699	0.8681	0.8662

2.20	0.0744	0.0743	0.0738	0.0732	0.0723	0.0711	0.0698	0.0684	0.0668	0.0651	0.0633
2.10	0.0709	0.0707	0.0701	0.0697	0.0687	0.0670	0.0666	0.0652	0.0636	0.0620	0.0603
2.00	0.0674	0.0672	0.0669	0.0663	0.0655	0.0645	0.0633	0.0620	0.0605	0.0590	0.0574
1.90	0.0639	0.0630	0.0634	0.0629	0.0621	0.0611	0.0600	0.0588	0.0574	0.0560	0.0545
1.80	0.0604	0.0603	0.0600	0.0595	0.0587	0.0578	0.0568	0.0555	0.0544	0.0530	0.0516
1.70	0.0570	0.0569	0.0566	0.0561	0.0554	0.0546	0.0536	0.0522	0.0513	0.0500	0.0487
1.60	0.0535	0.0534	0.0532	0.0527	0.0521	0.0513	0.0504	0.0492	0.0482	0.0470	0.0458
1.50	0.0501	0.0500	0.0498	0.0493	0.0487	0.0480	0.0472	0.0462	0.0452	0.0441	0.0430
1.40	0.0467	0.0466	0.0464	0.0460	0.0454	0.0448	0.0440	0.0431	0.0421	0.0411	0.0400
1.30	0.0433	0.0432	0.0430	0.0427	0.0422	0.0415	0.0408	0.0400	0.0391	0.0381	0.0371
1.20	0.0399	0.0399	0.0397	0.0393	0.0389	0.0383	0.0376	0.0369	0.0360	0.0352	0.0342
1.10	0.0366	0.0365	0.0363	0.0360	0.0356	0.0351	0.0345	0.0338	0.0330	0.0322	0.0314
1.00	0.0332	0.0332	0.0330	0.0327	0.0323	0.0319	0.0313	0.0307	0.0300	0.0293	0.0285
0.90	0.0299	0.0298	0.0297	0.0294	0.0291	0.0287	0.0282	0.0276	0.0270	0.0263	0.0256
0.80	0.0265	0.0265	0.0263	0.0261	0.0258	0.0255	0.0250	0.0245	0.0240	0.0234	0.0228
0.70	0.0232	0.0232	0.0230	0.0228	0.0226	0.0223	0.0219	0.0214	0.0210	0.0205	0.0199
0.60	0.0199	0.0198	0.0197	0.0196	0.0193	0.0191	0.0187	0.0184	0.0180	0.0175	0.0171
0.50	0.0166	0.0165	0.0164	0.0163	0.0161	0.0159	0.0156	0.0153	0.0150	0.0146	0.0142
0.40	0.0132	0.0132	0.0131	0.0130	0.0129	0.0127	0.0125	0.0122	0.0120	0.0117	0.0114
0.30	0.0099	0.0099	0.0099	0.0098	0.0097	0.0095	0.0094	0.0092	0.0090	0.0088	0.0085
0.20	0.0066	0.0066	0.0066	0.0065	0.0064	0.0063	0.0062	0.0061	0.0060	0.0058	0.0057
0.10	0.0033	0.0033	0.0033	0.0033	0.0032	0.0032	0.0031	0.0031	0.0030	0.0029	0.0028

POTENTIAL DISTRIBUTION ALONG THE AXIS OF HIGHEST FIELD STRENGTH



0.0 0.10E 01 0.20E 01 0.30E 01 0.40E 01 0.50E 01 0.60E 01 0.70E 01 0.80E 01 0.90E 01 0.10E 02  
XMAX = 0.10000E 02 XMIN = 0.10000E 00 YMAX = 0.99666E 00 YMIN = 0.59605E-07

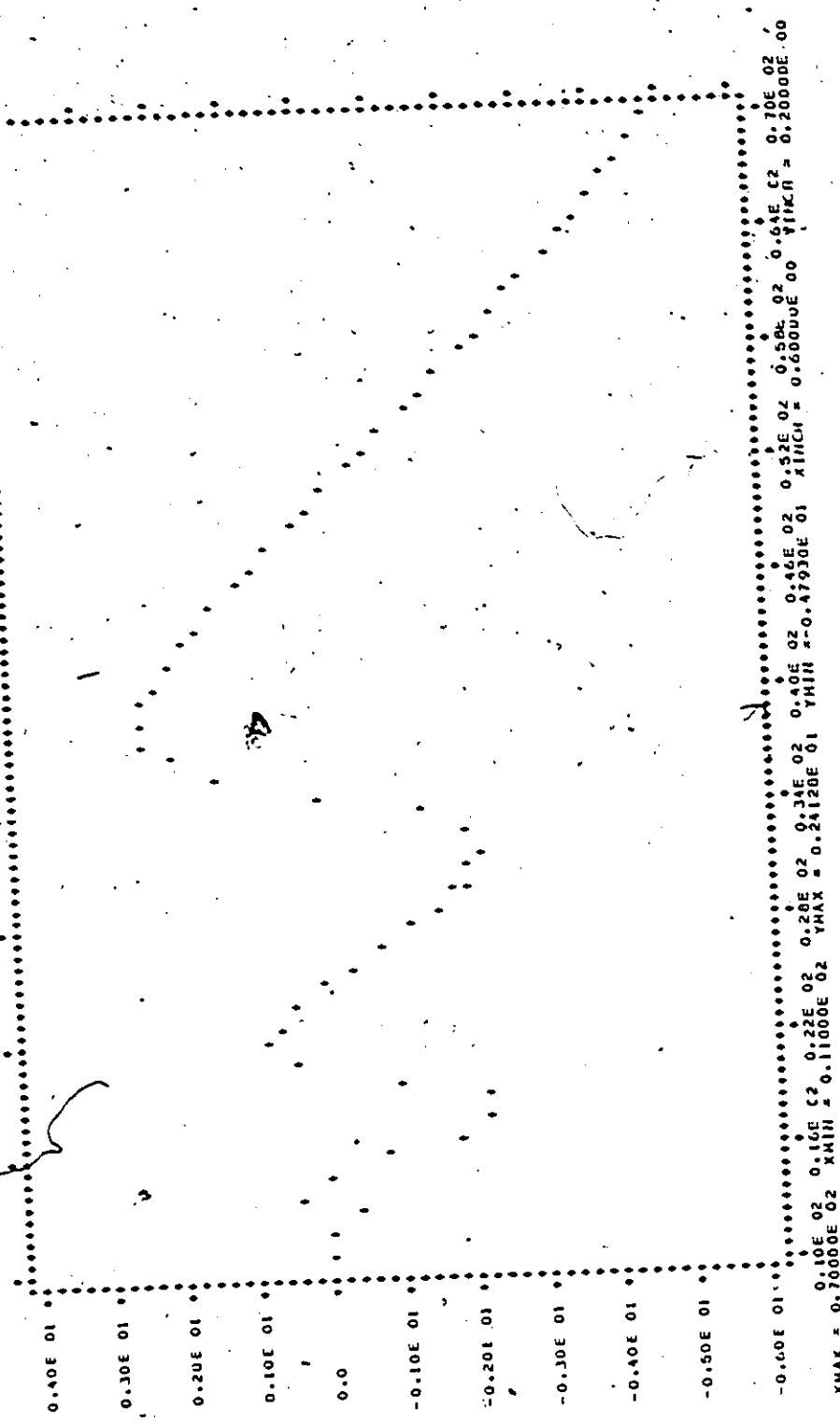


POTENTIAL DISTRIBUTION ON CYLINDRICAL PORTION OF THE BOUNDARY

R = 1.0

ZS	POTENTIAL
11.00	1.0000
12.00	1.0000
13.00	1.0046
14.00	0.9952
15.00	1.0000
16.00	1.0089
17.00	1.0172
18.00	1.0223
19.00	1.0211
20.00	1.0092
21.00	0.9963
22.00	0.9923
23.00	0.9931
24.00	0.9961
25.00	1.0000
26.00	1.0043
27.00	1.0085
28.00	1.0125
29.00	1.0161
30.00	1.0190
31.00	1.0209
32.00	1.0214
33.00	1.0195
34.00	1.0132
35.00	0.9996
36.00	0.9858
37.00	0.9791
38.00	0.9764
39.00	0.9759
40.00	0.9765
41.00	0.9778
42.00	0.9796
43.00	0.9817
44.00	0.9841
45.00	0.9866
46.00	0.9892
47.00	0.9918

POTENTIAL DISTRIBUTION ALONG THE CYLINDRICAL PART OF THE JUNCTION



0.10E 02  
0.10E 02  
0.14E 02  
0.18E 02  
0.22E 02  
0.26E 02  
0.30E 02  
0.34E 02  
0.38E 02  
0.42E 02  
0.46E 02  
0.50E 02  
0.54E 02  
0.58E 02  
0.62E 02  
0.66E 02  
0.70E 02  
XMAX = 0.7000E 02  
XMIN = 0.1100E 02  
YMAX = 0.2412E 01  
YMIN = -0.4793E 01  
ZMAX = 0.6000E 00  
ZMIN = 0.2000E 00

POTENTIAL DISTRIBUTION ON SPHERICAL PORTION OF THE BOUNDARY

ZS	R	POTENTIAL
10.00	0.0735	1.0000
10.01	0.1534	1.0000
10.03	0.2334	1.0000
10.05	0.3090	1.0000
10.08	0.3827	1.0000
10.11	0.4540	1.0000
10.15	0.5225	1.0000
10.19	0.5878	1.0000
10.24	0.6494	1.0000
10.29	0.7071	1.0000
10.35	0.7604	1.0000
10.41	0.8090	0.9999
10.48	0.8526	0.9999
10.55	0.8910	0.9999
10.62	0.9239	0.9998
10.69	0.9511	0.9998
10.77	0.9724	0.9997
10.84	0.9877	0.9997
10.92	0.9969	0.9998
11.00	1.0000	1.0000

POTENTIAL DISTRIBUTION ALONG THE SPHERICAL PART OF THE BOUNDARY

0.29E-01  
0.26E-01  
0.23E-01  
0.20E-01  
0.17E-01  
0.14E-01  
0.11E-01  
0.08E-02  
0.05E-02  
0.02E-02  
-0.00E-03  
XMAX = 0.10000E+01 XMIN = 0.78459E-01 YMAX = 0.27966E-01 YMIN = 0.0  
ZMAX = 0.30E-01 ZMIN = 0.00E+00 X1MAX = 0.63E+00 X1MIN = 0.0  
X2MAX = 0.73E+00 X2MIN = 0.10000E+01 Y1MAX = 0.93E+00 Y1MIN = 0.10E+01  
Y2MAX = 0.93E+00 Y2MIN = 0.00E+00 Z1MAX = 0.00E+00 Z1MIN = 0.00E+00  
Z2MAX = 0.00E+00 Z2MIN = 0.00E+00

## APPENDIX 2

### COMPUTER PROGRAM FOR THE POTENTIAL DISTRIBUTION OF A ROD-PLANE GAP USING THE OPTIMIZED CHARGE SIMULATION TECHNIQUE.

The following program represents a solution of equation 3.9 for nine semi-infinite line charges and one point charge. The variables of optimization are the positions of the charges  $(r_i, z_i)$  and their values  $Q_i$  ( $i=1,2,\dots,10$ ). The constraints imposed on the variables are given in Table 3.2.

The initial values of the variables are chosen within their corresponding constraints. In this case due to the relatively slow convergence of Rosenbroks optimization subroutine, the initial values used are the final values of the variables from a previous run. The overall computer time (on a IBM 360 (fast core) is approximately 70 min, and it is typical for optimization of a function with large number of variables using Rosenbroks optimization technique.

Note: As an addition to references provided in the main text, it should be noted that, Anis et-al (77) have recently presented a modified charge simulation technique by applying multiple linear regression to the number and position points  $(r, z)$  on the boundary surface, against the number of the fictitious charges. This is a quasi-optimization approach and like the method presented here it represents an improvement over the conventional charge simulation technique.



```

57 RR = 0.000
58 JJ=1
59 102 ZS = GG
60 II=1
61 DO 101 I = 1,5
62 YY(II)=ZS
63 J = II+I
64 POT(I) = XS(I)*DLJG((XS(J)+ZS+DSQRT(RR+(XS(J)+ZS)*(XS(J)+ZS)))/
1(XS(J)-ZS+DSCRT(RR+(XS(J)-ZS)*(XS(J)-ZS))))
65 101 CONTINUE
66 POT(10) = XS(10)*(1.000/DSQRT(RR+(XS(11)-ZS)*(XS(11)-ZS)) -
21.000/DSQRT(RR+(XS(11)+ZS)*(XS(11)+ZS)))
67 VTOTAL = C.000
68 DO 103 K = 1,10
69 VTOTAL = VTOTAL+POT(K)
70 103 CONTINUE
71 VOLT(II,JJ) = VTOTAL
72 Z1 = ZS-61.000
73 IF (F-Z1) 200,200,201
74 201 CONTINUE
75 IF(ZS-GG) 212,212,213
76 212 ZS = ZS-GG/100.000
77 II = II+1
78 IF(II-100) 105,105,231
79 213 CONTINUE
80 ZS = ZS+1.000
81 II = II+1
82 GO TO 105
83 231 CONTINUE
84 IF(R-5.000) 202,203,203
85 202 CONTINUE
86 R = R*.500
87 RR = R*R
88 JJ = JJ+1
89 GO TO 102
90 203 CONTINUE
C
91 WRITE (6,106)
92 106 FORMAT ('1',25X,4SHPOTENTIAL DISTRIBUTION IN INTER-ELECTRODE REGION
1N //,4X,5HZ / R,5X,3
1H0.0,8X,3H0.5,8X,3H1.0,8X,3H1.5,8X,3H2.0,8X,3H2.5, 8X,3H3.0,8X,3H3
2.5,8X,3H4.0,8X,3H4.5,8X,3H5.0)
93 WRITE (6,107) (YY(II),(VOLT(II,JJ),JJ=1,11),II=1,100)
94 107 FORMAT ('0',F7.2, 11F11.4)
95 DO 403 II = 1,100
96 VALT(II,1) = VOLT(II,1)
97 XCO(II) = YY(II)
98 YCO(II) = 1.000-VALT(II,1)
99 403 CONTINUE
100 WRITE(6,556)
101 596 FORMAT ('1',25X,'POTENTIAL DISTRIBUTION ALONG THE AXIS OF HIGHEST F
1IELD STRENGTH')
102 CALL PLOT 3(XCO,YCO,F00)
103 500 CONTINUE
C
C C COMPUTE POTENTIAL DISTRIBUTION ON CYLINDRICAL PORTION OF BOUNDARY
104 R = 1.000
105 RR = 1.000
106 JJ = 1
107 ZS = F
108 II = 1
109 GO TO 105
110 200 CONTINUE
C
C C WRITE POTENTIAL DISTRIBUTION ON CYLINDRICAL PORTION OF BOUNDARY
111 WRITE (6,206)
112 206 FORMAT ('1',25X,'POTENTIAL DISTRIBUTION ON CYLINDRICAL PORTION OF
1 THE BOUNDARY',//,53X,'R = 1.0',//,53X,'ZS',7X,'POTENTIAL')
113 WRITE (6,207) (YY(II),VOLT(II,1),II=1,60)
114 207 FORMAT ('0',50X,F7.2,F11.4)
115 DO 401 II = 1,60
116 VALT(II,1) = VOLT(II,1)
117 XCCI(II) = YY(II)
118 YCCI(II) = (1.000-VALT(II,1))*100.000
119 401 CONTINUE
C
C C COMPUTE ZS AND R COORDINATES OF SPHERICAL PORTION OF BOUNDARY

```

```

120 WRITE(6,18C1)
121 1801 FORMAT('1',30X,'POTENTIAL DISTRIBUTION ALONG THE CYLINDRICAL PART
122 OF THE BOUNDARY')
123 CALL PLOT 3(XCOI,YCOI,50)
124 JJ = 1
125 II = 1
126 DO 259 L = 1,20
127 T1 = 3.1415926/(2.000*20.000)
128 TS = T1*L
129 R = DSIN(TS)
130 ZS = GG+(1.000-DCOS(TS))
131 YY(II) = ZS
132 XX(II) = R
133 RR = R*R

```

C  
C  
C

COMPUTE POTENTIAL DISTRIBUTION ON SPHERICAL PORTION OF BOUNDARY

```

133 DO 258 I = 1,9
134 J = II+I
135 POT(I) = XS(I)*DLOG((XS(J)+ZS+DSCRRT(RR+(XS(J)+ZS)*(XS(J)+ZS)))/
1 (XS(J)-ZS+DSCRRT(RR+(XS(J)-ZS)*(XS(J)-ZS))))
136 258 CONTINUE
137 POT(10) = -XS(10)*(1.000/DSCRRT(RR+(XS(11)-ZS)*(XS(11)-ZS)) -
21.000/DSCRRT(RR+(XS(11)+ZS)*(XS(11)+ZS)))
138 VTCTAL = 0.000
139 DO 109 K = 1,10
140 VTOTAL = VTCTAL+POT(K)
141 109 CONTINUE
142 VOLT(II,JJJ) = VTOTAL
143 II = II+1
144 259 CONTINUE

```

C  
C  
C

WRITE POTENTIAL DISTRIBUTION ON SPHERICAL PORTION OF BOUNDARY

```

145 WRITE (6,320)
146 320 FORMAT ('1',40X,'POTENTIAL DISTRIBUTION ON SPHERICAL PORTION OF TH
1E BOUNDARY',//,50X,'ZS',9X,'R',7X,'POTENTIAL')
147 WRITE (6,321) (YY(II),XX(II),VOLT(II,1),II=1,20)
148 321 FORMAT ('0',47X,F6.2,F11.4,F11.4)
149 DO 402 II = 1,20
150 VALT(II,1) = VOLT(II,1)
151 YCOJ(II) = (1.000-VALT(II,1))*100.000
152 XCCJ(II) = XX(II)
153 402 CONTINUE
154 WRITE(6,18C2)
155 1802 FORMAT('1',30X,'POTENTIAL DISTRIBUTION ALONG THE SPHERICAL PART OF
1 THE BOUNDARY')
156 CALL PLOT 3(XCOJ,YCCJ,20)
157 STOP
158 END

```



SUBROUTINE SUB REPRESENTS THE OBJECTIVE FUNCTION 'U', THAT IS TO BE MINIMIZED. U IN THIS CASE IS THE ACCUMULATIVE SQUARE ERROR ALONG 15 POINTS ON THE SPHERICAL PART OF THE ELECTRODE, AND 50 POINTS ALONG THE CYLINDRICAL PART.

CCCCC

```

159 SUBROUTINE SLB(NVAR,X,NFCN,U,G,H)
160 DOUBLE PRECISION X(20),FX1,FX2,FX3,FX4,T,T1,DSIN,DCOS,R,Z,FX5
161 DOUBLE PRECISION G(20),H(20),U,POT(99),TT(5)
162 DOUBLE PRECISION DSORT,FX6,CLOG,P,CABS,F,ZZ(7),GG
163 J = 0
164 FX5 = 0.000
165 FX4 = 0.000
166 FX2 = 0.000
167 GG = 10.000
168 F = GG+1.000
169 X(11) = F
170 X(12) = F
171 II = 1
172 T = 0.0100
173 1 R = DSIN(T)
174 Z = F-DCOS(T)
175 DO 5 I = 1,5
176 J = I+11
177 FX1 = X(I)*DLOG((X(J)+Z+DSORT(R*R+(X(J)+Z)*(X(J)+Z)))/
1 (X(J)-Z+DSORT(R*R+(X(J)-Z)*(X(J)-Z))))
178 7 FX2 = FX2+FX1
179 5 CONTINUE
180 FX5 = X(10)*(1.000/DSORT(R*R+(X(11)-Z)*(X(11)-Z)) -
11.000/DSORT(R*R+(X(11)+Z)*(X(11)+Z)))
181 FX2 = FX2+FX5
182 POT(11) = FX2
183 FX3 = (1.000-FX2)*(1.000-FX2)
184 FX4 = FX4+FX3
185 T1 = (180.000/3.1415900)*T
186 FX2 = 0.0000000
187 II = II+1
188 T = T+0.100
189 IF(T-1.500) 1,1,6
190 6 CONTINUE
191 FX2 = 0.000
192 R = 1.000
193 K = 1
194 Z = F
195 20 DO 25 I = 1,5
196 J = I+11
197 FX1 = X(I)*DLOG((X(J)+Z+DSORT(R*R+(X(J)+Z)*(X(J)+Z)))/
1 (X(J)-Z+DSORT(R*R+(X(J)-Z)*(X(J)-Z))))
198 25 CONTINUE
199 FX5 = X(10)*(1.000/DSORT(R*R+(X(11)-Z)*(X(11)-Z)) -
200 11.000/DSORT(R*R+(X(11)+Z)*(X(11)+Z)))
201 FX2 = FX2+FX5
202 POT(K) = FX2
203 FX3 = (1.000-FX2)*(1.000-FX2)
204 FX6 = FX6+FX3
205 K = K+1
206 FX2 = 0.000
207 IF(Z-(F+2.000)) 30,40,40
208 30 Z = Z+0.500
209 GOTO 20
210 40 Z = Z+1.000
211 IF(Z-(GG+50.000)) 20,20,50
212 50 CONTINUE
213 U = FX4 + FX6
214 RETURN
215 END

```

SUBROUTINE CLIMBD(NVR,X, NON,U,NFIG,S,LS,KWRT,G,H,INDEX,NTRIPV,FCN)

275

FUNCTIONAL OPTIMIZATION BY ROSENBROCK'S METHOD OF HILL-CLIMBING

THE ARRAY S MUST BE DIMENSIONED AT LEAST NVAR\*(NVAR+5)+NCON

KWRT SET AS FOLLOWS FOR OUTPUTS - 2 OUTPUTS SUPPRESSED  
1 AT START AND END ONLY  
0 AT END OF EACH STAGE  
-N AFTER EVERY N TRIALS

INDEX POSITIVE FOR SIGNIFICANT FIGURE CONVERGENCE CRITERION  
1 NO CONSTRAINTS ON INDEPENDENT VARIABLES - SETS G,H LARGE  
2 FINITE CONSTRAINTS ON INDEP. VARIABLES SUPPLIED ON ENTRY  
3 FOR RE-ENTRY WITHOUT INITIALIZATION  
4 AS IN 3 BUT KTRIAL = 0  
INDEX NEGATIVE OF ABOVE FOR EXIT ONLY AFTER SPECIFIED TRIALS

IMPLICIT REAL\*8(A-H,O-Z)  
DIMENSION E(3),G(NON),H(NON),X(NON),S(LS)

INITIALIZATION  
A LINE COUNTER IS SET SO THAT HEADINGS WILL BE PRINTED AT THE HEAD  
OF EVERY PAGE.

LINES=60  
NCCN=NON-IAES(NVR)  
NVAR=IAES(NVR)  
SGN=NVR/NVAR  
NWRT=IAES(K\*RT)  
NTCT=NVAR+NCCN  
N2=NVAR\*(NVAR+1)  
N3=N2+NTCT  
N4=N3+NVAR  
N5=N4+NVAR  
NTRIAL=NTRIPV\*NVAR  
NCCNS=NTCT  
NT=NVAR\*(NVAR+5)+NCON  
NEND=0  
CONV=.500\*(.100)\*\*NFIG  
IND=IAES(INDEX)  
THE COMPROMISE VALUES OF THE 3 HILL-CLIMBING PARAMETERS FOLLOW  
THE COMPROMISE VALUES OF THE 3 HILL-CLIMBING PARAMETERS FOLLOW  
ALPHA AND BETA ARE FORWARD AND BACKWARD STEPPING PARAMETERS.

ALPHA=2.00  
BETA=.500  
FAIL=1.00  
CLIFF=.000100  
IND1=0  
GOTO(1,2,150,5),IND  
KTRIAL=0  
IND1=1  
MWRT=NWRT  
GOTO39  
DO2I=1,NVAR  
NCCNS=NCCNS-1  
G(1)=-1.00+7E  
T(1)=-G(1)  
DO4I=1,NT  
S(1)=0.00  
IF(KWRT.GT.1)GOTO11  
IF(SGN)10,7,7  
WRITE(6,101)NVAR,NCCNS  
GOTO11  
WRITE(6,102)NVAR,NCCNS  
FORMAT(///EX,'MAXIMUM OF FUNCTION OF ',I3,' VARIABLES WITH ',I3,'  
\* CCNSTRANTS')  
102 FORMAT(///SX,'MINIMUM OF FUNCTION OF ',I3,' VARIABLES WITH ',I3,'  
\* CCNSTRANTS')  
11 B(2)=0.00  
E(3)=C.D0  
KTRIAL=0  
MWRT=NWRT  
DO15I=1,NVAR  
IF(G(I)-F(I))13,14,13  
S(I)=.100  
NI=(NVAR+1)\*I  
S(NI)=1.00  
BIG=CABS(X(1))  
IF(NVAR.EC.1)GOTO185  
DO18I=2,NVAR

280  
281

282  
283  
284  
285  
286  
287  
288  
289  
290  
291  
292  
293  
294  
295  
296  
297

298  
299  
300  
301  
302  
303  
304  
305  
306  
307  
308  
309  
310  
311  
312  
313  
314  
315  
316  
317  
318  
319

320

321  
322  
323  
324  
325  
326  
327  
328  
329  
330  
331  
332

10  
101  
102  
11  
13  
14  
15  
16

```

333 ABX=DABS(X(1))
334 IF(ABX.GT.EIG)BIG=ABX
335 18 CONTINUE
336 185 BIG=10.DO*(ALPHA-1.DO)*BIG+1.DO
337 KCCNV=0
338 X0=1.DO
339 19 IF(X0.GT.BIG)GOTO21
340 20 KCCNV=KCCNV+1
341 X0=ALPHA*X0
342 GOTO19

C
C CHECK INITIAL VALUES WRT. CONSTRAINTS
343 21 IF(NCON.LT.1)GOTO225
344 215 NV1=NVAR+1
345 NCI=NVAR+NCCN
346 DD22I=NV1,NC1
347 22 X(I)=.5DO*(G(I)+H(I))
348 225 NG=0
349 DD38 I=1,NTCT
350 IF(H(I)-G(I))35.25.25
351 25 IF(X(I)-G(I))27.26.26
352 26 IF(H(I)-X(I))28.38.38
353 27 IF(DABS(G(I))-1.DO)24.24.23
354 23 X(I)=G(I)+CLIFF*DABS(G(I))
355 GOTO30
356 24 X(I)=CLIFF
357 GOTO30
358 28 IF(DABS(H(I)-1.DO))37.37.36
359 36 X(I)=H(I)-CLIFF*DABS(H(I))
360 GOTO30
361 37 X(I)=CLIFF
362 30 IF(NG.NE.0)GOTO22
363 31 WRITE(6,105)
364 105 FORMAT(/SX,'INITIAL VALUES MUST NOT LIE OUTSIDE OR ON CONSTRAINTS'
*//)
365 NG=1
366 32 IF(G(I)-H(I))33.34.33
367 33 WRITE(6,106)I,X(I)
368 106 FORMAT(10X,'VARIABLE',I4,' TAKEN AS ',G16.7)
369 GOTO38
370 34 X(I)=G(I)
371 WRITE(6,107)I,X(I)
372 107 FORMAT(10X,'VARIABLE',I4,' CONSTRAINED TO BE ',G16.7)
373 GOTO38
374 35 WRITE(6,108)I,G(I),H(I)
375 108 FORMAT(/SX,'FOR VARIABLE',I4,' LOWER LIMIT',E15.8,' AND UPPER',
*LIMIT',E15.8,' HAD TO BE INTERCHANGED'/)
376 G1=G(I)
377 G(I)=H(I)
378 H(I)=G1
379 GOTO25
380 38 CONTINUE
381 U1=C.DO
382 IF(NTRIAL.EQ.C)GOTO26
383 39 CONTINUE
384 CALLFCN(NVAR,X,NCON,U1,G,H)
385 U1=SGN*U1
386 DD40 I=1,NTCT
387 N2I=N2+I
388 40 S(N2I)=U1
389 IF(KWRT.EQ.2)GOTO90
390 GOTO82

C
C BEGINNING OF HILL-CLIMBING
C
C STAGE OUTPUTS OR END OF CALCULATION
391 80 IF(KWRT-1)22.81.23
392 305 IF(KTRIAL.EQ.3820)GOTO871
393 81 IF(KTRIAL.EQ.0)GOTO22
394 IF(NEND.NE.1)GOTO90
395 82 CALLFCN(NVAR,X,NCON,B(1),G,H)
396 IF(LINES.LT.60)GOTO999
397 871 CONTINUE
398 PRINT99
399 99 FORMAT('1'//T06,'NO. OF CURRENT TRIAL LAST SUCCESSFUL TOTAL DIS
*TANCE CHANGE IN DIRECTN'/T6,'TRIALS VALUE OF FUNCTIONAL VAL
*UE MCVED OF MOTION'/T14,'IND VARIABLES',T47,'DURING
* STAGE FROM LAST STAGE'//)

```

```

402 110  FORMAT(111.16X.3G16.7/(11X.G16.7))
403      IF(KTRIAL.EQ.3820)GOTO66
404      LINES=LINES+NVAR+1
405      IF(KWRT.EC.1)GOTO88
406 83    IF(KTRIAL.LT.NTRIAL)GOTO88
407 86    CALLFCN(NVAR,X.NCON,B(1),G,H)
408      U=B(1)
409      RETURN
410 88    IF(NEND.LT.1)GOTO90
411 89    IF(KWRT.GE.2)GOTO86
412 91    WRITE(6,113)NFIG
413 113   FORMAT(/5X,'CONVERGENCE TO',14,' SIGNIFICANT FIGURES REACHED IN
      *ALL INDEPENDENT VARIABLES.*/)
414 87    GOTO86
      C
      C  BEGINNING OF STAGE
      C
      C  FORWARD STEP OF VARIABLES
415 90    IF(IND1.EC.1)GOTO93
416 97    DO92J=1,NVAR
417      N3J=N3+J
418      N5J=N5+J
419      S(N3J)=0.00
420 92    S(N5J)=0.00
421 93    JS=1
422      IND1=0
423      NEND=0
424 94    DO96 I=1,NVAR
425      IF(G(I)-H(I))95,96,95
426 95    NI=NVAR*I+JS
427      X(I)=S(NI)*S(JS)+X(I)
428 96    CONTINUE
      C
      C  FUNCTION EVALUATION
429      KTRIAL=KTRIAL+1
430      CALLFCN(NVAR,X.NCON,U2,G,H)
431      IF(KTRIAL.EC.3820)GOTO871
432      U2=SGN*U2
      C
      C  CHECK CONSTRAINTS
433      DO128 I=1,NTOT
434      N2 I=N2+I
435      IF(G(I)-H(I))125,128,125
436 125   IF(U1-U2)126,126,145
437 126   IF(X(I)-G(I))145,145,127
438 127   IF(H(I)-X(I))145,145,128
439 128   CONTINUE
440      DO135 I=1,NTOT
441      N2 I=N2+I
442      IF(G(I)-H(I))120,134,120
443 120   IF(DABS(G(I))-1.00)121,121,122
444 121   SN1=CLIFF
445      GOTO123
446 122   SN1=CLIFF*CAES(G(I))
447 123   IF(X(I)-(G(I)+SN1))129,130,130
448 129   GO=(G(I)+SN1-X(I))/SN1
449      GOTO132
450 130   IF(DABS(H(I)-1.00))136,136,137
451 136   SN1=CLIFF
452      GOTO138
453 137   SN1=CLIFF*CAES(H(I))
454 138   IF(H(I)-SN1-X(I))131,133,133
455 131   GO=(X(I)-H(I)+SN1)/SN1
456 132   HO=U2-S(N2 I)
457      U2=U2+GO*HC*((4.00-2.00*GO)*GO-3.00)
458      IF(U1-U2)135,135,145
459 133   S(N2 I)=U1
460      GOTO135
461 134   S(I)=0.00
462 135   CONTINUE
463      IF(G(JS)-H(JS))140,142,140
464 140   N4J=N4+JS
465      N5J=N5+JS
466      IF(S(N5J)-.500)141,142,142
467 141   S(N4J)=0.00
468      S(N5J)=1.00
469 142   N3J=N3+JS
470      S(N3J)=S(N3J)+S(JS)
471      U1=U2

```

```

473      GOTO150
C
C      UNDO UNSUCCESSFUL STEP AND REVERSE DIRECTION WITH REDUCED STEP
474      145  DO148I=1,NVAR
475          IF(G(I)-H(I))146,148,146
476      146  NI=NVAR*I+JS
477          X(I)=X(I)-S(NI)*S(JS)
478      148  CONTINUE
479          S(JS)=-BETA*S(JS)
480          N4J=N4+JS
481          S(N4J)=S(N4J)+1.00
C
C      CHECK FOR STAGE OPTIMUM IN EVERY DIRECTION
482      150  IF(KTRIAL.GE.NTRIAL)GOTO30
483      151  DO155I=1,NVAR
484          IF(G(I)-H(I))152,155,152
485      152  N4I=N4+I
486          NSI=NS+I
487          IF(S(N4I)+.500-FAIL)150,153,153
488      153  IF(S(NSI)-.500)160,155,155
489      155  CONTINUE
490          GOTO41
491      160  JS=JS+1
492          IF(JS.GT.NVAR)GOTO165
493      164  IF(KWRT.GE.0)GOTO170
494      165  IF(KTRIAL.LT.MWRT)GOTO170
C
C      INTERMEDIATE FORCED OUTPUTS
495      166  MWRT=MWRT+N*RT
496          UP=SGN*U1
497          *WRITE(6,115)KTRIAL,UP,(X(I),S(I),I=1,NVAR)
498      115  FORMAT(31X,110.16X,G16.7/(11X,G16.7,15X,G16.7))
499      170  IF(JS.LE.NVAR)GOTO94
500          GOTO93
501      169  IF(KTRIAL.LT.KCCNV)GOTO164
502      171  IF(INDEX.LE.C)GOTO164
C
C      CONVERGENCE TESTS
503      172  DO180I=1,NVAR
504          DX=0.00
505          DO173K=1,NVAR
506          NI=NVAR*I+K
507      173  DX=DX+S(NI)*S(K)
508          IF(0ABS(X(I))-1.00)174,174,175
C
C      IF RELATIVE CONVERGENCE TESTS ARE DESIRED FOR LESS THAN UNITY
C      MAGNITUDES THE PREVIOUS STATEMENT SHOULD BE CHANGED TO SUIT USER'S
C      NEED. FOR EXAMPLE IF(ABS(X(I))) 175,174,175 MAY BE USED
C      BUT UNDERFLOWS MAY OCCUR IF MAGNITUDES ARE VERY SMALL
509      174  CRIT=CABS(CX)
510          GOTO176
511      175  CRIT=0ABS(CX/X(I))
512      176  IF(CRIT.GE.CCNV)GOTO164
513      180  CONTINUE
514          NEND=1
515          GOTO80
516      306  IF(KTRIAL.EQ.3820)GOTO271
C
C      TRANSFORMATION OF COORDINATES AT END OF STAGE BY GRAM-SCHMIDT. ORTH
517      41  DO45I=1,NVAR
518          NN=NVAR*I+NVAR
519          S(NN)=S(N4)*S(NN)
520          DO45J=2,NVAR
521          NJ=NVAR-J+1
522          N3J=N3+NJ
523          NI=NVAR*I+NJ
524      45  S(NI)=S(N3J)*S(NI)+S(NI+1)
525          IF(NVAR.EQ.1)S(3)=0.000
526      47  DO50J=2,3
527          E(J)=0.00
528          DO49I=1,NVAR
529          NI=NVAR*I+J-1
530      49  B(J)=S(NI)**2+B(J)
531      50  B(J)=OSQRT(E(J))
532          E(3)=B(3)/E(2)
533          J=1
534          K=1
535      57  IF(K.EQ.J)GOTO68
536      58  B(1)=0.00
537          DO60I=1,NVAR

```

553  
5540  
5541  
5542  
5544  
5545  
5546  
5547  
5548  
5549  
5550  
5551  
5552  
5553  
5554  
5555  
5556  
5557  
5558

```
60 NK=NI-K  
B(1)=B(1)+S(NI)*S(NK)  
0065 I=1,NVAR  
NI=NVAR*I+J  
65 NK=NI-K  
S(NI)=-S(NK)*E(1)+S(NI)  
K=K+1  
GOTO57  
68 E(1)=0.00  
0070 I=1,NVAR  
ZI=NVAR*I+J  
70 B(1)=B(1)+S(NI)**2  
B(1)=DSQRT(E(1))  
0075 I=1,NVAR  
NI=NVAR*I+J  
75 S(NI)=S(NI)/E(1)  
J=J+1  
IF(NVAR.GE.J)GOTO56  
GOTO80  
END
```

MINIMUM OF FUNCTION OF 20 VARIABLES WITH 20 CONSTRAINTS

NC. OF TRIALS	CURRENT TRIAL VALUE OF IND VARIABLES	LAST SUCCESSFUL FUNCTIONAL VALUE	TOTAL DISTANCE MOVED DURING STAGE	CHANGE IN DIRECTN OF MOTION FROM LAST STAGE
0		4.319623	0.0000000	0.0000000
	13.46400			
	-18.09600			
	1.952700			
	3.549000			
	-0.6850000			
	-0.31700000-C1			
	-0.15300000-C1			
	-0.41600000-C1			
	-0.90600000-C2			
	-0.79000000-C1			
	11.00000			
	11.00000			
	11.11900			
	11.45700			
	11.48700			
	12.17600			
	12.93700			
	27.56000			
	11.01700			
	58.46900			

NC. OF TRIALS	CURRENT TRIAL VALUE OF IND VARIABLES	LAST SUCCESSFUL FUNCTIONAL VALUE	TOTAL DISTANCE MOVED DURING STAGE	CHANGE IN DIRECTN OF MOTION FROM LAST STAGE
3820		C.56849400-C6	0.2688220-01	0.1133980
	13.47005			
	-18.09311			
	1.954576			
	3.542860			
	-0.6839622			
	-0.31961660-C1			
	-0.1747350-C1			
	-0.39123600-C1			
	-0.54003720-C2			
	0.2307157			
	11.00000			
	11.00000			
	11.10970			
	11.38584			
	11.49070			
	12.19665			
	24.47829			
	47.16338			
	11.01959			
	58.97390			

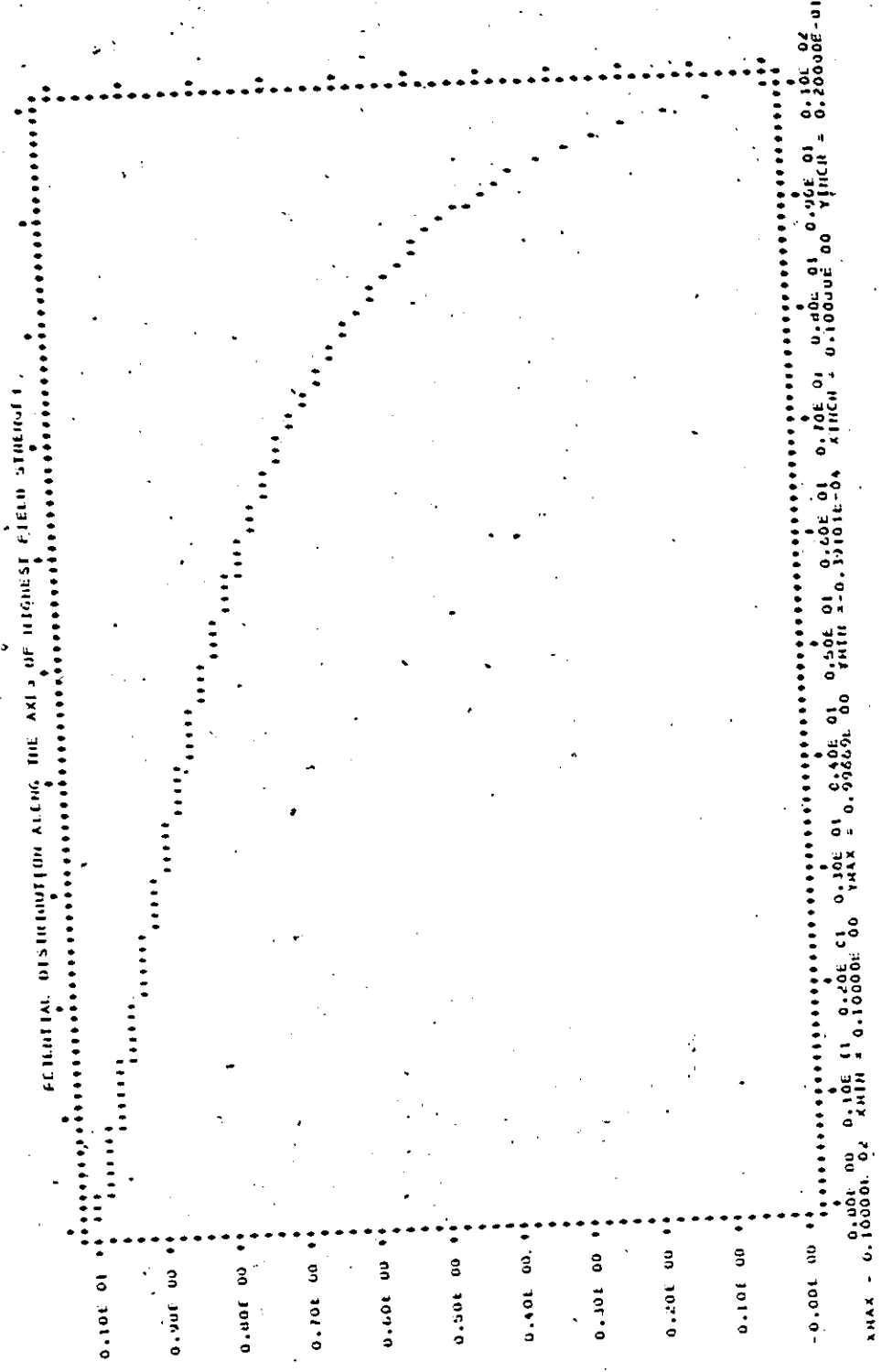
POTENTIAL DISTRIBUTION IN ILLUM-ELECTRODE REGION

Z / H	0.0	0.5	1.0	1.5	2.0	2.5	3.0	3.5	4.0	4.5	5.0
10.00	1.0000	0.9131	0.7654	0.6495	0.5671	0.5062	0.4590	0.4210	0.3895	0.3628	0.3397
9.90	0.9230	0.8374	0.7155	0.6323	0.5555	0.4976	0.4522	0.4153	0.3846	0.3580	0.3359
9.80	0.8601	0.7663	0.7069	0.6151	0.5439	0.4890	0.4453	0.4096	0.3797	0.3542	0.3321
9.70	0.8048	0.7247	0.6758	0.5902	0.5321	0.4801	0.4384	0.4039	0.3748	0.3499	0.3282
9.60	0.7590	0.7250	0.6542	0.5816	0.5207	0.4715	0.4314	0.3961	0.3699	0.3456	0.3244
9.50	0.7181	0.6969	0.6300	0.5653	0.5092	0.4628	0.4244	0.3923	0.3649	0.3412	0.3204
9.40	0.6819	0.6554	0.6072	0.5455	0.4948	0.4541	0.4174	0.3869	0.3599	0.3360	0.3165
9.30	0.6456	0.6207	0.5856	0.5342	0.4865	0.4454	0.4104	0.3800	0.3548	0.3314	0.3126
9.20	0.6205	0.6045	0.5656	0.5154	0.4724	0.4360	0.4035	0.3747	0.3498	0.3280	0.3086
9.10	0.5942	0.5805	0.5465	0.5050	0.4645	0.4292	0.3965	0.3669	0.3448	0.3235	0.3047
9.00	0.5701	0.5583	0.5245	0.4912	0.4539	0.4197	0.3896	0.3630	0.3397	0.3191	0.3007
8.90	0.5481	0.5370	0.5115	0.4778	0.4434	0.4114	0.3827	0.3572	0.3347	0.3146	0.2968
8.80	0.5277	0.5168	0.4955	0.4650	0.4332	0.4031	0.3750	0.3500	0.3296	0.3102	0.2928
8.70	0.5086	0.5010	0.4802	0.4526	0.4232	0.3950	0.3690	0.3450	0.3246	0.3050	0.2888
8.60	0.4913	0.4843	0.4658	0.4406	0.4134	0.3869	0.3621	0.3399	0.3196	0.3013	0.2858
8.50	0.4749	0.4687	0.4520	0.4291	0.4039	0.3790	0.3556	0.3341	0.3146	0.2969	0.2808
8.40	0.4595	0.4540	0.4389	0.4180	0.3947	0.3713	0.3490	0.3285	0.3096	0.2925	0.2769
8.30	0.4451	0.4401	0.4265	0.4073	0.3856	0.3636	0.3425	0.3220	0.3047	0.2881	0.2729
8.20	0.4314	0.4269	0.4146	0.3970	0.3760	0.3561	0.3361	0.3172	0.2997	0.2837	0.2689
8.10	0.4185	0.4144	0.4032	0.3870	0.3682	0.3488	0.3297	0.3117	0.2948	0.2793	0.2650
8.00	0.4062	0.4025	0.3923	0.3773	0.3599	0.3415	0.3234	0.3062	0.2900	0.2749	0.2610
7.90	0.3946	0.3912	0.3818	0.3680	0.3517	0.3344	0.3173	0.3007	0.2851	0.2706	0.2572
7.80	0.3835	0.3804	0.3718	0.3590	0.3430	0.3257	0.3085	0.2923	0.2770	0.2620	0.2492
7.70	0.3729	0.3701	0.3621	0.3503	0.3360	0.3207	0.3051	0.2900	0.2756	0.2620	0.2492
7.60	0.3627	0.3602	0.3528	0.3418	0.3285	0.3140	0.2992	0.2847	0.2708	0.2574	0.2445
7.50	0.3530	0.3506	0.3438	0.3336	0.3211	0.3074	0.2934	0.2795	0.2661	0.2534	0.2415
7.40	0.3437	0.3415	0.3352	0.3256	0.3139	0.3010	0.2876	0.2743	0.2615	0.2492	0.2376
7.30	0.3347	0.3327	0.3260	0.3179	0.3069	0.2947	0.2819	0.2692	0.2569	0.2450	0.2337
7.20	0.3261	0.3242	0.3187	0.3104	0.3000	0.2885	0.2763	0.2642	0.2521	0.2408	0.2298
7.10	0.3178	0.3160	0.3110	0.3024	0.2913	0.2804	0.2708	0.2602	0.2497	0.2392	0.2293
7.00	0.3097	0.3081	0.3033	0.2960	0.2869	0.2784	0.2705	0.2620	0.2544	0.2468	0.2395
6.90	0.3019	0.3004	0.2960	0.2891	0.2804	0.2728	0.2654	0.2580	0.2514	0.2444	0.2378
6.80	0.2944	0.2930	0.2888	0.2823	0.2742	0.2668	0.2598	0.2528	0.2464	0.2398	0.2331
6.70	0.2871	0.2858	0.2819	0.2750	0.2680	0.2604	0.2536	0.2466	0.2404	0.2338	0.2273
6.60	0.2800	0.2788	0.2751	0.2682	0.2620	0.2546	0.2484	0.2414	0.2352	0.2286	0.2223
6.50	0.2732	0.2720	0.2685	0.2631	0.2562	0.2491	0.2430	0.2364	0.2302	0.2234	0.2174
6.40	0.2665	0.2654	0.2621	0.2570	0.2504	0.2438	0.2376	0.2314	0.2252	0.2184	0.2124
6.30	0.2600	0.2589	0.2559	0.2510	0.2444	0.2382	0.2320	0.2258	0.2196	0.2134	0.2074



6.20	0.2516	0.2526	0.2450	0.2452	0.2393	0.2323	0.2290	0.2160	0.2007	0.2006	0.1927
6.10	0.2475	0.2465	0.2438	0.2395	0.2339	0.2273	0.2260	0.2124	0.2046	0.1960	0.1891
6.00	0.2414	0.2406	0.2300	0.2339	0.2205	0.2222	0.2153	0.2000	0.2005	0.1729	0.1855
5.90	0.2356	0.2347	0.2121	0.2204	0.2233	0.2173	0.2107	0.2030	0.1964	0.1851	0.1820
5.80	0.2298	0.2280	0.2267	0.2230	0.2182	0.2124	0.2061	0.1993	0.1924	0.1854	0.1789
5.70	0.2242	0.2224	0.2212	0.2177	0.2111	0.2077	0.2016	0.1951	0.1884	0.1816	0.1759
5.60	0.2187	0.2169	0.2157	0.2126	0.2082	0.2030	0.1971	0.1907	0.1845	0.1779	0.1714
5.50	0.2131	0.2116	0.2107	0.2075	0.2031	0.1981	0.1927	0.1860	0.1805	0.1742	0.1679
5.40	0.2080	0.2074	0.2055	0.2025	0.1985	0.1937	0.1884	0.1827	0.1767	0.1706	0.1645
5.30	0.2029	0.2023	0.2005	0.1976	0.1938	0.1892	0.1841	0.1780	0.1728	0.1669	0.1611
5.20	0.1978	0.1972	0.1953	0.1924	0.1891	0.1844	0.1799	0.1740	0.1690	0.1633	0.1576
5.10	0.1928	0.1923	0.1906	0.1880	0.1846	0.1804	0.1757	0.1706	0.1652	0.1598	0.1543
5.00	0.1879	0.1874	0.1859	0.1834	0.1801	0.1761	0.1715	0.1666	0.1615	0.1562	0.1509
4.90	0.1831	0.1826	0.1811	0.1788	0.1750	0.1710	0.1674	0.1626	0.1578	0.1527	0.1475
4.80	0.1784	0.1779	0.1765	0.1742	0.1712	0.1676	0.1634	0.1592	0.1541	0.1492	0.1442
4.70	0.1737	0.1733	0.1719	0.1696	0.1669	0.1634	0.1594	0.1550	0.1504	0.1457	0.1409
4.60	0.1692	0.1687	0.1674	0.1654	0.1626	0.1594	0.1554	0.1513	0.1468	0.1422	0.1376
4.50	0.1647	0.1642	0.1630	0.1610	0.1584	0.1552	0.1515	0.1475	0.1432	0.1388	0.1343
4.40	0.1602	0.1598	0.1587	0.1568	0.1542	0.1512	0.1476	0.1438	0.1397	0.1354	0.1311
4.30	0.1558	0.1555	0.1543	0.1525	0.1501	0.1472	0.1438	0.1401	0.1361	0.1320	0.1278
4.20	0.1515	0.1512	0.1501	0.1484	0.1461	0.1432	0.1400	0.1364	0.1326	0.1287	0.1246
4.10	0.1473	0.1469	0.1459	0.1442	0.1420	0.1393	0.1362	0.1328	0.1291	0.1253	0.1214
4.00	0.1431	0.1427	0.1418	0.1402	0.1381	0.1355	0.1325	0.1292	0.1257	0.1220	0.1182
3.90	0.1387	0.1386	0.1377	0.1362	0.1341	0.1316	0.1288	0.1254	0.1222	0.1187	0.1151
3.80	0.1344	0.1345	0.1336	0.1322	0.1302	0.1277	0.1251	0.1221	0.1188	0.1154	0.1119
3.70	0.1307	0.1305	0.1296	0.1282	0.1264	0.1241	0.1215	0.1186	0.1154	0.1121	0.1088
3.60	0.1267	0.1265	0.1257	0.1243	0.1226	0.1204	0.1179	0.1153	0.1121	0.1089	0.1047
3.50	0.1228	0.1225	0.1217	0.1205	0.1188	0.1167	0.1143	0.1116	0.1087	0.1057	0.1026
3.40	0.1189	0.1186	0.1179	0.1167	0.1150	0.1130	0.1107	0.1082	0.1054	0.1025	0.0995
3.30	0.1150	0.1147	0.1140	0.1129	0.1113	0.1094	0.1072	0.1047	0.1021	0.0993	0.0964
3.20	0.1111	0.1109	0.1102	0.1091	0.1076	0.1058	0.1037	0.1014	0.0988	0.0963	0.0933
3.10	0.1073	0.1071	0.1065	0.1054	0.1040	0.1022	0.1002	0.0980	0.0955	0.0929	0.0903
3.00	0.1035	0.1033	0.1027	0.1017	0.1004	0.0987	0.0968	0.0946	0.0923	0.0898	0.0872
2.90	0.0997	0.0996	0.0990	0.0981	0.0968	0.0952	0.0933	0.0913	0.0890	0.0867	0.0842
2.80	0.0961	0.0959	0.0954	0.0944	0.0932	0.0917	0.0899	0.0880	0.0858	0.0835	0.0812
2.70	0.0924	0.0922	0.0917	0.0909	0.0897	0.0882	0.0865	0.0847	0.0826	0.0804	0.0782
2.60	0.0888	0.0886	0.0881	0.0873	0.0862	0.0848	0.0832	0.0814	0.0794	0.0774	0.0752
2.50	0.0852	0.0850	0.0845	0.0837	0.0827	0.0814	0.0798	0.0781	0.0762	0.0743	0.0722
2.40	0.0816	0.0814	0.0809	0.0802	0.0792	0.0780	0.0765	0.0749	0.0731	0.0712	0.0693
2.30	0.0780	0.0778	0.0774	0.0767	0.0757	0.0746	0.0732	0.0716	0.0699	0.0682	0.0663

2.20	0.0744	0.0743	0.0739	0.0732	0.0723	0.0712	0.0699	0.0684	0.0660	0.0651	0.0633
2.10	0.0707	0.0708	0.0704	0.0690	0.0689	0.0670	0.0666	0.0652	0.0637	0.0621	0.0604
2.00	0.0674	0.0673	0.0669	0.0663	0.0655	0.0643	0.0633	0.0623	0.0606	0.0591	0.0575
1.90	0.0639	0.0630	0.0625	0.0619	0.0621	0.0612	0.0601	0.0588	0.0575	0.0561	0.0546
1.80	0.0604	0.0603	0.0600	0.0595	0.0588	0.0577	0.0568	0.0550	0.0544	0.0531	0.0516
1.70	0.0570	0.0569	0.0566	0.0561	0.0554	0.0546	0.0536	0.0525	0.0513	0.0501	0.0487
1.60	0.0536	0.0535	0.0532	0.0527	0.0521	0.0513	0.0504	0.0494	0.0483	0.0471	0.0458
1.50	0.0501	0.0501	0.0498	0.0494	0.0488	0.0481	0.0472	0.0462	0.0452	0.0441	0.0429
1.40	0.0467	0.0467	0.0464	0.0460	0.0455	0.0448	0.0440	0.0431	0.0422	0.0411	0.0400
1.30	0.0433	0.0433	0.0430	0.0427	0.0422	0.0416	0.0408	0.0400	0.0391	0.0382	0.0372
1.20	0.0400	0.0400	0.0397	0.0394	0.0389	0.0383	0.0377	0.0369	0.0361	0.0352	0.0343
1.10	0.0366	0.0365	0.0363	0.0360	0.0356	0.0351	0.0345	0.0338	0.0330	0.0322	0.0314
1.00	0.0332	0.0332	0.0330	0.0327	0.0324	0.0319	0.0313	0.0307	0.0300	0.0293	0.0285
0.90	0.0299	0.0298	0.0297	0.0294	0.0291	0.0287	0.0282	0.0276	0.0270	0.0264	0.0257
0.80	0.0265	0.0265	0.0264	0.0261	0.0258	0.0255	0.0250	0.0245	0.0240	0.0234	0.0228
0.70	0.0232	0.0232	0.0231	0.0229	0.0226	0.0223	0.0219	0.0215	0.0210	0.0205	0.0199
0.60	0.0199	0.0199	0.0198	0.0196	0.0194	0.0191	0.0188	0.0184	0.0180	0.0175	0.0171
0.50	0.0166	0.0165	0.0165	0.0163	0.0161	0.0159	0.0156	0.0153	0.0150	0.0146	0.0142
0.40	0.0132	0.0132	0.0132	0.0130	0.0127	0.0127	0.0125	0.0122	0.0120	0.0117	0.0114
0.30	0.0099	0.0099	0.0099	0.0098	0.0097	0.0095	0.0094	0.0092	0.0090	0.0088	0.0085
0.20	0.0066	0.0066	0.0066	0.0065	0.0064	0.0064	0.0062	0.0061	0.0060	0.0058	0.0057
0.10	0.0033	0.0033	0.0033	0.0032	0.0032	0.0032	0.0031	0.0031	0.0030	0.0029	0.0028



POTENTIAL DISTRIBUTION ON CYLINDRICAL PORTION OF THE BOUNDARY

$R = 1.0$

ZS	POTENTIAL
11.00	1.0025
12.00	1.0130
13.00	1.0000
14.00	0.9756
15.00	0.9736
16.00	0.9802
17.00	0.9896
18.00	0.9993
19.00	1.0034
20.00	1.0161
21.00	1.0217
22.00	1.0244
23.00	1.0221
24.00	1.0108
25.00	0.9913
26.00	0.9794
27.00	0.9752
28.00	0.9748
29.00	0.9763
30.00	0.9789
31.00	0.9821
32.00	0.9856
33.00	0.9893
34.00	0.9931
35.00	0.9959
36.00	1.0006
37.00	1.0042
38.00	1.0077
39.00	1.0109
40.00	1.0138
41.00	1.0164
42.00	1.0186
43.00	1.0202
44.00	1.0210
45.00	1.0204
46.00	1.0174
47.00	1.0131

POTENTIAL DISTRIBUTION ALONG THE CYLINDRICAL PART OF THE JUNCTION

0.52E 01  
 0.42E 01  
 0.32E 01  
 0.22E 01  
 0.12E 01  
 0.20E 00  
 -0.10E 00  
 -0.18E 01  
 -0.28E 01  
 -0.38E 01  
 -0.48E 01

0.10E 02 0.15E 02 0.25E 02 0.30E 02 0.35E 02 0.40E 02 0.45E 02 0.50E 02 0.55E 02 0.60E 02  
 XMAX = 0.6000E 02 XMIN = 0.1100E 02 YMAX = 0.2642E 01 YMIN = -0.2431E 01 ZMAX = 0.5000E 00 ZMIN = 0.2000E 00

POTENTIAL DISTRIBUTION ON SPHERICAL PORTION OF THE BOUNDARY

ZS	R	POTENTIAL
10.00	0.0735	1.0000
10.01	0.1504	1.0001
10.03	0.2334	1.0001
10.05	0.3090	1.0002
10.08	0.3827	1.0002
10.11	0.4540	1.0003
10.15	0.5225	1.0003
10.19	0.5878	1.0004
10.24	0.6494	1.0004
10.29	0.7071	1.0004
10.35	0.7604	1.0004
10.41	0.8090	1.0004
10.48	0.8526	1.0004
10.55	0.8910	1.0003
10.62	0.9239	1.0003
10.69	0.9511	1.0004
10.77	0.9724	1.0005
10.84	0.9877	1.0008
10.92	0.9969	1.0014
11.00	1.0000	1.0023

POTENTIAL DISTRIBUTION ALONG THE SPHERICAL PART OF THE BOUNDARY

0.10E-01  
-0.15E-01  
-0.10E-01  
-0.55E-01  
-0.70E-01  
-0.11E 00  
-0.14E 00  
-0.16E 00  
-0.17E 00  
-0.21E 00  
-0.24E 00

0.30E-01 0.13E 00 0.23E 00 0.13E 00 0.43E 00 0.53E 00 0.63E 00 0.73E 00 0.83E 00 0.93E 00  
XMAX = 0.1000E 01 AMIN = 0.7845E-01 YMAX = 0.4769E-02 YMIN = -0.2310E 00 AIRCH = 0.1000E-01 YINCH = 0.5000E-02

APPENDIX 3

This table contains utilization factors (U-F) and values of maximum field (Fmax) for different Gap-Length/point -radius ratios (G/R).

<u>G/R</u>	<u>U-F</u>	<u>Fmax</u>	<u>G/R</u>	<u>U-F</u>	<u>Fmax</u>
0.1	0.95845	10.43353	21.0	0.06363	0.74838
0.2	0.89633	5.57827	22.0	0.06112	0.74365
0.3	0.83866	3.97462	23.0	0.05882	0.73923
0.4	0.78732	3.17532	24.0	0.05668	0.73507
0.5	0.74158	2.69693	25.0	0.05471	0.73115
0.6	0.70061	2.37889	26.0	0.05287	0.72745
0.7	0.66371	2.15240	27.0	0.05116	0.72394
0.8	0.63035	1.98301	28.0	0.04956	0.72061
0.9	0.60009	1.85159	29.0	0.04806	0.71745
1.0	0.57253	1.74663	30.0	0.04666	0.71443
2.0	0.39270	1.27322	31.0	0.04534	0.71155
3.0	0.30046	1.10940	32.0	0.04409	0.70879
4.0	0.24448	1.02259	33.0	0.04291	0.70616
5.0	0.20678	0.96720	34.0	0.04180	0.70363
6.0	0.17960	0.92800	35.0	0.04075	0.70120
7.0	0.15902	0.89837	36.0	0.03975	0.69887
8.0	0.14287	0.87492	37.0	0.03880	0.69662
9.0	0.12984	0.85575	38.0	0.03789	0.69445
10.0	0.11909	0.83967	39.0	0.03703	0.69237
11.0	0.11007	0.82592	40.0	0.03621	0.69035
12.0	0.10238	0.81397	41.0	0.03543	0.68840
13.0	0.09574	0.80345	42.0	0.03468	0.68651
14.0	0.08995	0.79408	43.0	0.03397	0.68469
15.0	0.08485	0.78567	44.0	0.03328	0.68292
16.0	0.08033	0.77806	45.0	0.03262	0.68120
17.0	0.07628	0.77111	46.0	0.03199	0.67954
18.0	0.07265	0.76475	47.0	0.03138	0.67792
19.0	0.06935	0.75887	48.0	0.03080	0.67635
20.0	0.06636	0.75344	49.0	0.03024	0.67483



G/R	U-F	Fmax	G/R	U-F	Fmax
50.0	0.02970	0.67334	86.0	0.01826	0.63687
51.0	0.02918	0.67189	87.0	0.01807	0.63616
52.0	0.02868	0.67048	88.0	0.01788	0.63546
53.0	0.02820	0.66911	89.0	0.01770	0.63476
54.0	0.02773	0.66777	90.0	0.01752	0.63408
55.0	0.02728	0.66646	91.0	0.01735	0.63341
56.0	0.02685	0.66519	92.0	0.01718	0.63275
57.0	0.02642	0.66394	93.0	0.01701	0.63209
58.0	0.02602	0.66273	94.0	0.01685	0.63145
59.0	0.02562	0.66154	95.0	0.01669	0.63081
60.0	0.02524	0.66037	96.0	0.01653	0.63018
61.0	0.02487	0.65924	97.0	0.01638	0.62956
62.0	0.02451	0.65812	98.0	0.01622	0.62895
63.0	0.02416	0.65703	99.0	0.01608	0.62835
64.0	0.02382	0.65596	100.0	0.01593	0.62775
65.0	0.02349	0.65492	101.0	0.01579	0.62716
66.0	0.02317	0.65389	102.0	0.01565	0.62658
67.0	0.02286	0.65289	103.0	0.01551	0.62601
68.0	0.02256	0.65191	104.0	0.01537	0.62544
69.0	0.02226	0.65094	105.0	0.01524	0.62488
70.0	0.02198	0.64999	106.0	0.01511	0.62433
71.0	0.02170	0.64906	107.0	0.01498	0.62378
72.0	0.02143	0.64815	108.0	0.01486	0.62324
73.0	0.02116	0.64725	109.0	0.01473	0.62271
74.0	0.02091	0.64637	110.0	0.01461	0.62218
75.0	0.02066	0.64550	111.0	0.01449	0.62166
76.0	0.02041	0.64465	112.0	0.01437	0.62115
77.0	0.02017	0.64382	113.0	0.01426	0.62064
78.0	0.01994	0.64299	114.0	0.01415	0.62013
79.0	0.01971	0.64219	115.0	0.01403	0.61963
80.0	0.01949	0.64139	116.0	0.01392	0.61914
81.0	0.01927	0.64061	117.0	0.01382	0.61865
82.0	0.01906	0.63984	118.0	0.01371	0.61817
83.0	0.01885	0.63908	119.0	0.01360	0.61770
84.0	0.01865	0.063833	120.0	0.01350	0.61722
85.0	0.01845	0.063760	121.0	0.01340	0.61676

G/R	U-F	Fmax	G/R	U-F	Fmax
122.0	0.01330	0.61629	158.0	0.01051	0.60226
123.0	0.01320	0.61584	159.0	0.01045	0.60193
124.0	0.01310	0.61538	160.0	0.01039	0.60160
125.0	0.01301	0.61494	161.0	0.01033	0.60128
126.0	0.01292	0.61449	162.0	0.01027	0.60095
127.0	0.01282	0.61405	163.0	0.01021	0.60063
128.0	0.01273	0.61362	164.0	0.01016	0.60031
129.0	0.01264	0.61319	165.0	0.01010	0.60000
130.0	0.01255	0.61276	166.0	0.01005	0.59968
131.0	0.01247	0.61234	167.0	0.00999	0.59937
132.0	0.01238	0.61192	168.0	0.00994	0.59906
133.0	0.01230	0.61151	169.0	0.00988	0.59876
134.0	0.01221	0.61110	170.0	0.00983	0.59845
135.0	0.01213	0.61069	171.0	0.00978	0.59815
136.0	0.01205	0.61029	172.0	0.00972	0.59785
137.0	0.01197	0.60989	173.0	0.00967	0.59755
138.0	0.01189	0.61949	174.0	0.00962	0.59726
139.0	0.01181	0.60910	175.0	0.00957	0.59696
140.0	0.01173	0.60871	176.0	0.00952	0.59667
141.0	0.01166	0.60833	177.0	0.00947	0.59638
142.0	0.01158	0.60794	178.0	0.00942	0.59609
143.0	0.01151	0.60757	179.0	0.00938	0.59581
144.0	0.01144	0.60719	180.0	0.00933	0.59552
145.0	0.01137	0.60682	181.0	0.00928	0.59524
146.0	0.01129	0.60645	182.0	0.00924	0.59496
147.0	0.01122	0.60609	183.0	0.00919	0.59468
148.0	0.01115	0.60572	184.0	0.00914	0.59441
149.0	0.01109	0.60537	185.0	0.00910	0.59413
150.0	0.01102	0.60501	186.0	0.00905	0.59386
151.0	0.01095	0.60466	187.0	0.00901	0.59359
152.0	0.01089	0.60431	188.0	0.00897	0.59332
153.0	0.01082	0.60396	189.0	0.00892	0.59305
154.0	0.01076	0.61361	190.0	0.00888	0.59279
155.0	0.01069	0.60327	191.0	0.00884	0.59252
156.0	0.01063	0.60293	192.0	0.00879	0.59226
157.0	0.01057	0.60260	193.0	0.00875	0.59200

G/R	U-F	Fmax	G/R	U-F	Fmax
194.0	0.00871	0.59174	231.0	0.00742	0.58319
195.0	0.00867	0.59149	232.0	0.00739	0.58298
196.0	0.00863	0.59123	233.0	0.00736	0.58277
197.0	0.00859	0.59098	234.0	0.00734	0.58257
198.0	0.00855	0.59073	235.0	0.00731	0.58236
199.0	0.00851	0.59048	236.0	0.00728	0.58216
200.0	0.00847	0.59023	237.0	0.00725	0.58196
201.0	0.00843	0.58998	238.0	0.00722	0.58176
202.0	0.00839	0.58973	239.0	0.00719	0.58156
203.0	0.00836	0.58949	240.0	0.00717	0.58136
204.0	0.00832	0.58925	241.0	0.00714	0.58116
205.0	0.00828	0.58900	242.0	0.00711	0.58096
206.0	0.00825	0.58876	243.0	0.00709	0.58077
207.0	0.00821	0.58852	244.0	0.00706	0.58057
208.0	0.00817	0.58829	245.0	0.00703	0.58038
209.0	0.00814	0.58805	246.0	0.00701	0.58018
210.0	0.00810	0.58782	247.0	0.00698	0.57999
211.0	0.00807	0.58758	248.0	0.00695	0.57980
212.0	0.00803	0.58735	249.0	0.00693	0.57961
213.0	0.00800	0.58712	250.0	0.00690	0.57942
214.0	0.00796	0.58689	251.0	0.00688	0.57923
215.0	0.00793	0.58666	252.0	0.00685	0.57905
216.0	0.00789	0.58644	253.0	0.00683	0.57886
217.0	0.00786	0.58621	254.0	0.00680	0.57867
218.0	0.00783	0.58599	255.0	0.00678	0.57849
219.0	0.00780	0.58577	256.0	0.00675	0.57830
220.0	0.00776	0.58555	257.0	0.00673	0.57812
221.0	0.00773	0.58532	258.0	0.00671	0.57794
222.0	0.00770	0.58511	259.0	0.00668	0.57776
223.0	0.00767	0.58489	260.0	0.00666	0.57758
224.0	0.00764	0.58467	261.0	0.00664	0.57740
225.0	0.00760	0.58446	262.0	0.00661	0.57722
226.0	0.00757	0.58424	263.0	0.00659	0.57704
227.0	0.00754	0.58403	264.0	0.00657	0.57686
228.0	0.00751	0.58382	265.0	0.00654	0.57669
229.0	0.00748	0.58361	266.0	0.00652	0.57651
230.0	0.00745	0.58340	267.0	0.00650	0.57634

G/R	U-F	Fmax	G/R	U-F	Fmax
268.0	0.00648	0.57616	304.0	0.00577	0.57038
269.0	0.00645	0.57599	305.0	0.00575	0.57023
270.0	0.00643	0.57582	306.0	0.00573	0.57008
271.0	0.00641	0.57565	307.0	0.00572	0.56993
272.0	0.00639	0.57548	308.0	0.00570	0.56979
273.0	0.00637	0.57531	309.0	0.00568	0.56964
274.0	0.00635	0.57514	310.0	0.00566	0.56949
275.0	0.00632	0.57497	311.0	0.00565	0.56935
276.0	0.00630	0.57480	312.0	0.00563	0.56920
277.0	0.00628	0.57483	313.0	0.00561	0.56906
278.0	0.00626	0.57447	314.0	0.00560	0.56892
279.0	0.00624	0.57430	315.0	0.00558	0.56877
280.0	0.00622	0.57414	316.0	0.00557	0.56863
281.0	0.00620	0.57397	317.0	0.00555	0.56849
282.0	0.00618	0.57381	318.0	0.00553	0.56835
283.0	0.00616	0.57364	319.0	0.00552	0.56821
284.0	0.00614	0.57348	320.0	0.00550	0.56807
285.0	0.00612	0.57332	321.0	0.00549	0.56793
286.0	0.00610	0.57316	322.0	0.00547	0.56779
287.0	0.00608	0.57300	323.0	0.00545	0.56765
288.0	0.00606	0.57284	324.0	0.00544	0.56751
289.0	0.00604	0.57268	325.0	0.00542	0.56737
290.0	0.00602	0.57252	326.0	0.00541	0.56724
291.0	0.00600	0.57237	327.0	0.00539	0.56710
292.0	0.00598	0.57221	328.0	0.00538	0.56696
293.0	0.00597	0.57205	329.0	0.00536	0.56683
294.0	0.00595	0.57190	330.0	0.00535	0.56669
295.0	0.00593	0.57174	331.0	0.00533	0.56656
296.0	0.00591	0.57159	332.0	0.00532	0.56642
297.0	0.00589	0.57144	333.0	0.00530	0.56629
298.0	0.00587	0.57128	334.0	0.00529	0.56616
299.0	0.00586	0.57113	335.0	0.00527	0.56602
300.0	0.00584	0.57098	336.0	0.00526	0.56589
301.0	0.00582	0.57083	337.0	0.00524	0.56576
302.0	0.00580	0.57068	338.0	0.00523	0.56563
303.0	0.00578	0.57053	339.0	0.00522	0.56550

<u>G/R</u>	<u>U-F</u>	<u>Fmax</u>	<u>G/R</u>	<u>U-F</u>	<u>Fmax</u>
340.0	0.00520	0.56537	376.0	0.00474	0.56096
341.0	0.00519	0.56524	377.0	0.00473	0.56084
342.0	0.00517	0.56511	378.0	0.00472	0.56073
343.0	0.00516	0.56498	379.0	0.00471	0.56061
344.0	0.00515	0.56485	380.0	0.00470	0.56050
345.0	0.00513	0.56472	381.0	0.00468	0.56039
346.0	0.00512	0.56459	382.0	0.00467	0.56027
347.0	0.00511	0.56447	383.0	0.00466	0.56016
348.0	0.00509	0.56434	384.0	0.00465	0.56005
349.0	0.00508	0.56421	385.0	0.00464	0.55994
350.0	0.00507	0.56409	386.0	0.00463	0.55982
351.0	0.00505	0.56396	387.0	0.00462	0.55971
352.0	0.00405	0.56384	388.0	0.00461	0.55960
353.0	0.00503	0.56371	389.0	0.00459	0.55949
354.0	0.00501	0.56359	390.0	0.00458	0.55938
355.0	0.00500	0.56347	391.0	0.00457	0.55927
356.0	0.00499	0.56334	392.0	0.00456	0.55916
357.0	0.00497	0.56322	393.0	0.00455	0.55905
358.0	0.00496	0.56310	394.0	0.00454	0.55894
359.0	0.00495	0.56297	395.0	0.00453	0.55883
360.0	0.00494	0.56285	396.0	0.00452	0.55872
361.0	0.00492	0.56273	397.0	0.00451	0.55862
362.0	0.00491	0.56261	398.0	0.00450	0.55851
363.0	0.00490	0.56249	399.0	0.00449	0.55840
364.0	0.00489	0.56237	400.0	0.00448	0.55829
365.0	0.00487	0.56225	401.0	0.00447	0.55819
366.0	0.00486	0.56213	402.0	0.00446	0.55808
367.0	0.00485	0.56201	403.0	0.00445	0.55797
368.0	0.00484	0.56189	404.0	0.00444	0.55787
369.0	0.00482	0.56178	405.0	0.00443	0.55776
370.0	0.00481	0.56166	406.0	0.00442	0.55766
371.0	0.00480	0.56154	407.0	0.00441	0.55755
372.0	0.00479	0.56142	408.0	0.00440	0.55745
373.0	0.00478	0.56131	409.0	0.00439	0.55734
374.0	0.00476	0.56119	410.0	0.00438	0.55724
375.0	0.00475	0.56107	411.0	0.00437	0.55713

G/R	U-F	Fmax	G/R	U-F	Fmax
412.0	0.00436	0.55703	448.0	0.00403	0.55349
413.0	0.00435	0.55693	449.0	0.00402	0.55340
414.0	0.00434	0.55682	450.0	0.00402	0.55331
415.0	0.00433	0.55672	451.0	0.00401	0.55321
416.0	0.00432	0.55662	452.0	0.00400	0.55312
417.0	0.00431	0.55652	453.0	0.00399	0.55303
418.0	0.00430	0.55642	454.0	0.00398	0.55294
419.0	0.00429	0.55631	455.0	0.00398	0.55284
420.0	0.00428	0.55621	456.0	0.00397	0.55275
421.0	0.00427	0.55611	457.0	0.00396	0.55266
422.0	0.00426	0.55601	458.0	0.00395	0.55257
423.0	0.00425	0.55591	459.0	0.00394	0.55248
424.0	0.00424	0.55581	460.0	0.00394	0.55239
425.0	0.00423	0.55571	461.0	0.00393	0.55230
426.0	0.00422	0.55561	462.0	0.00392	0.55221
427.0	0.00422	0.55551	463.0	0.00391	0.55212
428.0	0.00421	0.55541	464.0	0.00390	0.55203
429.0	0.00420	0.55532	465.0	0.00390	0.55194
430.0	0.00419	0.55522	466.0	0.00389	0.55185
431.0	0.00418	0.55512	467.0	0.00388	0.55176
432.0	0.00417	0.55502	468.0	0.00387	0.55167
433.0	0.00416	0.55492	469.0	0.00387	0.55158
434.0	0.00415	0.55483	470.0	0.00386	0.55149
435.0	0.00414	0.55473	471.0	0.00385	0.55140
436.0	0.00414	0.55463	472.0	0.00384	0.55132
437.0	0.00413	0.55454	473.0	0.00384	0.55123
438.0	0.00412	0.55444	474.0	0.00383	0.55114
439.0	0.00411	0.55434	475.0	0.00382	0.55105
440.0	0.00410	0.55425	476.0	0.00381	0.55097
441.0	0.00409	0.55415	477.0	0.00381	0.55088
442.0	0.00408	0.55406	478.0	0.00380	0.55079
443.0	0.00407	0.55396	479.0	0.00379	0.55071
444.0	0.00407	0.55387	480.0	0.00378	0.55062
445.0	0.00406	0.55377	481.0	0.00378	0.55053
446.0	0.00405	0.55368	482.0	0.00377	0.55045
447.0	0.00404	0.55359	483.0	0.00376	0.55036

<u>G/R</u>	<u>U-F</u>	<u>Fmax</u>
484.0	0.00375	0.55028
485.0	0.00375	0.55019
486.0	0.00374	0.55011
487.0	0.00373	0.55002
488.0	0.00373	0.54994
489.0	0.00372	0.54985
490.0	0.00371	0.54977
491.0	0.00371	0.54969
492.0	0.00370	0.54960
493.0	0.00369	0.54952
494.0	0.00368	0.54944
495.0	0.00368	0.54935
496.0	0.00367	0.54927
497.0	0.00366	0.54919
498.0	0.00366	0.54910
499.0	0.00365	0.54902
500.0	0.00364	0.54894
501.0	0.00364	0.54886

Note: This table is derived using the conventional charge simulation technique for one set of charge positions ( $r_i', z_i'$ ). For better accuracy, the values of U-F and Fmax for  $G/R < 1.0$ , should be calculated individually using the optimized charge simulation technique.

## APPENDIX 4

### ANALYSIS OF THE PHOTOMULTIPLIER RESULTS

The photomultiplier (PM) results were initially interpreted on the basis of similar traces obtained in temporal growth measurements of pre-breakdown coronas (16). However, the absence of a current pulse corresponding to the last PM pulse (Figure 5.13) and Dale's (84) suggestion of saturation of the PM tube, led to a further analysis of the PM traces.

In pre-breakdown measurements, the space charge travels to the electrode of the opposite polarity under the force of the applied field, and recombination will generate a relatively broad pulse after a time depending on the distance of the space charge from the electrode and the diffusion velocity of the charge carriers. Under the present conditions, at the time of the first PM peak the impulse voltage collapses to zero and the electrostatic forces acting on the charge carriers are mainly of two types. First, electrostatic forces acting in the volume of the gas and second, forces acting on the image charges on the surface of the grounded electrodes and surrounding walls. Drift forces produced by electric wind will also be present but their effect is not clearly understood. Apart from these directional forces, the gas molecules in the neighborhood of the discharge are forced into random motion with kinetic energies related to the temperature of the spark channel and the thermal conductivity of the gas.

The recombination will therefore take place in the



volume of the gas, as well as on the grounded electrode and walls of the chamber. There are two major types of recombination

(1) Electron - Ion recombination.

(2) Ion - Ion recombination.

In an inert gas like nitrogen the recombination processes are mainly of type (1). In electronegative gases such as  $SF_6$  or  $SF_6/N_2$  mixtures, both types are expected to be present.

In the gas volume, recombination between ions of opposite charge has been found to be more efficient than that of an electron with a positive ion. The electrons due to their low mass move faster than the ions and this reduces the probability of their capture. The negative and positive ions have approximately the same mass and charge, and move with relatively low diffusion speeds. This increases the interaction time and the probability of the electron exchange between the two is quite high.

At the surface of the electrodes, the efficiency of the electron-ion recombination is probably the highest, due to the two dimensional diffusion of the ions and the high energy absorption of the solid surface. However, diffusion of ions to the electrodes is governed by the ambipolar diffusion in the volume of the gas. This depends on the number and position of the positive and negative ions with respect to each other and the electrode surfaces. Assuming that the two different charge carriers are uniformly distributed and have equal numbers, the recombination processes are principally of the ion - ion type and follow an exponential decay (30). In the presence of a space charge with uneven distribution and number of opposite polarity carriers, the type and rate of recombination becomes unpredictable.

Furthermore, the monitoring of the light emitted from the gap region will not give a true picture of the recombination rate since some reactions do not involve photon emission.

Therefore, on the basis of the limited information provided by the PM traces one had little alternative but to identify the last pulse as light emitted from the recombination process, which was thought to occur at the surface of the electrodes. Dale however, in a discussion with the author, pointed out that he had obtained similar photomultiplier results from breakdown of rod-plane gaps in air. In his experiments Dale used a streak camera simultaneously with the photomultiplier and compared the results. The time of streak  $t_s$  with respect to the PM output is shown in Figure D.1 (c). As it is seen, the PM current dropped sharply within the time  $t_s$ , while the streak photographs showed a constant light intensity. This led Dale to believe that the photomultiplier was saturating in some way, and that the final broad pulse was also a saturation effect. He explained the sharp drop of the first peak by assuming that the high illumination of the PM cathode creates a space charge above the cathode, which chokes further electron emission to the dynodes and reduces the PM signal. Not being able to explain the origin of the so called recombination pulse he tried to eliminate it by inserting neutral filters in front of the PM cathode. The reduction of the light did not result in a disappearance of the peak as one would have expected, but rather in a shift to shorter times of appearance.

A number of tests were also conducted by the author to test the present PM system for saturation. A light emitting

diode was placed close to the PM cathode and a square wave signal of variable frequency was applied across it. The input voltage to the diode and the output current of the photomultiplier are shown in Figure D.1 (a) and D.1 (b) respectively. At low light intensities the input and output signals were

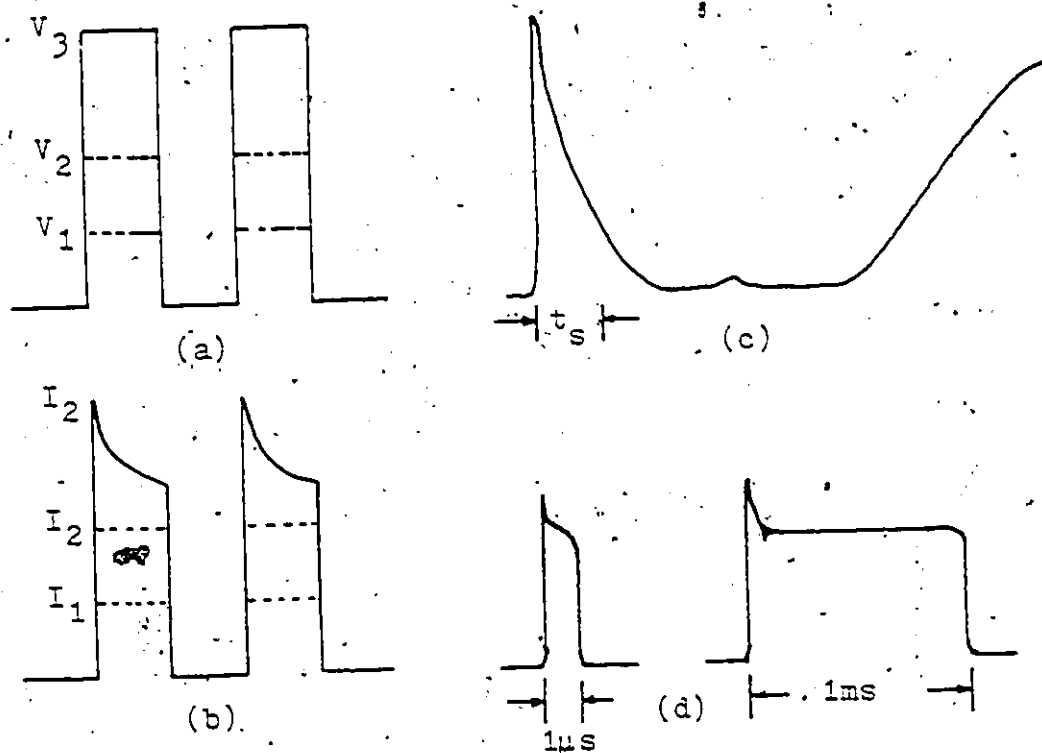


Figure D.1. (a) Voltage input to the light emitting diode (LED),  $V_3 > V_2 > V_1$ . (b) Photomultiplier current corresponding to different illumination intensities of the LED. (c) Photomultiplier trace and relative streak photograph duration. (d) Photomultiplier current for single light pulses (note that no secondary peaks are observed).

identical. As the intensity of the LED increased further, the PM output current did not respond accordingly, thus showing signs of saturation; and, for both repetitive and single pulses of light (Figure D.1 (d)), no secondary pulse similar to that of

Figure D.1 (c) was observed. In another test, the pin-hole regulating the light received by the photomultiplier cathode was made smaller. In reducing the diameter from 100 to 50 microns the magnitude of both peaks decreased considerably and the second pulse appeared at shorter intervals. In reducing the aperture to 10 microns the PM signal became compatible to noise in the system and while the second peak disappeared, the initial peak associated with the leader and main stroke resembled transient noise.

In conclusion, it is believed that the last broad pulse is in fact due to some type of photomultiplier saturation. It seems that the level of the PM signal at saturation free conditions is of the same order as the noise picked up by the anode of the photomultiplier and the signal cable. Hence, observation of any actual post breakdown activity under these conditions is extremely difficult.

The photomultiplier results were helpful in suggesting that the ionization mechanism operative in mixtures with a small trace of  $SF_6$  was different from that of pure  $N_2$  or pure  $SF_6$ . As shown in Figure 5.14(b) the luminosity of the coronas increased with the addition of 0.05% of  $SF_6$ , and at the pressure range where the voltage maximum occurred (around 2 bar) the luminosity of the spark channel also increased. Photographic evidence in agreement with this, showed that corona streamers not only increased in luminosity, but they also appeared to surround the cylindrical part of the electrode. Similarly, the higher luminosity at the point of breakdown was the result

of the longer spark due to the creep phenomenon of the discharge. In addition, the photomultiplier traces provided an accurate measurement of the time lag between the corona pulse and spark onset.

VITA AUCTORIS

Born January 1951 in Athens Greece.

Completed primary education in Athens. Moved to Sydney Australia in 1963 and attended the Bondi Junction High School (forms 1 to 4). Returned to Greece in 1967 and in 1968 graduated from Officers Hill High School - Athens. In 1969 moved back to Melbourne Australia and in 1973 graduated from the Royal Melbourne Institute of Technology with a B.Sc. in Applied Physics.

Joined Medtron Electronics Inc. as a project engineer in January 74 until May 1974 when moved to Windsor - Canada.

Graduated from the University of Windsor with a M.Sc degree in Physics in June 1975.

Joined the high voltage group of the Electrical Engineering Department in June 1975, candidate for a Ph.D degree in January 1978.